DOCTORAL THESIS

Mathematical Modeling and Control Strategies for Islanded Microgrids

Andreas Armstorfer

Mathematical Modeling and Control Strategies for Islanded Microgrids

ANDREAS ARMSTORFER

TAL
TECH
PRESS

TALLINN UNIVERSITY OF TECHNOLOGY
School of Engineering
Department of Electrical Power Engineering and Mechatronics

The dissertation was accepted for the defence of the degree of Doctor of Philosophy (electrical drives and power electronics) on 18 November 2022

Supervisor: Prof. Dr. Argo Rosin,
Department of Electrical Power Engineering and Mechatronics,
School of Engineering,
Tallinn University of Technology,
Tallinn, Estonia

Co-supervisor: Prof. Dr.-Ing. Dr. h.c. Helmuth Biechl,
Institute of Electrical Power Systems (IEES),
Kempten University of Applied Sciences,
Kempten, Germany

Opponents: Prof. Andres Annuk, PhD,
Chair of Energy Application Engineering,
Institute of Forestry and Engineering,
Estonian University of Life Sciences,
Tartu, Estonia

Assoc. Prof. Dr.Sc.Ing. Janis Zakis,
Institute of Industrial Electronics and Electrical Engineering,
Riga Technical University,
Riga, Latvia

Defence of the thesis: 19 December 2022, Tallinn

Declaration:
Hereby I declare that this doctoral thesis, my original investigation and achievement, submitted for the doctoral degree at Tallinn University of Technology, has not been submitted for any academic degree elsewhere.

Andreas Armstorfer

_____
signature

Saartalitluses mikrovõrkude matemaatiline modelleerimine ja juhtimisstrateegiad

ANDREAS ARMSTORFER

Contents

List of Publications

The thesis is based on the following publications:

   I A. Armstorfer, H. Biechl, and A. Rosin. Voltage and reactive power control in islanded microgrids without communication link. *Proceedings of the Biennial Baltic Electronics Conference, BEC*, pages 1–6, 2020

  II A. Armstorfer, H. Biechl, and A. Rosin. Analysis of black start strategies for microgrids with renewable distributed generation. *IECON Proceedings (Industrial Electronics Conference)*, pages 2121–2125, 2019

 III N. Beg, A. Armstorfer, A. Rosin, and H. Biechl. Mathematical modeling and stability analysis of a microgrid in island operation. *2018 International Conference on Smart Energy Systems and Technologies (SEST)*, pages 1–6, 2018

 IV A. Armstorfer, H. Biechl, and A. Rosin. Energy scheduling of battery storage systems in micro grids. *The Scientific Journal of Riga Technical University - Electrical, Control and Communication Engineering*, 12(1):27–33, 2017

  V A. Armstorfer, N. Beg, A. Rahmoun, A. Rosin, and H. Biechl. Mathematical modeling and evaluation of a microgrid demonstrator in island mode. *Conference on Sustainable Energy Supply and Energy Storage Systems NEIS 2017*, 1(1):39–44, 2017

 VI A. Rahmoun, A. Armstorfer, H. Biechl, and A. Rosin. Mathematical modeling of a battery energy storage system in grid forming mode. *2017 IEEE 58th International Scientific Conference on Power and Electrical Engineering of Riga Technical University (RTUCON)*, pages 1–6, 2017

VII A. Rahmoun, A. Armstorfer, J. Helguero, H. Biechl, and A. Rosin. Mathematical modeling and dynamic behavior of a lithium-ion battery system for microgrid application. *2016 IEEE International Energy Conference (ENERGYCON)*, pages 1–6, 2016

VIII N. Beg, A. Rahmoun, A. Armstorfer, A. Rosin, and H. Biechl. Determination methods for controller parameters of back-to-back converters in electric power grids. *2016 Electric Power Quality and Supply Reliability (PQ)*, pages 157–164, 2016

Author's Contributions to the Publications

The author's contributions to the papers are:

I   In I, Andreas Armstorfer as the main author analyzed the reactive power demand in rural distribution grids, developed the fuzzy-based control algorithm for voltage and reactive power control in islanded microgrids and verified the concept by specific simulations.

II   In II, Andreas Armstorfer as the main author developed the model for distributed generation based on the application guide VDE AR-N4105 and showed a verification by specific measurements. Further Andreas Armstorfer established the simulation model and analyzed the results for different scenarios.

III   In III, Andreas Armstorfer co-authored the paper, developed an improved genset model including comparison with measurements. Further Andreas Armstorfer was participating in the setup of the experiments as well as in the analysis of the measurement results.

IV   In IV, Andreas Armstorfer as the main author developed the algorithm, established the simulation model, and analyzed the results.

V   In V, Andreas Armstorfer co-authored the paper, developed the genset model, set up the experiments at the demonstrator microgrid and participated in the analysis of the measurement results including comparison with simulation results.

VI   In VI, Andreas Armstorfer co-authored the paper, was participating in the modeling of the control algorithm and in executing measurements at the existing battery storage system for comparison with mathematical models.

VII   In VII, Andreas Armstorfer co-authored the paper, analyzed the battery voltage response for different battery stages of aging and the corresponding effect on the current harmonics.

VIII   In VIII, Andreas Armstorfer co-authored the paper, described the system overview and supported the analysis of the simulation results.

Abbreviations

ABSS	Area Battery Storage System
AC	Alternate Current
APC	Active Power Control
AWU	Anti-Windup
B2B	Back-to-Back Station
BSS	Battery Storage System
CBSS	Campus Battery Storage System
CHP	Combined Heat and Power Plant
COP	Coefficient of Power
CSI	Current Source Inverter
DC	Direct Current
DG	Distributed Generation
GFU	Grid Forming Unit
GSU	Grid Supporting Unit
HBSS	Home Battery Storage System
HV	High Voltage
ICT	Information and Communication Technology
IEES	Institute of Electrical Power System of the University of Applied Sciences Kempten, Kempten (Germany)
LV	Low Voltage
MCW	Microgrid Campus Wildpoldsried
MISO	Multiple Input Single Output
MV	Medium Voltage
ODE	Ordinary Differential Equation
P2H	Power-to-Heat
PCC	Point of Common Coupling
PV	Photovoltaics System
RPC	Reactive Power Control
SISO	Single Input Single Output
SLD	Single Line Diagram
SOE	State of Energy
SM	Synchronous Machine
VLC	Voltage Level Control
VSI	Voltage Source Inverter

1 Introduction

The electrical energy system is in a transition process from centralized power plants to a decentralized power system with renewable energy sources. In Germany, this was enforced by the German Renewable Energy Sources Act (EEG) [34] in the year 2000 where a guaranteed feed-in price for renewable energy sources was defined.

In 2011, the nuclear phase-out was decided by the German Parliament [20] for the year 2022, which increased the importance of the energy transition.

The Paris Agreement from 2016, which was signed by 195 countries, defines the following goals:

(a) "Holding the increase in the global average temperature to well below 2 °C above pre-industrial levels and pursuing efforts to limit the temperature increase to 1.5 °C above pre-industrial levels, recognizing that this would significantly reduce the risks and impacts of climate change;

(b) Increasing the ability to adapt to the adverse impacts of climate change and foster climate resilience and low greenhouse gas emissions development, in a manner that does not threaten food production; and

(c) Making finance flows consistent with a pathway towards low greenhouse gas emissions and climate-resilient development." [68]

The combination of the described laws enforces the importance of power systems using renewable energy sources. This enables, but also requires new grid structures and concepts.

Microgrids [43] enable the structured integration of distributed generation (DG) units such as photovoltaics (PV) in combination with rotating generation units and inverter-based energy storage systems in interconnected, but also in island grids. Distinction is made between permanent island mode operation (without connection to further grid areas) and temporary island operation, which is also described in the German concept of the *cellular approach* [98]. Due to the capability of islanded microgrids for black start and resynchronization, also a bottom up grid restoration in case of major failures is possible.

Another aspect which influences the demand of electrical energy is the transition in heating, also based on the Paris Law [68]. An increasing number of heat pumps is installed instead of conventional gas systems.

This thesis deals with islanded microgrids in general, but the focus is set on rural low voltage (LV) grids in Germany. Therefore, special regulations regarding DG operation and grid quality are considered, such as *VDE AR-N4105* [99] or *DIN EN 50160* [29]. That means that control strategies are optimized for these regulations.

Therefore, simulation models for different microgrid assets are developed and later verified by specific measurements at a demonstration and test grid at the Microgrid Campus Wildpoldsried (MCW), which is located in the south of Germany.

Fig. 1 outlines the experiment area MCW.

Further control strategies for the operation of islanded microgrids, which are considering the local regulations, are developed and verified by simulations.

The goal of this thesis is to develop resilient strategies under consideration of a high grade of practical application.

The models and control strategies can be used as a basis for planning and dimensioning of islanded microgrids on the one hand and for the design of a microgrid control system on the other hand.

Figure 1 – Overview of the MCW area (copyright: Fotodesign Suchy).

1.1 Thesis Objectives

The main objective of this scientific work is to develop and analyse a resilient strategy for planning, dimensioning and operation of islanded microgrids with improved consideration of the specific operation behavior of distributed energy sources and storage systems in Germany based on verified mathematical asset models.

A further aim is to consider of delays due to low-bandwidth data communication between distributed assets in the research and development of microgrid control systems.

1.2 Hypotheses

The main hypotheses of this thesis are:

- Novel developed centralized microgrid control improves the dynamic behavior and stability of systems with delays due to (Ethernet-based) communication.

- Novel energy scheduling algorithm for battery storage systems will improve the usage of distributed generation and thus reduce the consumption of (fossil) primary energy in islanded microgrids.

- New failsafe control algorithm will reduce the reactive power exchange and increase the voltage stability in island grids without centralized communication system or communication link.

- New failsafe control will also enhance the interaction between battery storage systems and generation sets to improve the usage of distributed generation in case of communication loss.

1.3 Research Tasks

The central research tasks of the thesis are:

1. Mathematical modeling of microgrid assets including verification at existing assets located at the MCW.

2. Analysis of parallel operation of inverter-based and rotating assets by simulation and specific measurements in island mode operation.

3. Development of control strategies using a centralized control center under consideration of Ethernet-based communication.

4. Development of a resilient control strategy for failsafe operation without communication link between the assets.

5. Further control strategies such as energy scheduling, black start and resynchronization.

1.4 Contribution and Dissemination

This thesis gives an extensive insight into the design of islanded microgrids considering the feasibility in practical application. Contributions were delivered in the modeling of microgrid assets and the control strategy for islanded microgrids with respect to the specific operation behavior of distributed generation regarding VDE AR-N4105 as well as low-bandwidth communication between distributed grid forming assets. It is recommended to microgrid designers as well as island grid operators.

Scientific Novelties:
- A method for nonlinear modeling of generation sets with turbocharged prime mover based on Fuzzy logic and comparison with a linear model.

- An improved centralized control approach for island grids with distributed grid forming units considering communication delays caused by Ethernet-based connection and protocol converters.

- A failsafe strategy for active power control and reactive power exchange minimization in case of communication loss.

Practical Novelties:
- Verified models for typical island grid assets such as grid forming battery storage systems, grid supporting battery storage systems, generation sets, photovoltaic plants, and heat pumps.

- Improved strategies for resilient island grid dimensioning and planning based on verified models under consideration of effects such as delay times in real applications.

The research presented in this thesis has been disseminated in 7 international conference papers, 1 peer-reviewed international journal and 2 doctoral schools in form of oral presentations.

2 State of the Art

The nuclear phase-out [20] and emission reduction according to the Paris Agreement [68] necessitate an increase of the usage of renewable energy sources. The transition from an electrical power system based on few fossil or nuclear power plants to a grid consisting of a very high amount of distributed volatile energy sources enables grid concepts such as microgrids [43].

It is distinguished between AC and DC microgrids [39] whereas AC systems are dominating as the majority of electrical loads are designed for that voltage type. Therefore, DC microgrids are not further investigated in the frame of this work.

Microgrids can be operated in grid-connected mode, but also as island grids [96]. In the grid-connected mode, assets such as BSSs are operated as current source inverters with control of active and reactive power. However, in islanded microgrids, at least one grid forming unit with frequency and voltage control is obligatory. As the focus in this thesis is set on islanded microgrids, in this chapter, the state of the art with focus on control strategies is explained.

2.1 Fundamentals of Droop Control Concept for Grid Forming Units

Grid forming units (GFUs) play an essential role in islanded microgrids. These assets are in charge to ensure a stable frequency and voltage within predefined limits and are compulsory for black start. GFUs are, for example, gensets or battery storage systems with grid forming capability.

A common control method for voltage and frequency is based on droop control [39]. This enables active power sharing of GFUs without direct communication link between the assets as the steady state grid frequency is varied depending on the active power demand in the grid and equal at all assets.

For reactive power, the concept is used for reactive power/voltage control. As the voltage is a local phenomena, it cannot be used for accurate reactive power sharing. Nevertheless it can reduce reactive power exchange between the GFUs.

First, distinction is made between droop control typically used for conventional (transmission) grids and that for islanded microgrids.

Table 1 presents the fundamental differences between the strategies.

Table 1 – Overview of droop control characteristics including comparison of conventional (transmission grids) and islanded microgrids.

Conventional (Transmission) Grids	Islanded Microgrids
$P(f)$ characteristics $\rightarrow$ increased active power feed-in in the case of decreasing frequency	$f(P)$ characteristics $\rightarrow$ intended frequency decrease in the case of raising active power demand
$Q(V)$ characteristics for grid voltage stabilization	$V(Q)$ characteristics for improved reactive power sharing
In islanded microgrids: grid supporting units (section 3.3)	Used for inverter-based grid forming units (section 3.2)

In islanded microgrids, everal operation strategies can be distinguished. Main strategies are:

1. Standalone operation of one grid forming unit (GFU)

2. Parallel operation of GFUs

3. Parallel operation of grid forming and grid supporting units

For standalone GFUs, the grid frequency is controlled to the rated frequency in steady state. It has to be ensured that the allowed limits of voltage are not exceeded at any node inside the grid. For Germany, the norm DIN EN 50160 [29] defines the voltage limits at $\pm 10\%$ around the rated voltage. Further, this norm defines characteristics regarding voltage quality such as flicker, voltage harmonics or asymmetrical voltage; these have to be taken into account in the design of the system, but are not investigated in this work.

In islanded microgrids with parallel operated GFUs, a stable voltage and frequency as well as controlled power sharing between grid forming assets have to be ensured. One common concept is based on droop control. Several sources have discussed this topic for grids with inverters and/or gensets [83, 48, 35, 88, 76]. In this control strategy, the grid frequency is used for very fast communication between the assets without the need of extra communication links such as Ethernet-based systems. It is based on the fact that considering steady state, the grid frequency is equal in the complete grid area. Depending on the load, a corresponding frequency deviation is accepted. The correlation between load and frequency deviation is called *droop factor* k_f.

In conventional (transmission) grids, for active power and frequency, a $P(f)$ characteristic is used. That means that power plants are increasing the active power feed-in at decreasing frequency. For reactive power, a $Q(V)$ characteristic is used for voltage stabilization of the grid.

In islanded microgrids, the inverse droop concept with a $f(P)$ characteristic is widely used. That means an intended frequency decrease at a raising active power demand at each GFU. Further, a $V(Q)$ characteristic is assumed for an improved reactive power sharing.

For active power and frequency, the mathematical relation is as follows [39]:

$$f_{set} = f_0 - \frac{1}{k_f} \cdot \frac{1}{1 + sT_{kf}} \cdot (P - P_0) \tag{1}$$

This leads to a defined active power sharing between GFUs.

By analogy, the correlation between reactive power and voltage is defined as [39]:

$$V_{set} = V_0 - \frac{1}{k_V} \cdot \frac{1}{1 + sT_{kV}} \cdot (Q - Q_0) \tag{2}$$

The voltage droop in islanded microgrids is used for the reduction of reactive power flow between GFUs. As the voltage is a local phenomenon, the usage of voltage droop can reduce unwanted reactive power exchange. Consideration of further optimizations (e.g., by virtual impedance) was not defined as a goal of this work.

It can be realized, for example, by a higher level control system (optimization criteria: e.g., minimization of losses or reactive power). The control system using voltage droop is a resilient system as no ICT is necessary.

The control behavior is defined by the no-load resp. rated parameters (f_0, V_0, P_0 and Q_0) and by the frequency droop factor k_f resp. voltage droop factor k_V. To avoid oscillations and instabilities, smoothing time constants (T_{kf} resp. T_{kV}) are introduced.

A graphical form is shown in Fig. 2.

The frequency droop leads to a defined active power sharing between grid forming units in islanded microgrids, whereas the voltage droop can support the reduction of reactive power circuit flow between grid forming units.

(a) Frequency droop
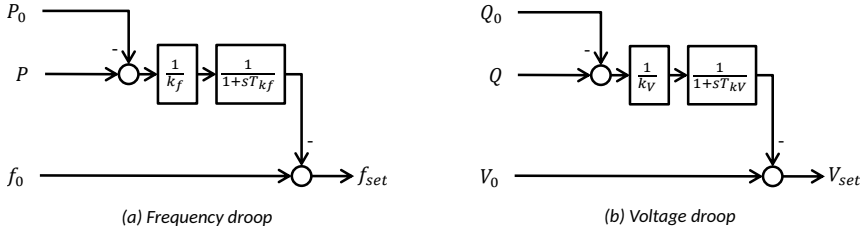
(b) Voltage droop

Figure 2 – Droop control structure for frequency/active power (a) and voltage and reactive power (b).

The implementation of this control concept is described in the following sections (3.2 - 3.4). The effect of parallel operated GFUs is investigated in section 4.1 in detail.

2.2 German Application Guide AR-N4105

The German Application Guide *VDE AR-N4105 (Erzeugungsanlagen am Niederspannungs-netz; Engl. Power generation units in the low voltage grid* [97] defines the behavior of DGs and BSSs (exception: grid forming units) in the grid.

In the analysis of island grids, the following functions have to be taken into account:

- DG startup behavior

- Power factor depending on active power feed-in

- Frequency behavior

In the following, each feature is explained in detail.

2.2.1 DG Startup Behavior

In VDE AR-N4105, the startup behavior of a DG connected to the LV grid is defined. Before feeding in, at least for 60s, the voltage has to be in the range of $85\% V_r \leq V \leq 110\%$ and the frequency in the range of $47.5Hz \leq f \leq 50.05Hz$.

After that is fulfilled, the active power feed-in is limited by a ramp with a slow of maximum 10% per minute regarding the maximum power.

2.2.2 Power Factor Depending on Active Power Feed-In

One important feature for the research in islanded microgrids is the maximum power factor depending on active power feed-in for decentralized generation in distribution grids on LV level. Fig. 3 presents the power factor ($\cos \varphi$) characteristic for active power feed-in that is considered in the mathematical model of grid supporting battery storage systems.

The corresponding equation for the maximum power factor depending on the active power setpoint P_{set} and the rated power P_r is represented in Eq. (3) [97].

$$\cos \varphi_{set,max}^{ind.} = \begin{cases} 1.1 - 0.2 * \dfrac{P_{set}}{P_r} & \text{for } P_{set} \geq 0.5 P_r \\ 1 & \text{else} \end{cases} \tag{3}$$

The relation between P_{set}, Q_{set} and $\cos \varphi_{set}$ is

$$P_{set} = S_{set} \cdot \cos \varphi_{set} = \sqrt{P_{set}^2 + Q_{set}^2} \cdot \cos \varphi_{set}$$

17
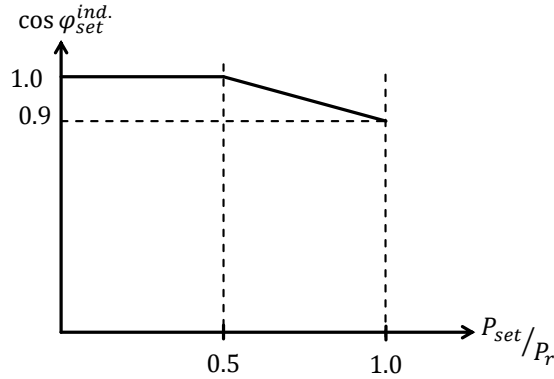
Figure 3 – Maximum power factor depending on active power feed-in.

As the requested reactive power is inductive, Q_{set} has the negative sign due to the convention used in Fig. 20:

$$Q_{set,max} = -\sqrt{\frac{1}{\cos\varphi_{set}} - 1} \cdot P_{set} \qquad (4)$$

By combining Eq. (3) and (4), the maximum reactive power is calculated (note: inductive reactive power has the negative sign!):

$$Q_{set,min}^{ind.} = \begin{cases} -\sqrt{\dfrac{1}{\left(1.1 - 0.2 * \frac{P_{set}}{P_r}\right)^2} - 1} \cdot P_{set} & \text{for } P_{set} \geq 0.5 P_r \\[2em] 0 & \text{else} \end{cases} \qquad (5)$$

The described characteristics can be modified to any other (nonlinear) behavior.

Next, the effect of power factor control regarding AR-N 4105 is analyzed for an LV grid with a cable from type NAY2Y 4x150mm² (see Chapter 3.1). A line length of 1km is assumed. Figure 4 presents the comparison of the constant power factor $\cos\varphi = 1$ and the variable power factor as described in this chapter. Without power factor control, the maximum active power is limited to $74kW$ due to voltage band limitations ($+10\%$). By using power factor control, this boundary is extended to 85kW, which means that in this example approx. 15% of additional active power can be supplied without voltage violations.

2.2.3 Frequency Behavior

In conventional power systems but also in island grids with droop control, an increase of frequency is an indication of exceeding generation. Therefore, the VDE AR-N4105 forces a feed-in reduction depending on the frequency, as shown in Fig. 5.

For grid frequencies in the range of $50.2Hz < f < 51.5Hz$, the active power feed-in is reduced by a gradient of 40% per Hertz [97]:

$$\Delta P_{DG} = 20 \cdot P_M \cdot \frac{50.2Hz - f}{50Hz} \qquad (6)$$

P_M is the actual active power at the moment when the frequency of $50.2Hz$ is exceeded.
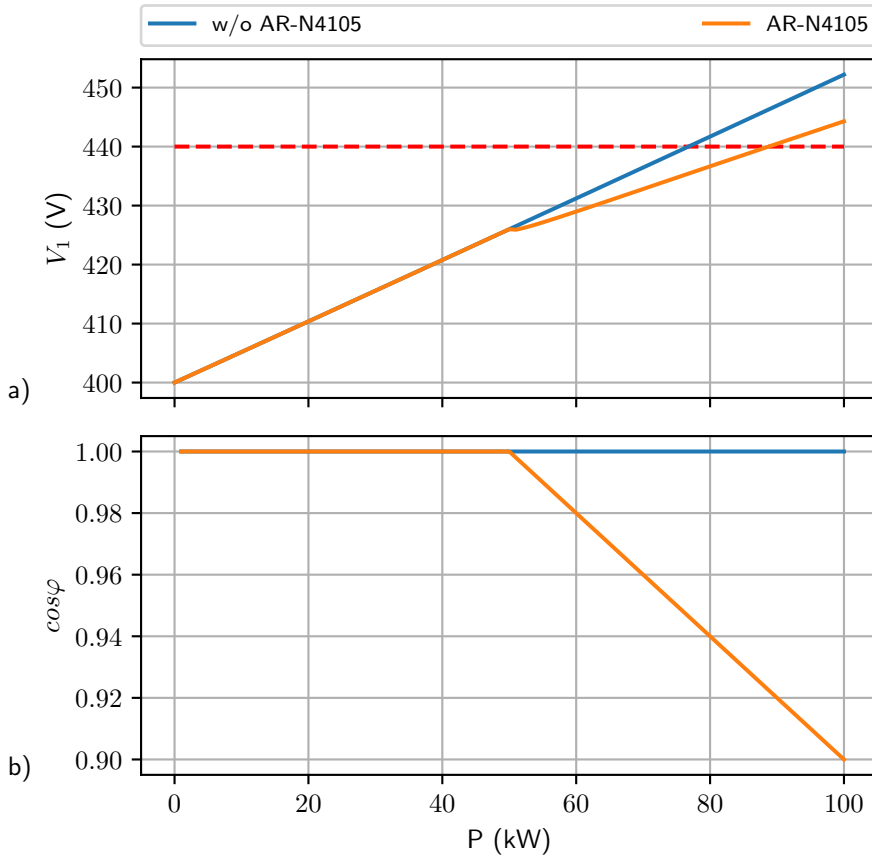
Figure 4 – Comparison of resulting voltage for active power feed-in for a GSU without power factor control (blue) and power factor control regarding VDE AR-N4105 (orange) for active power from $0 \ldots 100 kW$. Example of a cable length of 1km (type: NAY2Y 4x150mm^2).
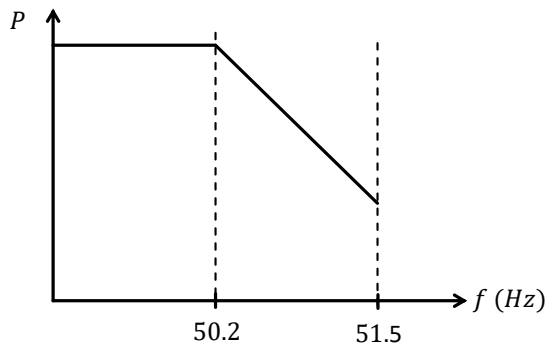
Figure 5 – Active power feed-in reduction depending on frequency.

2.3 Multi-Layer Control Approach for Islanded Microgrids

In island grids with droop control, as described in section 2.1, active power leads to frequency deviation – also in steady state. Thus, additional control strategies have to be used. In general, a centralized approach as presented, e.g., in [55, 39, 16] and a decentralized approach [100, 84, 65, 85, 41, 32, 52, 93, 61, 9, 37, 62, 59] are distinguished.

Further islanded microgrids are typically equipped with a black start capability. In literature, several black start strategies have already been discussed, e.g., in [92, 54, 58, 63, 101] where controllable loads or a communication link to the DGs is assumed.

In temporary island grids, resynchronization functionality is implemented as well [46, 33, 31, 82, 49, 89, 102, 56, 21].

This thesis research extends knowledge for systems considering distributed generation with VDE AR-N4105 specification.

2.4 Conclusion

In the state of the art analysis, the concept of droop control for stable operation of grid forming units in islanded microgrids is researched. Further the German application guide, which defines the behavior of generation units in the LV grid, is described. Further a literature research for multi-layer control approaches as well as typical island grid features, such as black start or resynchronization strategies, was done.

Based on these knowledge, the mathematical models for all considered assets were developed and verified by specific measurements in an islanded microgrid. Further, the interaction of droop-based grid forming units was investigated by simulation and compared with measurements. In addition, novel microgrid control algorithms considering distributed generation considering VDE AR-N4105 were developed.

3 Mathematical Modeling of Microgrid Assets

In this section, the mathematical modeling of assets typically used in islanded microgrids is presented. Besides the electrical structure, the focus is set on its specific control strategy. First, the considered grid structure is described and the specific behavior of the electrical lines regarding active and reactive power transmission is investigated analytically as this influences the control strategies of the assets.

Next, mathematical description including control algorithms is presented for the following assets:

- Battery storage systems (BSS) in grid forming mode

- Battery storage systems in grid supporting mode

- Gensets (Generator sets)

- Photovoltaic (PV) systems

- Heat Pump

3.1 Low Voltage Grids for Island Operation

All assets described in this chapter are connected to a $400V$ low voltage (LV) grid with a nominal frequency of $50Hz$. The assets are mainly interconnected by 4-wire underground cables with a cross-section area of $150mm^2$ each (Type *NAY2Y*). In Fig. 6, a slice of the cross-section is shown.

Figure 6 – Cross-section of a LV cable (type: NAY2Y 4x150mm²)

In the literature, the modeling of electrical lines is widely discussed (e.g., [67, 64]). Especially for transmission lines, the lines are typically modeled in *T* structure or Π structure (Fig. 7a). As the admittance Y is affected by the voltage by square, it can be neglected in LV grids due to the low voltage level. Thus, the line model is simplified to the line impedance $\underline{Z} = R + jX$ (Fig. 7b).

In the literature [64, p. 954f], the following values for a LV cable based on aluminium (Type NAY2Y) are listed:

- $R'_{line} = 0.207\Omega/km$

- $X'_{line} = 0.0807\Omega/km$

(a)   *(b)*
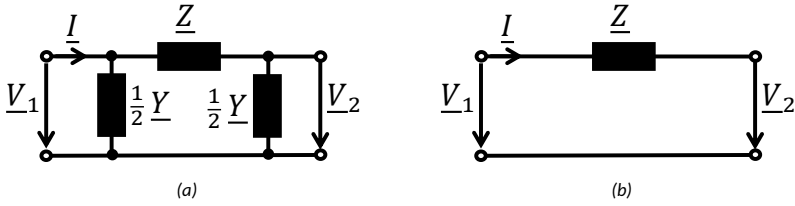
Figure 7 – Single line diagram (SLD) for line model. a) Π model; b) simplified series model.

The corresponding X/R ratio is $X/R \approx 0.4$, which means that the ohmic part is dominating (approx. 2.5 times higher than the inductive part). At high voltage (HV) overhead lines, the line inductance is dominating, whereas the ohmic part is small. An overview of typical model parameters and X/R ratios for different voltage levels is presented in Table 2.

Table 2 – Typical model parameters of different voltage levels and line types [64].

$V_{LL,rated}$ (kV)	Type	R' (Ω/km)	X' (Ω/km)	X/R
0.4	Cable (NAY2Y, $4x150mm^2$)	0.207	0.0807	0.4
	Overhead Line ($120mm^2$)	0.155	0.305	1.97
110	Overhead Line	0.033	0.266	8.1
380	Overhead Line	0.027	0.260	9.6

The focus in this work is set on LV microgrids. Therefore, a $0.4kV$ cable network is assumed, whereas the behavior of LV overhead lines resp. higher voltage levels such as $110kV$ or $380kV$ grids are not considered.

3.1.1 Influence of Active and Reactive Power on the Voltage

The behavior of a typical LV cable (*NAY2Y-4x150mm^2*) is analyzed theoretically. The presumed test setup is shown in Fig. 8, where a mains connected grid (conventional distribution grid, no island grid) is assumed. On the left side of the line (represented by $\underline{Z}_{line}$), an equivalent circuit for a LV grid fed by a 20kV/0.4kV transformer consisting of an ideal voltage source $\underline{V}_{Tr}$ and a series impedance $\underline{Z}_{Tr}$ is connected. At the end of the line, a voltage source $\underline{V}_1$ is assumed. As the focus of this part is set on the investigation of the line behavior, a more accurate transformer model (e.g., in *T* structure) is not taken into account.

The line impedance $\underline{Z}_{line}$ is

$$\underline{Z}_{line} = R_{line} + jX_{line} \tag{7}$$

with

$$R_{line} = R'_{line} \cdot l_{line} \tag{8}$$

and

$$X_{line} = X'_{line} \cdot l_{line} \tag{9}$$

where line length is l_{line}.

First, the voltage depending on the cable length is investigated for different values of active and reactive power. The transformer voltage is set as constant to $\underline{V}_{Tr} = 400V$ and also the transformer impedance $\underline{Z}_{Tr}$ is assumed as constant.
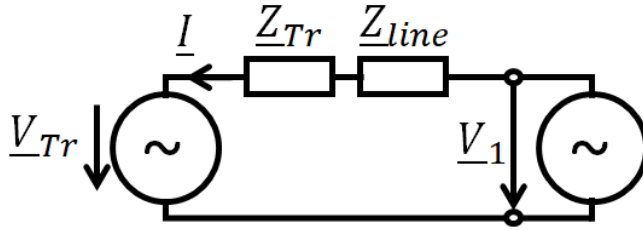
Figure 8 – SLD of cable modeling setup. $\underline{V}_{Tr}$, $\underline{Z}_{Tr}$: transformer equivalent circuit. $\underline{Z}_{line}$: cable impedance. $\underline{V}_1$: resulting voltage of current $\underline{I}$.

Regarding the regulation DIN EN 50160 [29], the allowed voltage band is defined as $\pm 10\%$ (for LV grids: $360V \leq V \leq 440V$).

The corresponding vector diagrams for a cable length of 1km are presented in Fig. 9. In Fig. 10, the voltage $\underline{V}_1$ depending on the cable length is illustrated for

1. Active Power Feed-In ($P = 100kW$, $Q = 0$)

2. Reactive Power Feed-In ($P = 0$, $Q = 100kvar$)

3. Reactive Power Consumption ($P = 0$, $Q = -100kvar$)

It can be seen that active power has more impact on the voltage than reactive power. For a cable length of 1km, the resulting voltage for $P = 100kW$ (blue) is approx. $450V$, whereas for $Q = 100kvar$ the voltage is approx. $425V$.
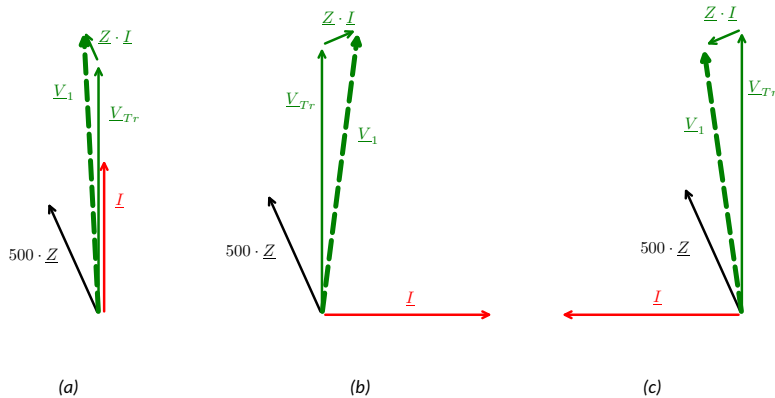
Figure 9 – Vector diagrams of power feed-in at a LV cable (NAY2Y 4x150mm²) in generator convention. a) active power (P=100kW, Q=0); b) reactive power feed-in (P=0, Q=100kvar); c) reactive power consumption (P=0, Q=-100kvar).

In conventional HV energy systems, additional reactive power is used for voltage control. This effect is investigated for a LV grid by variation of power factor to $\cos\varphi = 1$, $\cos\varphi = 0.9_{cap}$ and $\cos\varphi = 0.9_{ind}$ at a constant active power feed-in of $P = 100kW$. The results are shown in Fig. 11.
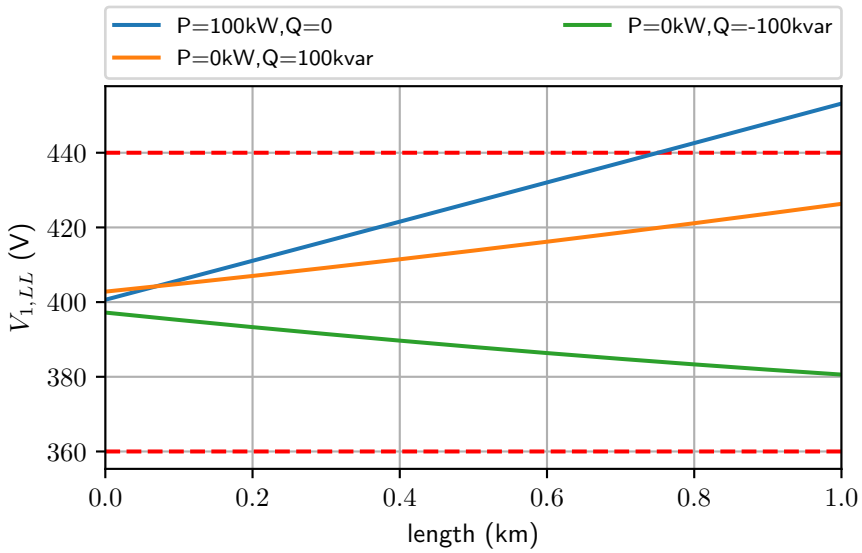
Figure 10 – Voltage depending on cable length for active power feed-in (blue), reactive power feed-in (orange) and reactive power consumption (Green).
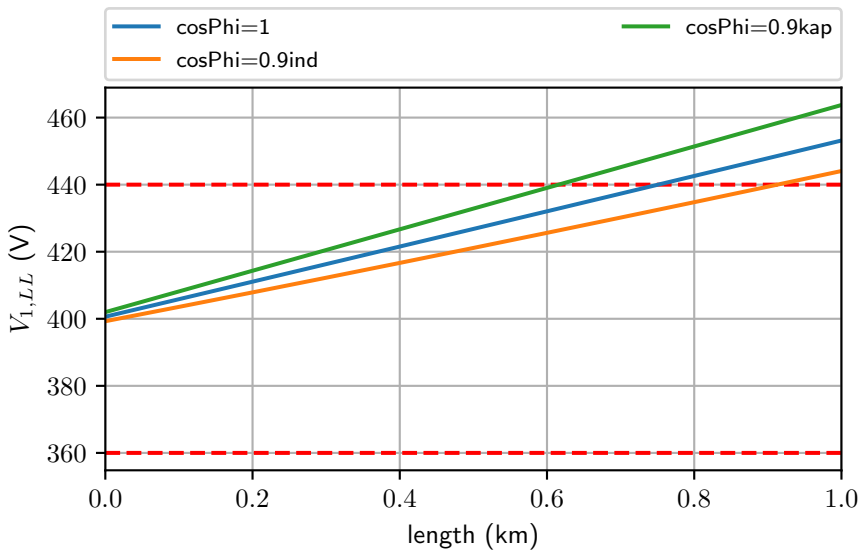
Figure 11 – Voltage depending on cable length for active power feed-in of $P = 100kW$ and $\cos\varphi = 1$ (Blue), $\cos\varphi = 0.9_{ind}$ (orange) and $\cos\varphi = 0.9_{kap}$ (green).

Fig. 12 shows the resulting voltage V_1 depending on reactive power for a cable length of 1km and for three setpoints of active power ($P = 0kW$, $P = 100kW$, $P = -100kW$). It has to be ensured that the voltage is between $360V$ and $440V$.
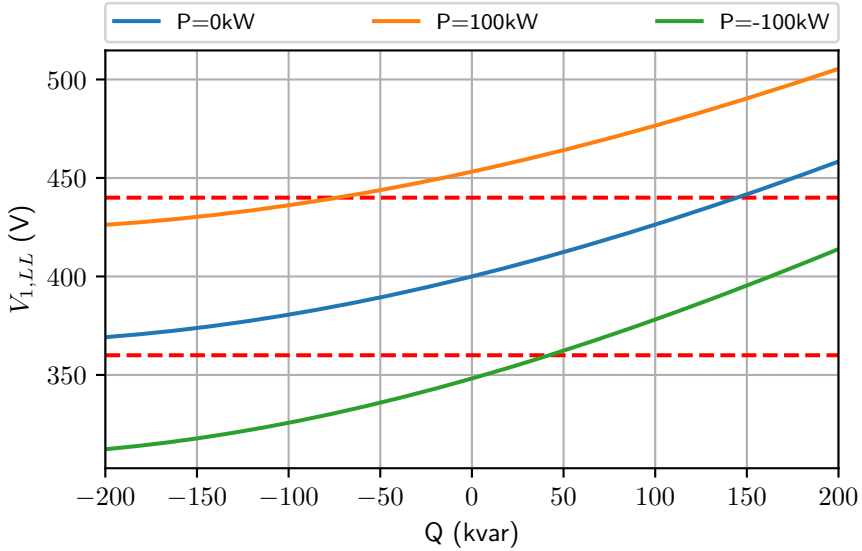
Figure 12 – Voltage depending on reactive power for a cable length of 1km and $P = 0$ (blue), $P = 100kW$ (orange) and $P = -100kW$ (green).

As seen, a relatively high amount of reactive power is needed to control the voltage significantly. Looking at the result for $P = 100kW$ (Fig. 12, *orange*), a reactive power of $Q = -100kvar$ is needed to reduce the voltage from $450V$ to $440V$.

Next, the transformer reactance is set in relation to the line reactance depending on the cable length. The transformer is assumed as a 20kV/0.4kV transformer with a rated power of $S_{Tr} = 630kVA$, a short circuit factor $u_K = 4.5\%$ and a ratio between X_{Tr} and R_{Tr} of $(X/R)_{Tr} = 4.56$ (with $\underline{Z}_{Tr} = R_{Tr} + jX_{Tr}$). From this data, the absolute value of the transformer impedance can be calculated:

$$|\underline{Z}_{Tr}| = u_K \cdot \frac{V_{Tr,LL}^2}{S_{Tr}} \tag{10}$$

Thus, the transformer reactance and resistance are calculated:

$$X_{Tr} = \frac{|\underline{Z}_{Tr}|}{\sqrt{\frac{1}{(X/R)_{Tr}^2} + 1}} \tag{11}$$

$$R_{Tr} = \frac{|\underline{Z}_{Tr}|}{\sqrt{(X/R)_{Tr}^2 + 1}} \tag{12}$$

The result in Fig. 13 shows that line reactance is dominating the transformer reactance for cable lengths greater than approx. 130m. For other transformers and line types, this value will differ.
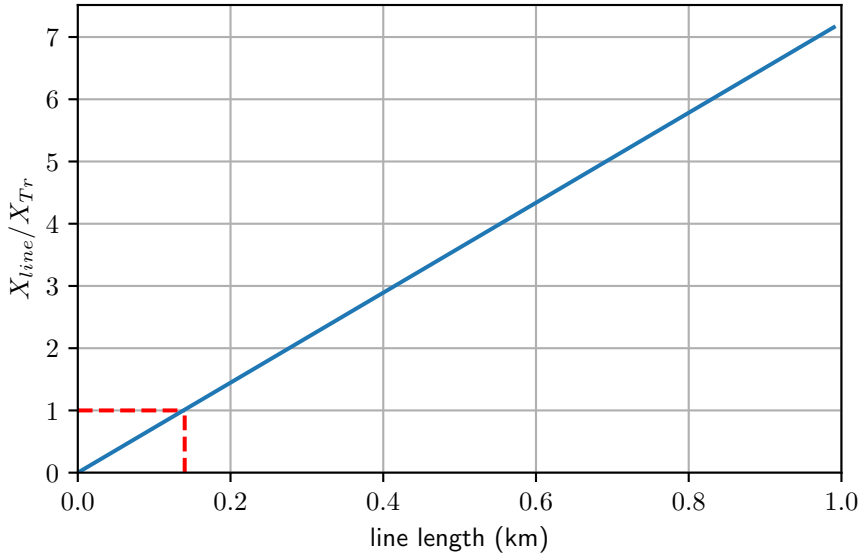
Figure 13 – Ratio of the line reactance X_{line} to the transformer reactance X_{Tr}.

In this theoretical analysis it was shown that the voltage in a LV grid is influenced significantly by active power and not by reactive power. The load in low voltage distribution grids is typically dominated by active power (see section 3.1.2) and thus the impact of additional reactive power on voltage stabilization is smaller than in HV grids (due to X/R ratio regarding Table 2).

Therefore, STATCOMs as control assets in LV grids are not considered in this work as the effect of reactive power on voltage is less than by active power.

3.1.2 Active and Reactive Power Consumption in LV grids

Active power consumption in rural LV grids is typically dominated by active power. From September 2012 until January 2015, active and reactive power consumption was measured at different LV substations in a rural area in Southern Germany in the frame of the research project IRENE [17]. The results of four substations (for time-synchronous data with a period of 1 minute) are presented in Fig. 14.

The corresponding density diagram of the power factor is shown in Fig. 15.

It can be seen that at more than 85% of the time, the power factor is higher than $\cos\varphi = 0.9$ (substation 1, 3 and 4) resp. at more than 60% for substation 2. At more than 95% of the time, the power factor is higher than $\cos\varphi = 0.8$.

It should be pointed out that the number of analyzed substations is too small for a general statement (only 4 substations); nevertheless, a tendency is presented that rural LV grids are dominated by active power.
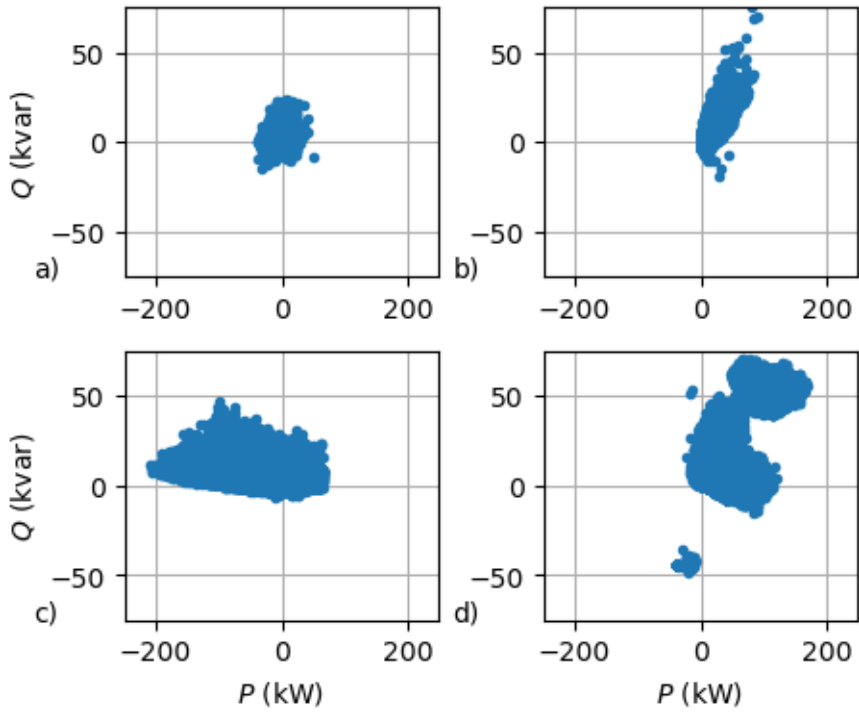
Figure 14 – Active and reactive power distribution of substations sub1 (a), sub2 (b), sub3 (c) and sub4 (d).
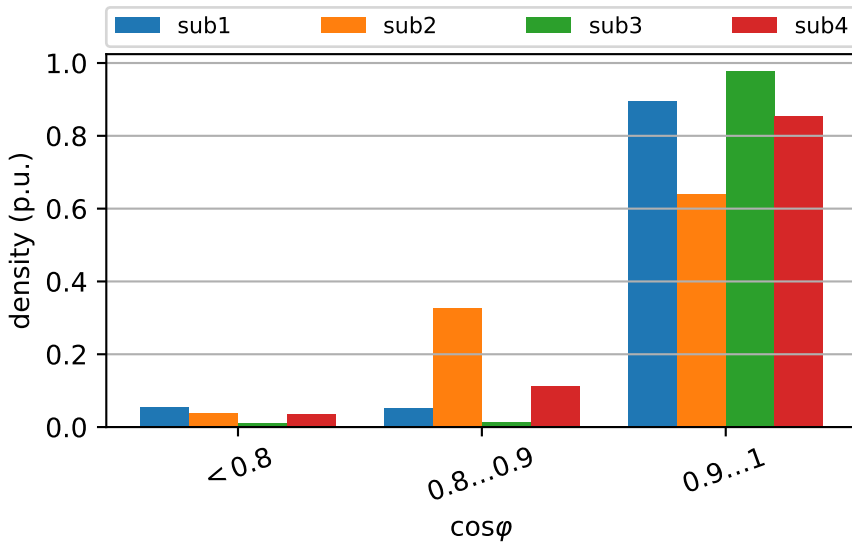
Figure 15 – Density of power factors measured at four substations (sub1…sub4) in a rural area in Germany.

3.2 Battery Storage System in Grid Forming Mode

In modern island grids, electrical components with power electronics are used in different applications. Besides inverter-based DGs such as PV systems (section 3.5), stationary battery storage systems (BSSs) play an increasing role. On the one hand, BSSs like home storage systems are installed for an optimized usage of DG systems (e.g., optimization of self consumption) and are operated in parallel to an existing grid.

In islanded microgrids with high penetration of renewable DG systems, BSSs can be equipped with further functionality. These are mainly:

- Frequency and voltage control as a grid forming unit (GFU) for standalone application

- Black start capability

- Droop control for distributed frequency and voltage control (in combination with further BSSs or rotational units such as gensets)

In this section, a mathematical model for BSSs in grid forming mode based on the concept of droop control (as explained in the previous section) is described. The hierarchical structure is based on an existing BSS located at the MCW (section 5.2.1). In section 6.1.1 the concept is verified with specific measurements at this BSS at the test site.

The model structure of a BSS with grid forming capability is shown in Fig. 16. It is considering an inverter, grid filter (e.g. in LCL structure), coupling transformer and is connected to other assets in an (islanded) grid. The inverter itself is controlled by the concept of droop control which is described in section 2.1.
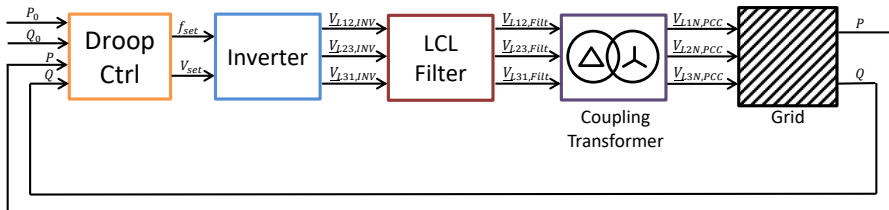
Figure 16 – Block diagram of a voltage source inverter (grid forming mode) with droop control.

The structure of the inverter is typically a three-phase voltage source converter with a dc link capacitor. The structure as well as distinctions of current source converters are investigated in detail in [8]. To ensure a sinusoidal-like voltage output, the inverter is connected to the grid by a filter (e.g., in LCL structure).

For an investigation of the GFU itself and its internal electrical behavior, a detailed modeling approach shown in Fig. 17 has to be considered.

A mathematical model for Lithium-ion batteries with a dynamic internal resistance consisting of a constant series resistance R_0 and a RC-element (R_{OTC}, C_{OTC}) as a first order time constant is considered. For some investigations also higher order models with two or three time constants and considering a high frequency model may be required [74], but it is not taken into account in this thesis.

It is followed by a DC link capacitor and a 6-pulse bridge whereas also other inverter technologies such as multi-level converters can be used. The inverter is followed by an LCL filter and a transformer (in YNd5 structure) that is used for both voltage adaption and neutral point creation.
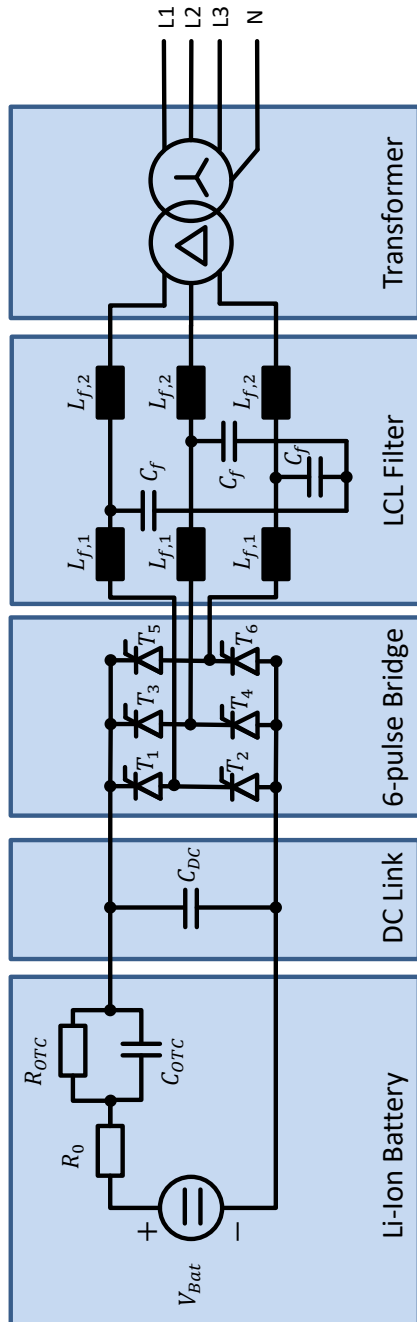
Figure 17 – Detailed 3-phase electrical model of a BSS.

For the analysis of the interaction of several assets operated in parallel, a simplified model approach shown in detail in [72, 70, 3] is sufficient and it will not be explained in detail in the frame of this work.

Also, for planning and dimensioning of an islanded microgrid, the simplified modeling approach is preferred, as in practical application not all electrical and control parameters are known from the manufacturer side. The SLD of the simplified model is shown in Fig. 18.
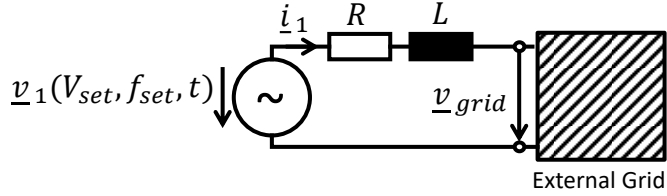
Figure 18 – Simplified SLD of a BSS as GFU.

It consists of a controlled voltage source $\underline{v}_1(V_{set}, f_{set}, t)$ and an internal impedance (R and L) as an aggregation of the inverter, filter and transformer.

The voltage $\underline{v}_1$ is a function of V_{set} (Eq. (2)) and f_{set} (Eq. (1)). The time dependent function is

$$\underline{v}_1(t) = \hat{V}_{set} \cdot e^{j(2\pi f_{set} \cdot t + \varphi_0)} \tag{13}$$

whereas φ_0 is the phase angle at simulation startup.

The described mathematical model is implemented in the software package DIgSILENT PowerFactory for numerical grid simulations. As already mentioned, verification of the model at a real BSS is shown in section 6.1.1.

3.3 Battery Storage System in Grid Supporting Mode

Besides BSSs in grid forming mode, systems without direct voltage and frequency control also exist [77]. These systems are operated in mains parallel operation and are controlled to active and reactive power setpoints (*grid feeding mode*). This type of BSS is widely used, e.g., in households (for optimization of self consumption).

By adding an additional outer control loop it is possible to extend these BSSs to grid supporting control. In that case, it is operated in parallel to grid forming units using droop control and can support the grid with active and reactive power in islanded microgrids.

In Fig. 19 an overview over all control parts of the mathematical model is presented.
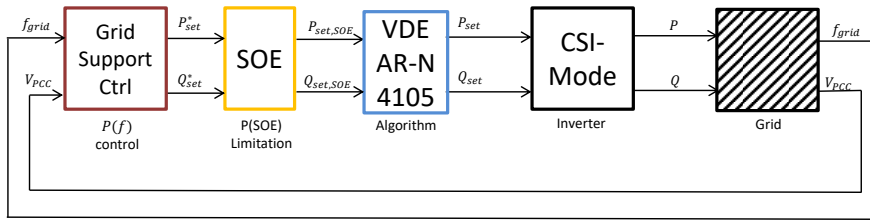
Figure 19 – Overview of mathematical model of a BSS in grid supporting mode.

The fundamental inverter control is realized as a current source inverter (*CSI mode*). At the boundaries of the usable battery capacity, the active power (for charging and discharging) is limited regarding configurable characteristics.

The German Application Guide *VDE AR-N 4105* [97] prescribes that all generation units (also storage systems during discharge) with a rated power higher than $13.8kVA$ need to follow a defined behavior of the power factor depending on active power ($\cos\varphi(P)$ characteristics). In the modeling described in this thesis, this option is included, but can also be deactivated.

Further, another outer control loop for the grid supporting mode control is added for realizing the droop characteristics.

A single line diagram of the electric structure shown in Fig. 20 consists of a controlled voltage source $\underline{v}_1$ and a lumped internal impedance (R resp. L). A higher grade of detail (including inverter's switching elements and the dynamic behavior of the battery cells) is not considered.

As BSSs in grid supporting mode are only operated in mains parallel operation, the external grid is represented as well.
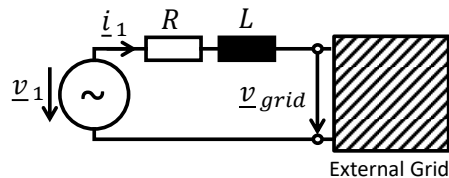
Figure 20 – SLD of a BSS as GSU.

3.3.1 Current Source Inverter (CSI) Mode Control

Grid supporting BSSs are controlled to active and reactive power independently, which is realized by dq-transformation (Park transformation). Besides the separation of active and reactive power control, in the dq frame, conventional control algorithms such as PI controllers can be used as the voltages and currents are constant in steady state and not oscillating with the frequency. The CSI mode control is realized by an inner current control loop and an outer power control loop. The control is realized for active and reactive power by separation into the d and q part using Park transformation.

For a three phase system with phases a,b and c, the fundamental differential equation is

$$\underbrace{\begin{bmatrix} \Delta v_{L1} \\ \Delta v_{L2} \\ \Delta v_{L3} \end{bmatrix}}_{\Delta \mathbf{v}} = \underbrace{\begin{bmatrix} v_{1,L1} \\ v_{1,L2} \\ v_{1,L3} \end{bmatrix}}_{\mathbf{v}_1} - \underbrace{\begin{bmatrix} v_{grid,L1} \\ v_{grid,L2} \\ v_{grid,L3} \end{bmatrix}}_{\mathbf{v}_{grid}} = R \cdot \underbrace{\begin{bmatrix} i_{1,L1} \\ i_{1,L2} \\ i_{1,L3} \end{bmatrix}}_{\mathbf{i}_1} + L \cdot \underbrace{\begin{bmatrix} \dot{i}_{1,L1} \\ \dot{i}_{1,L2} \\ \dot{i}_{1,L3} \end{bmatrix}}_{\dot{\mathbf{i}}_1} \tag{14a}$$

$$\Delta \mathbf{v} = \mathbf{v}_1 - \mathbf{v}_{grid} = R \cdot \mathbf{i}_1 + L \cdot \dot{\mathbf{i}}_1 \tag{14b}$$

First, Eq. (14) is transformed to space phasor representation with a rotating coordination system ([66, p. 14]). Therefore $\Delta \mathbf{v}$, $\mathbf{i}_1$ as well as $\dot{\mathbf{i}}_1$ are transformed by Eqs. (15), (16) and (17) to $\Delta \mathbf{v}_r$, $\mathbf{i}_{1,r}$ and $\dot{\mathbf{i}}_{1,r}$. The rotational angle is defined as ϑ.

The voltage $\underline{v}_r^*$ is the conjugated complex voltage.

$$\begin{bmatrix} \Delta v_{L1} \\ \Delta v_{L2} \\ \Delta v_{L3} \end{bmatrix} = \frac{1}{2} \cdot \underbrace{\begin{bmatrix} e^{j\vartheta} & e^{-j\vartheta} \\ e^{j\left(\vartheta - \frac{2\pi}{3}\right)} & e^{-j\left(\vartheta - \frac{2\pi}{3}\right)} \\ e^{j\left(\vartheta + \frac{2\pi}{3}\right)} & e^{-j\left(\vartheta + \frac{2\pi}{3}\right)} \end{bmatrix}}_{\mathbf{T}} \cdot \begin{bmatrix} \Delta \underline{v}_r \\ \Delta \underline{v}_r^* \end{bmatrix} \tag{15}$$

$\mathbf{T}$ is the transformation matrix from the three phase system to the rotational space phasor representation.

$$\begin{bmatrix} i_{1,L1} \\ i_{1,L2} \\ i_{1,L3} \end{bmatrix} = \mathbf{T} \cdot \begin{bmatrix} \underline{i}_{1,r} \\ \underline{i}_{1,r}^* \end{bmatrix} \tag{16}$$

$$\begin{bmatrix} \dot{i}_{1,L1} \\ \dot{i}_{1,L2} \\ \dot{i}_{1,L3} \end{bmatrix} = \dot{\mathbf{T}} \cdot \begin{bmatrix} \underline{i}_{1,r} \\ \underline{i}_{1,r}^* \end{bmatrix} + \mathbf{T} \cdot \begin{bmatrix} \dot{\underline{i}}_{1,r} \\ \dot{\underline{i}}_{1,r}^* \end{bmatrix} \tag{17}$$

The transformation's derivation $\dot{\mathbf{T}}$ is

$$\dot{\mathbf{T}} = j\dot{\vartheta} \cdot \mathbf{T} \tag{18}$$

This leads to the rotational space phasor system $\underline{v}_r$:

$$\begin{bmatrix} \Delta \underline{v}_r \\ \Delta \underline{v}_r^* \end{bmatrix} = (R + j\dot{\vartheta}L) \cdot \begin{bmatrix} \underline{i}_{1,r} \\ \underline{i}_{1,r}^* \end{bmatrix} + L \cdot \begin{bmatrix} \dot{\underline{i}}_{1,r} \\ \dot{\underline{i}}_{1,r}^* \end{bmatrix} \tag{19}$$

The rotational space phasors $\Delta \underline{v}_r$, $\underline{i}_{1,r}$ and $\underline{\dot{i}}_{1,r}$ can be written in dq-form by separation of the real and imaginary part as well:

$$\Delta \underline{v}_r = \Delta v_d + j\Delta v_q \tag{20}$$

$$\underline{i}_{1,r} = i_{1,d} + ji_{1,q} \tag{21}$$

$$\underline{\dot{i}}_{1,r} = \dot{i}_{1,d} + j\dot{i}_{1,q} \tag{22}$$

The index d is used for direct axis, whereas q is used for the quadrature axis of the Park transformation.

This leads to the following equations for the voltage Δv_d resp. Δv_q depending on the currents $i_{1,d}$ resp. $i_{1,q}$ as well as $\dot{i}_{1,d}$ resp. $\dot{i}_{1,q}$:

$$\Delta v_d = R \cdot i_{1,d} + L \cdot \dot{i}_{1,d} - \dot{\vartheta} \cdot L \cdot i_{1,q} \tag{23}$$

$$\Delta v_q = R \cdot i_{1,q} + L \cdot \dot{i}_{1,q} + \dot{\vartheta} \cdot L \cdot i_{1,d} \tag{24}$$

As the voltage now is separated into d and q parts, the corresponding currents $i_{1,d}$ and $i_{1,q}$ can be controlled independently.

The related block diagram is shown in Fig. 21. A cascaded control consisting of an inner current control and an outer power control is assumed for d-axis as well as for q-axis.
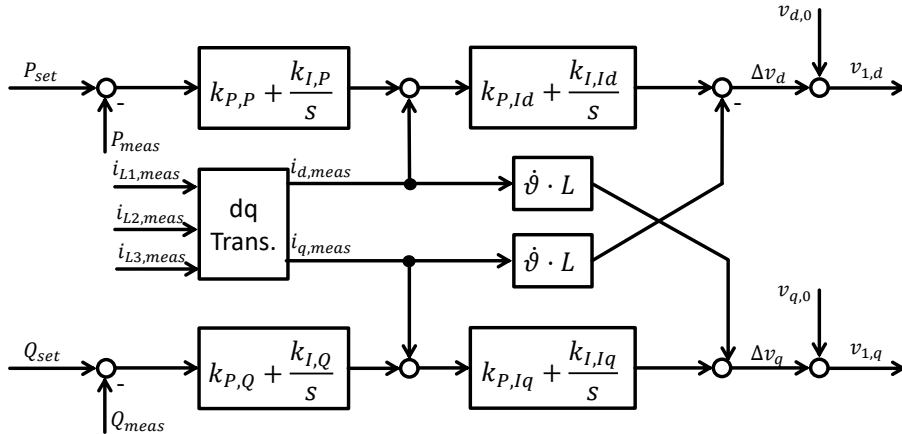
Figure 21 – Block diagram of active and reactive power control of GSU in dq-frame.

P_{set} and Q_{set} are setpoints of the control system, whereas P_{meas}, Q_{meas}, $i_{d,meas}$ and $i_{q,meas}$ are instantaneous measurement values. The controller parameters $k_{P,P}$, $k_{I,P}$, $k_{P,Id}$, $k_{I,Id}$, $k_{P,Q}$, $k_{I,Q}$, $k_{P,Iq}$, $k_{I,Iq}$ have to be set. For a proper decoupling of P and Q control, the inductance L has to be known as well as a parameter for the control system.

3.3.2 Power Factor Control regarding VDE AR-N4105

In the BSS as GSU model, the relevant functions of the Application Guide VDE AR-N4105 for island grids are included. A detailed description of the considered functions can be found in section 2.2.

3.3.3 State of Energy Consideration

The state of energy (SOE) is defined as [103]:

$$SOE(t) = SOE_0 - \frac{1}{E_{total}} \cdot \int_0^t P(t) + (1 - \eta) \cdot |P(t)| dt' \tag{25}$$

SOE_0 is the initial SOE, E_{total} is the total energy capacity of the BSS, η the efficiency during charging and discharging depending on the ac power P at the point of common coupling (PCC) of the BSS.

As the SOE limits cannot be exceeded, the active power has to be limited at the boundaries. For high resp. low values of SOE, the active power limit for charging resp. discharging can be defined by a ramp (Fig. 22). In the mathematical modeling of the grid supporting BSS the power limits are considered by a look-up table with linear approximation.
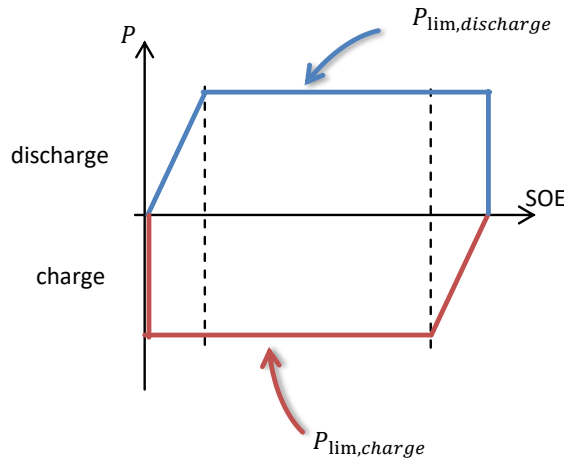
Figure 22 – Active power limitation depending on the State of Energy (SOE).

3.3.4 Grid Supporting Control

As battery storage systems cannot be operated in grid forming mode, no direct $f(P)$ or $V(Q)$ droop control can be realized. Nevertheless, BSSs in grid supporting mode can provide contributions to the island grid control in order to maintain the GFUs.

As illustrated in Fig. 19, the BSSs in grid supporting mode are controlled to active and reactive power setpoints. By adding an additional outer control loop (*Grid Support Control*), droop control for active and reactive power can be realized.

Furthermore, it is known from measurements at real systems that - due to digital signal transmission and protocol conversion - an aggregated transportation delay (dead time) has to be considered. In this model approach, this aggregated dead time is added in the block *Grid Supporting Control*, but it can be placed in other blocks as well.

In contrast to GFUs (as described in section 3.2), the dependency of $P(f)$ and $Q(V)$ is realized:

$$P_{set}^* = P_0 + k_f \cdot (f_0 - f_{grid}) \cdot e^{-sT_{delay}} \tag{26}$$

P_0 is the active power at the nominal frequency f_0 whereas f_{grid} is the measured grid frequency. The active power droop factor is defined by k_f.

A reactive power and voltage droop can be realized as well by the following relation:

$$Q^*_{set} = Q_0 + k_V \cdot (V_0 - V_{grid}) \cdot e^{-sT_{delay}} \tag{27}$$

As parameters of Eq. (27) the reactive power feed-in Q_0 at the nominal voltage V_0 as well as the reactive power droop factor k_V have to be defined. V_{grid} is the measured voltage at the PCC of the BSS.

At the microgrid demonstrator MCW, the Campus Battery Storage System *CBSS* (section 5.2.2) is operated in grid supporting mode. Simulation results and a comparison with measurements are presented in section 6.1.2.

3.4 Gensets Fueled with Plant-Oil, Diesel or Bio Mass

Fuel-driven generator sets (gensets) still play a role in electrical power systems. Gensets are used, for example, as uninterruptible power supplies for critical infrastructures like hospitals, but also in data processing centers.

In addition, gensets are often used in islanded microgrids, even under consideration of a high amount of renewable energy sources. Depending on the generation structure, gensets are used as backup assets in case of failure or in longer periods without sufficient renewable generation – or under consideration of economical optimization of the island grid [11].

A genset consists of a combustion engine coupled to an electrical machine by a shaft and optionally by a gearbox.

Distinction should be made between direct coupled gensets and gensets with a frequency converter. The advantage of using a frequency converter is high dynamics regarding frequency and voltage control due to power electronics in comparison to electrical machines. One disadvantage is lower reliability due to a more complex setup as an additional component is used. Further direct coupled gensets can supply higher short-circuit currents than systems with power electronics. The modeling in this chapter is focused on direct coupled systems,

An overview over the mechanical structure of a direct coupled genset is shown in Fig. 23.
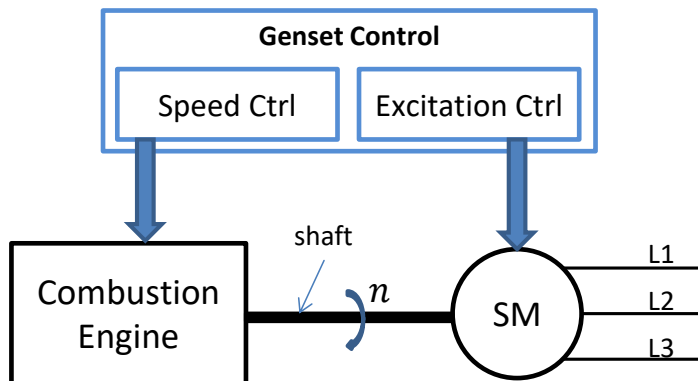
Figure 23 – Overview of the mechanical structure of a genset consisting of a combustion engine (motor), a synchronous machine (SM) as generator and a control block.

It consists of a combustion engine (e.g., fueled by plant oil, diesel or bio gas) and a direct coupled synchronous machine (SM). The genset control is essentially responsible for the engine speed control, the voltage control (excitation control of the SM), but also for other tasks like synchronization or black start.

A dynamic mathematical model for gensets used in islanded microgrids is essential for investigating the interaction with other assets such as storage systems or PV systems. Hence, the dynamics regarding frequency and voltage have to be represented adequately.

The general model structure is shown in Fig. 24. It consists of an engine model as well as a generator model which are coupled mechanically. For parallel operation with other grid forming units, a droop control with $f(P)$ and $V(Q)$ characteristics is assumed. In the following, the mentioned blocks are described in detail.
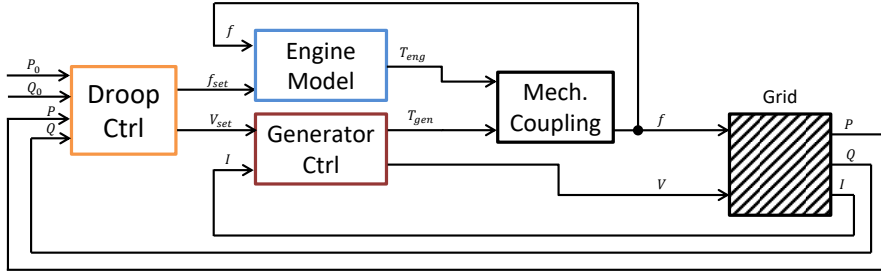
Figure 24 – Generic block diagram of a genset with droop control for island mode operation.

3.4.1 Mechanical Coupling

At a genset with the assumed structure, the combustion engine is directly coupled with the generator by a shaft. Regarding the second law of Newton, the rotational acceleration $\dot{\omega}$ is defined by the difference of the engine torque (T_{eng}) and the generator torque (T_{gen}) as well as the inertia J:

$$\dot{\omega} = \frac{1}{J} \cdot (T_{eng} - T_{gen}) \tag{28}$$

The inertia J aggregates the rotational parts of the engine, the shaft as well as the generator.

3.4.2 Droop Control

The frequency and voltage droop control is considered by the $f(P)$ and $V(Q)$ characteristics. The control behavior is defined by the parameters for active and reactive power as well as the frequency and voltage (P_0, Q_0, f_0, V_0), but also by the frequency droop factor k_f and the voltage droop factor k_V.

In steady state, the frequency setpoint f_{set} resp. voltage setpoint V_{set} is defined by

$$f_{set} = f_0 - \frac{1}{k_f} \cdot \frac{1}{1 + sT_{kf}} \cdot (P - P_0) \tag{1}$$

$$V_{set} = V_0 - \frac{1}{k_V} \cdot \frac{1}{1 + sT_{kV}} \cdot (Q - Q_0) \tag{2}$$

The corresponding block diagram is shown in Fig. 2 in section 2.1 where the droop control is explained in general.

3.4.3 Synchronous Machine

As illustrated in Fig. 24, the mechanical power is converted to electrical power by a direct coupled synchronous generator. The dynamic behavior of the synchronous machine is represented by a transient model in dq frame based on stationary, transient and subtransient reactances and time constants. This is the state of the art well-described in the literature (e.g., [53], [18], [19]). Therefore, a detailed description and derivation of the equation set needed for the modeling of a genset model used in microgrid applications are not shown in this thesis.

3.4.4 Synchronous Machine Excitation Control

In systems with external excited synchronous machines, voltage is controlled by the field (excitation) winding current. A closed loop control (PI structure) is used to establish a grid voltage V_{grid} equal to the setpoint ($V_{grid} = V_{set}$ for stationary operation). It should be mentioned that the dynamics for voltage control is low in comparison to inverter-based systems due to the high time constant of the excitation winding (typically some hundred milliseconds and higher).

3.4.5 Engine Model

A combustion engine is assumed as the prime mover in the genset model.

In different publications, focus is on the mathematical modeling of gensets. The main model approaches can be categorized as follows:

- Linear model (PT1-Element) and dead time ([79, 80])

- Thermodynamic approach ([42, 22, 27, 45, 81, 23, 24])

- Non-linear gray-box model

The setup of a thermodynamic model is complicated for end users as many parameters and control strategies are not published by the manufacturers.

Thus in this work, the focus is set on the linear model and on a non-linear gray-box model.

The mechanical structure of a modern diesel engine is shown in Fig. 25 [75]. It consists of:

1. Camshaft
2. Valves
3. Piston
4. Fuel Injection System
5. Cylinder
6. Exhaust Gas Recirculation (EGR)
7. Inlet Manifold
8. Exhaust Gas Turbocharger
9. Exhaust Pipe
10. Cooling System
11. Piston Rod
12. Lubrication System
13. Engine Block
14. Crankshaft
15. Flywheel Mass

As the thermodynamic approach is out of scope of this work, the dynamic torque production depending on combustion is not considered.

3.4.5.1 Linear Approach

First, the linear engine model in combination with torque limitation is shown (Fig. 26). It consists of a closed loop frequency control with a PI controller and a first order time constant (T_{mot}). From engine manufacturers it is known that T_{mot} is relatively small in comparison to the inertia J introduced in Eq. 28.

A torque limitation ($T_{eng,min}$, $T_{eng,max}$) as well as an anti wind-up algorithm (f_{AWU}) are also introduced.
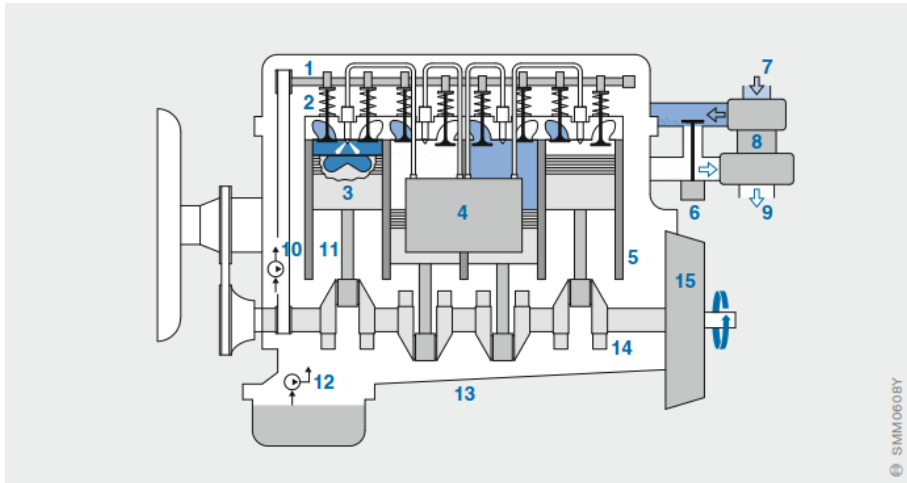
Figure 25 – Mechanical structure of a diesel engine (source:[75]).

As long as the unlimited engine torque T_{eng}^* is in the range between $T_{eng,min}$ and $T_{eng,max}$, the engine torque T_{eng} is equal to T_{eng}^* and thus the engine model structure is linear. Depending on the application (e.g. steady state investigations like energy management development), this model simplification might be sufficient. In chapter 6.1.3 the model parameter estimation basing on characteristic measurements as well as a model verification is presented for a real genset (described in section 5.2.3).
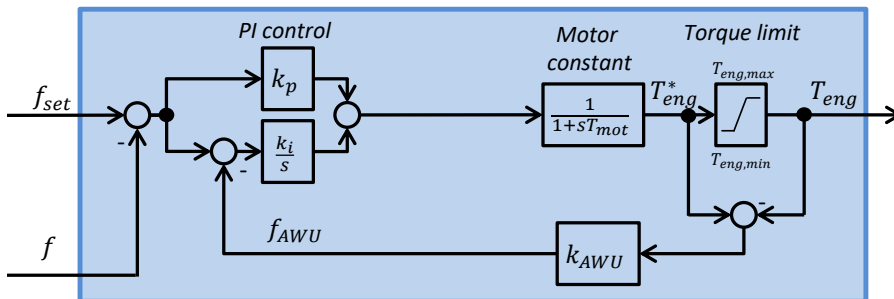
Figure 26 – Linear engine model of a genset with torque limitation.

One advantage of the linear approach is the low number of parameters that describe the dynamic engine behavior. The dominating parameters k_p and k_i (PI controller) can be determined by characteristic measurements and curve fitting methods.

3.4.5.2 Fuzzy-based Model Approach

Modern combustion engines are complex systems with additional components such as variable-geometry turbochargers and exhaust gas recirculation and have to fulfill high requirements regarding contaminant reduction. All these features lead to a nonlinear behavior depending on many input parameters which are not published by the manufacturers. Due to that reason a phenomenological approach basing on fuzzy logic is introduced. The suggested control is a MISO system with two inputs (frequency deviation $\Delta f = f - f_{set}$ and the delayed engine torque $T_{eng,delay}$) and one output (engine torque T_{eng}). It consists of a fuzzy logic followed by a PI control with anti-windup (Fig. 27).
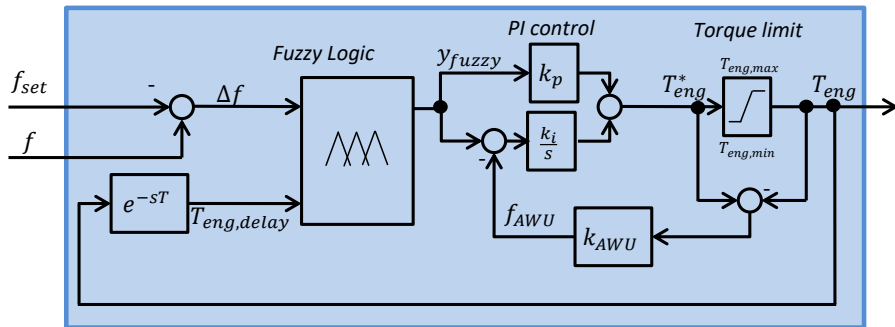
Figure 27 – Fuzzy-based engine model of a genset.

The fuzzy logic is based on 3 steps [94]:

1. Fuzzification

2. Inference

3. Defuzzification

First, both of the input signals are fuzzified. Therefore, the membership functions $\mu_{f,x}$ and $\mu_{Teng,x}$ are introduced. Due to simplification, the membership functions are defined in trapezoidal form (with four parameters each) or in triangular form (three parameters each). Nevertheless, it can be defined as functions with any shape. For Δf, four membership functions ($\mu_{f,LL}$, $\mu_{f,L}$, $\mu_{f,N}$, $\mu_{f,H}$) are defined (Fig. 28a). The input T_{eng} is fuzzified by three membership functions ($\mu_{T,L}$, $\mu_{T,N}$, $\mu_{T,H}$) as plotted in Fig. 28b.

In the second step (inference), the linguistic terms are defined (in this case, six terms are sufficient):

- IF Δf = "LL", THEN y_{fuzzy} = "Y_1"

- IF Δf = "L", THEN y_{fuzzy} = "Y_2"

- IF Δf = "N", THEN y_{fuzzy} = "Y_3"

- IF Δf = "H" AND $T_{eng,delay}$ = "L", THEN y_{fuzzy} = "Y_4"

- IF Δf = "H" AND $T_{eng,delay}$ = "N", THEN y_{fuzzy} = "Y_5"

- IF Δf = "H" AND $T_{eng,delay}$ = "H", THEN y_{fuzzy} = "Y_6"
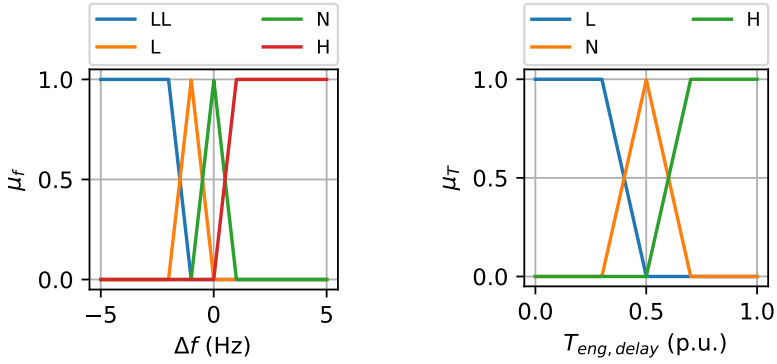
(a) Membership functions for input Δf.   (b) Membership functions for input T_{eng}.

Figure 28 – Membership functions of inputs Δf and T_{eng} for fuzzification.

Table 3 – Inference table for fuzzy-based engine model approach of a genset.

		Δf			
		LL	L	N	H
$T_{eng,delay}$	L	Y_1	Y_2	Y_3	Y_4
	N	Y_1	Y_2	Y_3	Y_5
	H	Y_1	Y_2	Y_3	Y_6

Table 3 shows the inference in tabular form.

In mathematical form, the linguistic terms are represented by *min*-functions for the "AND" operator and by *max*-functions for the "OR" operator. This leads to the following set of equations:

$$a_1 = \mu_{f,LL}(\Delta f; T_{eng,delay}) \tag{29a}$$

$$a_2 = \mu_{f,L}(\Delta f; T_{eng,delay}) \tag{29b}$$

$$a_3 = \mu_{f,N}(\Delta f; T_{eng,delay}) \tag{29c}$$

$$a_4 = min\left(\mu_{f,H}(\Delta f; T_{eng,delay}); \mu_{Teng,L}(\Delta f; T_{eng,delay})\right) \tag{29d}$$

$$a_5 = min\left(\mu_{f,H}(\Delta f; T_{eng,delay}); \mu_{Teng,N}(\Delta f; T_{eng,delay})\right) \tag{29e}$$

$$a_6 = min\left(\mu_{f,H}(\Delta f; T_{eng,delay}); \mu_{Teng,H}(\Delta f; T_{eng,delay})\right) \tag{29f}$$

The fuzzification and inference are followed by the defuzzification. Each output $Y_1 \ldots Y_6$ is defined as a so-called "singleton", which is a scalar gain. This simplifies the calculation

of the fuzzy output y_{fuzzy} to the following equation for the six linguistic terms used in this model:

$$y_{fuzzy} = \frac{a_1 \cdot y_1 + a_2 \cdot y_2 + a_3 \cdot y_3 + a_4 \cdot y_4 + a_5 \cdot y_5 + a_6 \cdot y_6}{a_1 + a_2 + a_3 + a_4 + a_5 + a_6} \tag{30}$$

In general, it can be written as

$$y_{fuzzy} = \frac{\sum_{k=1}^{N} a_k \cdot y_k}{\sum_{k=1}^{N} a_k} \tag{31}$$

The fuzzy logic with output y_{fuzzy} is followed by a PI control; the overall output of the engine (control) circuit regarding Fig. 27 is the engine torque T_{eng}.

Section 6.1.3 presents the parameter estimation for the fuzzy-based engine model and compares it with the linear approach, but also with measurements at a genset driven by plant oil.

By the fuzzy-based approach, it is possible to consider nonlinear effects caused by the control strategy, which is not published by the engine manufacturers. Nevertheless, a high number of parameters needs to be defined (at least four parameters for each membership function as well as 6 resulting outputs $y_1 \ldots y_2$).

3.4.6 Complete Block Diagram of a Genset Model

Based on all sub-models described above, the genset is modeled regarding Fig. 29. The detailed block diagram includes droop control, synchronous machine (SM) excitation control, a synchronous machine model as well as a nonlinear engine model based on fuzzy logic, as described above.
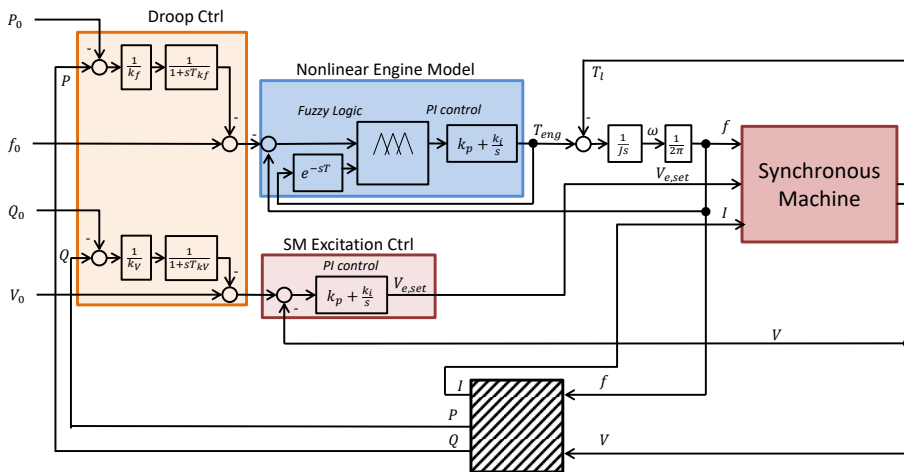
Figure 29 – Complete block diagram of a genset including nonlinear engine model and droop control.

3.5 PV system under consideration of German Application Guide VDE AR-N 4105

One essential renewable energy source in islanded microgrids is photovoltaic (PV) systems.

The PV model is based on the German Application Guide *VDE AR-N4105* [99] which describes the requirements for grid integration of renewable energy sources on LV level. The relevant parts for island grid investigations are presented in section 2.2.2

For modeling of microgrids in island operation, two aspects play an important role. On the one hand, the startup procedure of a PV plant during black start has to be taken into account (section 4.4), on the other hand, the power feed-in depending on the grid frequency should be considered.

The controller's block diagram is shown in Fig. 30. An active and reactive power controller without grid forming capability is assumed (*CSI-Mode*, see chapter 3.3.1). The intermediate signals P_{set} and Q_{set} are generated in the block *PV Ctrl*. For dynamic (long term) simulations, power profiles ($P_{set,profile}$ resp. $Q_{set,profile}$) can be set. The conversion from solar radiation to electrical power depending on temperature, orientation, season and installation angle is not considered in this model (as in [1] or [104]). Further, the PV cells' modeling, the inverter technology, but also the inverter control (e.g., by Maximum Power Point Tracking - MPPT) described, e.g., in [15, 36, 51, 78, 91, 87] are not taken into account in this model as the focus is set on the grid integration and the interaction with other microgrid assets in island operation. In section 6.1.4, a comparison with measurements at a real PV system located at the MCW is presented.
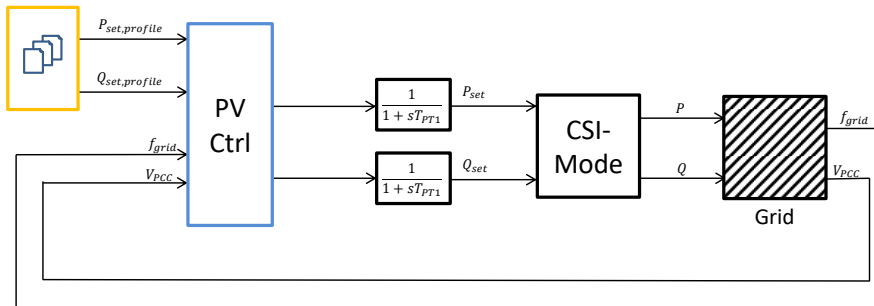
Figure 30 – Block diagram of the mathematical model of a PV plant.

Besides the $\cos\varphi(P)$ relation (equal to section 3.3.2), the startup behavior after grid connection is taken into account in the PV modeling. It is realized by a state machine shown in Fig. 31.

The states $0\ldots4$ are defined as:

- 0: simulation start-up

- 1: no active power feed-in allowed ($P_{DG} = 0$)

- 2: normal operation (without power limitation)

- 3: active power reduction at over-frequency
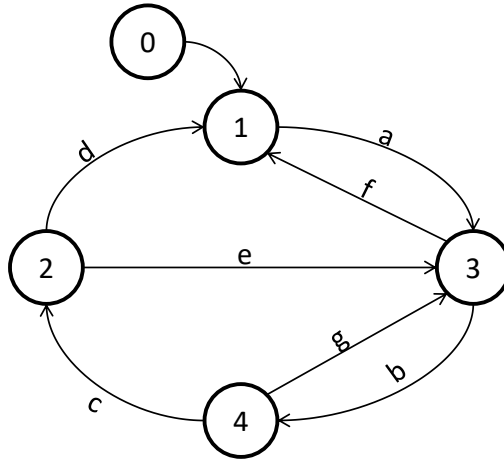
Figure 31 – State machine for PV control.

- 4: active power feed-in ramp limiter

The conditions for the state transitions a...g are:

- a: Grid frequency is in the range of $47.5Hz < f < 50.05Hz$ and voltage is in the range of $85\% \, V_r \leq V \leq 110\% \, V_r$ for at least 60s

- b: Grid frequency $f < 50.2Hz$

- c: Active power ramp up completed

- d: Grid frequency $f < 47.5Hz$

- e: Grid frequency $f > 50.2Hz$

- f: Grid frequency $f \geq 51.5Hz$

- g: Grid frequency $f > 50.2Hz$

Based on the above, the startup sequence can be described as follows. After simulation start, no active power feed-in is allowed (state *1*) until the grid frequency and grid voltage are in a predefined range for at least 60s (transition *a*) and state *3* is reached. If the grid frequency is lower than $50.2Hz$, state *4* is activated and the active power feed-in is limited by a ramp (according to VDE AR-N4105: maximum 10% per minute regarding maximum power). After completing the ramp up, state *2* is responsible for normal operation as long as the grid frequency is in the range between $47.5Hz \leq f_{grid} < 50.2Hz$.

In case of over-frequency, state *3* is activated by transition *e*. For a grid frequency lower than 47.5 Hz, the active power feed-in is set to zero (state *1* over transition *d*).

3.6 Heat Pump

In actual energy systems, building climatization by heat pumps plays an increasing role. In Germany, the amount of new installed heat pumps in new created buildings increased from less than 1% in the year 2000 to more than 45% in the year 2020 (Fig. 32).
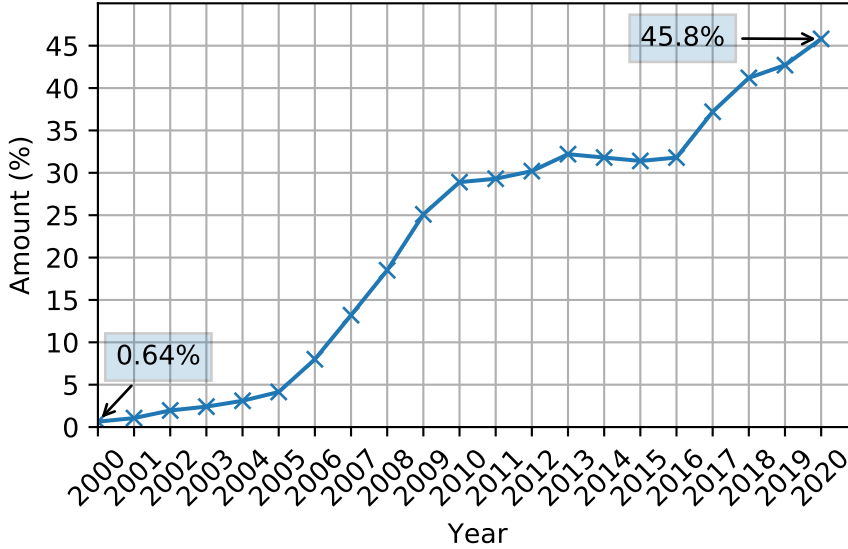
Figure 32 – Development of new installed heat pumps in new created buildings in Germany (from: [90]).

For modeling and planning of a microgrid, a dynamic mathematical model was developed as a coupled model consisting of a thermal part (section 3.6.1) and an electrical part (section 3.6.2).

For the thermal model, an equal room temperature inside of the building is assumed. A more complex thermal model could be integrated as well, but this was not the aim of this work. Therefore, the mentioned simplification and an appropriate approximation for the behavior of a heat pump are assumed.

3.6.1 Thermal Modeling of a Building

In the thermal model for a building with equal temperature distribution, the heating system, the solar radiation, the thermal losses caused by non-ideal insulation as well as the inside and outside temperature are considered.

A first order ODE is used to describe the derivation of the enthalpy, which depends on the sum of all relevant heat flows (heating $\dot{Q}_{heating}$, solar radiation $\dot{Q}_{solar}$ and thermal losses $\dot{Q}_{losses}$) and is contained in Eq. (32).

$$\frac{dH}{dt} = \dot{Q}_{heating} + \dot{Q}_{solar} - \dot{Q}_{losses} \tag{32}$$

Further, the derivative of the enthalpy depends on the heat capacity C_p of the building and the derivative of the temperature inside the building ϑ_{inside} (Eq. (33)).

$$\frac{dH}{dt} = C_p \cdot \frac{d\vartheta_{inside}}{dt} \tag{33}$$

45

In Fig. 33 the heat flow is represented graphically.
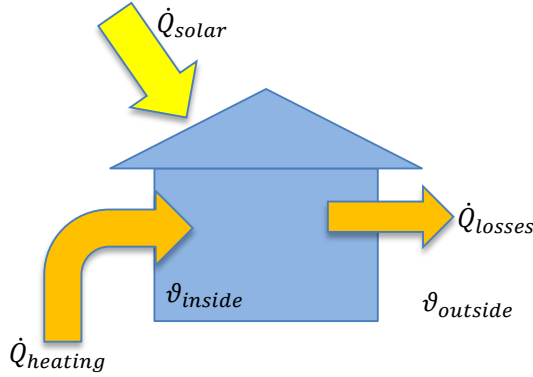
Figure 33 – Heat flow and temperatures in a simplified building model.

A first order ODE is determined by combining Eqs. (32) and (33) to Eq. (34).

$$\frac{d\vartheta_{inside}}{dt} = \frac{1}{C_p} \cdot \left(\dot{Q}_{heating} + \dot{Q}_{solar} - \dot{Q}_{losses} \right) \tag{34}$$

The heat flow caused by solar radiation is described by a linear correlation:

$$\dot{Q}_{solar} = k_{solar} \cdot G_{solar} \tag{35}$$

G_{solar} is the global solar radiation. The constant k_{solar} is an aggregated coefficient introduced for considering the relevant surface area of the building and its insulation and will be determined by specific measurements.

The thermal losses are represented by the difference between inside and outside temperature and the heat transmission coefficient H_T:

$$\dot{Q}_{losses} = H_T \cdot (\vartheta_{inside} - \vartheta_{outside}) \tag{36}$$

From Eqs. (34), (35) and (36), a first order ODE is obtained, as expressed in Eq. (37).

$$\frac{d\vartheta_{inside}}{dt} = \frac{1}{C_p} \cdot \left[\dot{Q}_{heating} + k_{solar} \cdot G_{solar} - H_T \cdot (\vartheta_{inside} - \vartheta_{outside}) \right] \tag{37}$$

Input variables of this model are $\dot{Q}_{heating}$, G_{solar} and $\vartheta_{outside}$. The model constants are the heat capacity C_p, the solar constant k_{solar} as well as the heat transmission coefficient H_T, which need to be determined by calculations or specific measurements as proposed in section 3.6.3.

3.6.2 Electrical Modeling of a Heat Pump

Besides the thermal behavior, the electrical power consumption P_{HP} depends on the inside temperature setpoint $\vartheta_{inside,set}$, the COP (coefficient of power) curve and on the control strategy for the temperature inside the building. A nonlinear closed loop control model is shown in Fig. 34.

The *COP* describes the dependency of the thermal heat flow $\dot{Q}_{heating}$ and the consumed active power P_{HP} depending on the outside temperature $\vartheta_{outside}$, as shown in
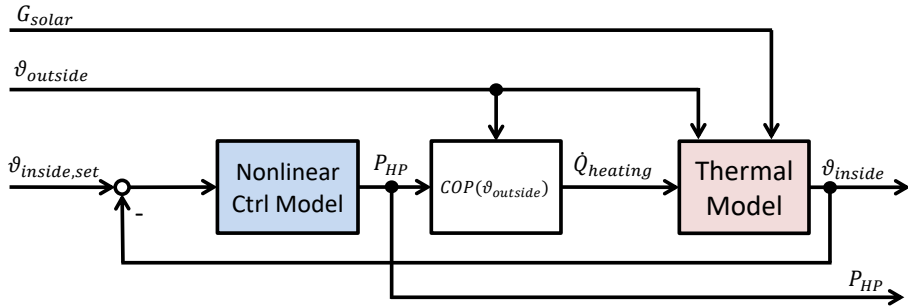
Figure 34 – Heat pump closed loop model including nonlinear control.

Eq. (38) [30]. As an example, the function $COP(\vartheta_{outside})$ curve for a specific heat pump (DAIKIN FAA71A/RZAG71MY1 [25]) is shown in Fig. 35.

$$\dot{Q}_{heating} = COP(\vartheta_{outside}) \cdot P_{HP} \tag{38}$$
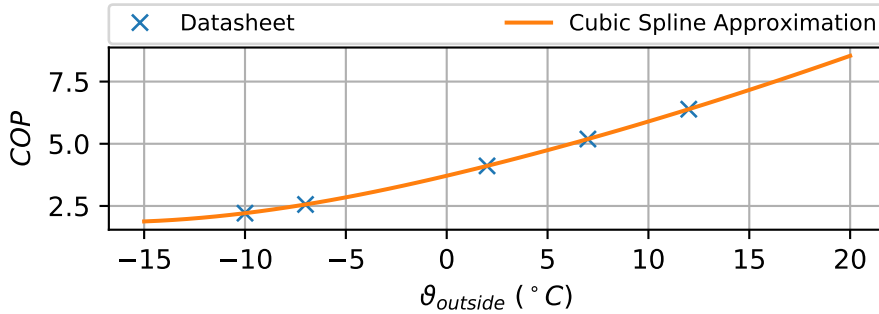
Figure 35 – Coefficient of power (example of DAIKIN FAA71A/RZAG71MY1 from [25]).

An overview of the assumed nonlinear control structure of the inside temperature is represented in Fig. 36.

The control model allows the consideration of a specific startup behavior. In the case of the investigated heat pump of the manufacturer *DAIKIN* (Type: *FAA71A/RZAG71MY1* [25]), the consumed electrical power P_{HP} is increased during the startup process (Fig. 37a) during 2800s. The corresponding cumulated energy E_{HP} for five experiments (exp1 … exp5) for the first 2800s is plotted in Fig. 37b whereas the outside temperature during these experiments is shown in Fig. 37c.

The dependency of the consumed energy E_{HP} on the outside temperature during start up $(0 \dots 2800s)$ is shown in Fig. 38 for measured data as well as the resulting linearized function.

In this special heat pump, the active power consumption $P_{HP}(t)$ at startup based on the outside temperature is estimated by cubic splines and an optimization algorithm with the following objective function:

$$\int_0^{2800s} P_{HP}(t)dt = E_{HP,startup}(\vartheta_{outside}) \tag{39}$$
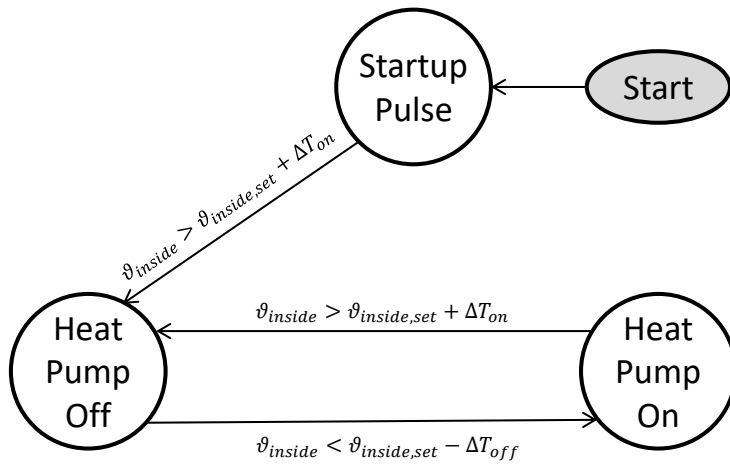
Figure 36 – Nonlinear heat pump control in state machine representation.
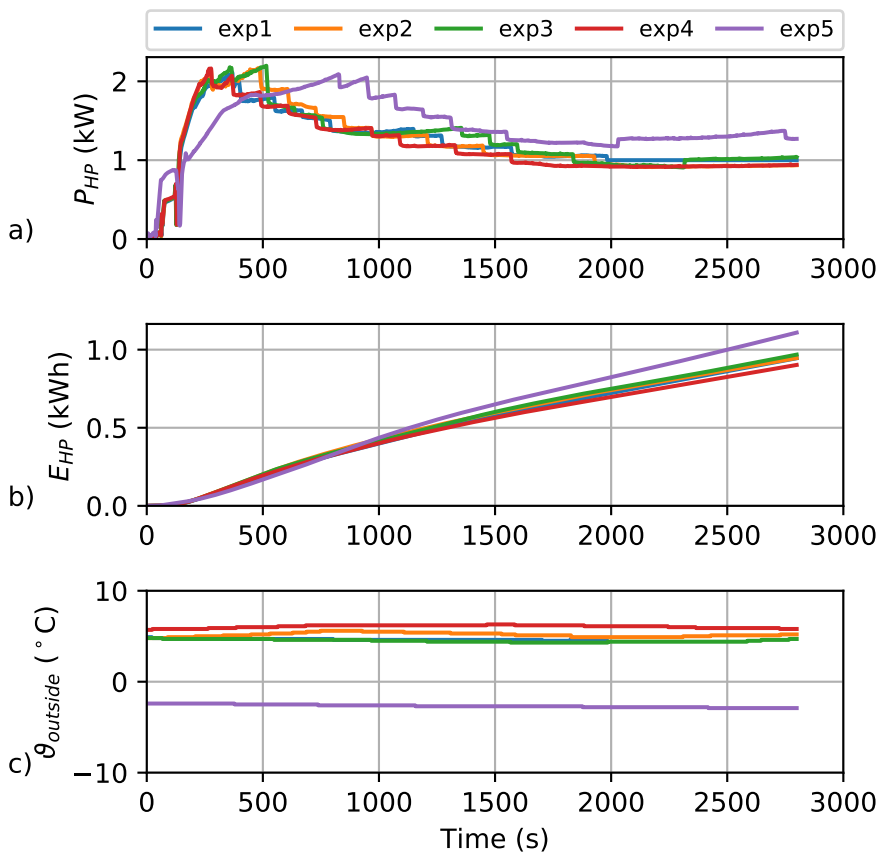
Figure 37 – Startup behavior of a heat pump for five different experiments (exp1...exp5). a) active power consumption P_{HP}; b) cumulated energy consumption E_{HP}; c) outside temperature $\vartheta_{outside}$.
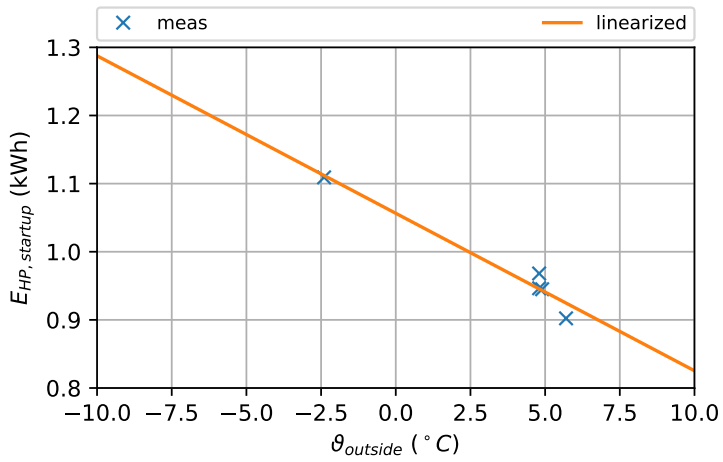
Figure 38 – Consumed energy during heat pump startup depending on outside temperature.
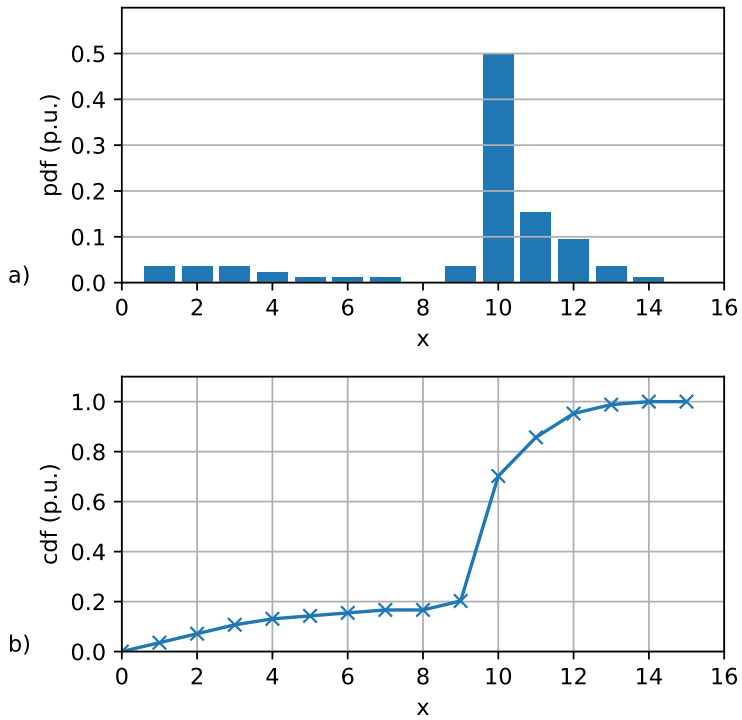
Figure 39 – Distribution of high power pulses during heat pump operation (heat pump on). a) discrete probability density function; b) cumulated density function.

3.6.3 Procedure for Model Parameter Estimation

For the thermal model parameter estimation, the following procedure is supposed.

1. Measurement of inside temperature ϑ_{inside}, outside temperature $\vartheta_{outside}$ and solar radiation G_{solar} without heating ($\dot{Q}_{heating} = 0$).
   $\rightarrow$ Determination of coefficients $\frac{k_{solar}}{C_p}$ and $\frac{H_T}{C_p}$ (Eq. (37)) by curve fitting methods.

2. Forced heating (with electric heater) inside the building and measurement of ϑ_{inside}, $\vartheta_{outside}$, G_{solar} as well as the heat flow $\dot{Q}_{heating}$ (which can be approximated by the power consumption of the electric heater).
   $\rightarrow$ Determination of coefficients C_p, k_{solar} and H_T by usage of curve fitting methods.

3. Introduction of electrical power consumption, temperature hysteresis and coefficient of power (COP) in the heat pump model (e.g., from data sheet).

4. Analysis of electrical behavior to carry out specific effects, e.g., startup power rise or defrost effects).

The resulting curves for parameter identification and verification are shown in Fig. 40.

3.6.4 Consideration of Manufacturer Specific Behavior in the Heat Pump Model

The heat pump modeling shown in this work is based on a heat pump of the manufacturer *DAIKIN* (Type *FAA71A/RZAG71MY1* [25]). Two specific effects of this device are taken into account. After power on and during heating up of the building, an increased active power consumption is measured. The height and duration depend on the outside temperature $\vartheta_{outside}$ (as shown in Fig. 38).

The simulation result of the complete model regarding Fig. 34 and a comparison with measurements at the MCW are shown in Fig. 43.
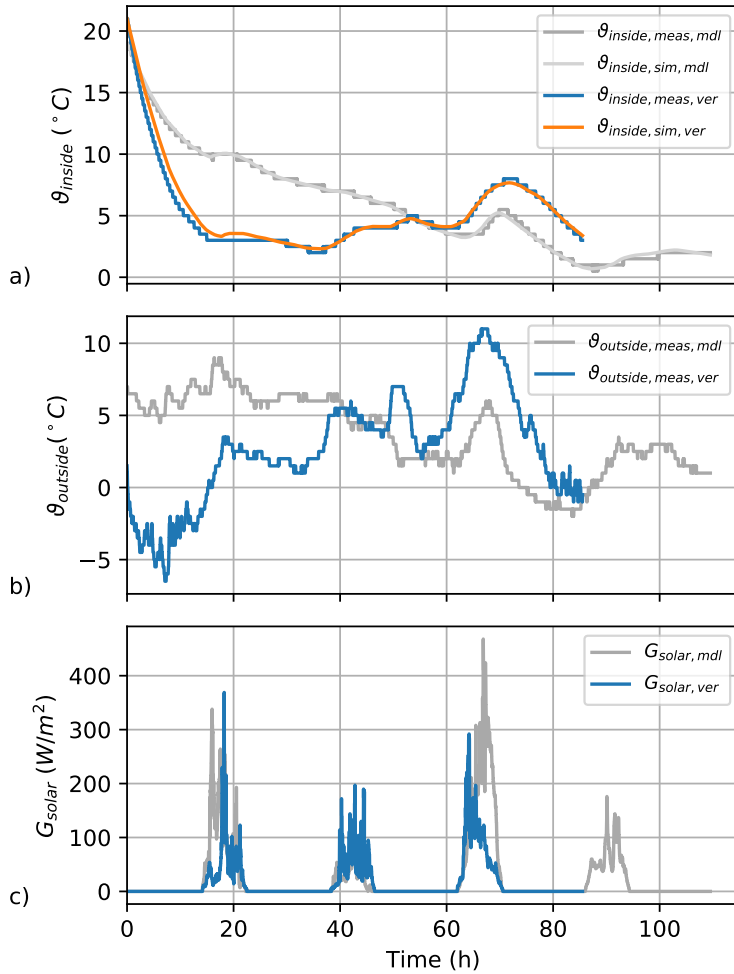
Figure 40 – Comparison of measurement and simulation for the parameter identification of the example building "control center". Gray (dark/light): measurement data used for parameter identification resp. simulation result. Blue: verification measurement and corresponding simulation result (orange) for parameter estimation step 1. a) inside temperature; b) outside temperature; c) Solar Radiation.
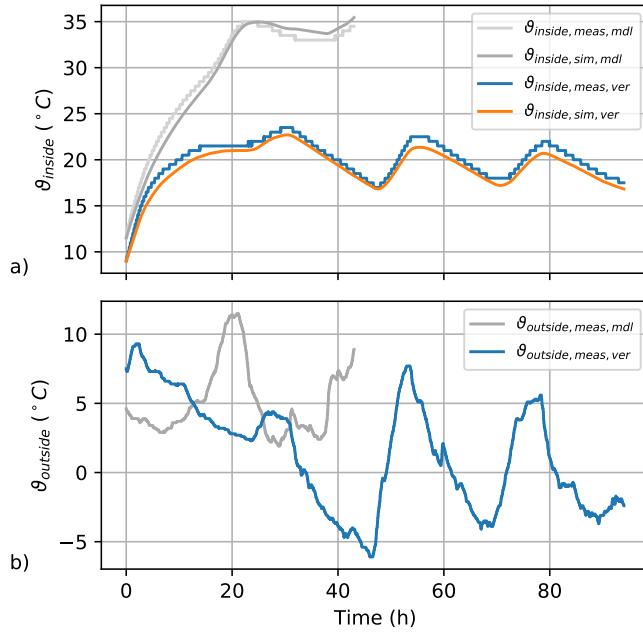
Figure 41 – Modeling and verification result for parameter estimation step 2. Gray: data for parameter identification. Blue/orange: verification. a) inside temperature; b) outside temperature.
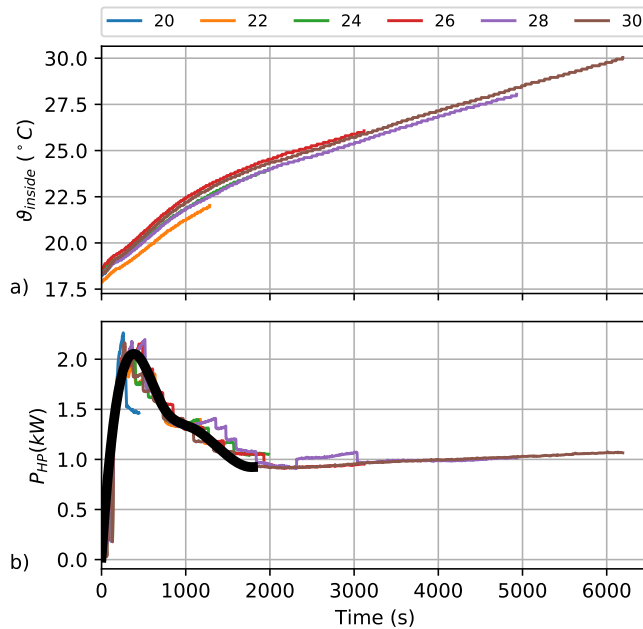
Figure 42 – Power consumption at startup of a heat pump for inside temperature setpoints from $20°C$ (blue) to $30°C$ (brown). Black: approximated spline function for power consumption. a) inside temperature; b) heat pump power consumption.
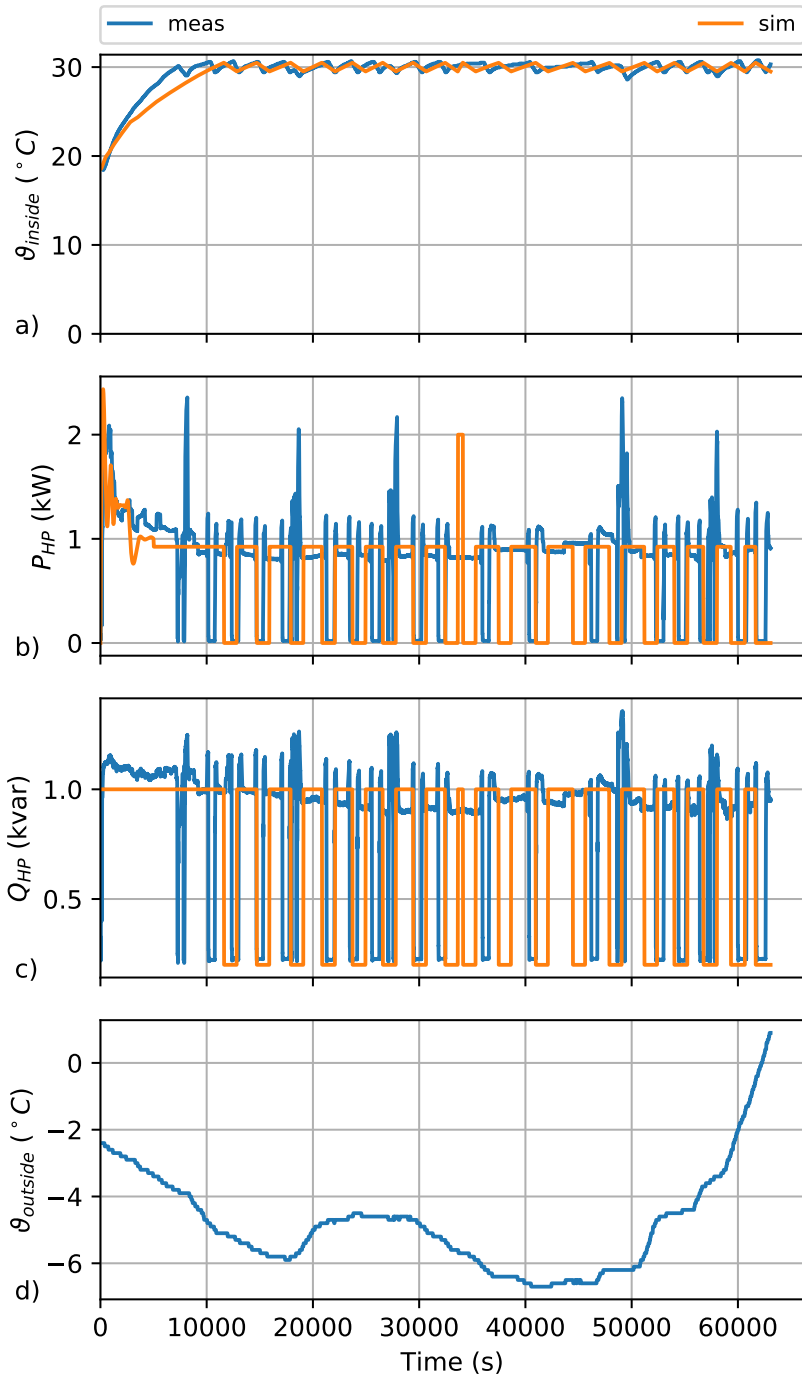
Figure 43 – Simulation result (orange) and comparison with measurement data (blue) for heat pump operation with inside temperature setpoint of $30°C$. *a) inside temperature; b) active power consumption; c) corresponding reactive power; d) outside temperature.*

3.7 Conclusion

The development of microgrid control algorithms and the analysis regarding dynamic behavior require mathematical models for all relevant assets.

In this chapter, a modeling approach is described for the following assets:

- Electrical line modeling for a typical earth cable used in LV grids.

- Grid forming BSS including droop control using a simplified modeling approach based on Thévenin's theorem. A detailed modeling including battery cell model, inverter, filter and transformer is not considered in the described model.

- Grid supporting BSS under consideration of SOE limitation, grid restrictions regarding VDE AR-N4105, grid supporting droop control as well as dead times measured in existing plants.

- Genset model with

   1. Linear Engine Model
   2. Nonlinear Engine Model based on Fuzzy Logic

- PV system under consideration of VDE AR-N4105

- Heat Pump including control and consideration of the building. A method for parameter determination is presented as well.

Each model includes the relevant control algorithms to describe the dynamic behavior properly. The objective of the mathematical models is the analysis of interaction and the research and development of microgrid control algorithms and operating strategies. For an analysis of island grids regarding harmonics or flicker, a higher level of detail (e.g., consideration of PWM pulses in the inverter) is needed. It should be pointed out that more complex models lead to a higher computation time, but also the number of parameters increases, which has to be known from the manufacturer or determined by extensive measurements.

The described models are verified by comparison with specific measurements in section 6. Thus, the research and development of microgrid control strategies presented in section 4 is based on verified asset models.

4 Control strategies for microgrids in island mode operation

In this section, the interaction of different GFUs and GSUs with DGs and loads is investigated. Therefore, different aspects and control algrorithms are considered.

First, the parallel operation of GFUs and GSUs using droop control is investigated (section 4.1). Next, a concept for secondary control based on a centralized microgrid controller is developed (section 4.2). Further, concepts for energy scheduling of BSSs 4.3), black start (section 4.4) as well as resynchronization (section 4.5) are described. Finally, a failsafe control concept for the parallel operation of BSSs and gensets without communication link is presented (section 4.6).

4.1 Parallel Operation of Grid Forming and Grid Supporting Units using Droop Control for Active and Reactive Power

In islanded microgrids, typically, a set of various assets is operated in parallel, which means that, e.g., one BSS is operated in parallel to one genset or two BSSs with grid forming capability are responsible for voltage and frequency control. Parallel GFUs increase the resilience of the complete system due to redundancy effects. Furthermore, also grid supporting units (GSUs) operated in parallel to GFUs are examined.

The considered assets including control are described mathematically in Chapter 3. The investigated strategy is based on droop control of active and reactive power. Further, inverter control concepts such as virtual synchronous machines [12] or virtual impedance [38] are not considered.

The mathematical models for all relevant assets developed in section 3 are now combined in power system analysis software. In this case, the software tool PowerFactory from the manufacturer DIgSILENT [28] is chosen. In Fig. 44, the SLD of the islanded microgrid in PowerFactory is presented.

In the frame of this work, the following combinations of GFUs resp. GSUs are investigated:

1. Inverter GFUs

2. Inverter and Genset as GFUs

3. Inverter GFU and GSU

4. Genset and Inverter GSU

For these scenarios, specific calculation results based on dynamic simulations are compared with measurements at the microgrid demonstrator MCW (described in section 5) and are shown in section 6.2. Further, the effect of the load location as well as voltage droop factor variation are investigated by simulation.

4.1.1 Effect of Load Location

Based on the verified models, the effect of the load location on the dynamic behavior as well as the reactive power sharing are investigated by simulation. The corresponding SLD is shown in Fig. 45.

The line length between both assets *GFU1* and *GFU2* is set to $x_{tot} = 1km$. A LV cable from type *NAY2Y* (see section 3.1) is assumed.

The load location now is varied between both GFUs:

$$x_{line1} + x_{line2} = 1km \qquad (40)$$
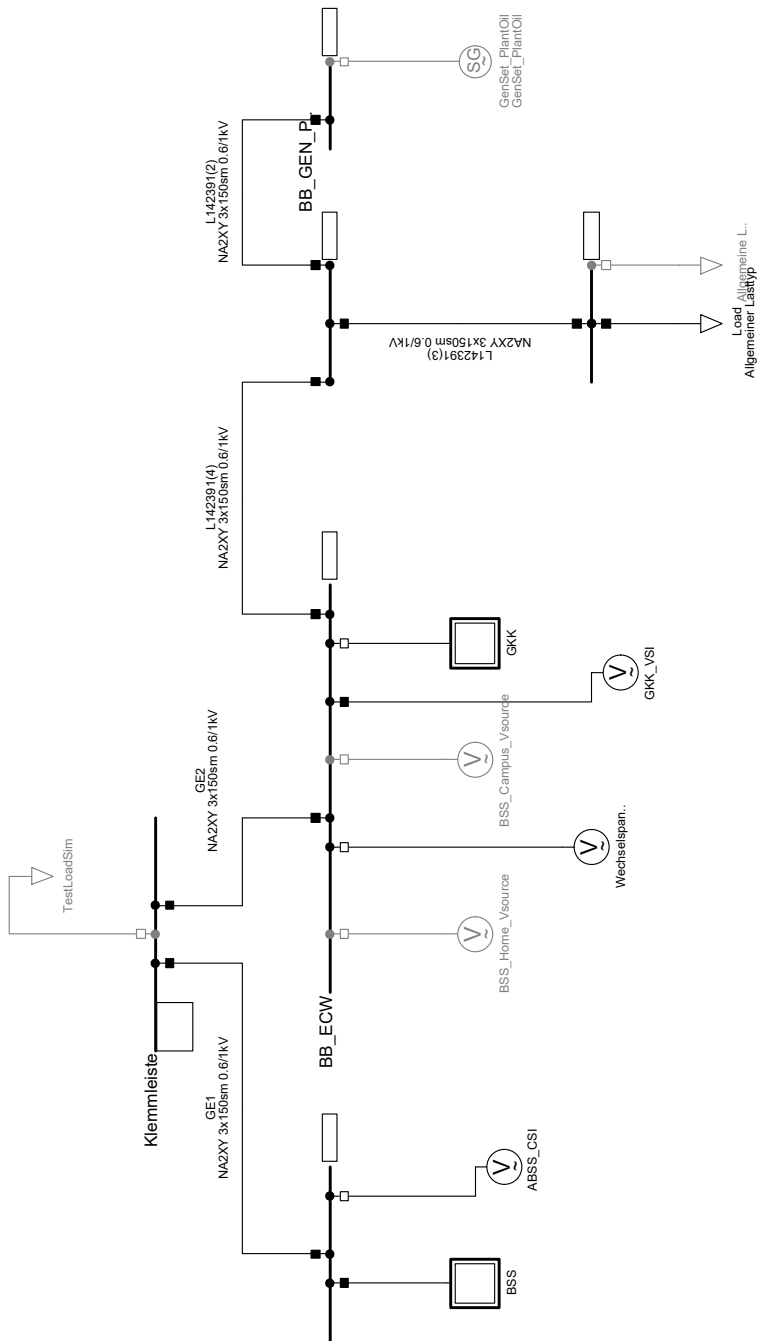
Figure 44 – Grid model (overview) in simulation software PowerFactory from manufacturer DIgSI-LENT for investigation of parallel operated GFUs and GSUs.
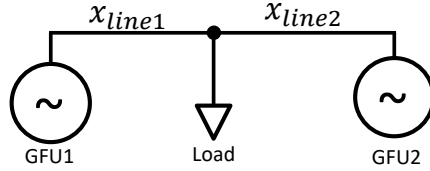
Figure 45 – Simplified SLD for the analysis of load location effect in islanded microgrids on dynamic behavior as well as reactive power sharing.

For both assets, the droop control is configured equally. The corresponding parameters are given in Table 4.

Table 4 – Droop control configuration of GFU1 and GFU2 for variation of the load location.

Parameter	k_f	k_V	f_0	V_0	P_0	Q_0	T_{kf}	T_{kV}
Value	$150kW/Hz$	$12kvar/V$	$50Hz$	$400V$	$0kW$	$0kW$	$0.15s$	$0.1s$

The results of the numeric simulation for variation of x_{line1} from $0.0km$ to $1.0km$ (and consequently x_{line2} from $1.0km$ to $0.0km$) for a load step of $100kW$ are shown in Fig. 46.

It can be seen that the transient behavior depends on the line length ratio. Active power distribution as well as the grid frequency show a damped oscillation behavior at a load step. In Fig. 46d, the time series for the reactive power distribution of $GFU1$ is shown. As a purely ohmic load is used and the reactive power demand in LV grids is small, the reactive power flow is mainly from one GFU to another.

For steady state operation, the reactive power flow depending on the load location resp. depending on x_{line1} is shown in Fig. 47.

It can be seen that the reactive power flow is minimized at an approximately equal line length of $x_{line1} \approx 0.5km$. As both GFUs have different internal impedances, the minimum differs from $0.5km$.

4.1.2 Voltage Droop Factor Variation

In the following, the effect of the voltage droop factor on reactive power distribution is investigated by simulation. It is varied in the range from $5kvar/V$ to $100kvar/V$ for two GFUs (GFU1 resp. GFU2). A load step of $150kW$ is applied to the grid. Fig. 48 shows the corresponding results.

It can be seen that higher voltage droop factors affect higher exchange of reactive power between GFUs (Fig. 48b) and therefore also lower power factors (Fig. 48c). As the voltage deviation is relatively small (in this example, Fig. 48d), lower voltage droop factors can be chosen.

This investigation shows that further concepts have to be taken into account regarding voltage and reactive power control in islanded microgrids. In the frame of this work, two different approaches are presented. The first approach is basing on a central microgrid controller (section 4.2), whereas the second concept presented in section 4.6 involves a decentralized approach.
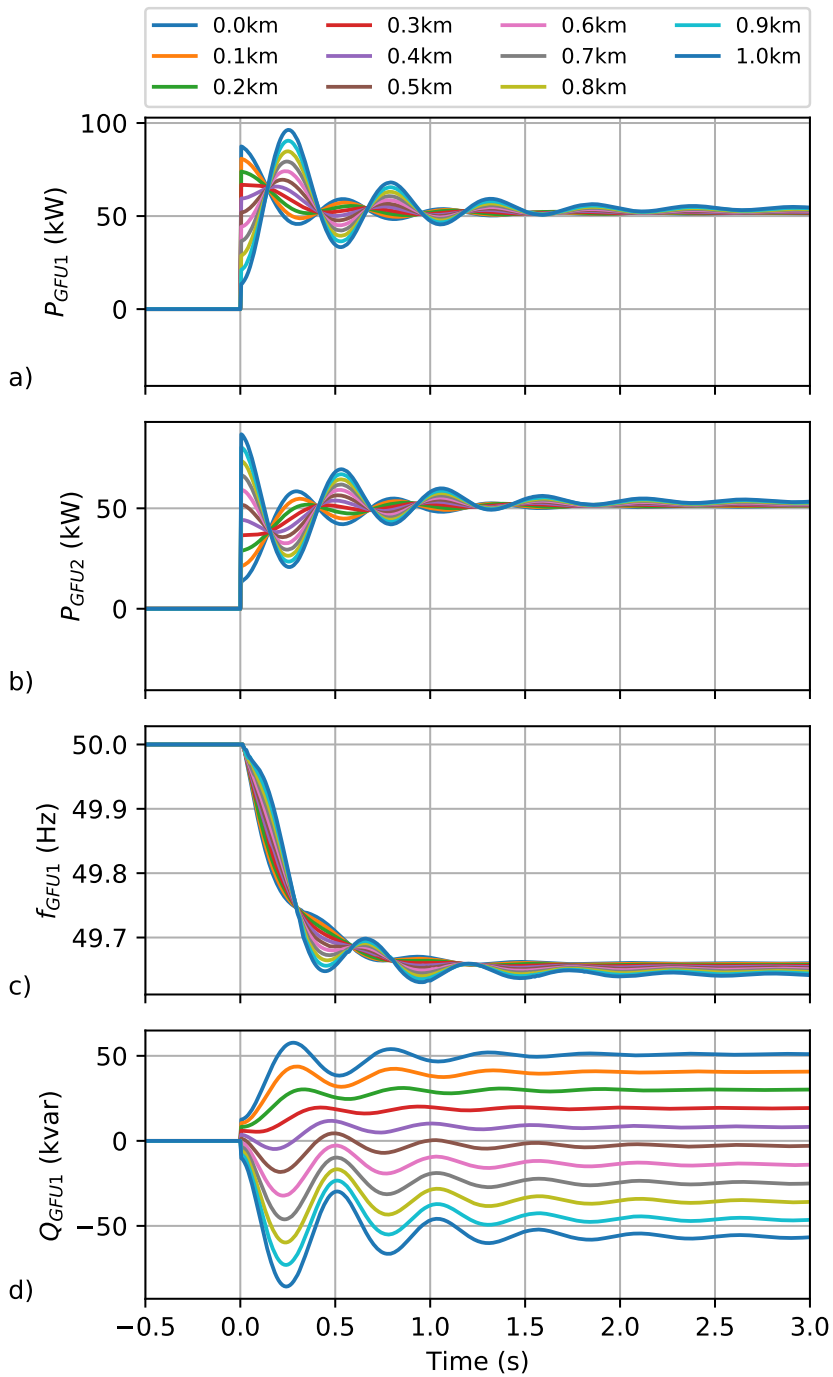
Figure 46 – Simulation results of different load locations by variation of x_{line1} from $0.0km$ to $1.0km$. a) active power distribution of GFU1; b) active Power of GFU2; c) grid frequency measured at GFU1; d) reactive power of GFU1.
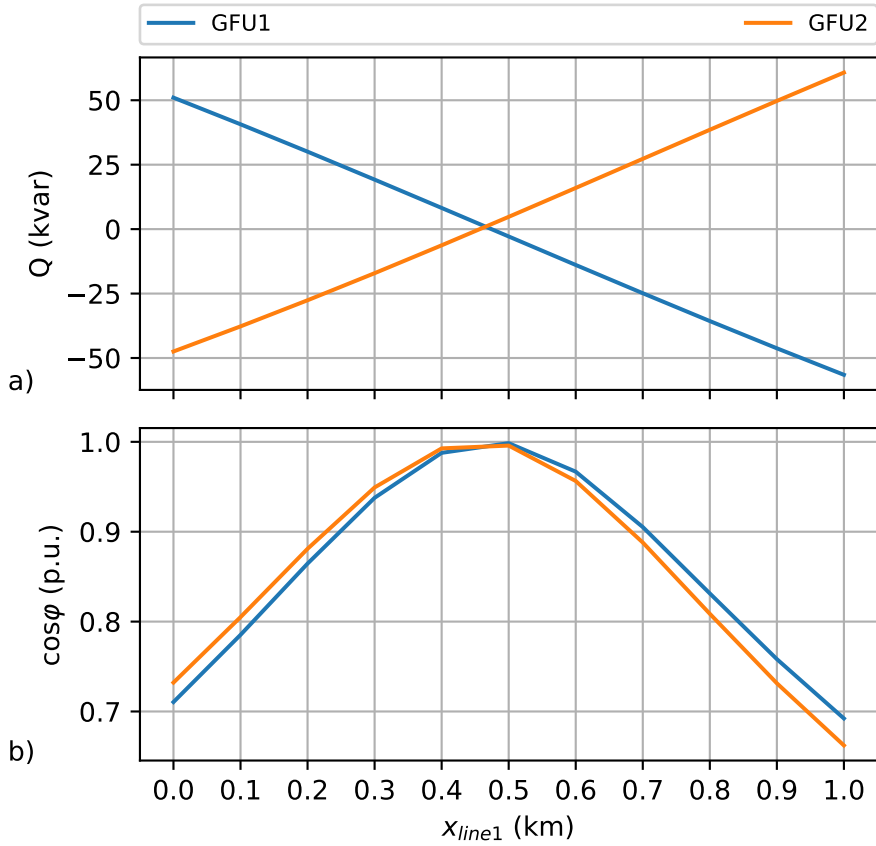
Figure 47 – Reactive power distribution depending on line length x_{line1}. a) reactive power for GFU1 (blue) and GFU2 (orange); b) power factor depending on x_{line1} for GFU1 and GFU2.
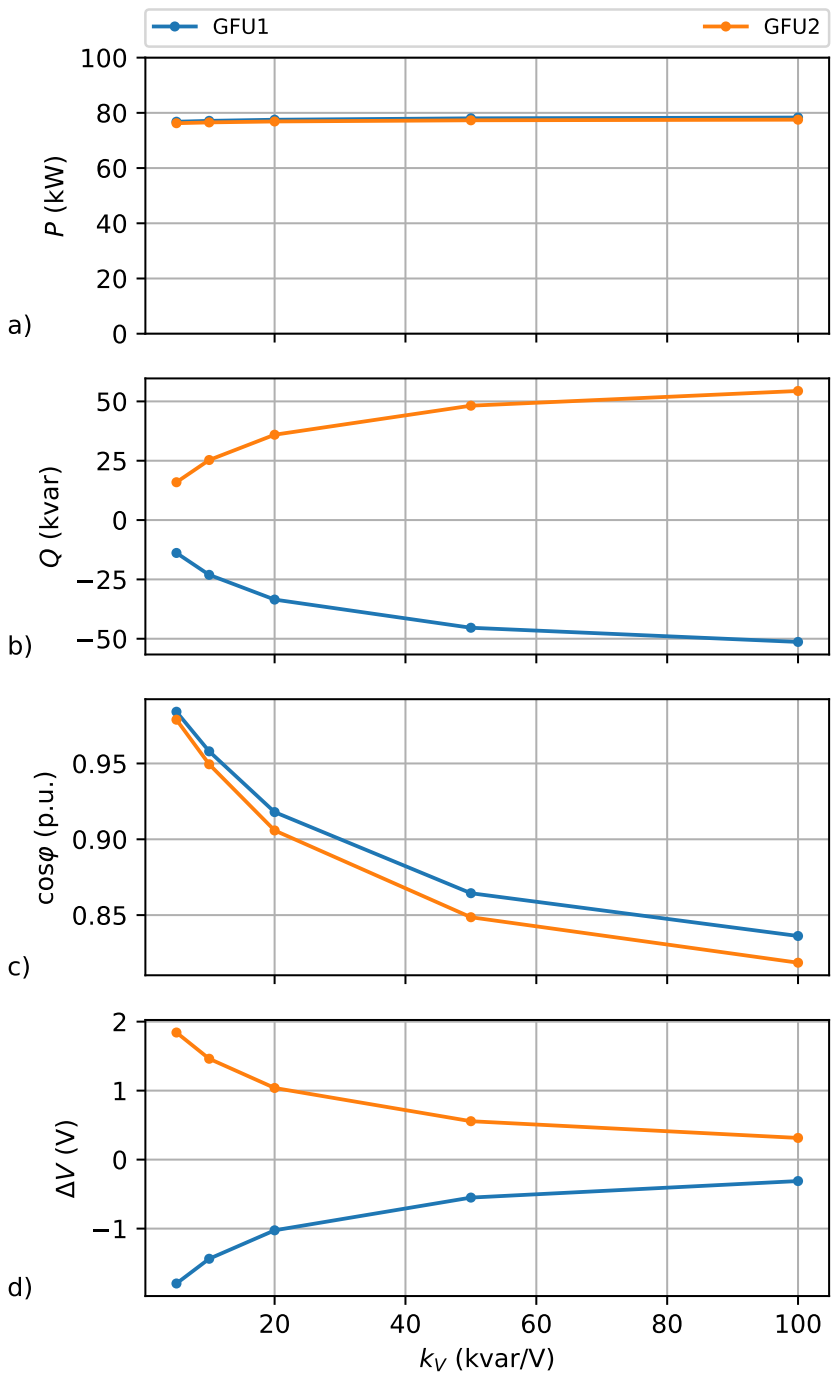
Figure 48 – Effect of voltage/reactive power droop factor variation for two GFUs (blue: GFU1, orange: GFU2). a) active power; b) reactive power; c) power factor $\cos\varphi$; d) voltage deviation.

4.2 Secondary Control Strategies for Active and Reactive Power

In the previous sections, simulation models for typical microgrid assets are described and operated together in island mode. For an optimized operation regarding voltage and frequency and therefore active and reactive power distribution, a centralized control system is set up.

In this multi-level control approach, primary control (droop control) is responsible for grid stabilization at load changes and disturbances by accepting small frequency deviations.

For minimization of the frequency and voltage deviations caused by droop control, secondary control on a superordinated layer is introduced [55, 39, 16]. For that reason, a central Microgrid Controller (MGC) is introduced.

Further concepts with decentralized control strategies are presented in [100, 84, 65, 85, 41, 32, 52, 93, 61, 9, 37, 62, 59] but not considered in this work as the scope in this part is set on a centralized concept. Nevertheless, a failsafe concept for stable grid operation without MGC is investigated in section 4.6.

The main prerequisites on the secondary controller are:

- Minimization of frequency deviation (caused by droop control)

- Active power distribution regarding planning

- Reactive power minimization

- Voltage level control

- Framework for higher level control strategies (e.g., Energy scheduling as described in section 4.3).

The controller structure including interaction with the asset level is shown in Fig. 49.

At least three controllers are implemented in the MGC. The *Active Power Control* (APC) is responsible for the active power management between the assets (e.g., depending on SOE) and frequency control. The *Reactive Power Control* (RPC) is responsible for the minimization of reactive power exchange between assets. The third controller is used for *Voltage Level Control* (VLC). That means that - in steady state - the voltage is either controlled to a constant voltage level at one node or to a minimum deviation to the rated voltage considering all assets.

First, the APC is described. The internal control structure is shown in Fig. 50.

The output $P_{0,1}^{set}$ is connected to the frequency droop controller at the asset level (regarding Eq. (1) resp. Fig. 2).

The control error Δf^* is smoothed to Δf by a PT1 element with time constant T_{APC}. By a controller (in PI structure; Anti-Windup is not shown due to clarity in the diagram), the total active power setpoint $P_{0,tot}$ is determined and allocated to each asset i regarding the singular active power participation factors $k_{APC,i}$. These factors can be adjusted depending on other measurements such as SOE, gensets' fuel tank level or the total active power in the grid.

Further, it is possible to define an active power offset $P_{0,i}^{offset}$ for each asset i.

The described combination of APC and active power droop control allows a distinguished active power distribution for transient time span (droop) as well as steady state (APC). An example is that the BSS is used for balancing fast load steps whereas another asset (e.g., genset or CHP) is used for long-term active power distribution. Some use cases and the corresponding results are presented in section 6.3.
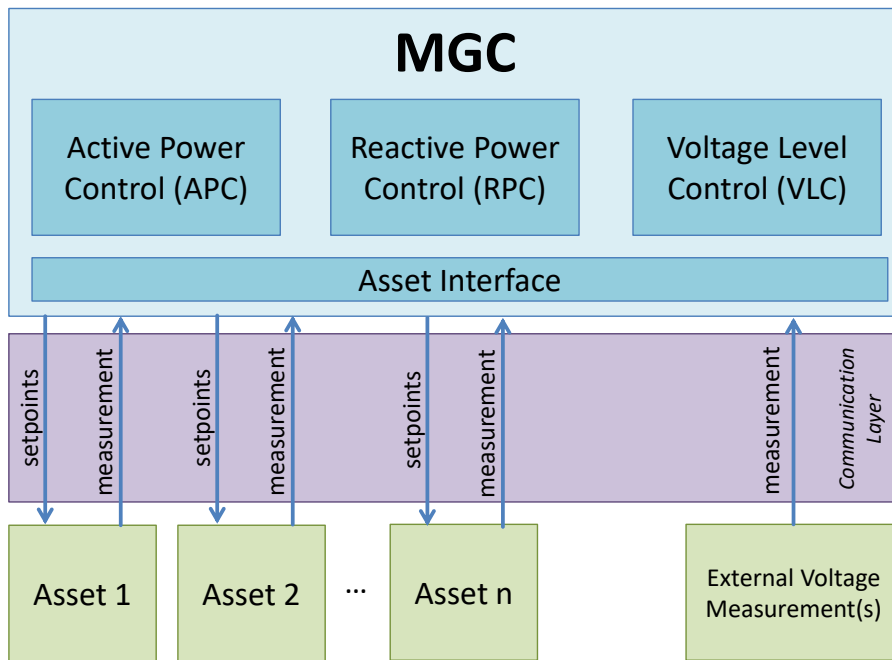
Figure 49 – Block diagram of microgrid controller (MGC) consisting of active power control (APC), reactive power control (RPC) and voltage level control (VLC) as well as communication and asset layer including signal flow.

Further, the reactive power distribution inside an island grid is controlled by the RPC. In contrast to frequency/active power droop control, voltage/reactive power droop control does not lead to a reactive power distribution regarding droop factors as voltage is a local phenomenon and not a global one like the grid frequency (in steady state). This leads to a modified RPC structure (Fig. 51). The reactive power distribution is defined by the participation factors $k_{RPC,i}$. Based on this, the smoothed total reactive power Q_{tot} is divided for all assets. As the voltage/reactive power droop control depends on the asset's voltage, the setpoints $Q_{0,i}^{set}$ are determined by a closed loop controller (in PI structure).

The closed-loop part can also be implemented directly in the asset control. A comparison, especially under consideration of signal delays caused by the communication level, is shown in section 6.3.

The voltage level control (VLC) as the third control part of the MGC has a block structure as shown in Fig. 52. A closed loop control with smoothing filter (PT1 element with T_{VLC}) is obtained. The resulting voltage offset $V_{0,set}$ is set in the voltage/reactive power droop control at the assets. The voltage V_{meas} that is obtained to be controlled can be measured at different nodes, e.g., at one specific asset or at any other node inside the grid. This can be a load with high power or – if the MG is not in island mode permanently – the PCC to another superordinated grid. Therefore, an external voltage measurement as shown in Fig. 49 is necessary.

For simulations of islanded microgrids with distributed assets and a centralized MGC, it is mandatory to consider the transportation delays at the communication between MGC and assets (Fig. 53). This dead time is caused by the (mostly Ethernet-based) communication itself and – especially if assets of different manufacturers are combined – from protocol converters. As an example, the usage of ModbusTCP, Profibus or IEC60870-5-104
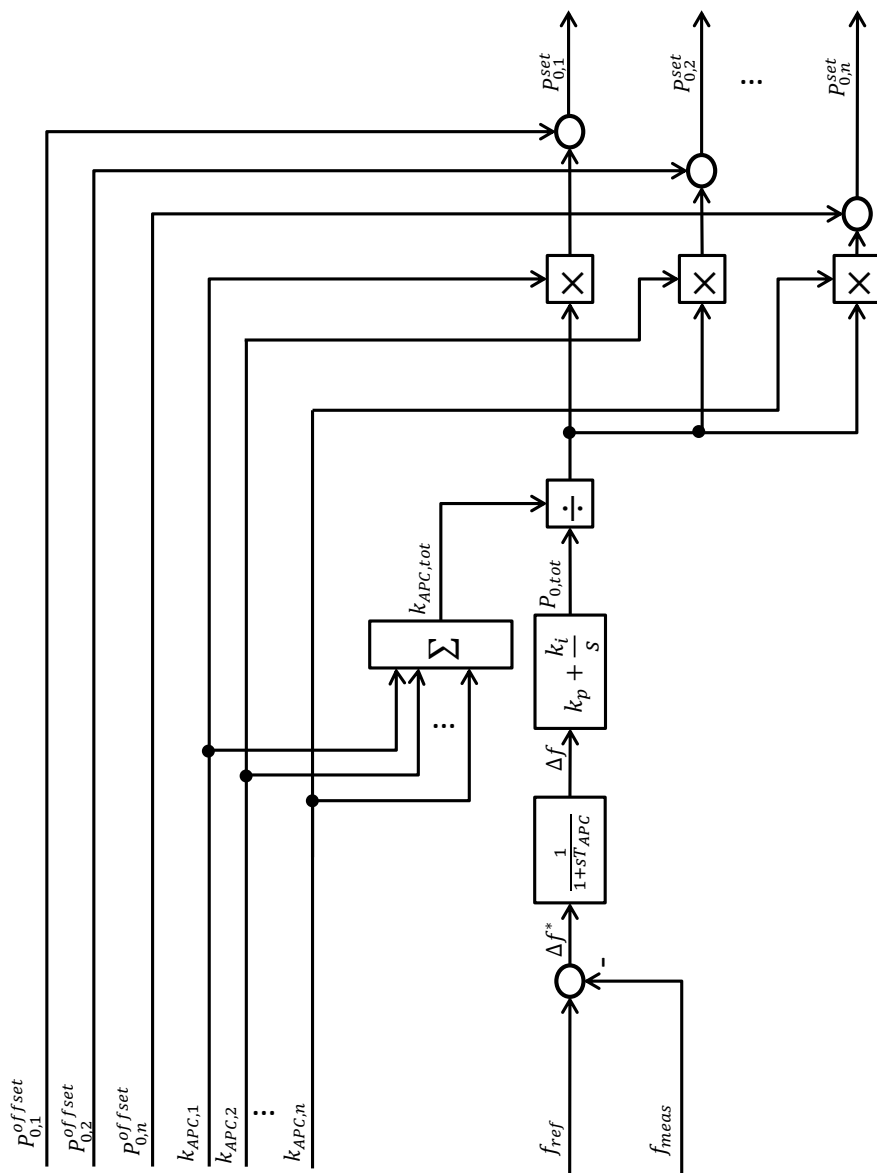
Figure 50 – Block diagram of active power control (APC).
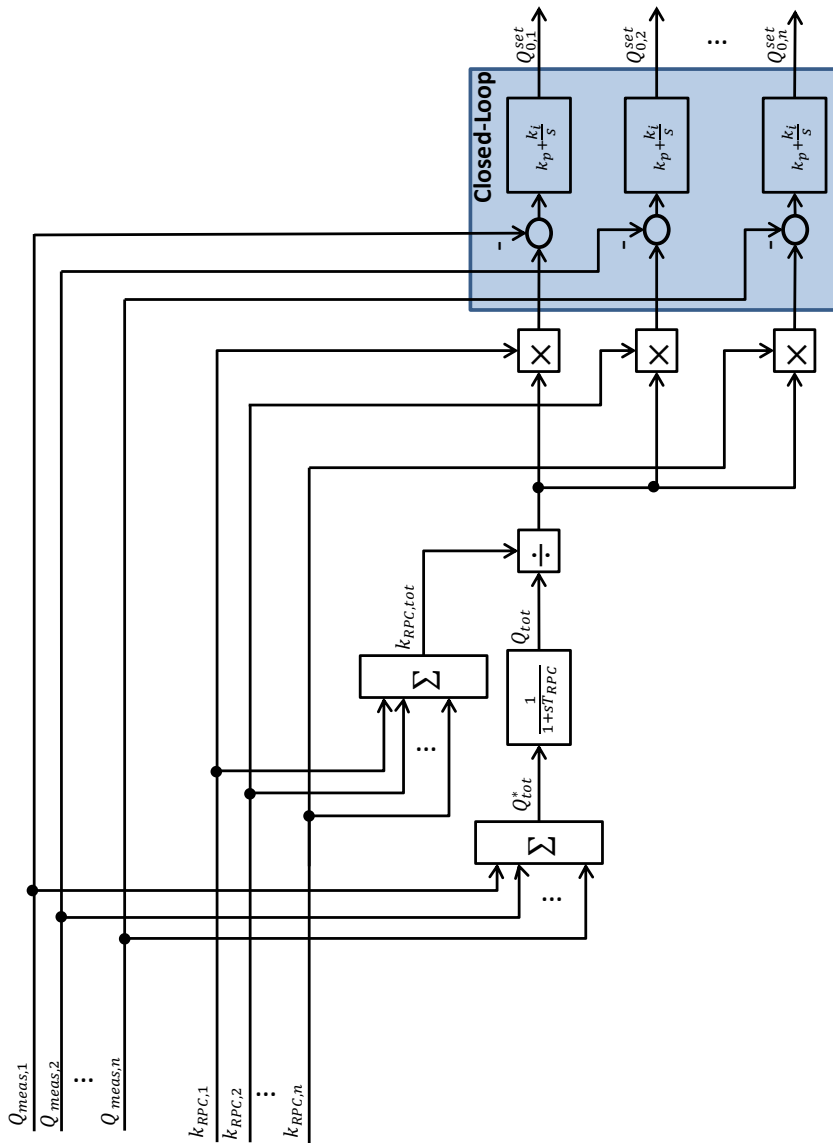
Figure 51 – Block diagram of reactive power control (RPC).
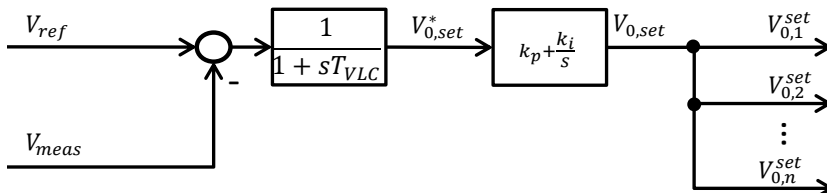
Figure 52 – Block diagram of voltage level control (VLC).

is mentioned. Further, in areas with distributed assets and low-bandwidth communication these delays play an important role in the control dimensioning.

Depending on the setup these communication delays can be in the range between some milliseconds up to almost one second.
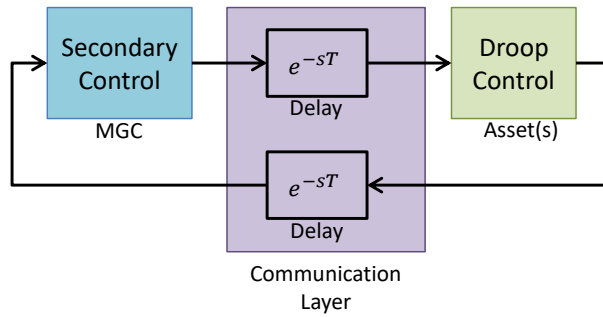
Figure 53 – Consideration of transportation delay caused at the communication Layer.

In the controller design, the delays have to be considered as the controller dynamics regarding stability is significantly affected. Some numerical simulation results with different delays and controller gains are shown in section 6.3. A deeper stability analysis regarding controller dimensioning is not part of this work.

4.3 Energy Scheduling for BSS

In islanded microgrids with a high penetration of renewable energy sources in combination with conventional generation such as diesel-driven gensets and battery storage systems (BSSs), it is desired to maximize the renewable energy usage to reduce the (fossil) primary energy sources (e.g., diesel, gas or wood). This goal is reached by energy scheduling of the BSSs based on the prediction of load and distributed generation. Prediction methods depending on data such as weather, time, weekday, season or past behavior are presented, e.g., in [86], [69], [10] or [60] and are not part of this work.

The structure of the extended control is basing on the MGC presented in section 4.2 and shown in Fig. 54.
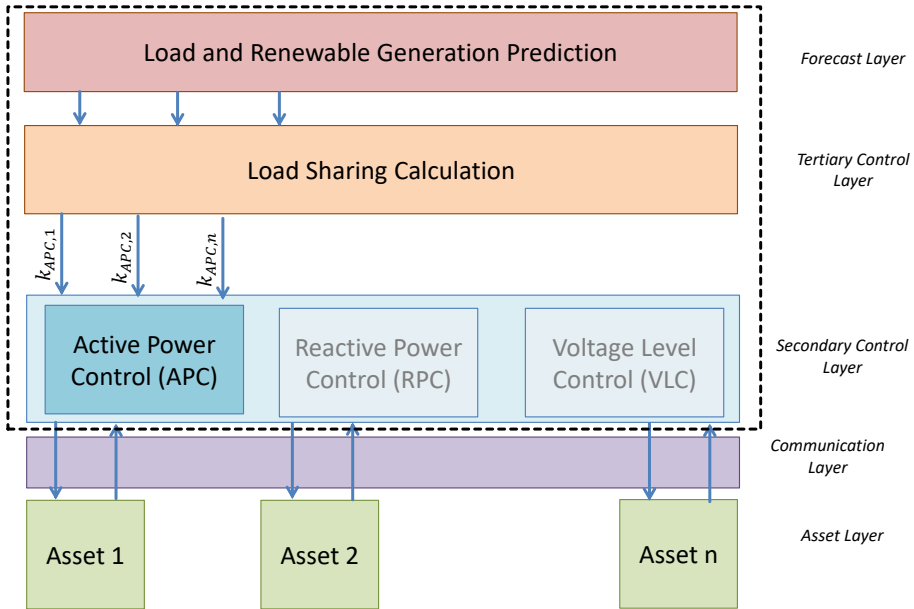
Figure 54 – Block diagram of the extended microgrid controller considering tertiary control layer (load sharing calculation) and forecast layer.

In addition to the controller described in section 4.2 (Fig. 49), a tertiary control layer as well as the forecast layer are added. As a result, an economic optimization is realized whereas the grid stability and quality is ensured on the asset resp. secondary control layer.

Further, the algorithm can be used as a planning tool for dimensioning of the BSSs depending on SOE_{min}, SOE_{max}, E_{total} amongst others for the design of a microgrid with island capability.

The inputs for the load sharing calculation are the forecasted load and DG and aggregated to P_{load} and P_{DG}.

Reactive power sharing calculation is not considered. Therefore, other methods, as described in sections 4.2 and 4.6.2, have to be used.

The assumed grid structure is shown in Fig. 55.

The difference between the aggregated active power consumption P_{load} and distributed generation P_{DG} is calculated to the residual power P_{res}:

$$P_{res} = P_{load} - P_{DG} \tag{41}$$
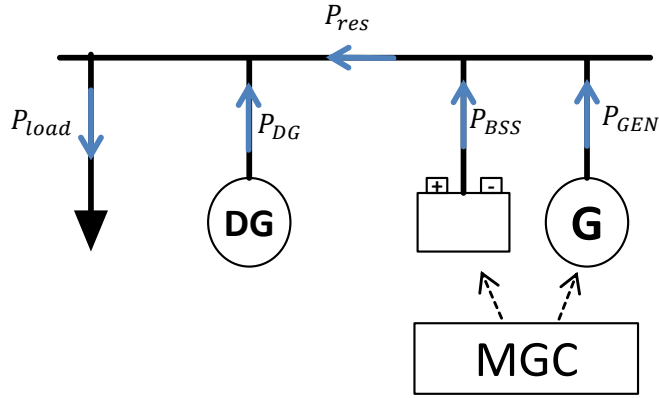
Figure 55 – Simplified SLD of an islanded microgrid consisting of aggregated load P_{load}, distributed generation P_{DG}, gensets P_{GEN}, battery storage systems P_{BSS} as well as a microgrid control center MGC.

This deviation is covered by P_{GEN} resp. P_{BSS}:

$$P_{res} = P_{GEN} + P_{BSS} \tag{42}$$

At least one genset resp. BSS must be operated as a GFU (as described in section 3.4 resp. 3.2) at any time; this is mandatory for a stable island grid operation.

For dimensioning of the load sharing planning, the following conditions are defined:

1. It is assumed that the energy consumption is higher than the energy production within a certain period, e.g. one day ($\Delta T = 24h$):

$$\int_t^{t+\Delta T} P_{res}(t')dt' > 0 \tag{43}$$

2. The BSS can store and supply energy but not consume or generate (besides losses that are neglected). Hence it is assumed after a certain periodical time span (e.g., $\Delta T = 24h$):

$$\int_t^{t+\Delta T} P_{BSS}(t')dt' = 0 \tag{44}$$

$$\int_t^{t+\Delta T} P_{res}(t')dt' = \int_t^{t+\Delta T} P_{GEN}(t')dt' \tag{45}$$

3. The genset power P_{GEN} is always positive (no power feedback):

$$P_{GEN}(t) \geq 0 \tag{46}$$

4. Gensets as well as BSS can feed the grid alone with respect to power, also without distributed renewable generation.

5. The energy stored in the BSS is defined as $E_{BSS}(t)$ and depends on the initial energy $E_{BSS,0}$ and on the integral of the active power:

$$E_{BSS}(t) = E_{BSS,0} - \int_0^t P_{BSS}(t')dt' \tag{47}$$

Losses (at charging and discharging, standby, self-discharge) are neglected. $P_{BSS}(t) > 0$ means BSS discharge.

6. The relative stored energy is defined as the State of Energy (SOE) [103]:

$$SOE(t) = \frac{E_{BSS}(t)}{E_{BSS,total}} \tag{48}$$

where $E_{BSS,total}$ is the total usable capacity of the BSS at the time of operation.

7. The energy $E_{BSS}(t)$ has to be in the range of:

$$E_{BSS,min} \leq E_{BSS}(t) \leq E_{BSS,max} \tag{49}$$

resp.

$$SOE_{min} \leq SOE(t) \leq SOE_{max} \tag{50}$$

Based on Eqs. (41) and (42), the residual power P_{res} (difference between active load and distributed generation) has to be covered by gensets and/or BSSs.

For the time series of the residual power $P_{res}(t)$, phases with $P_{res}(t) \geq 0$ and with $P_{res}(t) < 0$ have to be distinguished. Therefore, the predicted curve $P_{res}(t) = P_{GEN}(t) + P_{BSS}(t)$ is divided into N sections where the borders t_i are determined by the zero-crossing method. The resulting energy of each section can by calculated as

$$E_i = \int_{t_{i-1}}^{t_i} P_{res}(t')dt' \tag{51}$$

All sections considered means that the sum of all sections is equal to the total resulting energy over the considered period ΔT.

$$\int_{t}^{t+\Delta T} P_{res}(t')dt' = \sum_{i=1}^{N} E_i \tag{52}$$

An example for the split-up is shown in Fig. 56a. The residual active power P_{res} is divided into five sections. In the first, third and fifth, P_{res} is positive, i.e., active power has to be supplied by gensets and/or BSSs.

In sections 2 and 4, P_{res} is negative, which means that active power is exceeded. As gensets are not able to absorb power, the BSSs are charged. Thus, it has to be ensured that the SOE is small enough at the beginning of the certain section. The amount of each section is calculated to $E_1 \ldots E_5$.

At time t_1 resp. t_3, the BSS must have enough free capacity to store the energy E_2 resp. E_4 (Fig. 56b).

Under consideration of Eq. 49, the following conditions must be fulfilled:

$$E_{BSS,min} \leq E_{BSS}(t_1) \leq E_{BSS,max} - E_2 \tag{53}$$

$$E_{BSS,min} \leq E_{BSS}(t_3) \leq E_{BSS,max} - E_4 \tag{54}$$

$$E_{BSS,min} + E_2 \leq E_{BSS}(t_2) \leq E_{BSS,max} \tag{55}$$
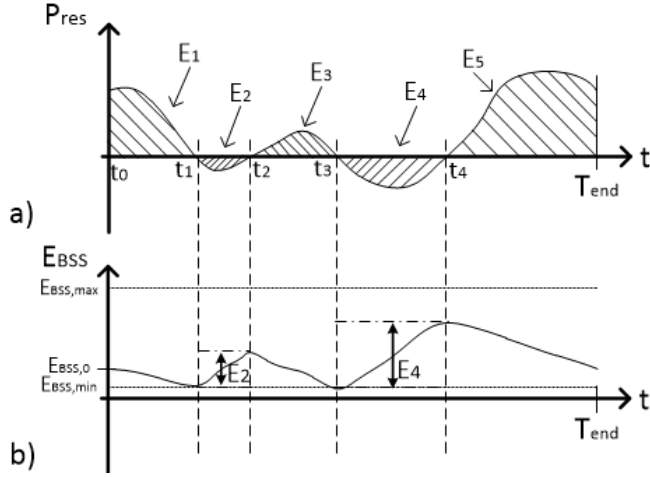
Figure 56 – Example for resulting power (a) and the related stored energy (b) of the BSS.

$$E_{BSS,min} + E_4 \leq E_{BSS}(t_4) \leq E_{BSS,max} \tag{56}$$

In a general form, $E_{BSS}(t_i)$ at the beginning of charging periods needs to be in the range of:

$$E_{BSS,min} \leq E_{BSS}(t_i) \leq E_{BSS,max} - E_{i+1} \tag{57}$$

After charging periods, $E_{BSS}(t_i)$ is in the range of

$$E_{BSS,min} + E_i \leq E_{BSS}(t_i) \leq E_{BSS,max} \tag{58}$$

As maximum renewable energy feed-in by DGs is one main goal, the BSS should always be able to store the excess energy completely. Thus it is necessary to keep the SOE at a low level, as low as possible but as high as necessary to fulfill the required demands of the following periods. Before a charging period, the SOE should be at SOE_{min}.

Besides this, at time $t = 0$, the stored energy is defined as

$$E_{BSS}(t = 0) = E_{BSS,0} \tag{59}$$

As BSSs do not generate or consume energy (besides losses), the stored energy at the end of the considered period is:

$$E_{BSS}(t = T_{end}) = E_{BSS,0} \tag{60}$$

As a result, the power setpoint curves for the BSS $P_{BSS}(t)$ as well as for the gensets $P_{GEN}(t)$ are estimated. Sections with $P_{res} \leq 0$ (case a) and $P_{res} > 0$ (case b) have to be distinguished:

a) $P_{res} \leq 0$: the DG power is higher than the load; no gensets are feeding in ($P_{GEN} = 0$). Thus, the BSS power in this time range equals

$$P_{BSS}(P_{res} \leq 0) = P_{res} \tag{61}$$

b) $P_{res} > 0$: the load power exceeds the DG power; the difference has to be covered by gensets and/or BSSs. The load sharing between gensets and BSSs depends on the predicted energy until the BSS is charged again.

Therefore, the load sharing factor $k_{BSS,i}$ is introduced for each section:

$$k_{BSS,i} = \frac{E_{BSS}(t_i) - E_{BSS,min}(t_{i+1})}{E_{res}(t_{i+1}) - E_{res}(t_i)} \tag{62}$$

where t_i and t_{i+1} are the borders of the time range of a section with positive P_{res}.

Before an interval in which the BSS needs to be charged according the prediction, the SOE has to be kept low enough, ideally at SOE_{min}. This defines $E_{BSS}(t_i)$ respectively $k_{BSS,i}$ and hence the participation of BSSs in the load sharing. Additionally, an uncertainty in both load and generation prediction must be taken into account.

If the available energy of the BSSs is greater than the needed energy, $k_{BSS,i}$ is limited:

$$0 \leq k_{BSS,i} \leq 1 \tag{63}$$

In that case, the gensets are not in operation in this section.

In general, for all sections i where P_{res} is negative, the BSS and genset active power are defined as

$$P_{BSS}(t) = k_{BSS,i} \cdot P_{res}(t) \text{ for } t_i \leq t \leq t_{i+1} \tag{64}$$

$$P_{GEN}(t) = (1 - k_{BSS,i}) \cdot P_{res}(t) \text{ for } t_i \leq t \leq t_{i+1} \tag{65}$$

Now the scheduling the active power of BSSs and gensets as well as the SOE of the storage systems are defined. If the BSSs are not capable of storing the excessive energy completely, further concepts like DG feed-in reduction or the usage of additional loads such as power-to-heat systems are necessary, but this is outside the scope of this work.

The simulation results of the presented load sharing concept are shown in section 6.4.

4.4 Black Start Strategy

Black start capability is an essential characteristic of islanded microgrids.

Black start is used to build up the grid from zero or after major failures not only in non-interconnected grids. Also, in mainly on-grid microgrids, black start can support the restart of an independent interconnected grid area if several small (temporary islanded) grid cells execute an independent black start and are resynchronized step by step (bottom-up approach).

As discussed in section 2.3, the black start strategies are assumed for controllable loads or the communication link to all relevant assets.

The approach presented here is based on non-controllable loads (such as households) and a high penetration of renewable DG (considering VDE AR-N 4105 [99] as described in section 3.5) without direct ICT-based communication link.

Further, it is assumed that all GFUs used for black start have a common PCC where the distributed load and generation are connected. That means that the residual load P_{res} as the difference between P_{load} and P_{DG} is covered by all GFUs (e.g., gensets and/or BSSs). Fig. 57 shows the corresponding SLD.
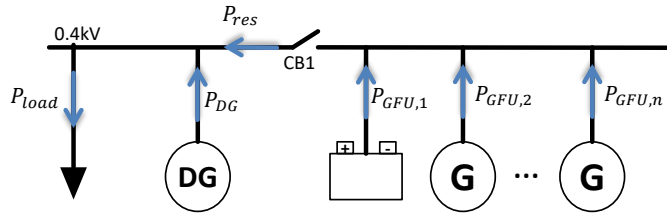
Figure 57 – SLD for the development and analysis of black start concept.

The investigated concept consists of the following steps:

1. Open CB1 (islanding)

2. Start-up of one GFU

3. Start-up of further GFUs and synchronization to the first GFU

4. Close CB1

5. DG start-up regarding VDE AR-N 4105 [99]

At step 4, the load is applied to the GFUs at once. Regarding VDE AR-N 4105, the decentralized renewable generation is connected when the grid conditions are fulfilled for a time period of $60s$ (section 3.5) (step 5). This requires a proper configuration of the droop control if no MGC regarding section 4.2 is available or active.

For the active power/frequency control, the droop equation for each asset n is (in steady state, regarding Eq. (1)):

$$f = f_{0,i} - \frac{1}{k_{f,i}} \cdot (P_i - P_{0,1}) \tag{66}$$

The total active power P_{res} in general is (by neglecting grid losses):

$$P_{res} = \sum_{i=1}^{N} P_n \tag{67}$$

71

where P_i is asset active power distribution of the corresponding asset.

$$P_{res} = \sum_{i=1}^{N} \left(k_{f,i} \cdot f_{0,i} \right) - \underbrace{\sum_{i=1}^{N} k_{f,i} \cdot f}_{k_{f,res}} + \underbrace{\sum_{i=1}^{N} P_{0,i}}_{P_{0,res}} \tag{68}$$

If all frequency setpoints are equal ($f_{0,1} = f_{0,2} = \ldots f_{0,N} = f_0$), Eq. (68) can be simplified as

$$P_{res} = k_{f,res} \cdot (f_0 - f) + P_{0,res} \tag{69}$$

For the startup of the DGs, the grid frequency f must be in the range between $f_{min} < f < f_{max}$. According to the German Application Rule VDE AR-N 4105, the frequency range for connecting DGs is defined as $f_{min} = 47.5Hz$ and $f_{max} = 50.05Hz$. This leads to:

$$k_{f,res} \geq max \left(\frac{P_{DG,max} + P_{0,res}}{f_{max} - f_0}; \frac{P_{load,max} - P_{0,res}}{f_0 - f_{min}} \right) \tag{70}$$

f_0 is the frequency setpoint equal for all assets.

Due to the DG startup characteristics regarding VDE AR-N4105 [99], the DG active power feed-in is calculated by

$$P_{DG}(t) = min \left(\int_0^t \frac{P_r}{600s} dt'; P_{DG,max}(t) \right) \tag{71}$$

In case that only BSSs are responsible for the black start, the initial SOE has to be at least greater than

$$SOE > \frac{\int_0^{60s} P_{load}(t) - P_{DG}(t) dt'}{E_{BSS,total}} \tag{72}$$

In section 6.6, some characteristic simulation results are presented for the described black start strategy.

4.5 Resynchronization

For islanded microgrids that are not permanently operated independently, a resynchronization strategy is mandatory. One possible method would be shutting down all GFUs and connect the deprecated grid by hard. As this is leading to a blackout, other methods are preferred. In the literature, several publications such as [46, 33, 31, 82, 49, 89, 102, 56, 21], address this topic.

In this section, one suitable approach for the resynchronization control is presented. It is based on the centralized secondary control described in section 4.2.

The assumed grid structure is shown in Fig. 58.
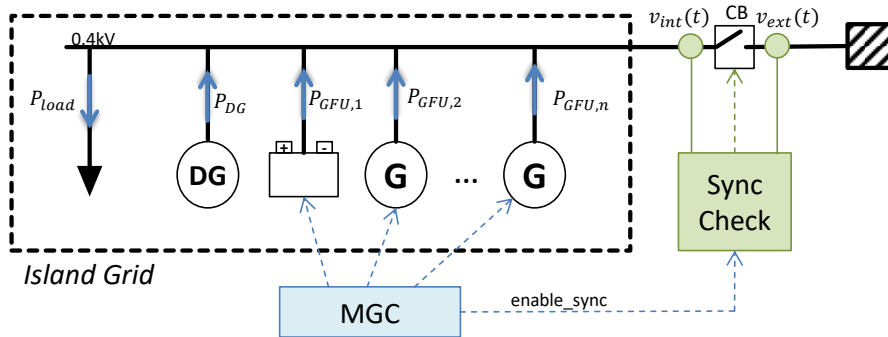
Figure 58 – SLD of assumed grid structure for resynchronization.

An island grid consisting of non-controllable loads (aggregated to P_{load}), volatile distributed generation (P_{DG}) as well as GFUs ($P_{GFU,1} \dots P_{GFU,n}$) is controlled by the MGC. Further, a circuit breaker (CB) in combination with a sync check device is added at the interface between the island grid and the external grid where the voltages $v_{int}(t)$ and $v_{ext}(t)$ are measured. The corresponding control block diagram is shown in Fig. 59.

In addition to the secondary control by a MGC, the blocks *Resync*, *Sync Check* and *Circuit Breaker* are necessary. The block *Resync* calculates setpoints for the MGC (consisting of APC, RPC and VLC) and enables the *Sync Check*.

Sync Check

For the synchronization of two grids, it is mandatory to minimize the voltage and frequency deviation as well as the phase angle between the two grids whereas all three criteria have to be fulfilled. In the proposed structure, the sync check in combination with a circuit breaker (CB) is located on the asset level and not implemented at the MGC. Therefore, it is independent of communication delays (analyzed in section 4.2) and the CB is actuated directly.

From the internal voltage $v_{int}(t)$ and external voltage $v_{ext}(t)$ measured at the CB, the differences of voltage magnitude, frequency and phase angle are calculated to ΔV, Δf and $\Delta\vartheta$. An example is shown in Fig. 60.

Resync

As already mentioned, small values of ΔV, Δf and $\Delta\vartheta$ calculated from $v_{int}(t)$ and $v_{ext}(t)$ are aspired.

Therefore, the voltage magnitude V_{ext} is used as a setpoint for the MGC's voltage control (VLC). Further, the external frequency is measured as well and - in combination - with
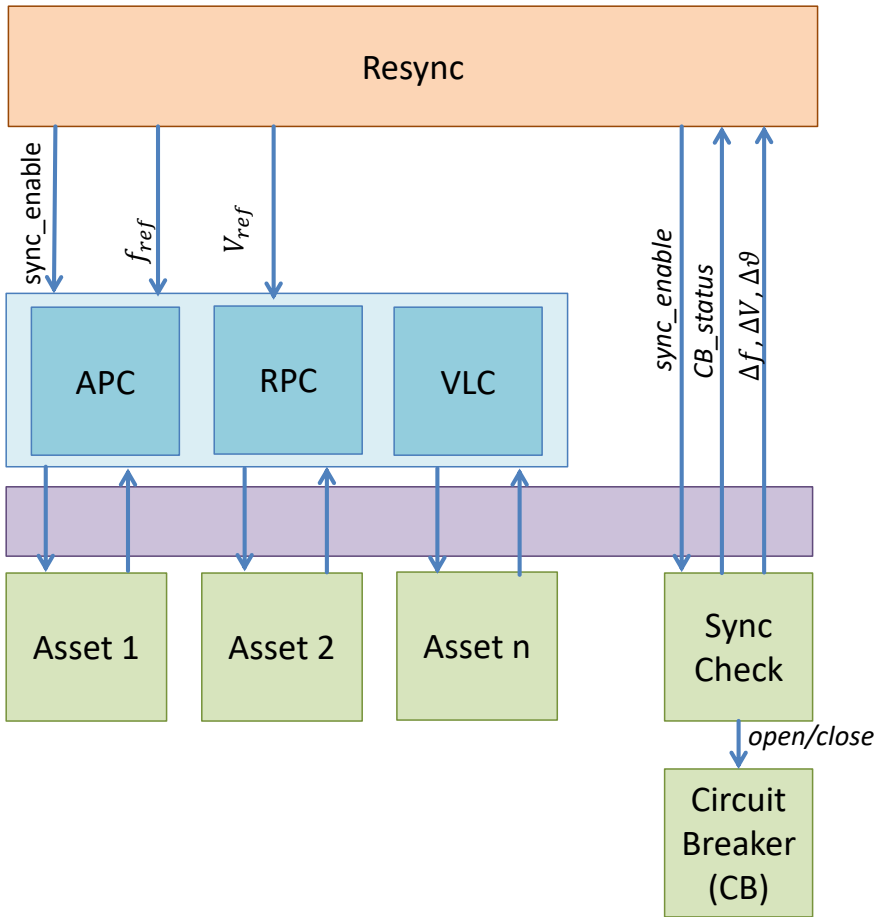
Figure 59 – Block diagram of extended MGC including resynchronization block considering signal flow.
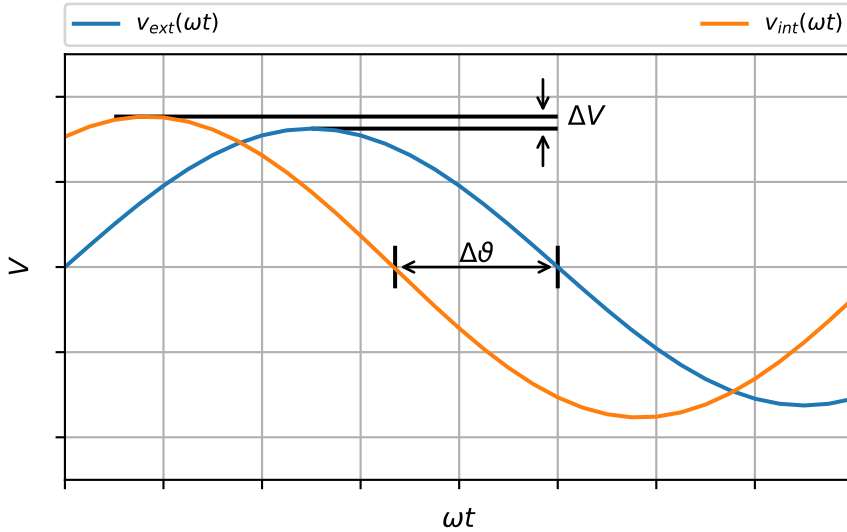
Figure 60 – Example of voltage and phase angle deviation at resynchronization.

a small deviation $\Delta f_{setpoint}$ - given to the APC. This is important as the phase angle will not change at equal frequency:

- $V_{ref} = V_{ext}$

- $f_{ref} = f_{ext} - \Delta f_{setpoint}$

Some specific simulation results are shown in section 6.7.

The method presented in this work is based on an independent sync check on asset level and a setpoint calculation on the MGC level. Due to this, the synchronization is basically independent of delays caused by the communication system. That leads to an increased resilience of the approach. The disadvantage is that it can take a relatively high time span until the synchronization process is completed.

4.6 Failsafe Concept for Grid Operation without Microgrid Control Center

Besides the centralized secondary control strategies described in section 4.2, a decentralized control system without direct communication – e.g., based on ICT – is developed as well. It can be used at communication loss, but also for grids where no communication system and MGC is installed. Exemplary applications are, e.g., cost efficient grids with lower requirements regarding frequency and voltage such as distant mines or island grids without critical loads regarding frequency deviations.

In the following, concepts of active and reactive power control are described separately as they can be used independently as well.

4.6.1 Active Power Control

The focus of this concept is set on the parallel operation of DGs (regarding VDE AR-N4105, as described in section 3.5) and loads in combination with BSSs and gensets operated as GFUs. The assumed grid structure is shown in Fig. 55.

The main goal is a stable grid operation in combination with high usage of renewable power. That means that a DG feed-in limitation due to over-frequency has to be obtained as long as possible. Furthermore, the genset(s) should only be active if BSS(s) cannot cover the residual load due to SOE limitation. Genset(s) are operated with constant power (in steady state) at optimized efficiency. The genset(s) as well as the BSS(s) must be able to handle the complete residual power at any time independently.

The basic idea behind this concept is the usage of the grid frequency for the communication between the GFUs (BSSs and genset) that are equipped with droop control.

It is desired that the gensets' operation time and usage are low and only BSSs are operated as GFUs. Therefore three BSS operation modes depending on the corresponding SOE are defined (Fig. 61).
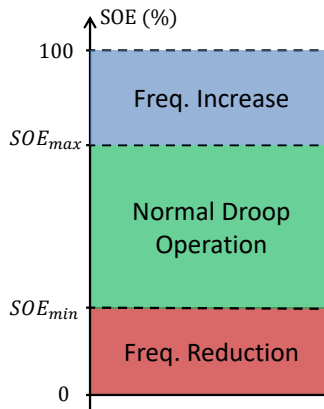
Figure 61 – BSS operation modes for failsafe active power control depending on SOE.

In normal operation ($SOE_{min} < SOE < SOE_{max}$), at least one BSS is operated in grid forming mode for frequency and voltage control without secondary control. Depending on the residual load ($P_{res} = P_{load} - P_{DG}$), the BSS(s) are charged resp. discharged. The power sharing between the GFUs is according to the droop factors $k_{f,i}$ for each asset i. That means that the frequency depends on the residual load and is not controlled by a reference value f_{ref}.

For $SOE < SOE_{min}$ and discharge of the BSS, the active power setpoint P_0 of the droop equation Eq. (1) is decreased, which leads to a reduction of the active power distribution (in case of several GFUs in parallel) or a frequency reduction (if no other GFU is in normal operation mode).

On the other hand, an increase of SOE to $SOE > SOE_{max}$ leads to a reduction of active power consumption or frequency increase as the BSS active power supply is controlled to zero as well.

Next, the operation mode depending on the grid frequency is illustrated in Fig. 62.
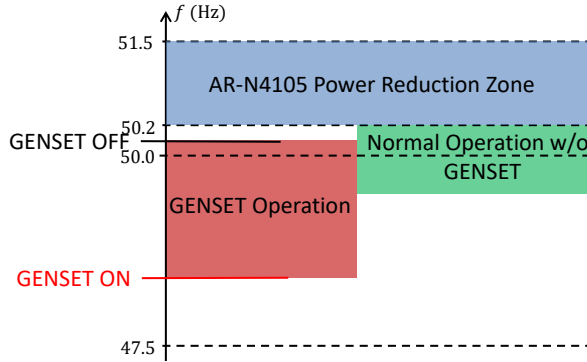
Figure 62 – Active power failsafe operation modes depending on grid frequency.

For grid frequencies $f_{grid} > 50.2 Hz$, the DG's active power feed-in is reduced due to the rule VDE AR-N4105 [99] and hence has to be avoided if possible. Therefore, the desired operation mode is *Normal Operation w/o GENSET* where the BSS(s) ensure an equilibrium between the load and the DG. In the case of SOE reduction lower than SOE_{min} and discharge, the frequency is reduced (as shown in Fig. 61). If the grid frequency is lower than $f_{GEN,min}$, the genset(s) is/are switched on and controlled to a constant active power feed-in (in steady state). During load changes, also droop control is active. As a result, the grid is supplied by the genset(s) and the BSS(s) is/are charged. This operation mode (*GENSET Operation*) is continued until the grid frequency is increased because of $SOE > SOE_{max}$. If the grid frequency $f > f_{GEN,max}$, the genset is disconnected from the grid. Then the grid is operated only by BSS(s) again (*Normal Operation w/o GENSET*).

Next, the internal structure of both controllers (BSS and genset) is described in detail.

For the BSS controller a nonlinear concept based on fuzzy logic in combination with PI control is implemented (Fig. 63) as a MISO system with two inputs (active power supply and SOE). The signal $P_{0,BSS}$ is the input for the subordinated droop control.

The fuzzy logic consists of three parts *fuzzification*, *inference* and *defuzzification*. In Fig. 64, the membership functions in trapezoidal shape for the fuzzification are shown.

The inference table of the fuzzy control is shown in Table 5. The outputs Y_1 resp. Y_2 are defined as singleton to:

$$Y_1 = P_{BSS} \tag{73}$$

$$Y_2 = 0 \tag{74}$$

In mathematical representation, the linguistic terms regarding Table 5 are written as

$$a_1 = max(\mu_{SOE,N}, min(\mu_{SOE,L}, \mu_{P,L}), min(\mu_{SOE,H}, \mu_{P,H})) \tag{75a}$$
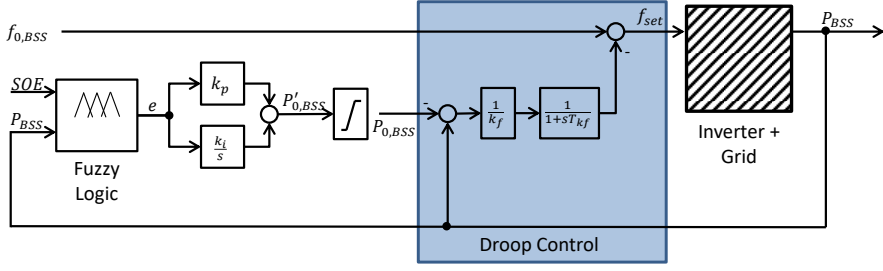
Figure 63 – BSS control block diagram of failsafe active power control.

(a) Membership functions for input fuzzification.

(b) Single trapezoidal fuzzy membership function with parameters x_a, x_b, x_c and x_d.
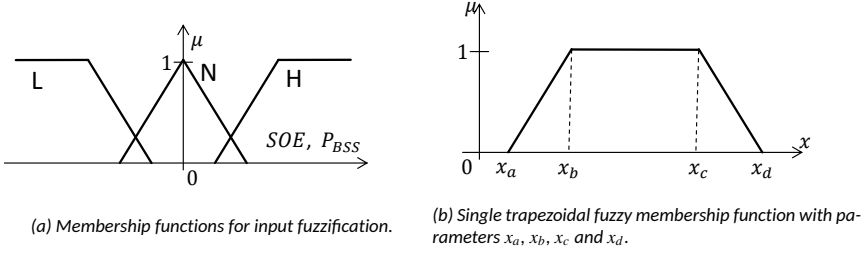
Figure 64 – Configuration of the fuzzy control membership function for failsafe active power control.

Table 5 – Failsafe Active Power Control - Inference Table for BSS' Fuzzy Logic.

		SOE		
		L	**N**	**H**
P	**L**	Y_1	Y_1	Y_2
	H	Y_2	Y_1	Y_1

$$a_2 = max(min(\mu_{SOE,L}, \mu_{P,H}), min(\mu_{SOE,H}, \mu_{P,L})) \tag{75b}$$

The fuzzy output signal is calculated to e (defuzzification):

$$e = \frac{a_1 * Y_1 + a_2 * Y_2}{a_1 + a_2} \tag{76}$$

Furthermore, the genset controller structure is shown in Fig. 65. Besides the droop control as shown in section 3.4.2, a closed loop control in PI structure for the active power setpoint $P_{0,GEN}$ is implemented.

As described above, the genset is not in continuous operation; it is switched on resp. off depending on the grid frequency.

For proper operation, the controller parameters have to be configured. The following prerequisites have to be fulfilled if VDE AR-N4105[99] characteristics for the DGs are assumed (note that $P_{BSS,charge,max}$ is negative whereas $P_{BSS,discharge,max}$ is positive):

- For full usage of DGs:

$$47.5Hz < f < 50.2Hz \tag{77}$$
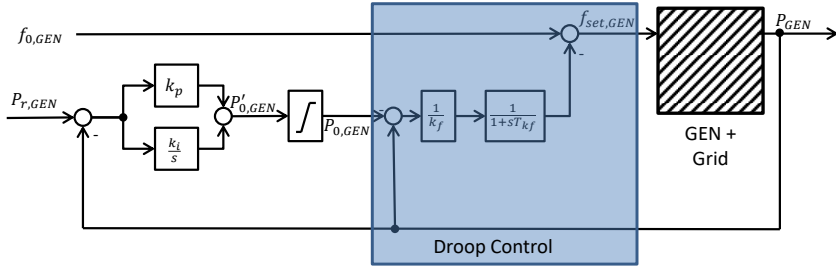
Figure 65 – Block diagram of failsafe active power genset control.

- Operation without genset (only BSS):

$$f_{0,BSS} - \frac{1}{k_{f,BSS}} \cdot P_{BSS,charge,max} < 50.2 Hz \tag{78}$$

- Genset switch on frequency (must be lower than minimum frequency caused by BSSs droop control):

$$f_{GEN,ON} < f_{0,BSS} - \frac{1}{k_{f,BSS}} \cdot P_{BSS,discharge,max} \tag{79}$$

- Genset switch off frequency:

$$f_{0,BSS} - \frac{1}{k_{f,BSS}} \cdot P_{BSS,discharge,max} < f_{GEN,OFF} < f_{0,BSS} - \frac{1}{k_{f,BSS}} \cdot P_{BSS,charge,max} \tag{80}$$

Simulation results for different residual load profiles are shown in section 6.5.

4.6.2 Reactive Power Control

Besides the active power/frequency control, also voltage and reactive power have to be controlled in case of communication failures or in grids without communication infrastructure (e.g., due to costs or reliability). One solution is the implementation of droop control for voltage and reactive power, as described in section 2.1. As the voltage is a local phenomenon (in contrary to the grid frequency), no adequate reactive power sharing by droop control is reached. This can lead to an exchange of reactive power between assets, which would lead to increased losses or overloading of assets and lines. In the literature, other concepts such such as basing on virtual impedance (e.g. in [40]) are not considered here.

As the reactive power demand in LV grids and especially in living areas is typically low, a master/slave concept for reactive power sharing is developed. One asset is defined as a master whereas all other assets are in slave operation. Fig. 66) show the grid structure whereas the position of the master and slave assets can be modified.

The control strategy presented here is that all reactive power demand (Q_{res}) is covered by the master asset whereas all slaves are controlled to zero (or in special cases to another value) – as long as voltage boundaries are not exceeded.

In this failsafe control strategy for voltage and reactive power, the droop control is not active for V and Q. At the master, a constant voltage is set, e.g., $V_0 = 400V$. This depends on the location in the island grid and can be determined by worst-case load flow calculations.
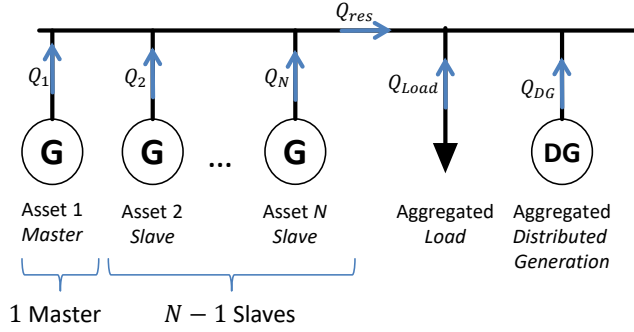
Figure 66 – Assumed grid and asset structure of failsafe reactive power control.

At the other assets, the voltage is controlled to a value where the reactive power is constant (in most cases: $Q_0 = 0$). As long as the master is in operation and no voltage boundaries are exceeded, the concept presented until here is working properly. However, a stable grid operation should also be ensured if the master is failing and not anymore in operation or voltage boundaries are exceeded at certain slave assets (master asset does not exceed voltage as it is controlled to a constant setpoint).

As a solution to this mentioned case, a fuzzy-based control concept is introduced. The corresponding block diagram for voltage and reactive power control is shown in Fig. 67.

The nominal voltage V_0 has to be set. It is the reference value for the master controller.

As the asset is used as a slave, the signal *enable_slave* has to be set to 1 (master: *enable_slave*=0). The considered control is a MISO system where the inputs of the slave controller $\Delta Q = Q_{meas} - Q_0$ resp. $\Delta V = V_{meas} - V_0$ are evaluated and used by fuzzy logic. Therefore, the inputs are converted into p.u. system. The output signal e is used as an input of a PI controller with Anti-Windup (with parameters k_p, k_i and k_{AWU}).

The fuzzy logic includes the three general steps *fuzzification*, *inference* and *defuzzification*.

The fuzzification of input ΔV is realized by membership functions in the same way as shown in Fig. 64. A trapezoidal shape is chosen, but also any other shape is possible. The voltage is divided into three sections: low voltage (membership function μ_L), normal voltage (μ_N) and high voltage (μ_H).

Under normal conditions (μ_N), the reactive power is controlled to Q_0. If the voltage exceeds this limits (μ_L resp. μ_H), the voltage is controlled to V_0. For smooth transition between the control strategies, the membership functions can be defined with overlapping.

The fuzzy output signal e is calculated as (defuzzification)

$$e = \frac{\mu_L \cdot \Delta V + \mu_N \cdot \Delta Q + \mu_H \cdot \Delta V}{\mu_L + \mu_M + \mu_H} \tag{81}$$

The control algorithm is evaluated by simulation. The results for some specific scenarios are shown in section 6.5.2.

Both concepts for active and reactive power can be used independently. Besides the application for failsafe operation in case of communication losses, also a low cost installation without a communication system can be a potential use case (depending on the prerequisites for voltage and frequency).
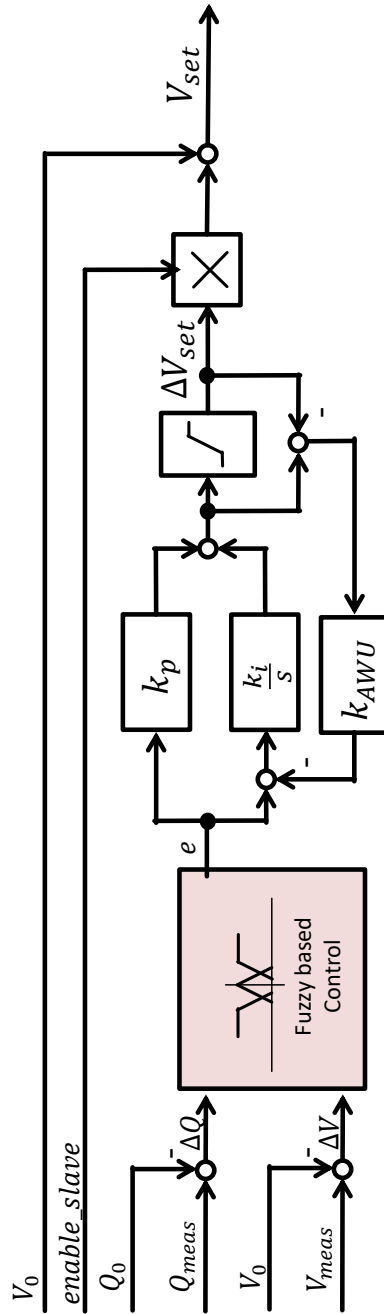
Figure 67 – Block diagram for failsafe reactive power control.

4.7 Conclusion

First, inverter-based GFUs and GSUs as well as gensets are operated in parallel. It was shown that load location inside the island grid affects the dynamic behavior of the active power distribution and frequency, but also the resulting steady state reactive power exchange between the assets. Further, it was shown by simulation that lower voltage droop factors reduce the reactive power exchange between the assets.

Next, a secondary control strategy for active and reactive power under consideration of communication dead times was developed. It consists of three controllers for active power, reactive power and voltage.

As a method for tertiary control, an energy scheduling approach for BSSs was developed based on forecasts for DG and active power consumption with respect to maximization of renewable energy sources and minimization of fossil energy, which is the main objective to reach the goals of the Paris Agreement [68].

Concepts for black start under consideration of VDE AR-N4105 [99] and for resynchronization of an islanded microgrid were investigated.

For island grids with parallel operation of genset(s) as well as BSS(s), the failsafe concept for grid operation without centralized control and communication link under consideration of DGs with VDE AR-N4105 characteristics was researched and developed.

The verification by specific simulations is shown in section 6, where also the evaluation of the control algorithms is presented.

5 Microgrid Demonstrator

The theoretical models of the assets developed in the frame of this thesis are verified by specific measurements in the field. In comparison to other microgrid laboratories, the MCW is part of a real existing grid. For experiments and demonstrations it is possible to include real customers (mainly households) into the islanded microgrid and not only the assets at the campus itself.

5.1 Overview

The MCW is located in the south of Germany in the village Wildpoldsried approximately 15km from Kempten and 100km from Munich. It was established in the frame of the research projects IRENE [17], IREN2 [4, 50], DeCAS [44] and pebbles [95] and enables many different research activities regarding interconnected and islanded microgrids. Fig. 1 in the introduction already shows an overview of the main part of the MCW area; some further assets such as an ohmic load bank or two gensets are located close to the areal shown in the picture.

An overview of the assets at the research facility related to this thesis is shown in Table 6 and described in detail in the following.

Table 6 – MCW: overview of assets used in this thesis including the corresponding rated power/energy.

Acronym	Asset Name	Rated Power/Energy
ABSS	Area Battery Storage System	$300kVA/160kWh$
B2B	Back-to-back station	$500kVA$
CBSS	Campus Battery Storage System	$50kVA/75kWh$
GEN	Genset	$100kW/135kVA$
LOAD	Ohmic Load Bank	$3x50kW$
PV	Photovoltaic Plant	$10kWp$

All assets are connected to a three-phase low voltage AC grid with 400V and 50Hz. A switchgear panel in combination with underground cables enables different grid configurations regarding the asset location within the grid. A SLD of the complete research grid is shown in Fig. 68.

5.2 Description of the Single Units

In the following, the single assets of the MCW used for this scientific work are described in detail.

5.2.1 Area Battery Storage System

The Area Battery Storage System (ABSS) is a Lithium-Ion based BSS established in 2012, which can be used as a grid supporting unit (GSU) in mains parallel operation with active and reactive power setpoints, but also as a grid forming unit (GFU) with voltage and frequency control. In the frame of this thesis, the mathematical modeling of the GFU mode is described in section 3.2 and verified in section 6.1.1.

The ABSS consists of three battery strings in combination with six inverters and grid filters, as described in [3].

This hardware configuration arose due to changes on the cell level and made it necessary to adapt the system to this structure. A detailed modeling considering internal
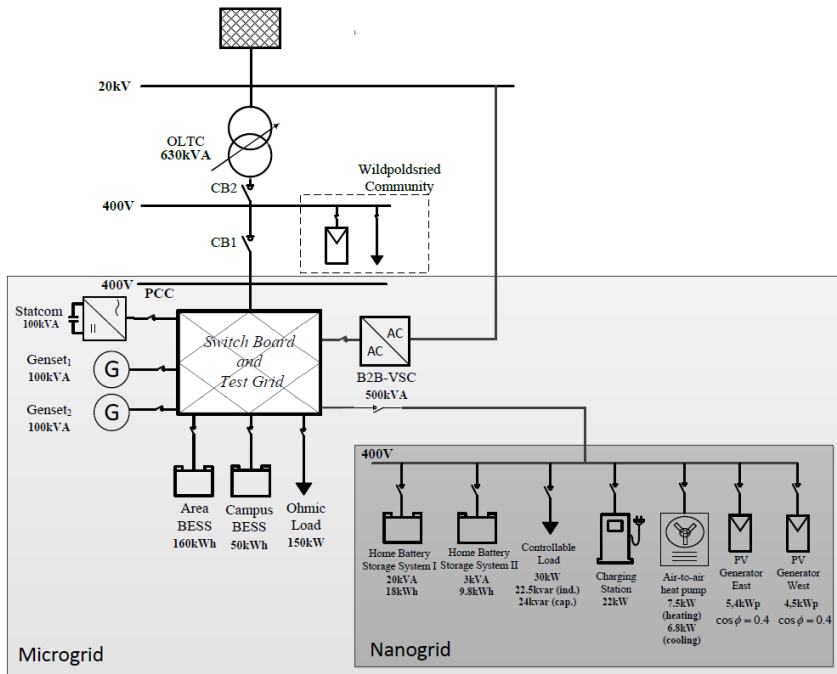
Figure 68 – SLD of the asset connection at the MCW [47].

processes and power flows between the inverters was presented in [74, 72].

As this work deals with the interaction of microgrid assets in an island grid, internal processes are neglected and the overall ABSS behavior is decribed mathematically.

A picture of the battery modules inside the ABSS located in a container is shown in Fig. 69.

The ABSS is designed for a rated maximum power of $300kVA$ and a capacity of $165kWh$.

5.2.2 Campus Battery Storage System

The Campus Battery Storage System (CBSS) is a stationary BSS used as a GSU, which means that no further functionality such as usage as a GFU or black start can be realized.

By the manufacturer, active and reactive power setpoints are realized under consideration of the German Application Guide VDE AR-N 4105 [97].

In the frame of this thesis, the CBSS was extended by an additional active power/ frequency control for GSU functionality. The mathematical modeling and verification is shown in sections 3.3 resp. 6.1.2.

5.2.3 Gensets

At the MCW, a Genset fueled by plant oil as a rotating energy source is installed. The prime mover is from the manufacturer Deutz [26] and the direct coupled synchronous machine from the manufacturer MeccAlte [57].

The nonlinear dynamic modeling is described in 3.4, whereas the model verification is presented in 6.1.3.

Fig. 70 shows a picture of the genset.

The prime mover from manufacturer *Deutz* is directly coupled to the synchronous generator, which means that it is an inverter-less system.

Figure 69 – Picture of the ABSS located at the MCW.

Figure 70 – Picture of the genset at the MCW.

5.2.4 Load Bank

Another asset used as a load for verification of theoretical investigations is the ohmic load bank with a rated power of $150kW$, i.e. $50kW$ per phase, which can be set independently in steps of $1kW$.

5.2.5 Back-to-Back Station

The back-to-back station (B2B) is a special asset which was assembled for the research with islanded microgrids. In simple terms, it is a frequency converter between two independent grids at the MCW between the investigated microgrid and an external grid (in this case: the MV grid over an independent LV substation).

The B2B can be controlled both as a GFU or as a GSU with usage of all four quadrants. From the island grid's point of view, it can be used, e.g., as a PV plant with a repeatable volatile behavior (such as sunny day with sporadic clouds). In this test case, the "renewable" source is fed by an external grid.

The other mode used in this thesis is the operation as a GFU, such as a further battery storage system. From the island grid's point of view, the component is used such as a BSS with limited power but "infinite" energy; instead of battery cells at the DC link, another inverter is connected to the external (MV) grid. This allows many investigations for research without limitation of the physical capacity of battery cells.

5.2.6 Nanogrid

As a sub-unit of the MCW, a so-called Nanogrid was assembled. It represents a modern living building consisting of PV, P2H, Home Battery Storage System (HBSS) and a controllable ohmic-inductive-capacitive load as a representation of the residential load.

In the frame of this thesis the PV system as well as the heat pump are used for the model development and verification shown in sections 3 and 6.

The PV plant is divided into two orientations (east and west) with an angle of approx. $15°$ and connected to the grid via two inverters (see Fig. 71). The total installed power is approx. 10kWp.

Figure 71 – Picture of the nanogrid's PV Inverters at the MCW.

The inverters are from the manufacturer *Steca*, including modified firmware which allows a high range of reactive power setpoints.

The P2H system is an air-to-air heat pump installed for the climatization of a container consisting the *control center*. The manufacturer of the P2H system is *Daikin* [25].

5.2.7 Test Grid and Switchgear Panel

One specialty of the MCW is the test grid in combination with the switchgear panel. Four LV earth cables from type *NAY2Y* and a length of each 250m are installed in the ground and can be connected flexibly between the assets. This allows many different grid configurations for investigation of microgrids, especially for control stability.

A picture of the hardware installation is presented in Fig. 72.

Figure 72 – Picture of the MCW's switchgear.

5.2.8 Control Center

For the control of the complex research grid at MCW, a control center was established. All assets are connected via Ethernet. To get an impression of the complexity, over 250 IP addresses exist at the MCW. For control and measurement purposes, all signals are linked to a common ModbusTCP interface where all assets can be controlled and observed from a central SCADA system. For the specific experiments of this thesis, the MCW is controlled by python scripts, which are dealing with the ModbusTCP interface.

6 Simulation Results and Verification

The mathematical models of relevant microgrid assets described in section 3 are evaluated by specific simulations and verified by comparison with measurements at the MCW (section 6.1).

The interaction of GFUs and GSUs with droop control are also verified by specific measurements (section 6.1.2). Based on these validated results, further control algorithms (secondary control, energy scheduling, blackstart, resynchronization, failsafe operation) are evaluated by numeric simulations shown in this section.

6.1 Model Verification for Microgrid Assets

The theoretical mathematical models for the microgrid assets described in section 3 are verified by specific measurements. The results are shown in the following.

6.1.1 Battery Storage System in Grid Forming Mode

The mathematical model for BSSs as GFUs investigated in section 3.2 is verified by specific measurements at the *Area Battery Storage System* (ABSS), which is located at the test site *MGC* (described in section 5.2.1). Therefore, the ABSS is operated in island mode operation. Ohmic load steps are applied by the ohmic load bank (see section 5.2.4), whereas reactive power tests are realized by using the B2B station (section 5.2.5).

Four scenarios are presented in this work; Table 7 shows the corresponding parametrization of the droop control.

Table 7 – Scenario definition for BSS in grid forming mode.

Scenario	Load Type	k_f (kW/Hz)	k_V (kvar/V)	Load Step
1	Active Power	300	12	$0 \rightarrow 150kW$
2		2000	12	
3	Reactive Power	300	12	$0 \rightarrow 150kvar$
4		300	20	

Figs. 73 - 76 present the simulation results in comparison to the measured results for active power P (a), grid frequency f (b), reactive power Q (c) and RMS grid voltage V_{LL} at the asset's PCC.

The simulations are executed in the software DIgSILENT PowerFactory. The presented active resp. reactive power are used as input signals for the simulation.

The result for scenario 1 regarding Table 7 is presented in Fig. 73. A good correlation between measurement (blue) and simulation (orange) can be seen for the frequency (Fig. 73b) as well as the grid voltage (Fig. 73d). It has to be pointed out that a suppressed-zero scale is used for frequency and voltage.

The same experiment is repeated for a higher frequency droop factor $k_f = 2000kW/Hz$ (scenario 2). The results are shown in Fig. 74. Also, in this case, a good correlation can be seen. The deviation between measured and simulated values shown in Fig. 74d is small ($< 1.5\%$).

In the next two scenarios 3 and 4, reactive power is applied to the BSS. Figs. 75 and 76 show the results for different voltage droop factors k_V, where again a good correlation between simulation and measurement is presented. In comparison to the active power step, which was applied instantaneously by an ohmic load bank, the reactive power "step"
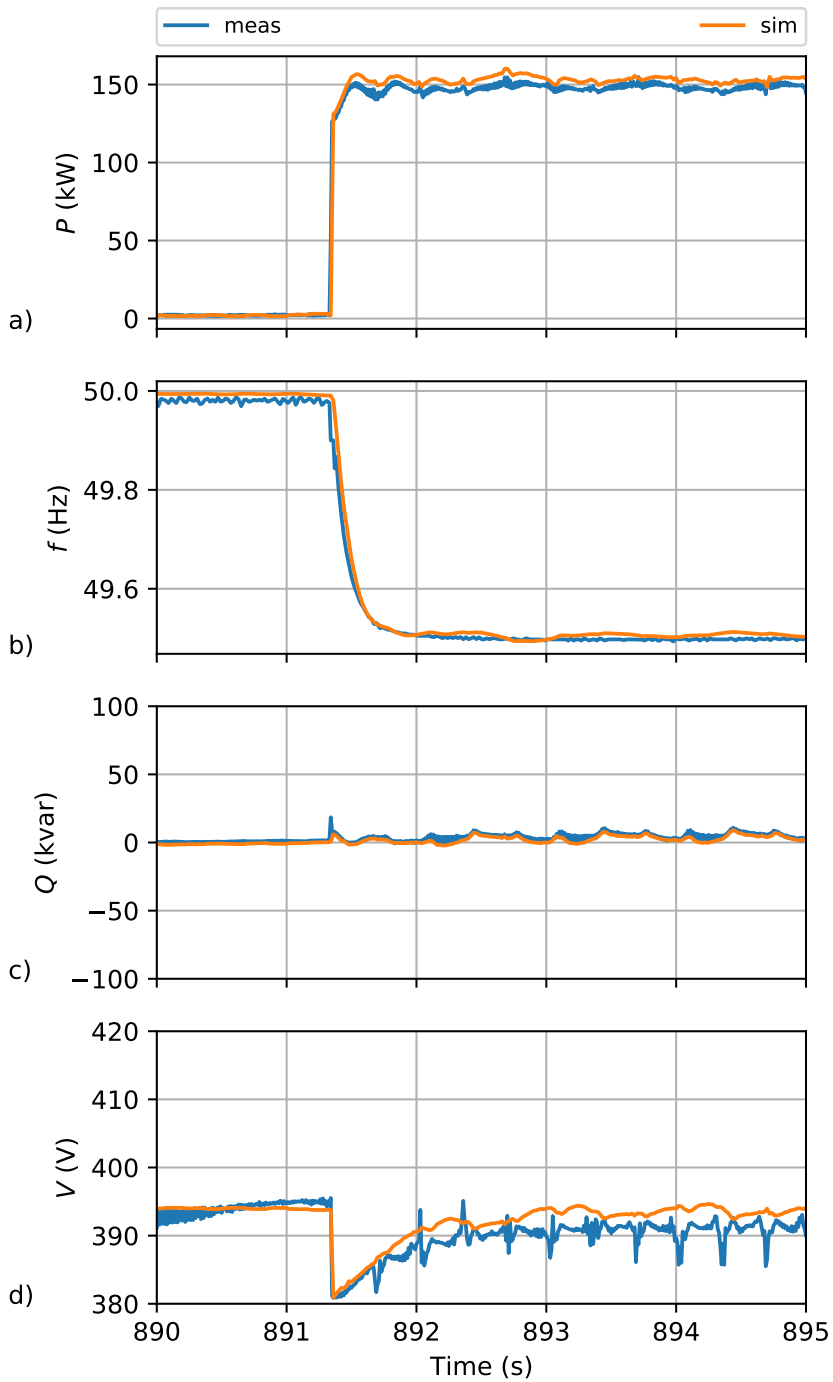
Figure 73 – BSS verification for $k_f = 300kW/Hz$. a) active power feed-in; b) grid frequency; c) reactive power distribution; d) grid voltage at PCC of the BSS. Comparison between measurement (blue) and simulation (orange).
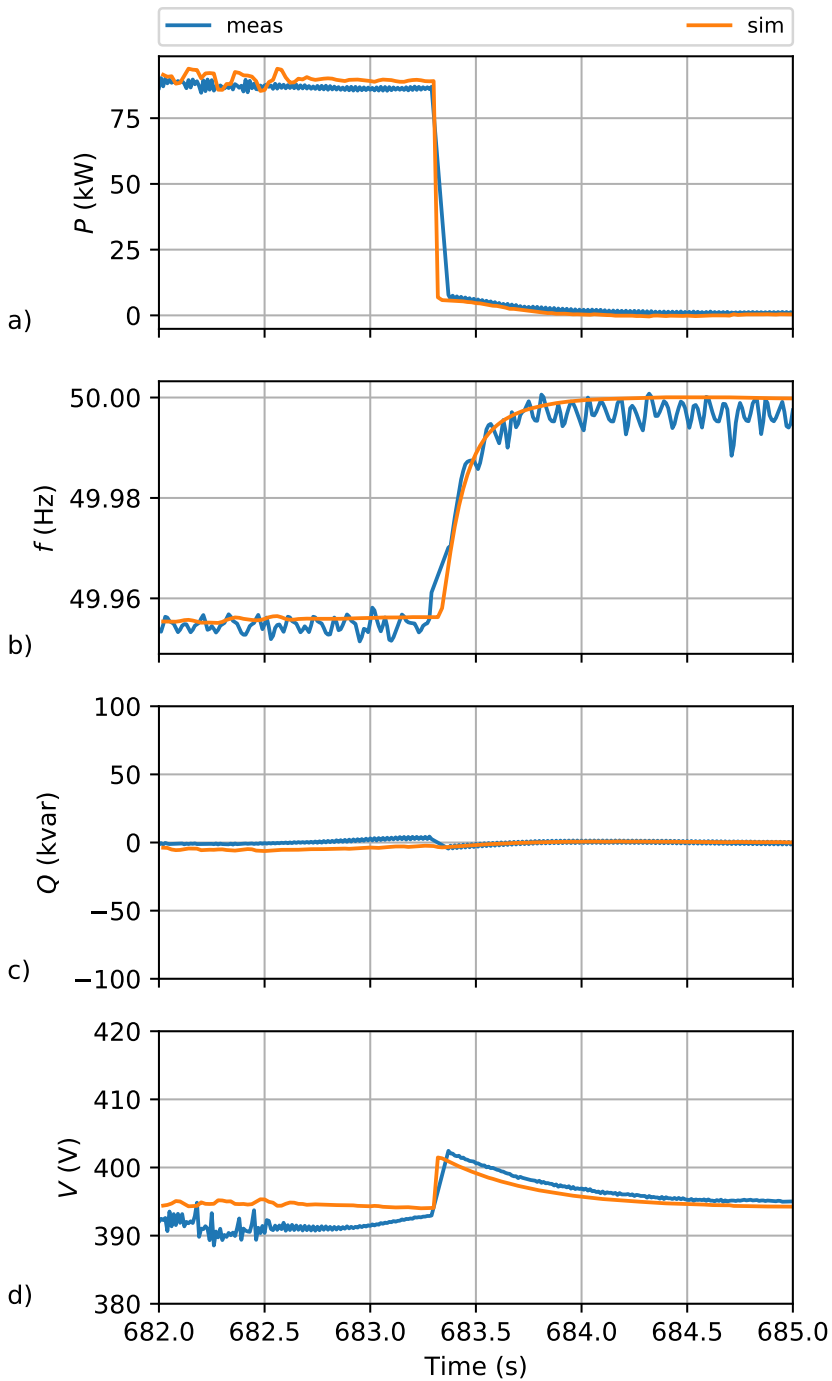
Figure 74 – BSS verification for $k_f = 2000kW/Hz$. a) active power distribution; b) grid frequency; c) reactive power distribution; d) grid voltage at PCC of the BSS. Comparison between measurement (blue) and simulation (orange).

was applied by controlled power electronics with internal ramp-up behavior and lower dynamics and hence no step function in the mathematical sense.

The comparison of simulation results and measurements at the MCW shows that the simplified model approach for BSS as GFU is sufficient regarding the electrical behavior at the asset's PCC for investigations in the time range of hundred milliseconds or higher. For higher resolution (such as investigation of harmonics), a model with a higher grade of detail regarding power electronics has to be used. However, this was not the goal of this work.
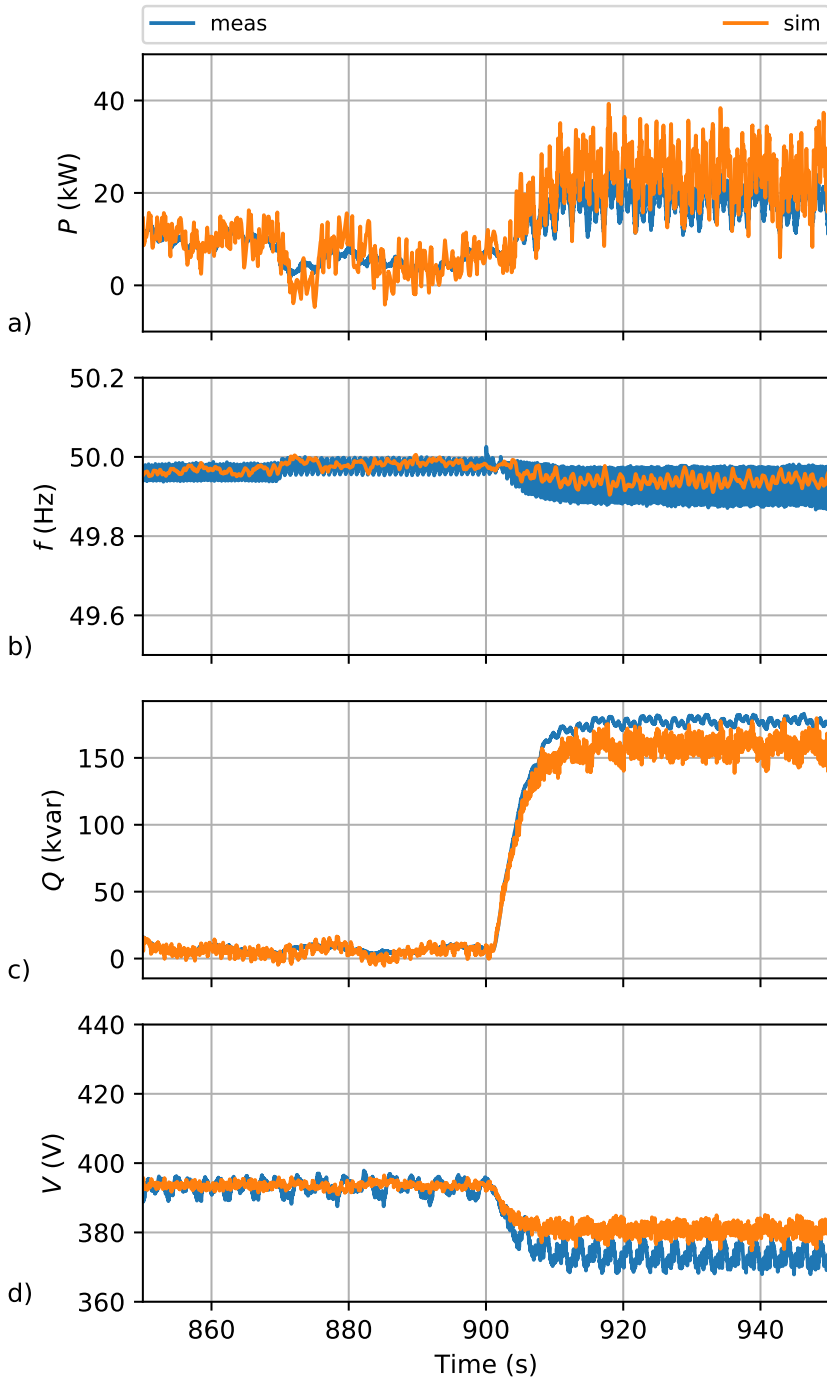
Figure 75 – BSS verification for $k_V = 12kvar/V$. a) active power distribution; b) grid frequency; c) reactive power distribution. d) grid voltage at PCC of the BSS. Comparison between measurement (blue) and simulation (orange).
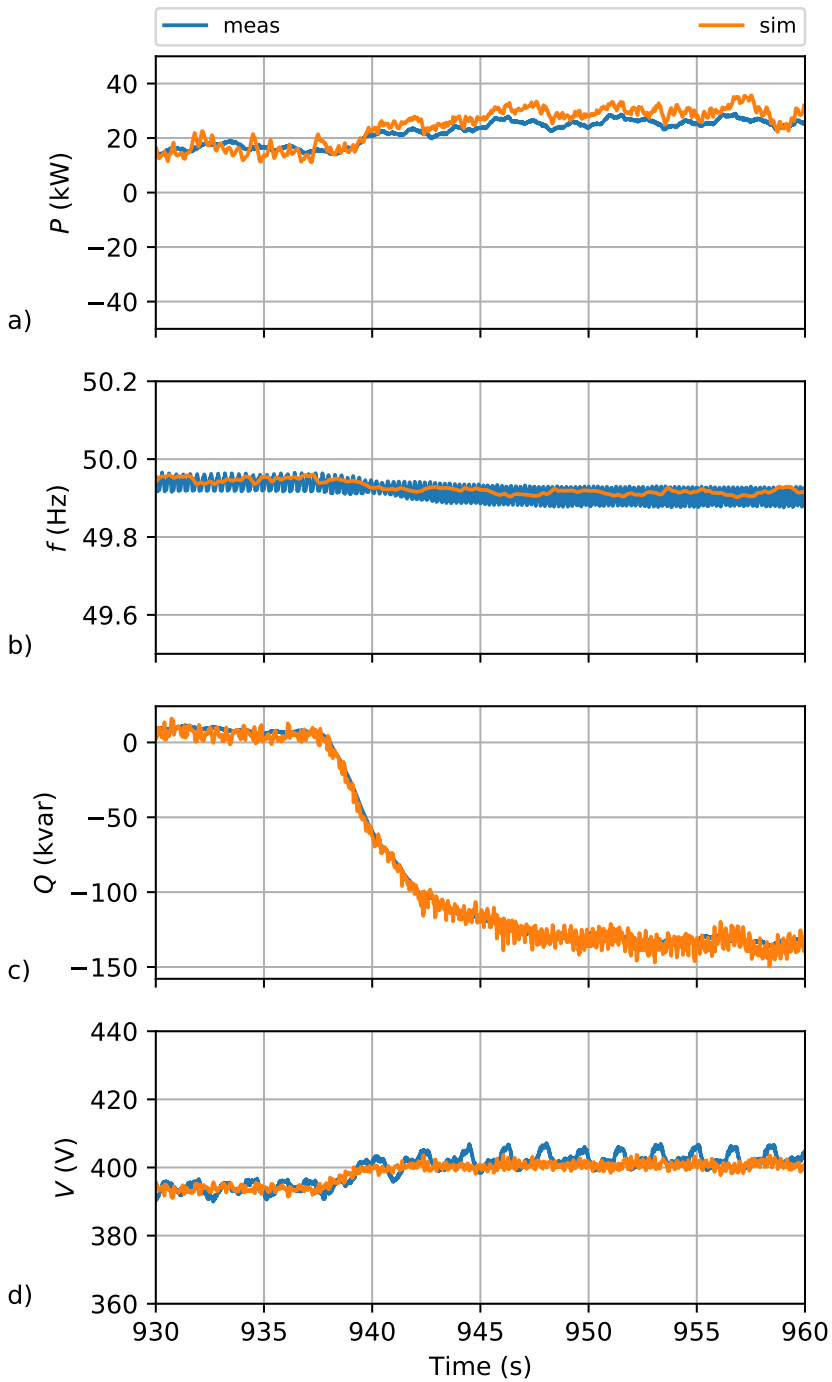
Figure 76 – BSS verification for $k_V = 20 kvar/V$. a) active power distribution; b) grid frequency; c) reactive power distribution; d) grid voltage at PCC of the BSS. Comparison of measurement (blue) and simulation (orange).

6.1.2 Battery Storage System in Grid Supporting Mode

The mathematical model for a BSS in grid forming mode (as described in section 3.3) is compared with characteristic measurements at the CBSS (Campus Battery Storage System) described in section 5.2.2.

The CBSS has a rated power of $50kVA$ and a capacity of $75kWh$. First, an active power profile is applied to the CBSS. A comparison of simulation and measurement results is presented in Fig. 77, whereas the setpoints $P_{set,sim}$ (blue) and $P_{set,meas}$ (orange) as well as the active power feed-in P_{sim} (green) and P_{meas} (red) are shown.

As long as the active power setpoint is lower than $25kW$ and thus lower than 50% of the rated power, the reactive power is approx. zero. For values of P greater than 50%, reactive power is consumed (negative sign). In the last active power step with a setpoint of $50kW$, the resulting active power is limited to approx. $45kW$ as the rated apparent power of $50kVA$ must not be exceeded. Regarding VDE AR-N4105, the power factor is increased until $\cos\varphi = 0.9$ at rated power. That means that the active power feed-in is reduced to $P = 45kW$.
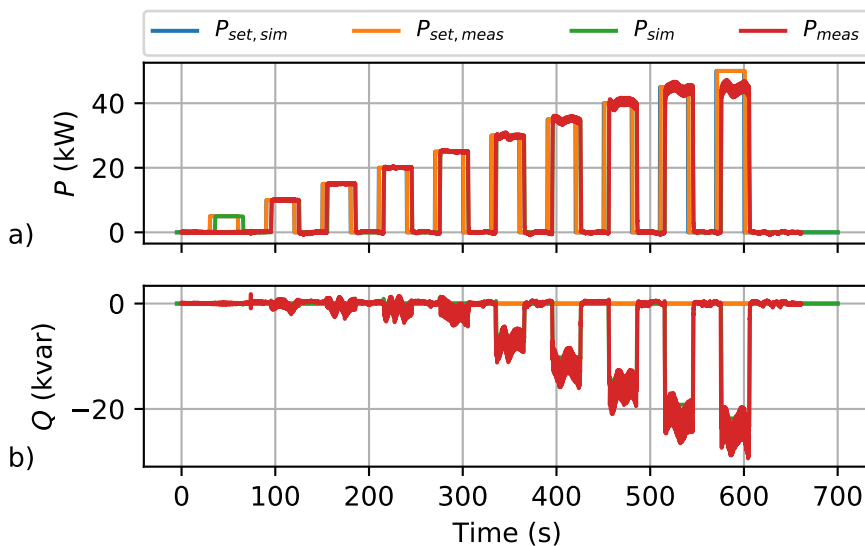
Figure 77 – Active power steps: comparison of simulation and measurement results for BSS as GSU. a) active power (blue: setpoint simulation; orange: setpoint measurement; green: active power feed-in simulation; red: active power feed-in measurement); b) reactive power.

In the next graph (Fig. 78), a zoom in of one power pulse is shown in detail. It can be seen that a delay of $T_d = 5.3s$ between setpoint and power feed-in is considered. A good correlation between simulation and measurement – also regarding the dynamic behavior – for active power pulse is shown.

Next, reactive power "pulses" are applied in simulation as well as at the CBSS. The corresponding result is shown in Fig. 79 for the complete experiment and in Fig. 80 for a detailed view of one single pulse.

The behavior of active power depending on the SOE is shown in Fig. 81 for an active power setpoint of $P = -50kW$ (charging) resp. $P = 50kW$ (discharging). A good correlation between simulation (blue) and measurement (orange) can be seen.
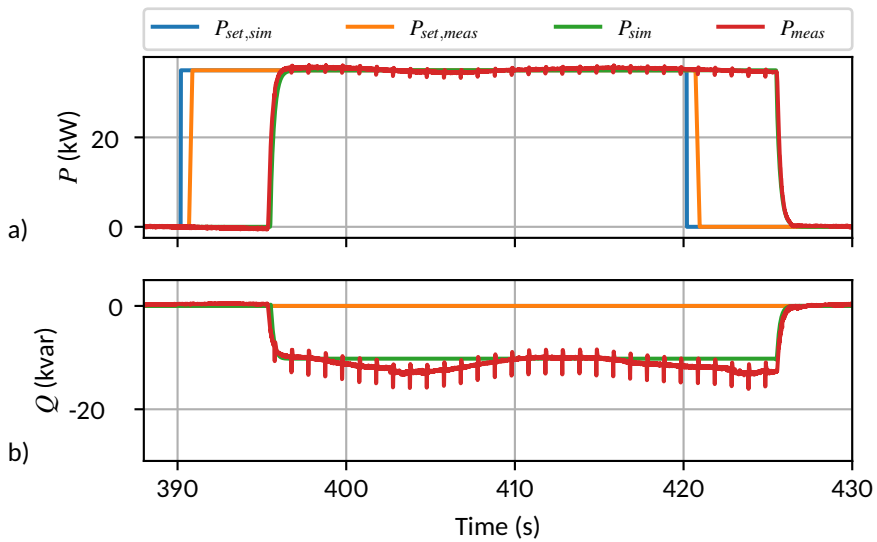
Figure 78 – Active power step (zoom-in): comparison of simulation and measurement results for BSS as GSU. a) active power (blue: setpoint simulation; orange: setpoint measurement; green: active power feed-in simulation; red: active power feed-in measurement); b) reactive power.
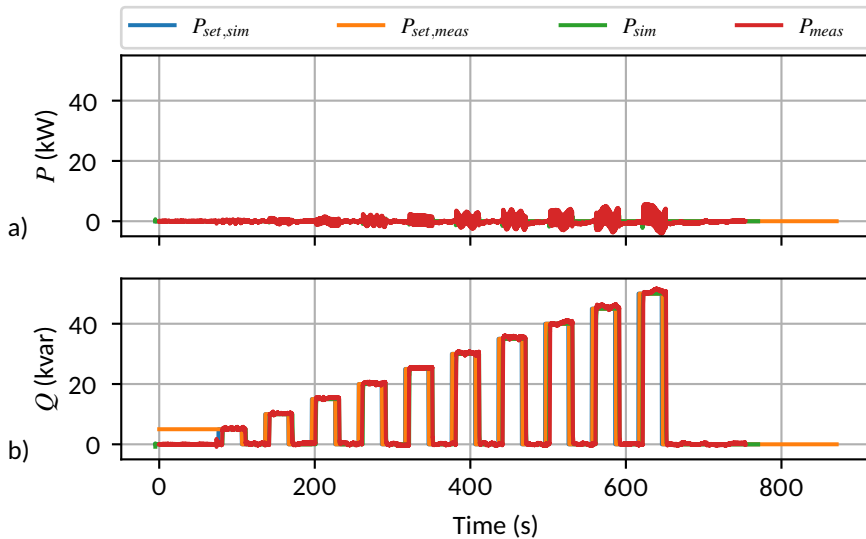
Figure 79 – Reactive power steps: comparison of simulation and measurement results for BSS as GSU. a) active power (blue: setpoint simulation; orange: setpoint measurement; green: active power feed-in simulation; red: active power feed-in measurement); b) reactive power.
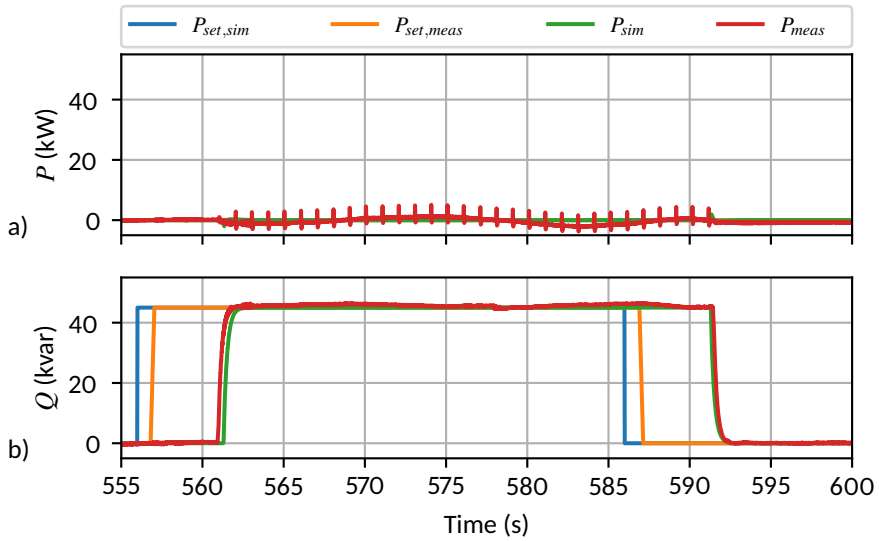
Figure 80 – Reactive power steps (zoom-in): comparison of simulation and measurement results for BSS as GSU. a) active power (blue: setpoint simulation; orange: setpoint measurement; green: active power feed-in simulation; red: active power feed-in measurement); b) reactive power.
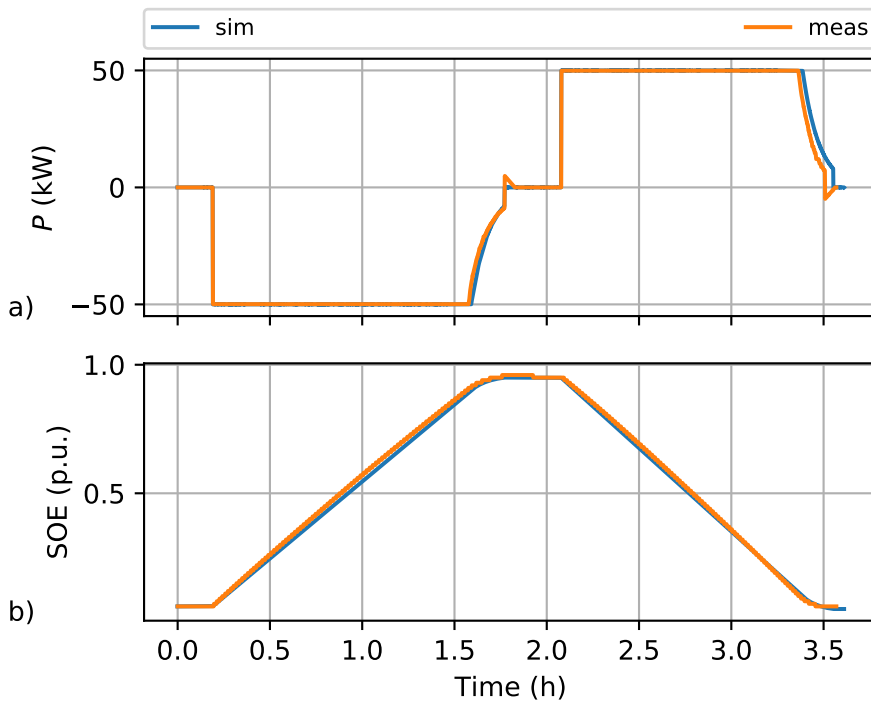
Figure 81 – Active power and SOE for a setpoint of $\pm 50kW$. Comparison of simulation (Blue) and Measurement (Orange). a) active power feed-In; b) SOE.

The experiment was repeated for an active power setpoint of $P = \pm37.5kW$. For this modified setpoint also a good correlation was revealed. The result is shown in Fig. 82.
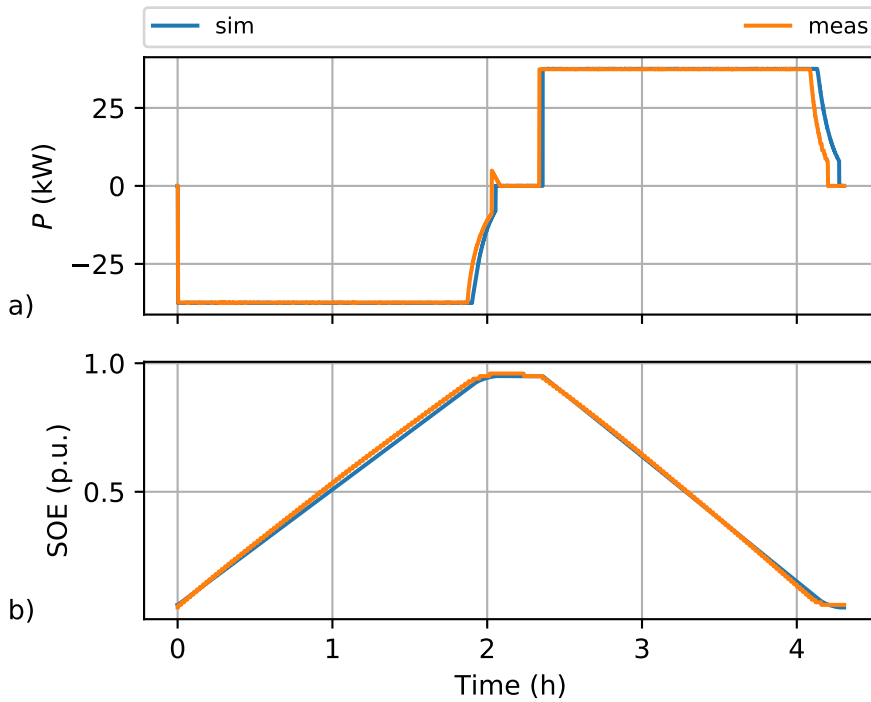
Figure 82 – Active power and SOE for a setpoint of $\pm37.5kW$. Comparison of simulation (blue) and measurement (orange). a) active power feed-in; b) SOE.

6.1.3 Genset

The mathematical model for generation units described in section 3.4 is applied for a genset fueled by plant oil (section 5.2.3).

For parameter identification and verification of the linear model approach as well as the fuzzy-based approach, the genset is operated in island mode as a GFU.

The ohmic load bank (section 5.2.4) consisting of heat resistances (without power-controlled inverter) as well as a fan for forced cooling (approx. $5kW$) is connected to the genset. Due to temperature variation in the ohmic resistances, the active power consumption by the ohmic load bank is not constant (especially for higher power setpoints).

An active power load profile is applied to the genset fueled with plant oil. The active power droop factor is set to $k_f = 80 \frac{kW}{Hz}$. For the model verification, the droop factor is varied to $k_f = 200 \frac{kW}{Hz}$, which leads to different steady state values.

6.1.3.1 Linear Approach

First, the linear modeling approach is verified. The simulation results gained by curve fitting method for active power steps are given in Fig. 83 where the linear modeling results are shown in blue and the measurement in orange. The following rounded parameters are determined by curve fitting:

- $k_p = 6.0$

- $k_i = 11.5$

Fig. 83b shows the frequency response. It can be seen that the frequency deviation is small for steady state.
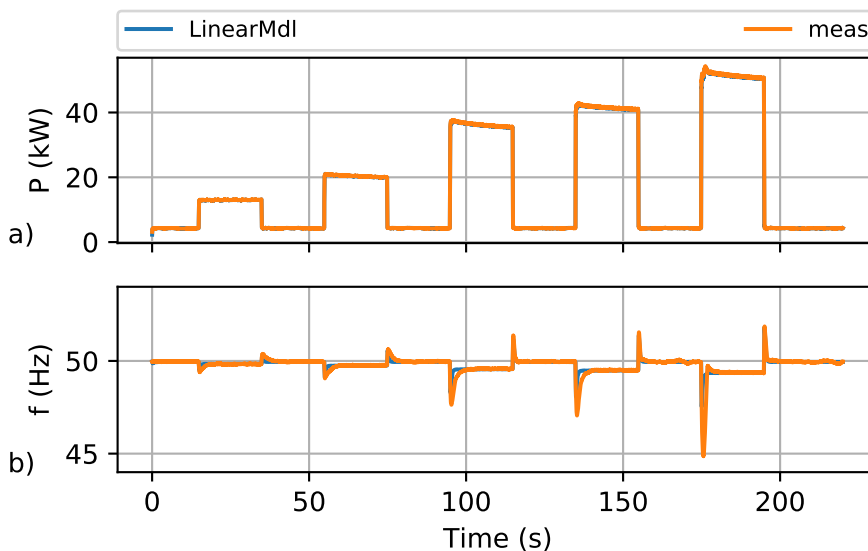
Figure 83 – Genset linear modeling approach. Comparison of measurement (orange) and linear modeling result (blue). a) active power generation; b) frequency.

In Fig. 84, the active power and frequency for an active power step of approx. $9kW$ is shown in comparison to the measured curve. A sufficient correlation for the frequency response is obtained.
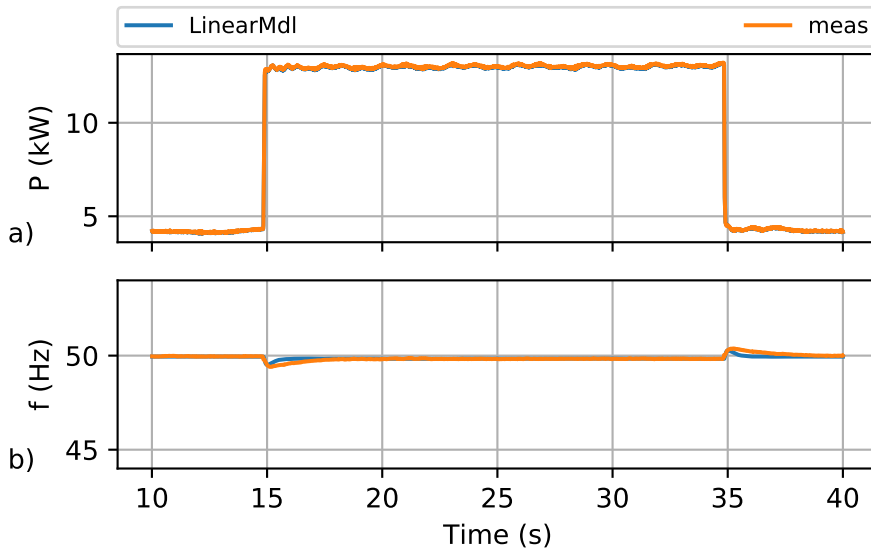
Figure 84 – Genset linear modeling approach. Comparison between measurement (orange) and linear modeling result (blue) for an active power step of 9kW (from approx. 4.5kW to approx. 13.5kW). a) active power generation; b) frequency.

In Fig. 85 resp. Fig. 86, the ohmic load step is increased to approx. $30kW$ resp. $50kW$. Now the limitation of the linear model approach can be seen as the frequency in the dynamic case cannot be represented adequately. Depending on the application of the model, a higher accuracy may be mandatory. Therefore, other model approaches (such as the fuzzy-based approach described in section 3.4.5.2) have to be selected.
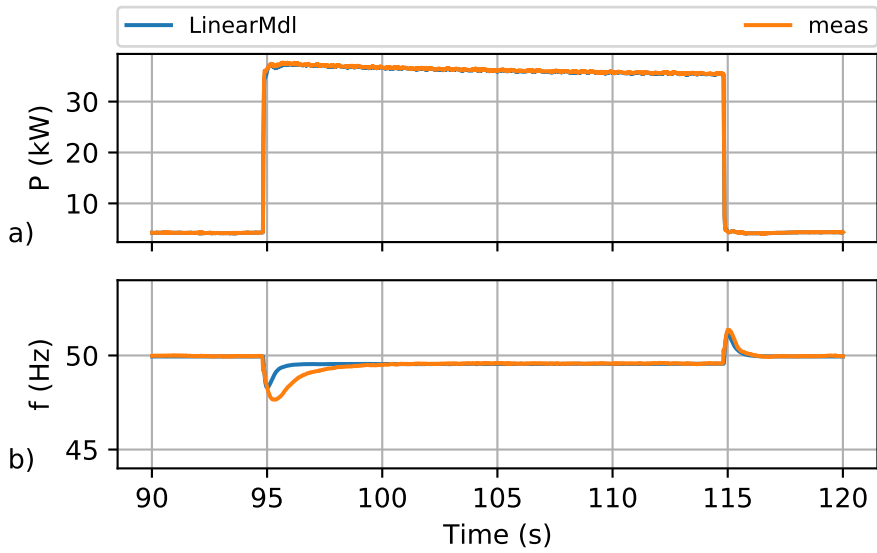
Figure 85 – Genset linear modeling approach. Comparison between measurement (orange) and linear modeling result (blue) for an active power step of $30kW$. a) active power generation; b) frequency.
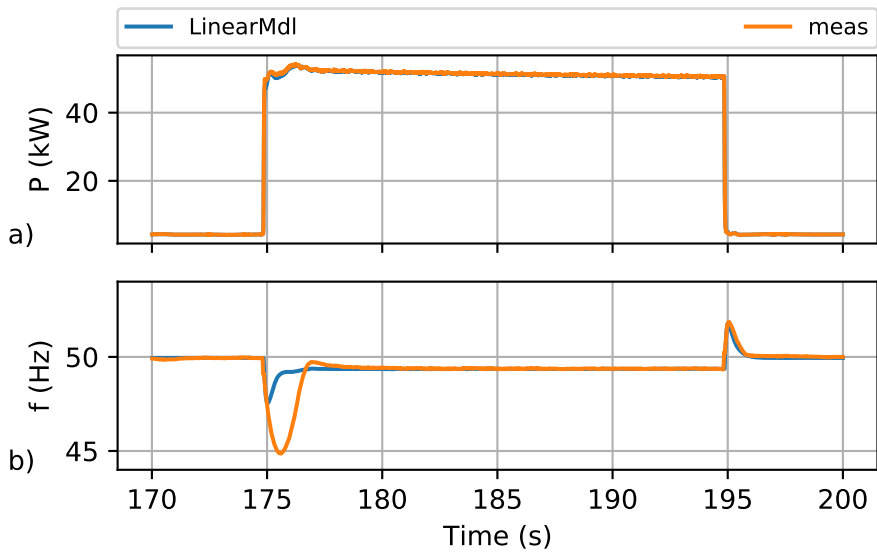
Figure 86 – Genset linear modeling approach. Comparison between measurement (orange) and linear modeling result (blue) for an active power step of $50kW$. a) active power generation; b) frequency.

6.1.3.2 Fuzzy-based Approach - Parameter Estimation

As the linear model approach for the engine modeling is not suitable for an accurate representation of the resulting frequency in a high range of power pulses, the developed model based on fuzzy logic is evaluated in this section as well.

The necessary model parameters are estimated by a mixture of systematic variation and curve fitting. This requires expert knowledge regarding modeling and evaluation of the results. The membership functions are defined in trapezoidal form with parameters *a,b,c* and *d* (Fig. 87). A detailed of over the membership parametrization for a normalized model in per-unit is given in Table 8.
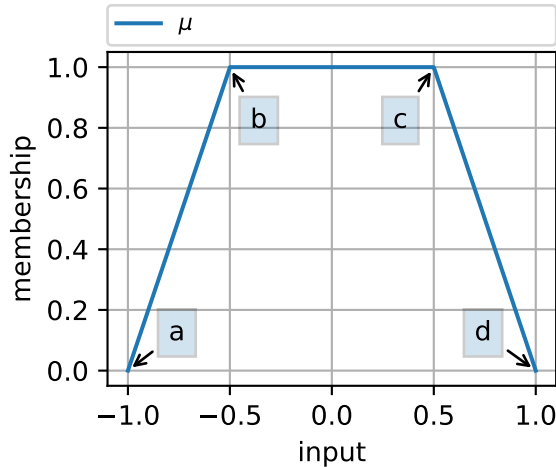
Figure 87 – Genset fuzzy-based approach. Membership function in trapezoidal form.

Table 8 – Genset fuzzy-based approach. Determined membership function parameters.

Parameter	a	b	c	d
$\mu_{f,LL}$	-99	-0.9	-0.05	-0.03
$\mu_{f,L}$	-0.05	-0.03	-0.03	0
$\mu_{f,N}$	-0.03	0	0	0.01
$\mu_{f,H}$	0	0.1	0.9	99
$\mu_{Teng,L}$	-99	0	0.15	0.25
$\mu_{Teng,N}$	0.15	0.25	0.25	0.35
$\mu_{Teng,H}$	0.25	0.35	1	99

Further parameters such as the singleton definitions are shown in Table 9.

Table 9 – Genset fuzzy-based approach. Set of parameters for simulation.

Parameter	k_p	k_i	Y_1	Y_2	Y_3	Y_4	Y_5	Y_6
Value	1.3	1.3	0.195	0.120	0	0.065	0.190	0.115

First, the active power profile from Fig. 88a is applied to the models. The resulting

frequency of the nonlinear approach in comparison to the linear modeling and the measurement result is plotted in Fig. 88b.

Figs. 89, 90 and 91 show the comparison of load steps of approx. $9kW$, $30kW$ and $50kW$. For small steps (Fig. 89), also the linear modeling approach is suitable. For higher load steps, the model accuracy can be significantly increased by the fuzzy-based approach (Fig. 90 resp. Fig. 91).
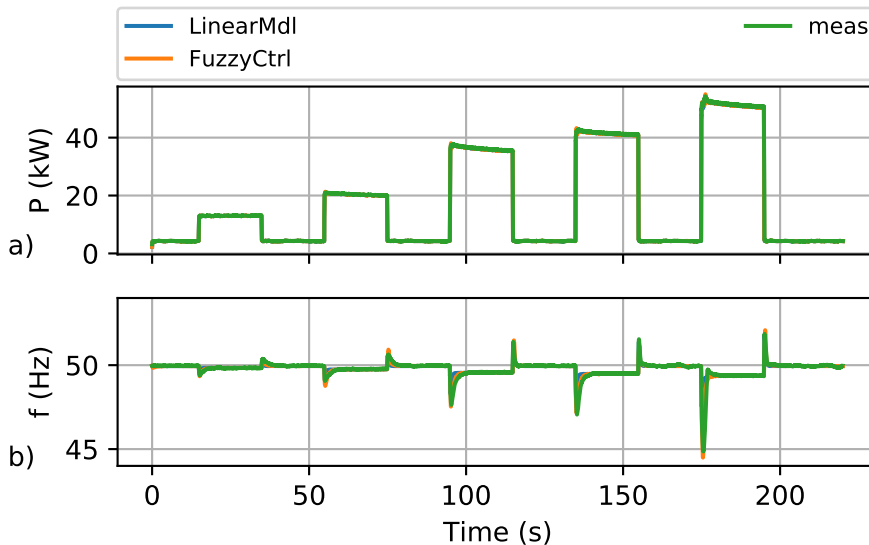
Figure 88 – Genset fuzzy-based approach. Comparison of fuzzy-based modeling (orange), linear approach (blue) and measurement (green) for the complete load profile. a) active power generation; b) frequency.

6.1.3.3 Model Verification

After parameter identification, active steps are applied to a different setup with different active power droop factor ($k_f = 200 \frac{kW}{Hz}$). The resulting frequency response is shown in Figs. 92-95.

The complete set of data is plotted in Fig. 92, whereas in Fig. 93-95, the results for active power steps of approx. $9kW$, $30kW$ resp. $50KW$ are applied.

Also, for model verification, as it can be seen, the fuzzy-based model leads to higher consistency than the linear approach.

6.1.3.4 Summary

The two model approaches developed in section 3.4 are parametrized and compared with measurements at a real genset system. Both approaches have advantages and disadvantages and the choice of the model structure depends on the application model. The comparison of the approaches is shown in Table 10.
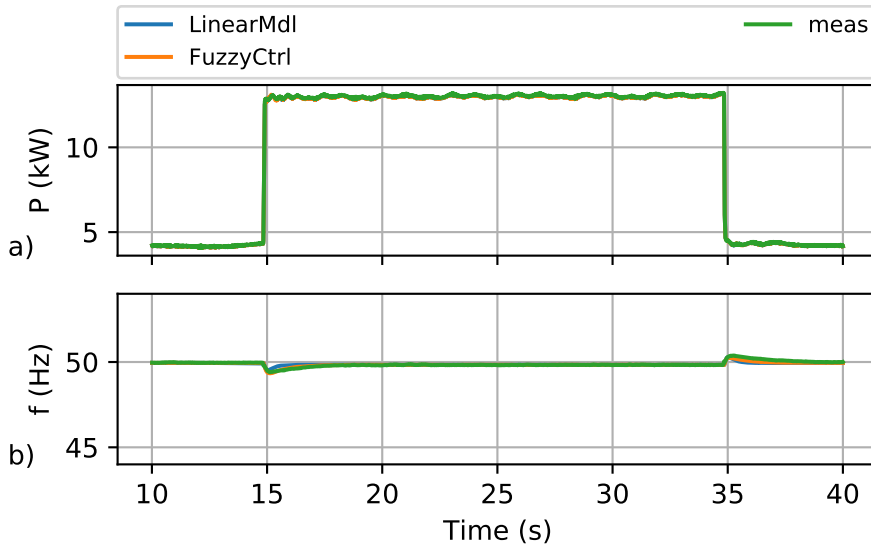
Figure 89 – Genset fuzzy-based approach. Comparison of fuzzy-based modeling (orange), linear approach (blue) and measurement (green) for an active power step of $9kW$. a) active power generation; b) frequency.
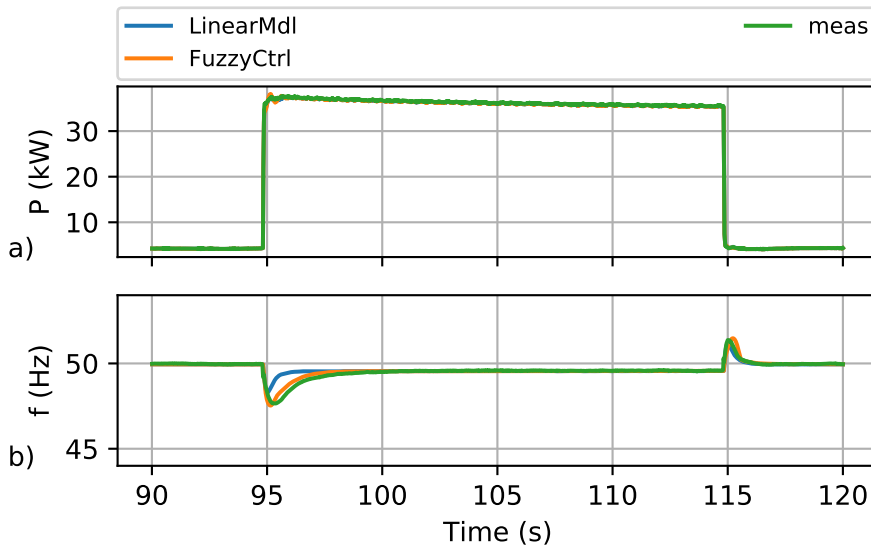
Figure 90 – Genset fuzzy-based approach. Comparison of fuzzy-based modeling (orange), linear approach (blue) and measurement (green) for an active power step of $30kW$. a) active Power generation; b) frequency.
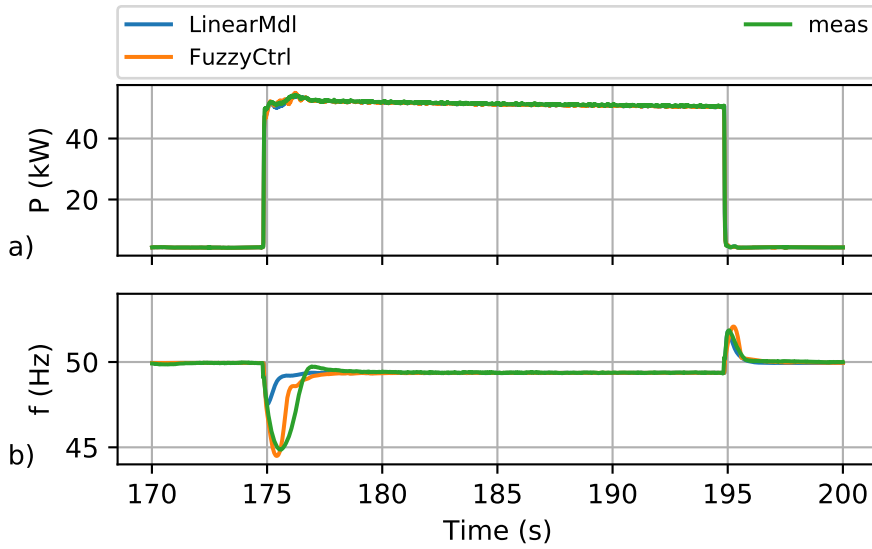
Figure 91 – Genset fuzzy-based approach. Comparison of fuzzy-based modeling (orange), linear approach (blue) and measurement (green) for an active power step of $50kW$. a) active power generation; b) frequency.
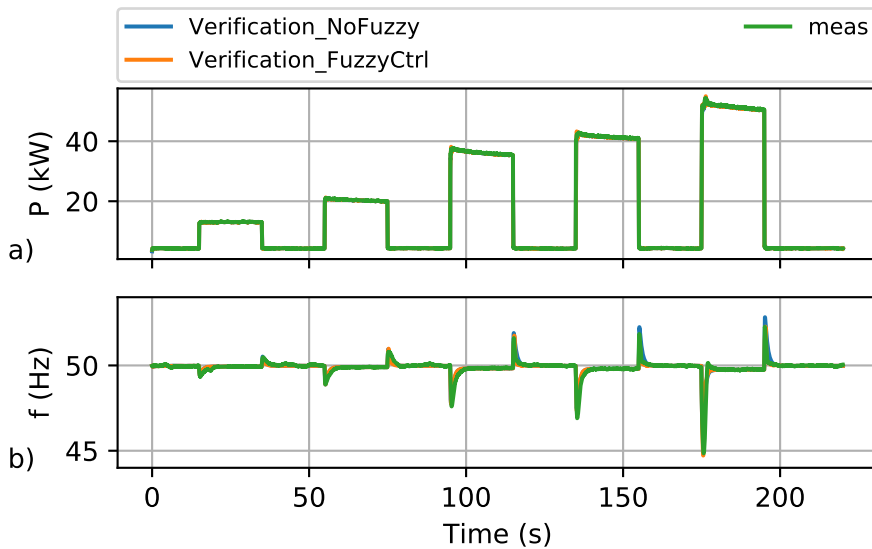
Figure 92 – Genset model verification. Comparison of fuzzy-based model (orange), linear approach (blue) and measurement (green) for active power steps and an active droop factor of $k_f = 200kW/Hz$
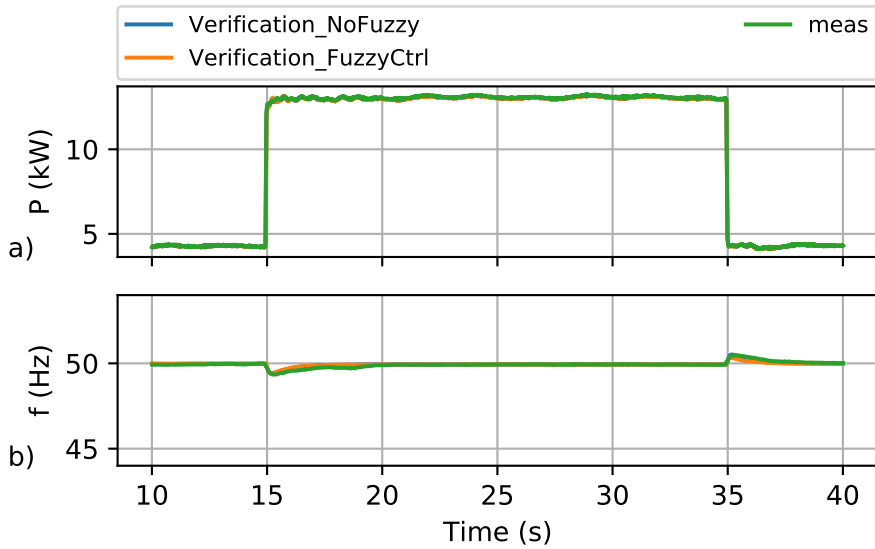
Figure 93 – Genset model verification. Comparison of fuzzy-based model (orange), linear approach (blue) and measurement (green) for an active power step of approx. 9kW and $k_f = 200kW/Hz$.
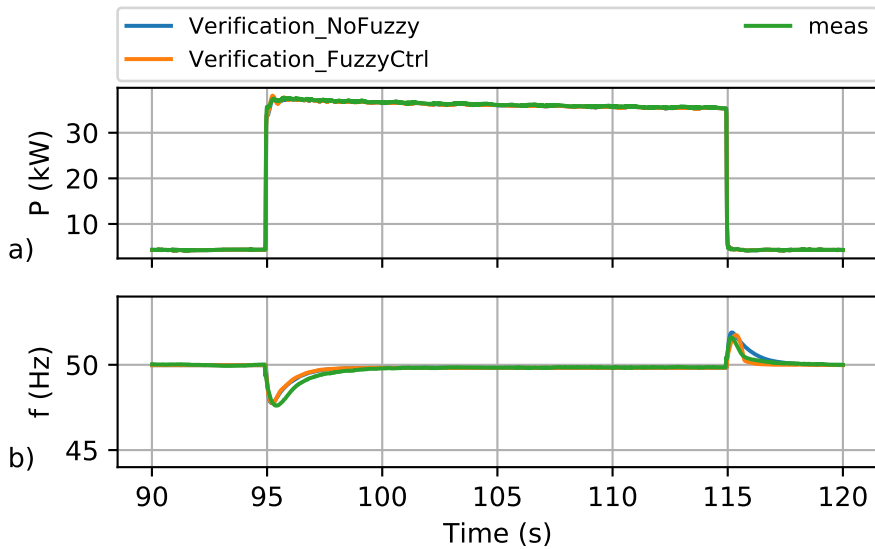
Figure 94 – Genset model verification. Comparison of fuzzy-based model (orange), linear approach (blue) and measurement (green) for an active power step of approx. 30kW and $k_f = 200kW/Hz$.
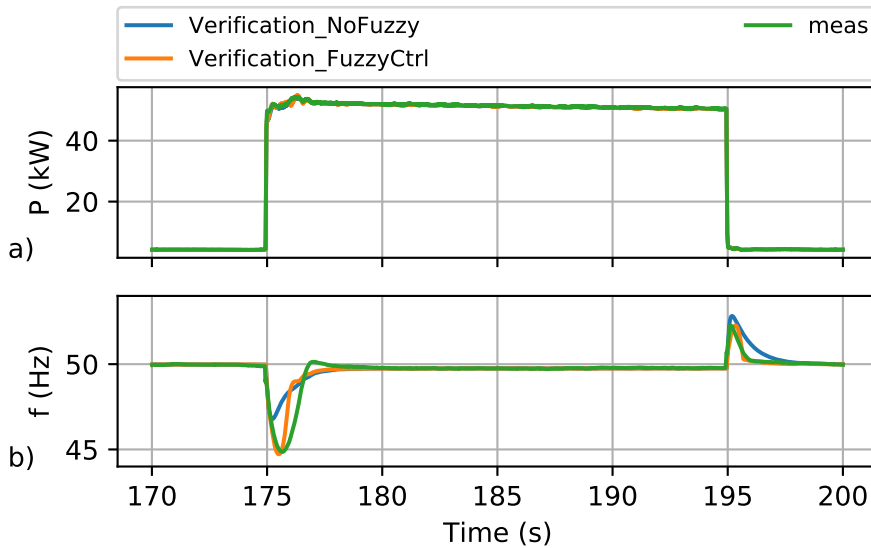
Figure 95 – Genset model verification. Comparison of fuzzy-based model (orange), linear approach (blue) and measurement (green) for an active power step of approx. 50kW and $k_f = 200kW/Hz$.

Table 10 – Genset modeling. Comparison of the linear approach and the fuzzy-based engine model.

Linear Modeling	Fuzzy-based Modeling
+ Low number of parameters	+ Higher model accuracy due to nonlinear representation
+ Fast parameter identification by curve fitting methods	
- No representation of nonlinear engine behavior	- High number of parameters (4 parameters for each membership function and singleton)
	- Expert knowledge necessary for parameter guess (systematic variation)

Core Statements:

1. Linear engine modeling approach sufficient of many applications (such as secondary control dimensioning)

2. For higher accuracy, fuzzy-based engine modeling is suggested. Nevertheless, the higher number of parameters need accurate measurements for parameter identification.

6.1.4 PV System

The mathematical modeling of a PV system under consideration of the German Applica-tion Guide *VDE AR-N4105* [99] is described in section 3.5. In the following, the model is validated for two scenarios by measurements at a real PV system mounted on the roofs at the test site MCW and included into the islanded microgrid.

First, the startup behavior is investigated. After connecting the PV system to the grid, the power feed-in can begin at least after a time period of $\Delta t = 60s$. Afterwards, the slope of the active power ramp should not exceed 10% of the rated power per minute. Fig. 96 shows the comparison of simulation (blue) and measurement (green) during the PV startup process.
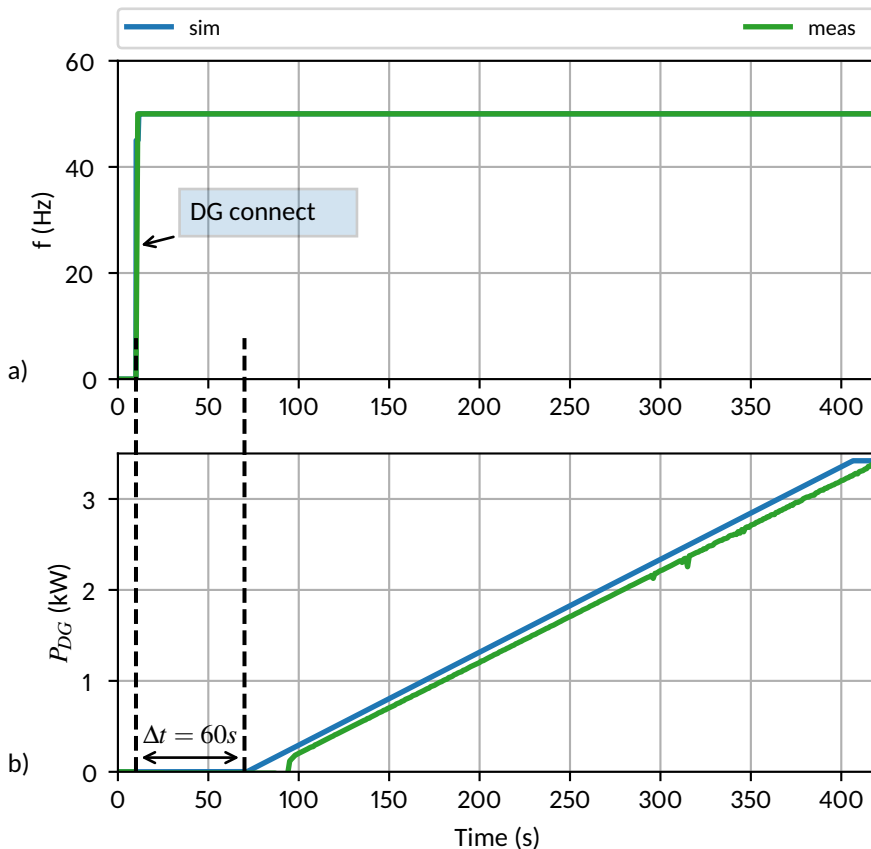
Figure 96 – PV system startup process. Comparison of simulation (blue) and measurement (green). a) grid frequency; b) active power feed-in.

In the second step, the active power feed-in reduction due to over-frequency is again compared between simulation and measurement. A good correlation is shown for a smooth-ing time constant T_{smooth} (shown in Fig. 30) equal to $20ms$.

This verified model for a specific PV plant now can be scaled up for PV plants connected to the LV grid as the fundamental control principle is based on a technical specification that systems have to fulfill.
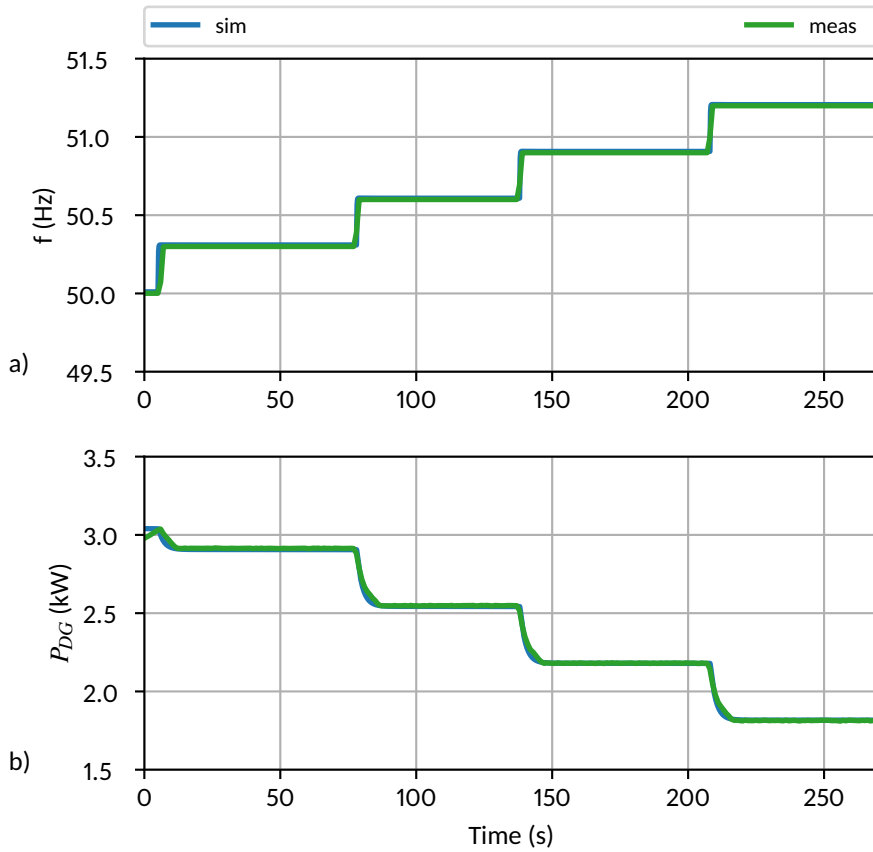
Figure 97 – PV system active power feed-in depending on grid frequency. a) grid frequency; b) active power feed-in. Blue: simulation result. Green: Measurement.

6.2 Parallel Operation of Grid Forming and Grid Supporting Units using Droop Control

In this section, the theoretical models and considerations from section 4.1 are verified with real measurements which are executed at the Microgrid Demonstrator MCW (section 5).

In almost all of the following experiments, an ohmic load profile, as shown in Fig. 98, is applied to parallel operated microgrid assets.
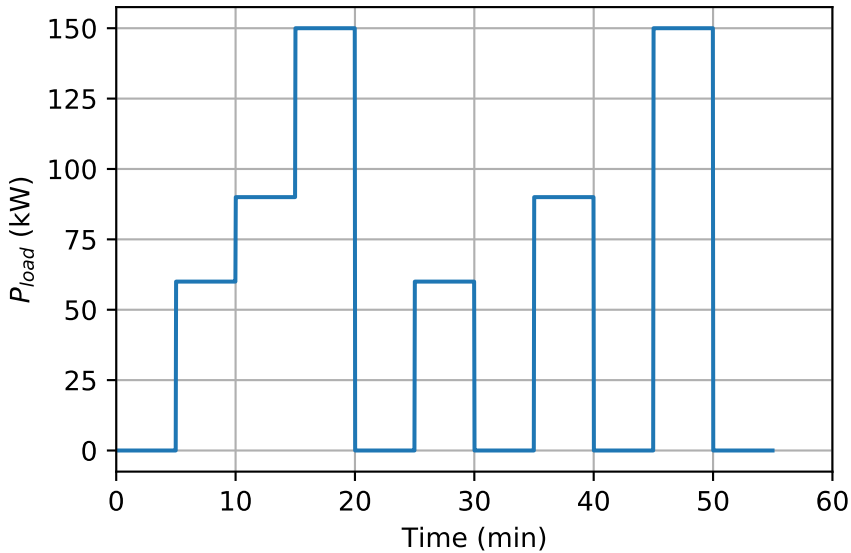
Figure 98 – Ohmic load profile applied to the islanded microgrid for investigation of parallel operation of grid forming and grid supporting units using droop control.

In the first case, two inverters-based GFUs (ABSS and B2B) are operated in parallel. In the second case, the parallel operation of an inverter-based GFU and a genset GFU is investigated. Next, a verification for the parallel operation of an inverter-based GFU with an inverter-based GSU is presented and finally, the results for a parallel operation of genset GFU and inverter-based GSU are shown.

6.2.1 Inverter-based GFUs in Parallel Operation

Based on the mathematical models developed in section 4.1, the parallel operation of two inverter-based GFUs (ABSS and B2B; see section 5) is verified by specific measurements for different controller parametrization.

First, an active power droop factor of $k_{f,GFUx} = 150kW/Hz$ is set for both assets. Further setpoints for voltage $V_0 = 400V$, frequency $f_0 = 50Hz$, active power $P_0 = 0$ and reactive power $Q_0 = 0$ are set for both assets equally.

The simulation result of the complete experiment is shown in Fig. 99. A good correlation between the measurement and the simulation can be seen.

The voltage droop control concept leads to a reactive power flow between both GFUs. (Fig. 99c), even in the case of an ohmic load without reactive power consumption or generation. That means that further concepts have to be taken into account for minimization of this effect, which causes additional losses, but also a higher utilization of the assets and even a reduction of the active power supply capability.
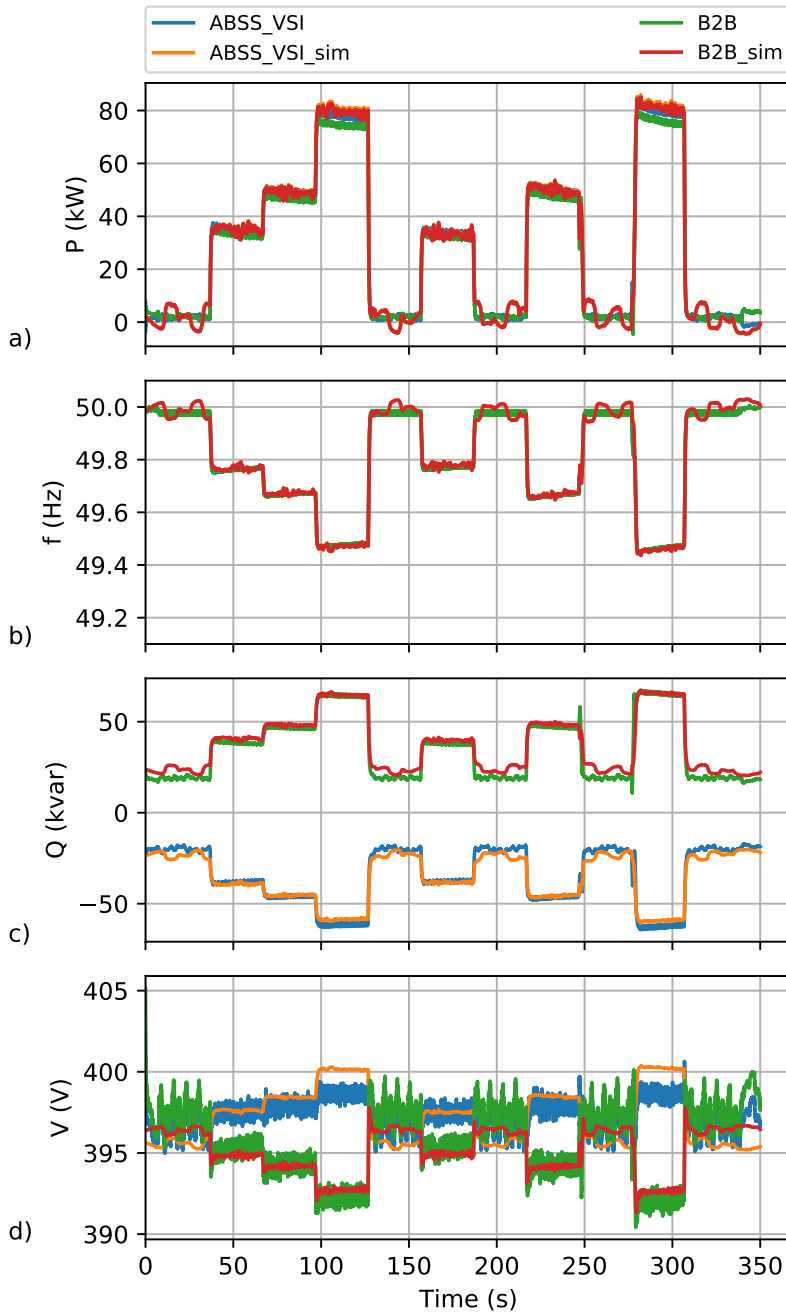
Figure 99 – Parallel operation of inverter-based GFUs (ABSS, B2B). Comparison of measurement and simulation results for droop factor $k_f = 150kW/Hz$. a) active power distribution; b) grid frequency; c) reactive power distribution; d) asset voltages. Blue: ABSS measurement. Orange: ABSS simulation. Green: B2B measurement. Red: B2B simulation.

Fig. 100 shows the zoom for a positive active power load step of 100kW. Also in this dynamic consideration a good correlation between measurement and simulation is revealed.

Next, the frequency droop factors are changed to $k_{f,ABSS} = 1000kW/Hz$ for the ABSS and $k_{f,B2B} = 2000kW/Hz$ for the B2B. Again, the load profile from Fig. 98 is applied. The corresponding results are shown in Fig. 101.

It can be seen that for the changed droop configuration with high frequency droop factors (which leads to a small frequency deviation) also, a stable operation can be simulated and measured.

A good correlation is given, which means means that the verified simulation models developed in the frame of this work can be used for further investigations regarding control strategies, but also as a planning tool for the design of an islanded microgrid.
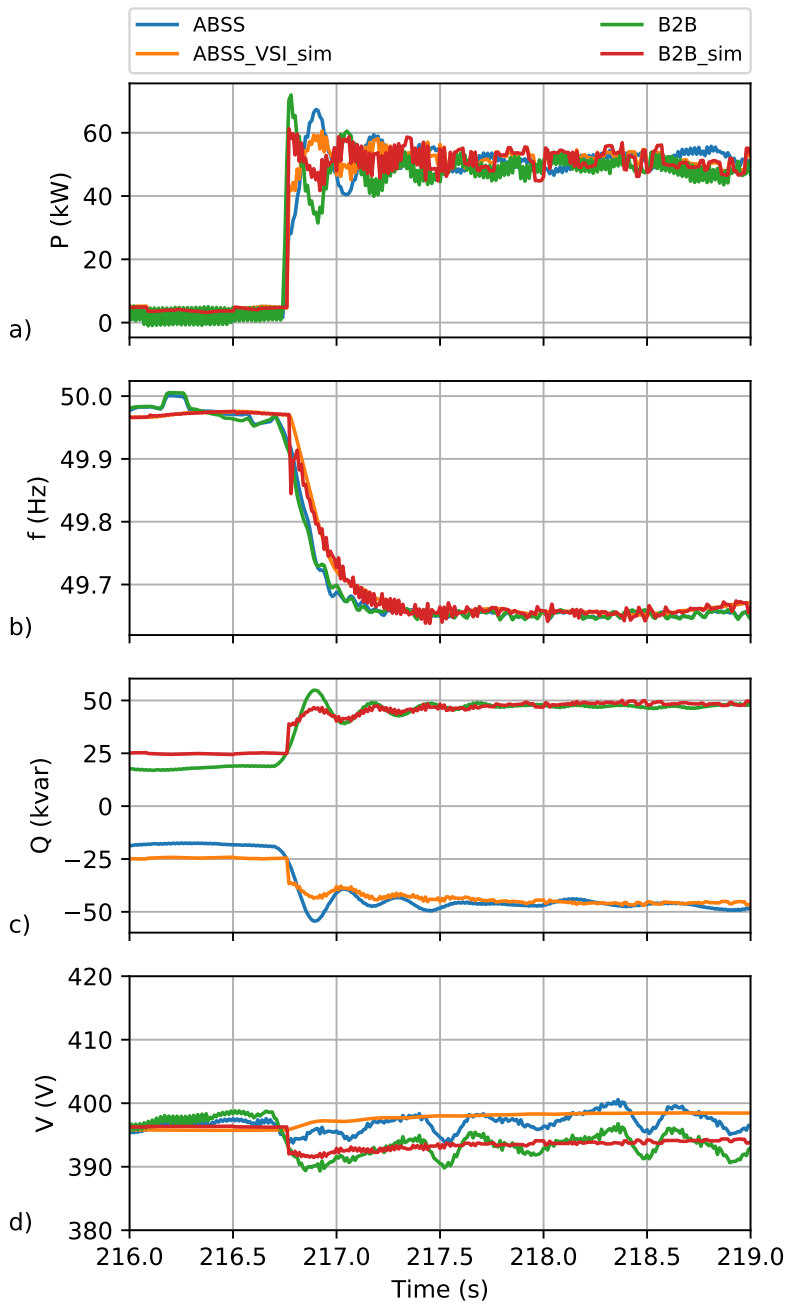
Figure 100 – Parallel operation of inverter-based GFUs (ABSS, B2B). Comparison of measurement and simulation results for droop factor $k_f = 150kW/Hz$. a) active power distribution; b) grid frequency; c) reactive power distribution; d) asset voltages. Blue: ABSS measurement. Orange: ABSS simulation. Green: B2B measurement. Red: B2B simulation. Zoom for active power step from approx. 0kW to approx. 100 kW.
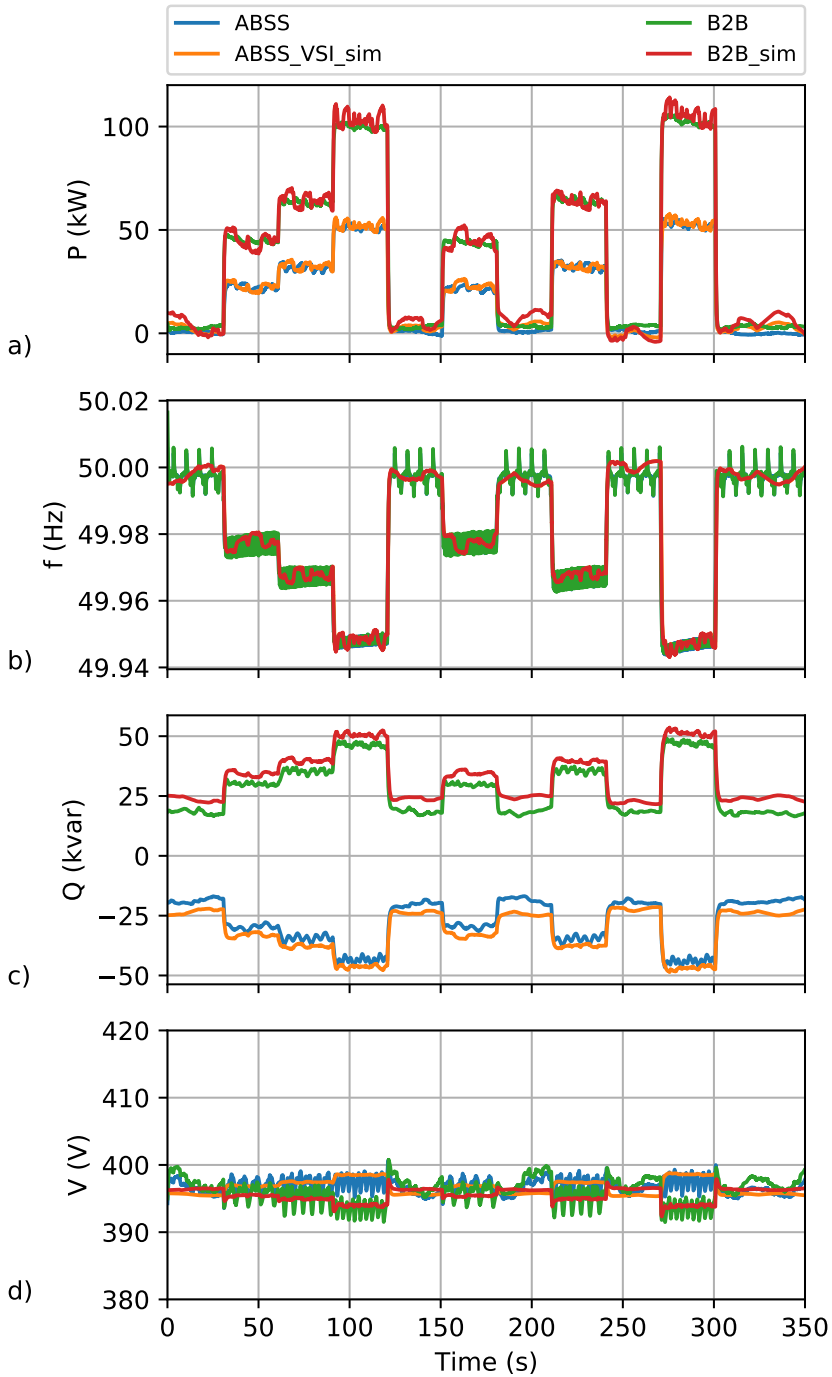
Figure 101 – Parallel operation of inverter-based GFUs (ABSS, B2B). Comparison of measurement and simulation results for droop factor $k_{f,ABSS} = 1000kW/Hz$ and $k_{f,ABSS} = 2000kW/Hz$. a) active power distribution; b) grid frequency; c) reactive power distribution; d) asset voltages. Blue: ABSS measurement. Orange: ABSS simulation. Green: B2B measurement. Red: B2B simulation.

6.2.2 Inverter GFU and Genset GFU in Parallel

The parallel operation of an inverter-based GFU and a genset GFU is investigated by sim-
ulation and verified by measurements at the MCW. Fig. 102 shows the corresponding re-
sults for three load steps from each $0kW$ to $75kW$, $100kW$ and $150kW$ for measurement
(blue) and simulation (orange). In Fig. 102a, the inverter's active power P_{INV} is illustrated,
whereas Fig. 102b shows the genset's active power. Fig. 102c and Fig. 102d show the
correpsonding reactive power and finally, the grid frequency is shown in Fig. 102e.

A correlation for the three load steps is given for the active power distribution between
the GFUs as well as the frequency behavior. For the reactive power, a correlation is given
as well, as the maximum deviation is small (max. approx. $5kvar$) and can be explained by
small voltage setpoint deviations in the reactive power/voltage droop function (Eq. (2))
for the no-load periods, but also by measurement uncertainties ($5kvar$ in comparison to
a rated power of $135kVA$ resp. $300kVA$). In the simulation, this effect does not appear.
The dynamic behavior is shown in Fig. 103 for an active power step of approx. $100kW$
which confirms the quality of the simulation models. The inverter GFU is covering almost
the complete load ($\approx 90kW$) in the first seconds after the load step (at time $t = 220s$, Fig
103a). Also, in the case of a negative load step ($t = 320s$), the inverter reacts very much
faster and is compensating the lower dynamics of the genset.

For the dimensioning of the assets, it has to be pointed out that the inverter GFU
must be capable of supplying the complete load – at least for some seconds. For the grid
frequency, also higher dynamics in comparison to the parallel operation of two inverter-
based GFUs can be seen. In the design of an islanded microgrid and its assets, it has to
be considered by specific simulations that the minimum and maximum frequency should
not exceed defined limits. In the case of using DGs with VDE AR-N4105 characteristics, the
frequency should not be smaller than $47.5Hz$ and not higher than $50.2Hz$ as both would
lead to a feed-in reduction or even to a disconnection from the grid.

Next, the same experiment is repeated for active power/frequency droop factors of
$k_{f,INV} = k_{f,GEN} = 500kW/Hz$. The results plotted in Fig. 104 show a deviation in the
active power distribution between the inverter-based GFU and the genset for all power
pulses. Due to the high droop factor, the frequency variation due to Eq. (1) is small. In that
case, also small measurement uncertainties have a high effect on the power split-up.

For replication of this measured effect in the simulation, a measurement uncertainty
at the measured frequency at the genset control (Fig. 26 resp. Fig. 27) is introduced:

$$f_{error} = f \cdot (1 + k_{f,error,rel}) + f_{offset} \tag{82}$$

By parameter variation in the simulation model, the measured behavior can be repli-
cated. The relative error $k_{f,error,rel}$ does not have a significant effect in this case; by set-
ting the offset to $f_{offset} = -0.0015p.u.$, a good correlation for the different active power
pulses is reached. Fig. 105 shows the corresponding simulation result.

Finally, the experiment for droop factors of $k_{f,INV} = k_{f,GEN} = 150/Hz$ is repeated un-
der consideration of the measurement offset of $f_{offset} = -0.0015p.u.$. As shown in Fig.
106, the introduction of the offset does not affect the result of lower values of droop fac-
tors.

From this experiment with different droop factors it can be seen that accurate mea-
surement devices inside the control system have to be used to establish a proper power
distribution by droop control. Even small tolerances (in this case: $f_{offset} = -0.0015p.u.$)
can lead to significant deviations in the power split-up.

For the design of islanded microgrids, a sufficiently high accuracy has to be ensured
from the assets' manufacturers.
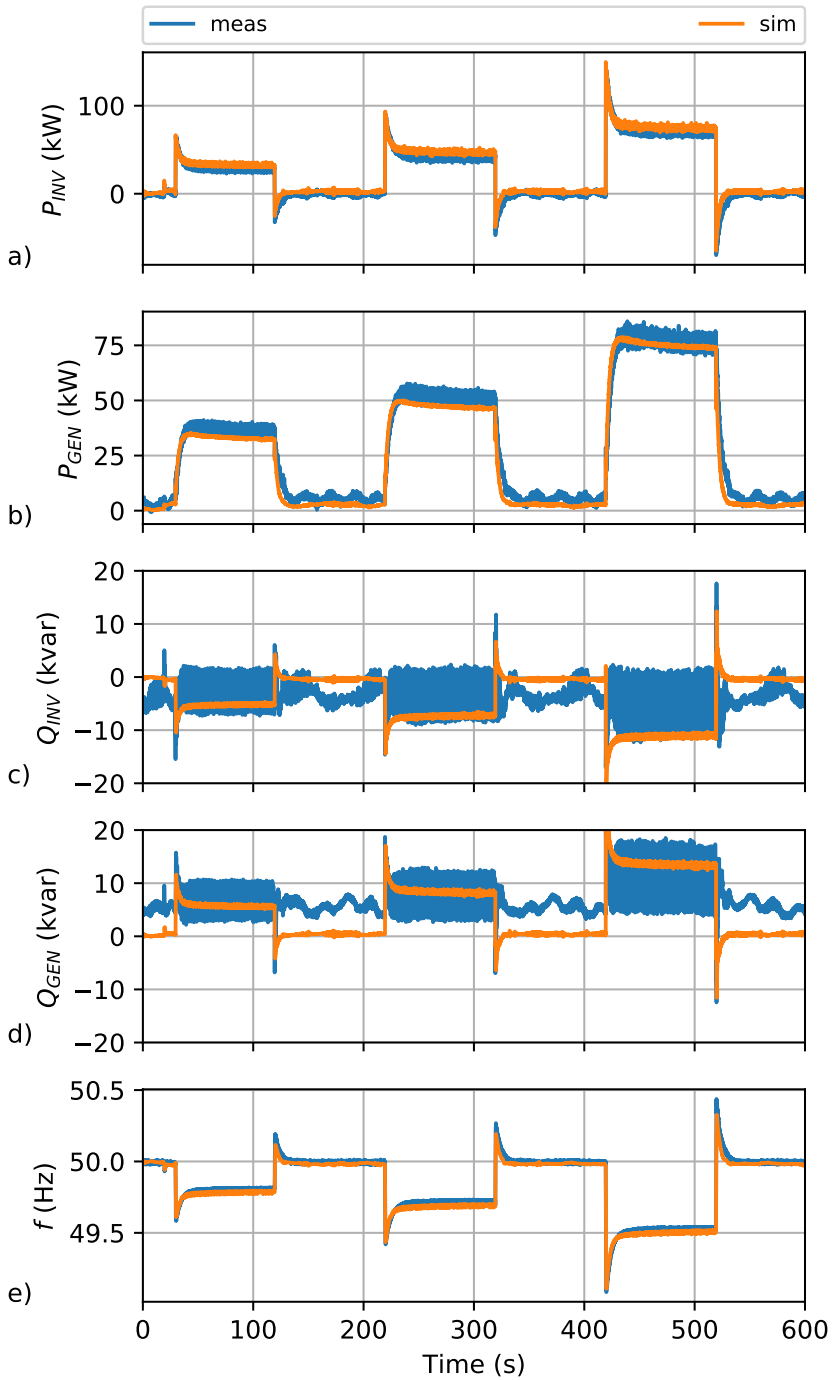
Figure 102 – Parallel operation of inverter GFU and genset GFU ($k_{f,INV} = k_{f,GEN} = 150 kW/Hz$). Comparison between simulation (orange) and measurement (blue). a) active power inverter; b) active power genset; c) reactive power inverter; d) reactive power genset; e) grid frequency.
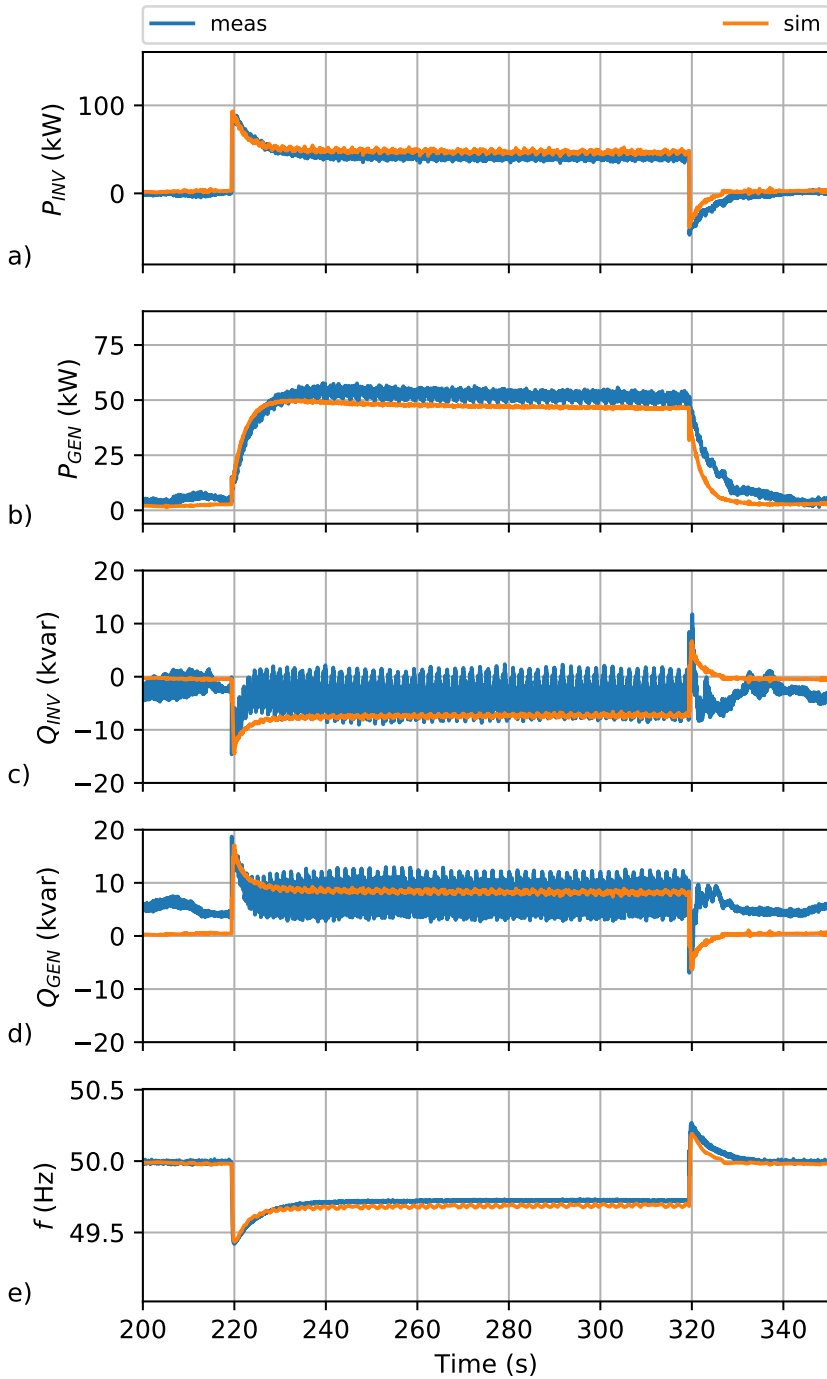
Figure 103 – Parallel operation of inverter GFU and genset GFU ($k_{f,INV} = k_{f,GEN} = 150kW/Hz$). Comparison between simulation (orange) and measurement (blue). a) active power inverter; b) active power genset; c) reactive power inverter; d) reactive power genset; e) grid frequency. Zoom-in for active power step from 0 to $100kW$.
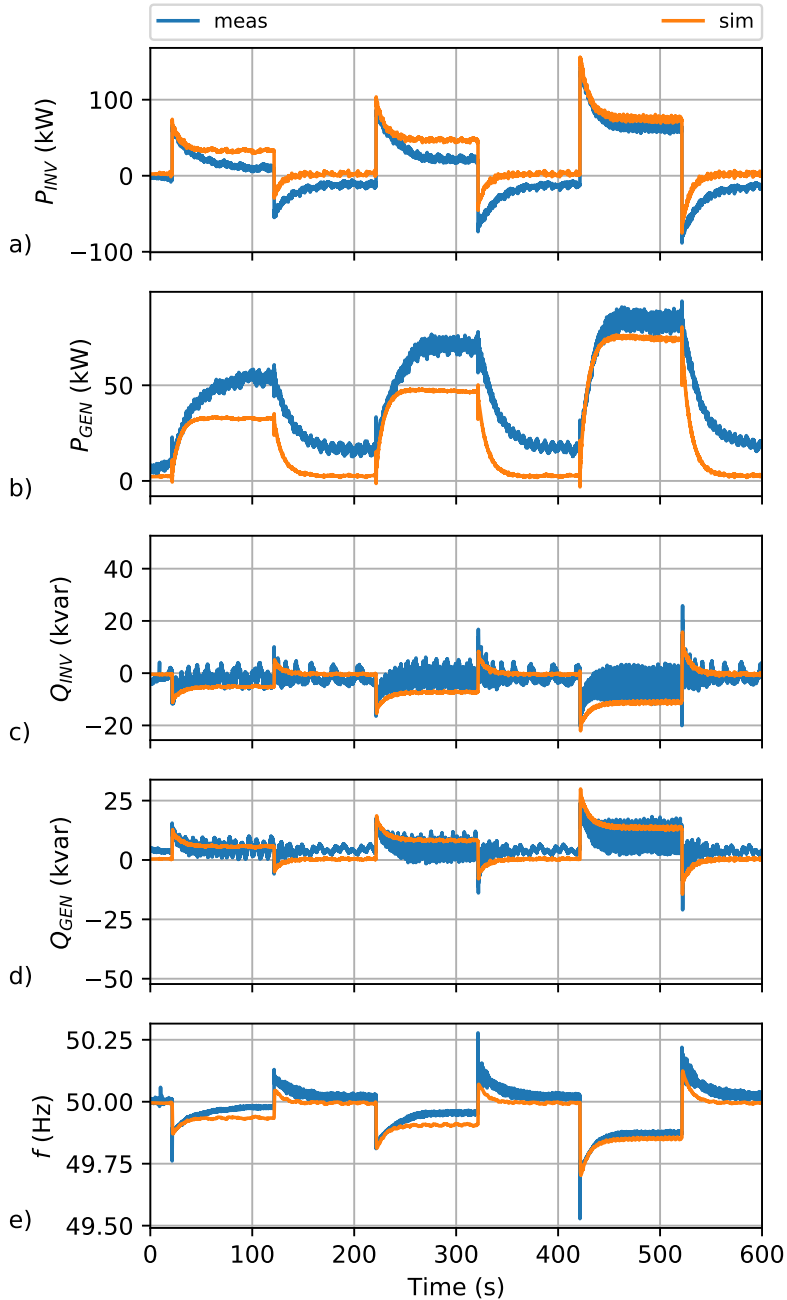
Figure 104 – Parallel operation of inverter GFU and genset GFU ($k_{f,INV} = k_{f,GEN} = 500/Hz$). Comparison between simulation (orange) and measurement (blue). a) active power inverter; b) active power genset; c) reactive power inverter; d) reactive power genset; e) grid frequency.
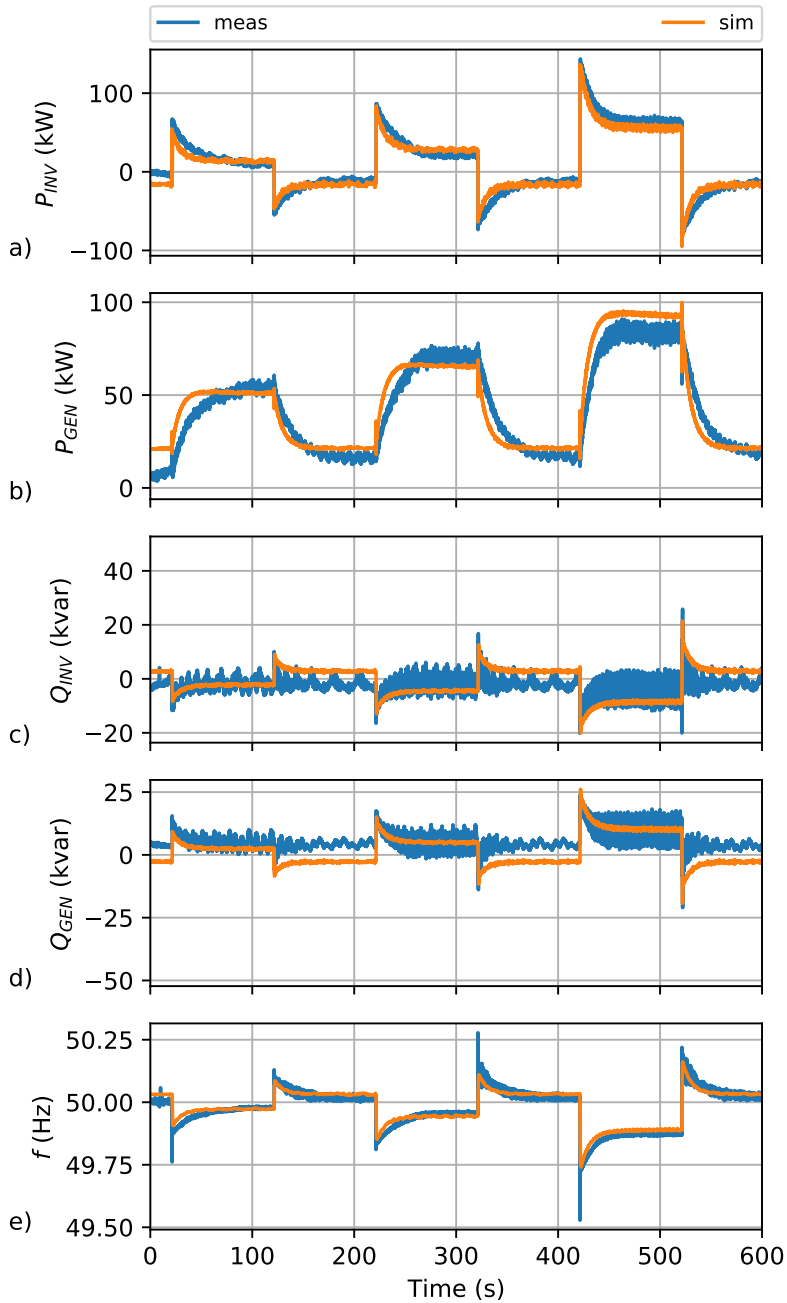
Figure 105 – Parallel operation of inverter GFU and genset GFU ($k_{f,INV} = k_{f,GEN} = 500kW/Hz$) with offset $f_{offset} = -0.0015p.u.$ Comparison between simulation (orange) and measurement (blue). a) active power inverter; b) active power genset; c) reactive power inverter; d) reactive power genset; e) grid frequency.
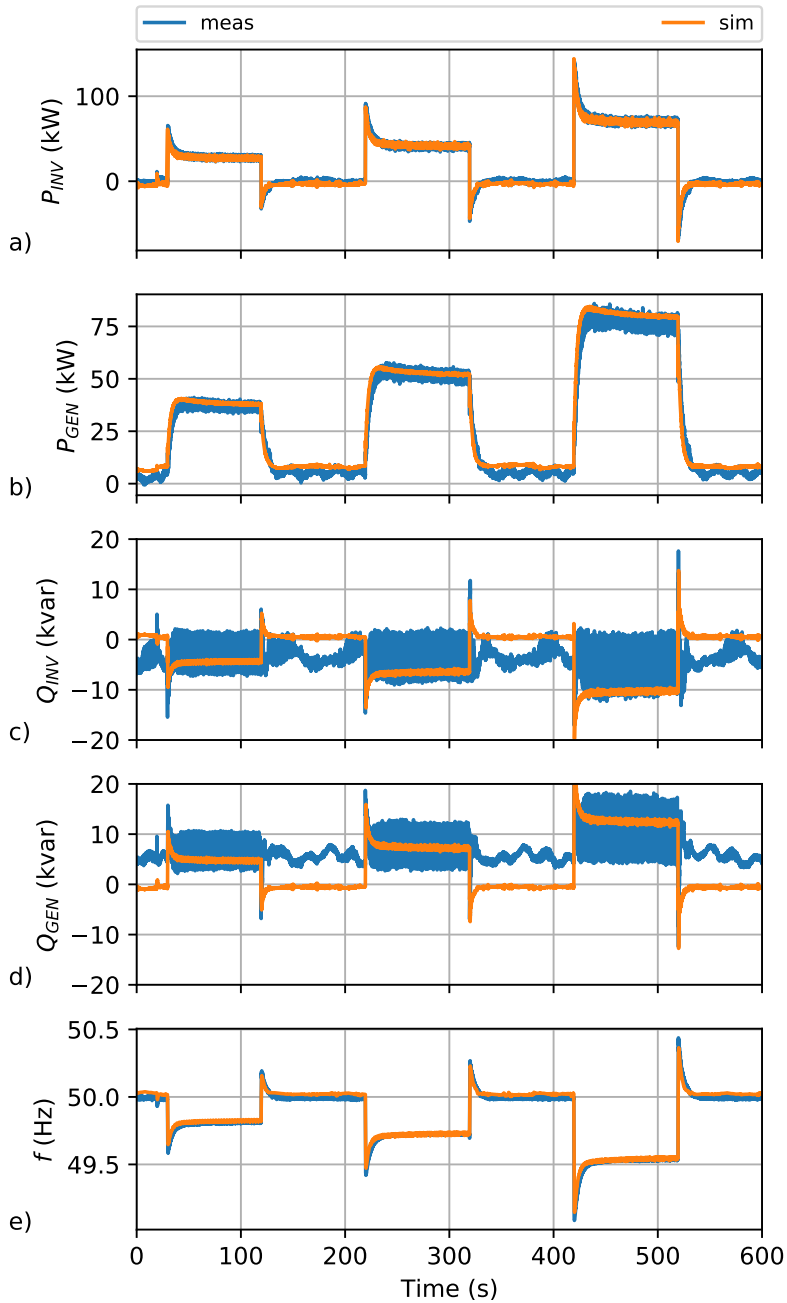
Figure 106 – Parallel operation of inverter GFU and genset GFU ($k_{f,INV} = k_{f,GEN} = 150kW/Hz$) with offset $f_{offset} = -0.0015 p.u.$ Comparison between simulation (orange) and measurement (blue). a) active power inverter; b) active power genset; c) reactive power inverter; d) reactive power genset; e) grid frequency.

6.2.3 Grid Forming Inverter and Grid Supporting Inverter in Parallel Operation

In the following, an inverter-based GSU is operated parallel to an inverter-based GFU to support the active power management within an islanded microgrid. As the GFUs are controlled to voltage and frequency ($V(Q)$ resp. $f(P)$ characteristics), an immediate response for active and reactive power distribution after load changes is expected. The GSUs are operated in parallel operation (without grid forming capability) and synchronized to the grid frequency and voltage. The closed-loop control for active and reactive power in combination with the droop characteristics $P(f)$ leads to a delayed power distribution response. This modeling is described in detail in section 3.3.4. The dead time of the GSU used in this experiment is $T_{delay} \approx 2s$.

In the experiment, the frequency droop factors $k_{f,GFU}$ and $k_{f,GSU}$ $300kW/Hz$. At the GFU, a voltage droop factor of $k_{V,GFU} = 12kvar/V$ is set, whereas at the GSU, no voltage droop is activated and thus the reactive power setpoint of the GSU is $Q_{set,GSU} = 0$. That means that (in steady state) the reactive power supply is realized only by the GFU. The result of the experiment with three active power pulses is shown in Fig. 107.

Next, the dynamic behavior is compared for a residual load step from $P_{res} = 0kW$ to $P_{res} = 100kW$. A detailed plot is shown in Fig. 108. A good correlation can be seen, also the measured small damped oscillation is represented adequately. It can be seen that the GFU has to cover the complete load for some seconds until the defined active power split-up is reached.

Further, it can be seen in Fig 108d that the grid frequency is reduced to approx. $f = 49.7Hz$ before a steady state value of $f \approx 49.83Hz$ is reached. This is also an effect of the delayed response of the GSU and has to be taken into account in the controller design of the islanded microgrid.

The effect of a negative residual load step ($100kW \rightarrow 0kW$) on the power distribution is investigated in Fig. 109 where also a good correlation is seen. It should be pointed out again that the GFU has to cover the difference between the residual load P_{res} and the GSU P_{GSU} in the transient time. That means that the GFU is consuming active power for some seconds until the steady state of ($P_{res} = P_{GFU} = P_{GSU} = 0$) is reached. Also, the grid frequency has to be considered; in the transient time ($1053s < t < 1056s$), the frequency must be within defined limits as no DG feed-in reduction due to over-frequency is desired.
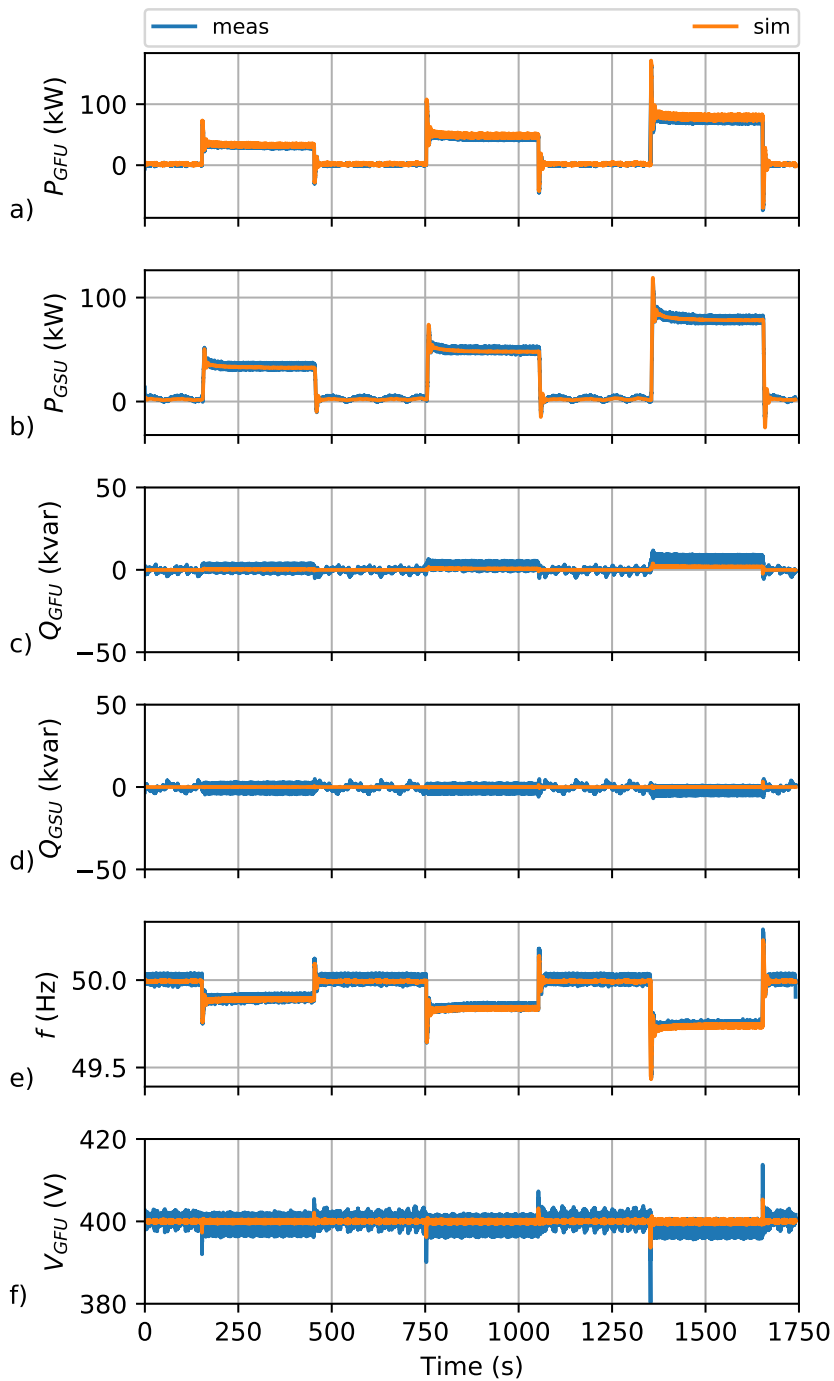
Figure 107 – Parallel operation of GFU and GSU ($k_{f,GFU} = k_{f,GSU} = 300kW/Hz$). Comparison of simulation (orange) and measurement (blue). a) active power GFU; b) active power GSU; c) reactive power GFU; d) reactive power GSU; e) grid frequency; f) GFU voltage.
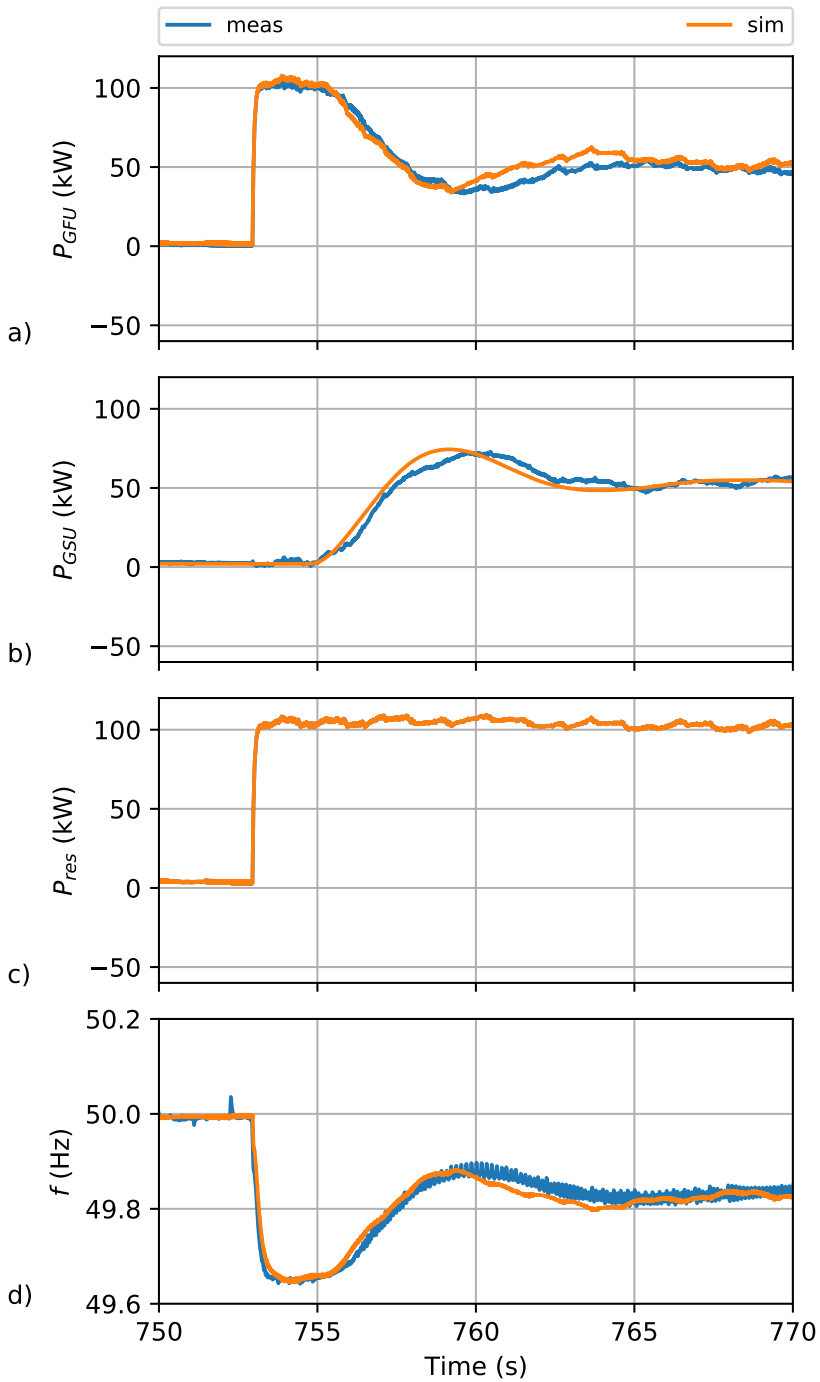
Figure 108 – Parallel operation of GFU and GSU ($k_{f,GFU} = k_{f,GSU} = 300kW/Hz$). Comparison of simulation (orange) and measurement (blue) for a load step of approx. $100kW$. a) active power GFU; b) active power GSU; c) residual load; d) grid frequency.
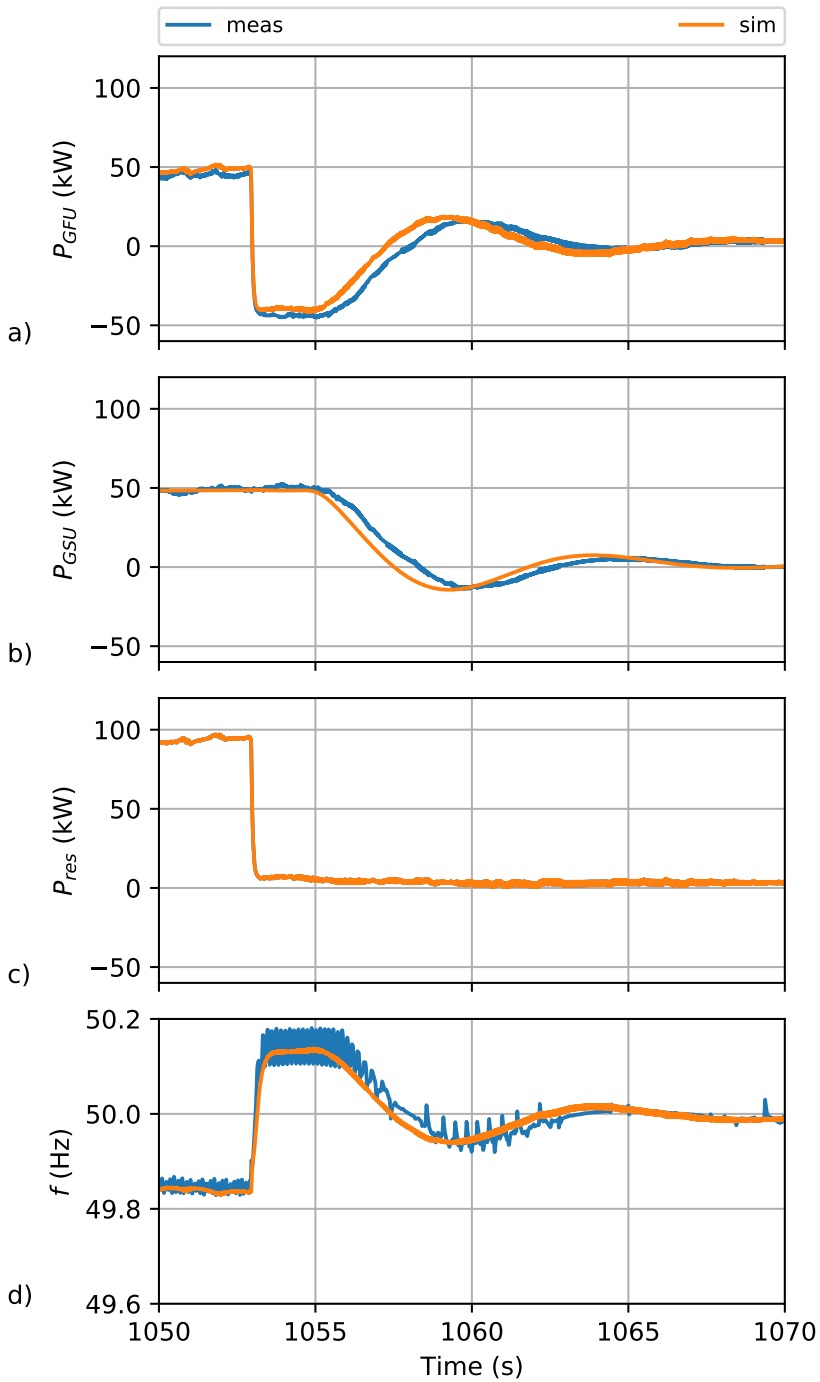
Figure 109 – Parallel operation of GFU and GSU ($k_{f,GFU} = k_{f,GSU} = 300kW/Hz$). Comparison of simulation (orange) and measurement (blue) for a load step from approx. $100kW$ to $0kW$. a) active power GFU; b) active power GSU; c) residual load; d) grid frequency.

6.2.4 Genset and GSU in Parallel

In the last investigation, a parallel operation of one Genset as GFU and an inverter-based GSU is analyzed. For active power droop factors in the range of $k_f = 150kW$ or higher, no stable operation (neither in simulation nor in practical operation) is possible under consideration of the assets with their parameters. Therefore, the active power droop was decreased until a stable operation could be achieved. The results are presented in the following.

Fig. 110 shows the result of measurement (blue) and the corresponding simulation (orange) for active power droop factors $k_{f,GEN} = k_{f,GSU} = 60kW/Hz$. The comparison between measurement and simulation for a second droop configuration ($k_{f,GEN}80kW/Hz$, $k_{f,GSU} = 40kW/Hz$) is shown in Fig. 111.

In both cases, it can be seen that the correlation between simulation and measurement is low. Nevertheless, an oscillating operation behavior can be observed in both cases.

The droop factors are chosen very low (lower than in typical practical application due to the high resulting frequency variation) and the operation point is close to the stability limit. Nevertheless, the droop configuration is varied in the simulation for droop factors of $k_f = \{60, 82, 85, 90\} \, kW/Hz$) and the results are presented in Fig. 112.

A decrease of the dead time T_{delay} in the GSU would improve the performance in the dynamic behavior.

It can be seen that the design close to a stability limit needs a variation of the parameters to avoid instabilities in the real system. It has to be ensured that sufficient stability margin is available.

Further, it can be seen that simulations and/or measurements of both assets in standalone operation are not sufficient. To design an islanded microgrid, it is mandatory to investigate the interaction between the assets as well. This requires detailed (control) models for all assets and the corresponding parameters tjat can be received from the manufacturer or by specific measurements.

In summary, this point cannot be neglected in the design of islanded microgrids as long as a parallel operation of gensets and GSUs is desired. More stability analyses for droop configuration were not performed as this is not the goal of this work. Neither is also the parallel operation of a higher number of GFUs and GSUs in parallel part of this thesis.

Core Statements:

1. In practical applications, active power droop factors must be set in a certain range to avoid high frequency deviations in steady state (at low droop factors) and non-accurate power split-up (at high droop factors due to measurement accuracy which has to be defined in requirement specification at asset ordering).

2. In case of parallel operation of inverter-based GFUs and gensets, the inverter-based GFUs have to be designed for maximum power peaks (at least for some seconds).

3. The parallel operation of gensets and inverter-based GSUs has to be analyzed by simulations for sufficient stability margin due to low dynamics and dead time constants.
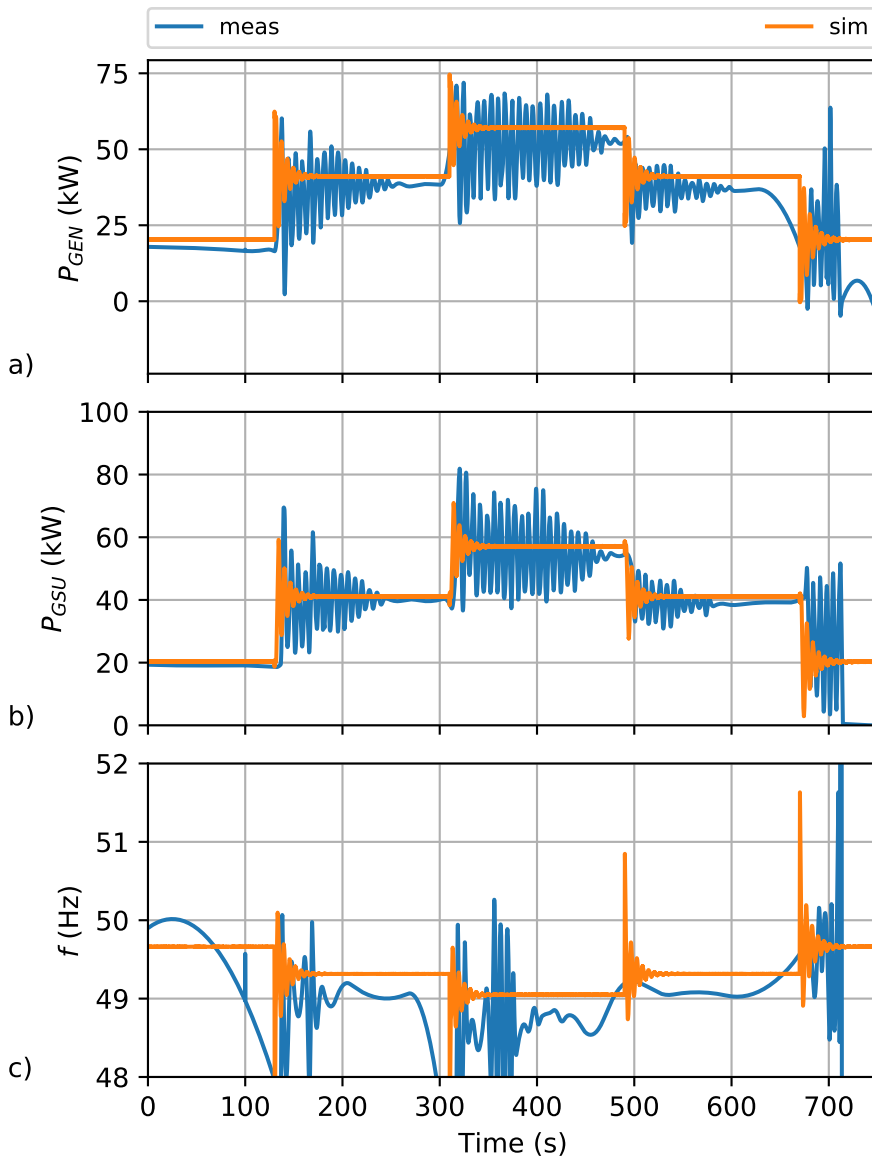
Figure 110 – Parallel operation of genset and GSU ($k_{f,GEN} = k_{f,GSU} = 60kW/Hz$). Comparison of simulation (orange) and measurement (blue). a) active power GEN; b) active power GSU; c) grid frequency.
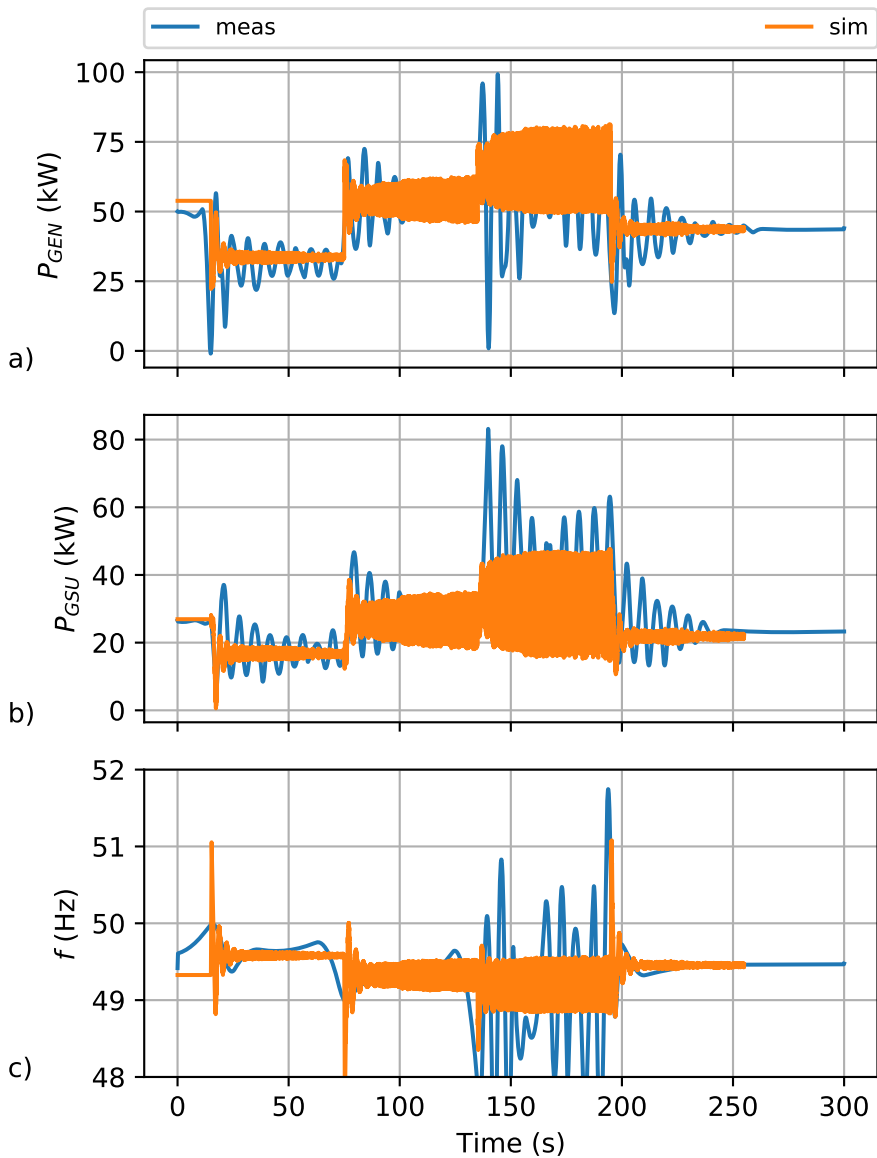
Figure 111 – Parallel operation of genset and GSU ($k_{f,GEN}$ 80kW/Hz, $k_{f,GSU} = 40kW/Hz$). Comparison of simulation (orange) and measurement (blue). a) active power GEN; b) active power GSU; c) grid frequency.
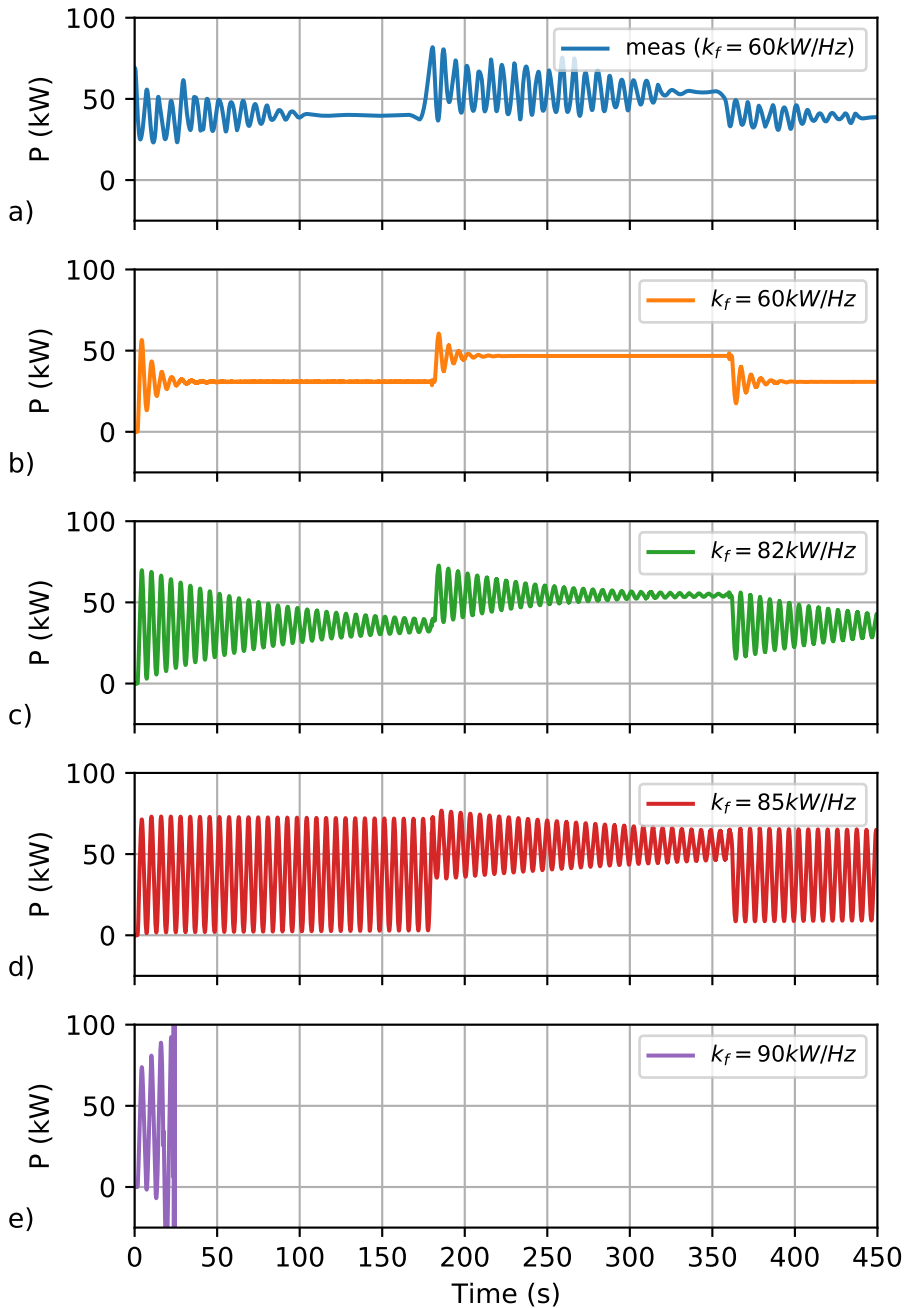
Figure 112 – Parallel operation of genset and GSU. Droop factor variation by simulation. a) measurement result (for $k_f = k_{f,GEN} = k_{f,GSU} = 60kW/Hz$); b) simulation for $k_f = 60kW/Hz$; c) simulation for $k_f = 82kW/Hz$; d) simulation for $k_f = 85kW/Hz$; e) simulation for $k_f = 90kW/Hz$.

6.3 Secondary Control for Active and Reactive Power Sharing

The secondary control concept for active and reactive power described in section 4.2 is analyzed by numeric grid simulation. Fig. 113 shows the corresponding SLD of the investigated islanded microgrid.
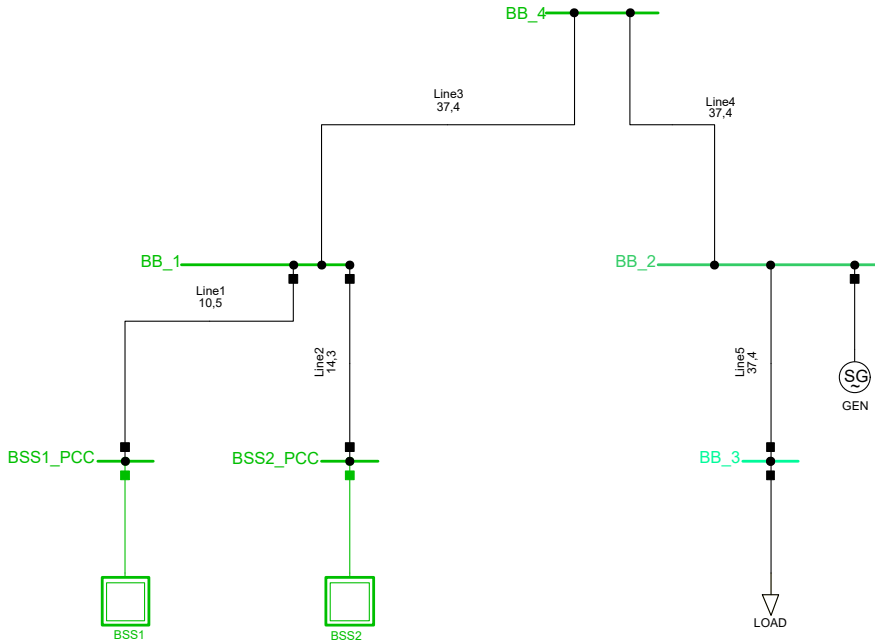
Figure 113 – SLD of the investigated grid for secondary control simulations.

Two BSSs (BSS1, BSS2) and a genset (GEN) are connected by LV cables (Type NAY2Y 4x150mm^2 as described in section 3.1) to an aggregated load (LOAD). The cable lengths used for the following simulations are summarized in Table 11.

Table 11 – Grid configuration for secondary control simulations.

Line	Length
Line1	$20m$
Line2	$20m$
Line3	$38m$
Line4	$94m$
Line5	$172m$

The droop control configuration of the assets BSS1, BSS2 and GEN is shown in Table 12. Table 13 presents the MGC configuration with all relevant parameters.

In this work, three different configurations of active GFUs are investigated (Table 14). For each variant, four different sub-scenarios (A...D) with different controller configurations are investigated and compared (Table 15).

In sub-scenario *A*, only droop control is active (no secondary control). Sub-scenario *B* shows the simulated results for a MGC considering APC, RPC and VLC where no ICT delays are considered, whereas sub-scenario *C* takes ICT delays into account ($\tau_{ICT,meas} = 0.25s$

Table 12 – Simulation parameters of droop control for assets BSS1, BSS2 and GEN.

Parameter	BSS1	BSS2	GEN
$k_f\ (kW/Hz)$	300	200	100
$k_V\ (kvar/V)$	10	10	10
$f_{0,ref}\ (Hz)$		50	
$P_{0,ref}\ (Hz)$		0	
$V_{0,ref}\ (V)$		400	
$Q_{0,ref}\ (Hz)$		0	

Table 13 – Simulation parameters for MGC.

	Parameter	Value
APC	k_p	10
	k_i	20
	T_{APC}	0.01
	$k_{APC,BSS1}$	3
	$k_{APC,BSS2}$	2
	$k_{APC,GEN}$	1
RPC	T_{RPC}	0.01
	$k_{p,BSS1}$	1
	$k_{i,BSS1}$	5
	$k_{p,BSS2}$	1
	$k_{i,BSS2}$	5
	$k_{p,GEN}$	1
	$k_{i,GEN}$	5
	$k_{RPC,BSS1}$	1
	$k_{RPC,BSS2}$	1
	$k_{RPC,GEN}$	1
VLC	T_{VLC}	0.01
	k_p	0
	k_i	1

Table 14 – Scenario definition of active assets for secondary control modeling.

Scenario	BSS1	BSS2	GEN
1	✓	✓	-
2	✓	-	✓
3	✓	✓	✓

and $\tau_{ICT,set} = 0.25s$). In sub-scenario D, the local RPC as a modified controller structure is investigated where the closed-loop part of the RPC is installed directly at the asset. As a result, no dead time occurs within the closed loop PI control circuit, which leads to reduced dynamics.

Scenario 1

In scenario 1, the parallel operation of two inverter-based BSSs is investigated. Fig. 114

Table 15 – Overview of sub-scenarios for secondary control modeling.

Sub-Scenario	MGC	$\tau_{ICT,meas}$	$\tau_{ICT,set}$	RPC Central	Local	Comment
A	-	0s	0s	-	-	No MGC
B	✓	0s	0s	✓	-	No ICT Delay
C	✓	0.25s	0.25s	✓	-	
D	✓	0.25s	0.25s	-	✓	

illustrates the result of scenario *1B* (MGC operation and no ICT delays) compared with scenario *1A* (only Droop Control, no MGC). In Fig. 114a, the active power distribution for BSS1 and BSS as well as for the total load is shown. As the APC participation factors are equal to the droop factors, the active power distribution is constant, whereas the grid frequency (Fig. 114b) is controlled to the nominal frequency of $50Hz$.

The power factor at the load is set to $\cos\varphi = 1$, which means that $Q_{load} = 0$. Due to voltage droop control with constant voltage setpoints, an exchange of reactive power between GFUs occurs depending on the power. By using MGC (especially RPC), reactive power supply (resp. consumption) of the GFUs is minimized. As the LV cables have a small demand of reactive power (see section 3.1), the resulting reactive power is divided equally (as $k_{RPC,BSS1} = k_{RPC,BSS2} = 1$ in this investigation).

Further, the MGC – especially the VLC – is configured for constant voltage at the load. The result, including comparison to scenario *1A*, is shown in Fig. 114d.

In scenario *1C*, the ICT delay is considered. In distributed energy systems in combination with low-bandwidth communication and eventually protocol converters, a delay of $\tau_{ICT,meas} = 0.25s$ for receiving data and $\tau_{ICT,set} = 0.25s$ for sending data is investigated. A complete dead time of $0.5s$ is not chosen as extremely high; in practical systems with protocol converters and/or further control loops, also greater dead times can occur. The results – again compared to scenario *1A* – are shown in Fig. 115. It can be seen that the active power distribution (Fig. 115a) and the frequency (Fig. 115b) behavior are not affected by the set of controller parameters chosen in this investigation (see Table 13). For reactive power, a damped oscillation between both BSSs can be seen (Fig. 115c). The voltage control is not affected by considering the delay.

In the last investigation regarding scenario 1, the closed-loop part of the RPC is now implemented directly on the asset level (scenario *1D*). Therefore, the closed-loop PI controllers for each GFU are not affected anymore by the delays $\tau_{ICT,meas}$ and $\tau_{ICT,set}$. This leads to a stable operation of the islanded microgrid using MGC with the same controller parameters. The simulation results are illustrated in Fig. 116.

Scenario 2

On the lines of the investigations in scenario 1, the parallel operation of one BSS and one genset is investigated in scenario 2. The following figures show the results of simulations without ICT delays (Fig. 117), with ICT delay and centralized RPC (Fig. 118) and with ICT delay and decentralized RPC (Fig. 119). It can be seen that the dynamics of the system regarding power distribution is reduced in comparison to a system which is set up only with power electronics if no MGC is used. Due to high dynamics of the BSS in comparison to a genset, a fast response regarding frequency control (by APC) is obtained (Fig. 117b). The reactive power flow between the GFUs is reduced due to RPC control as well (Fig. 117c). Also, voltage stabilization at the load node is implemented successfully.
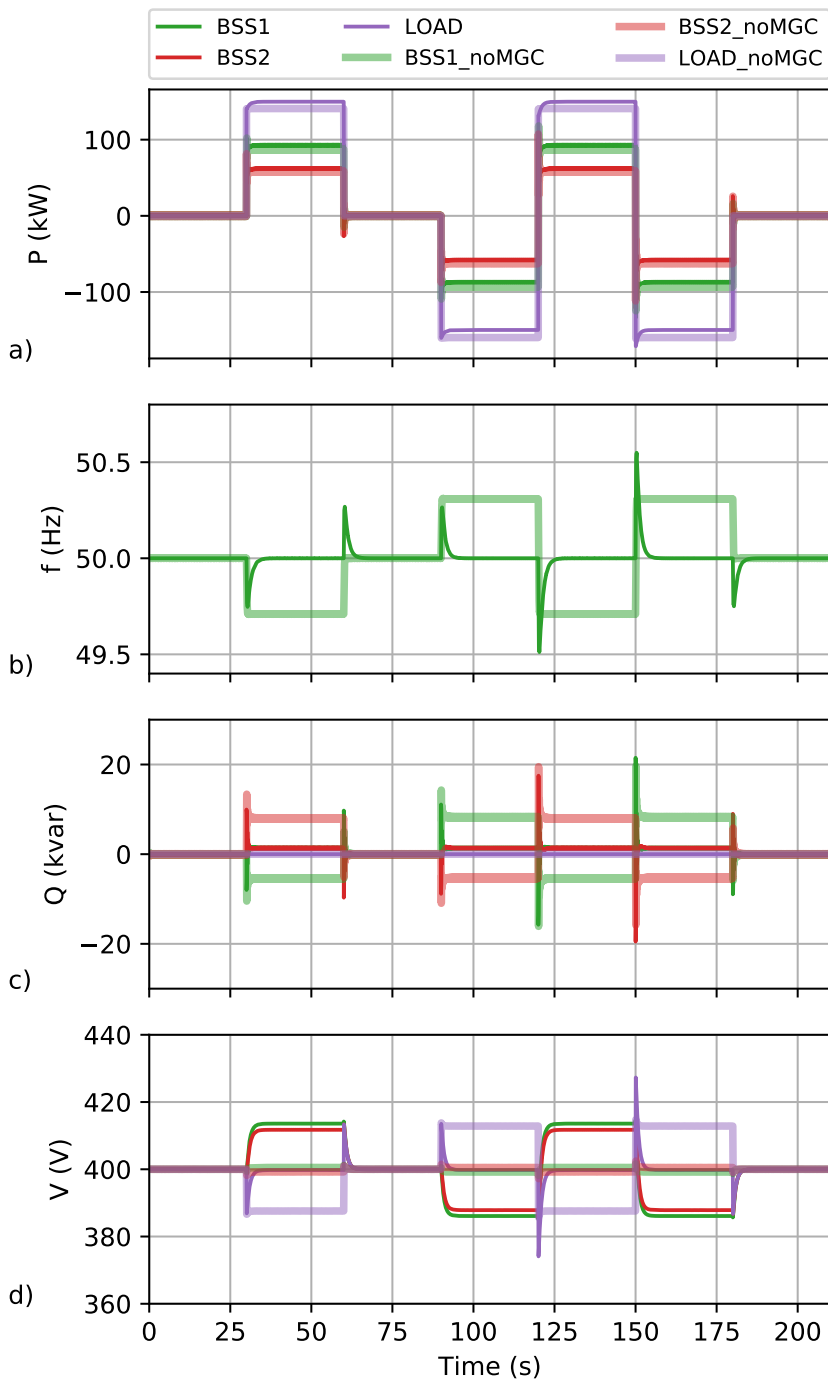
Figure 114 – Secondary control (scenario 1). Comparison of scenario 1B (MGC) with 1A (no MGC). a) active power at BSS1 (green), BSS2 (red) and LOAD (violet); b) grid frequency; c) reactive power distribution; d) grid voltage.
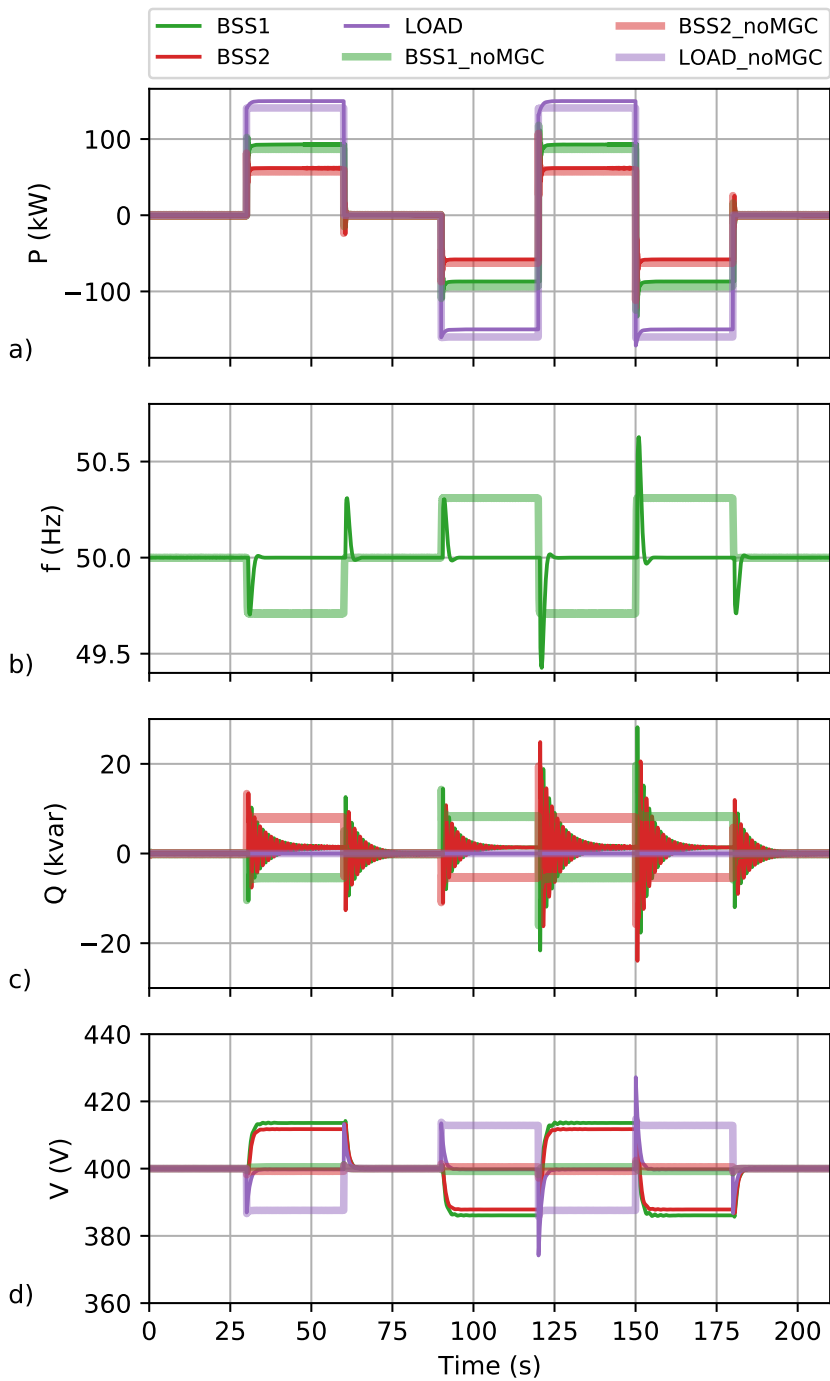
Figure 115 – Secondary control (scenario 1). Comparison of scenario 1C (MGC and ICT delays) with 1A (no MGC). a) active power; b) grid frequency; c) reactive power distribution; d) grid voltage.
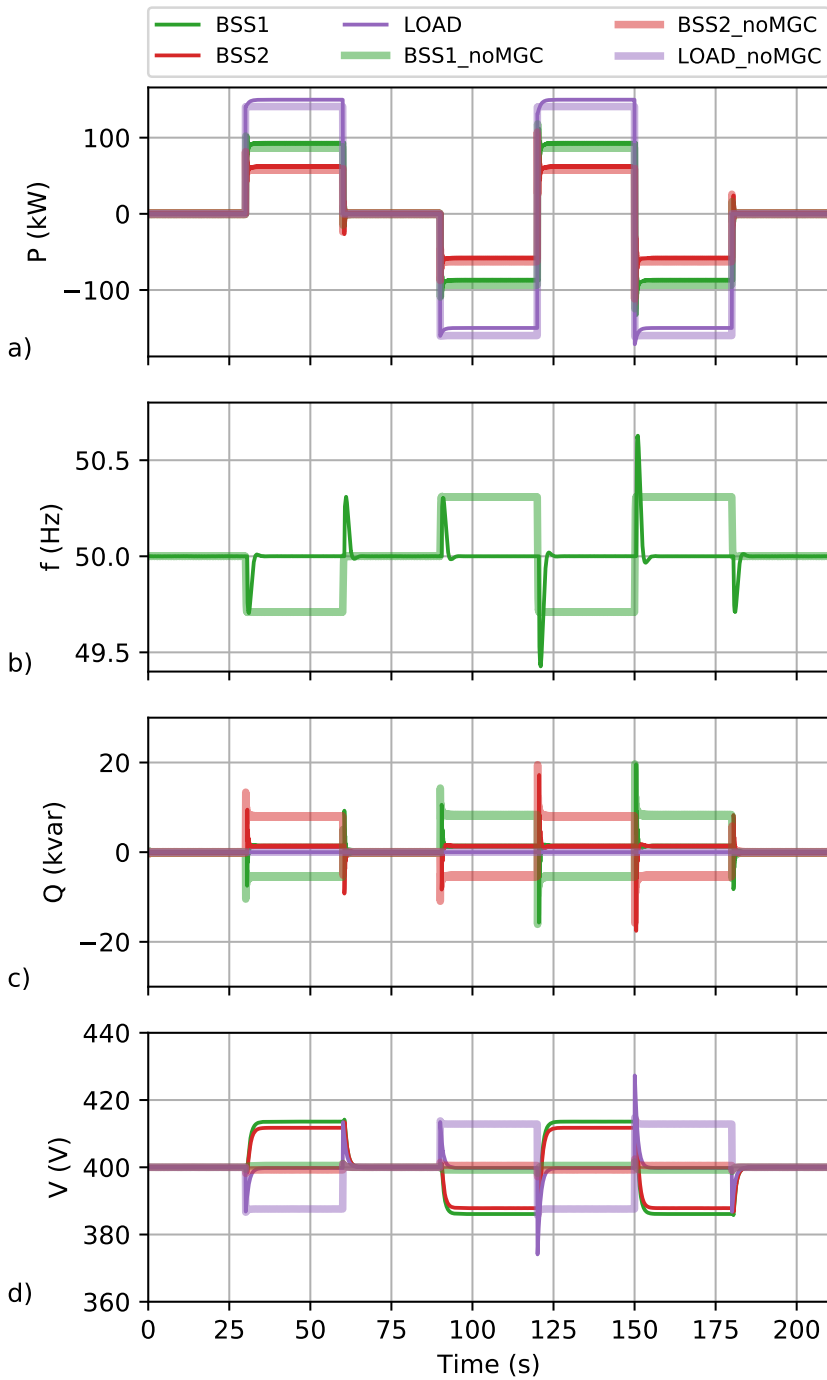
Figure 116 – Secondary control (scenario 1). Comparison of scenario 1D (MGC with ICT delays and local RPC) with 1A (no MGC). a) active power; b) grid frequency; c) reactive power distribution; d) grid voltage.
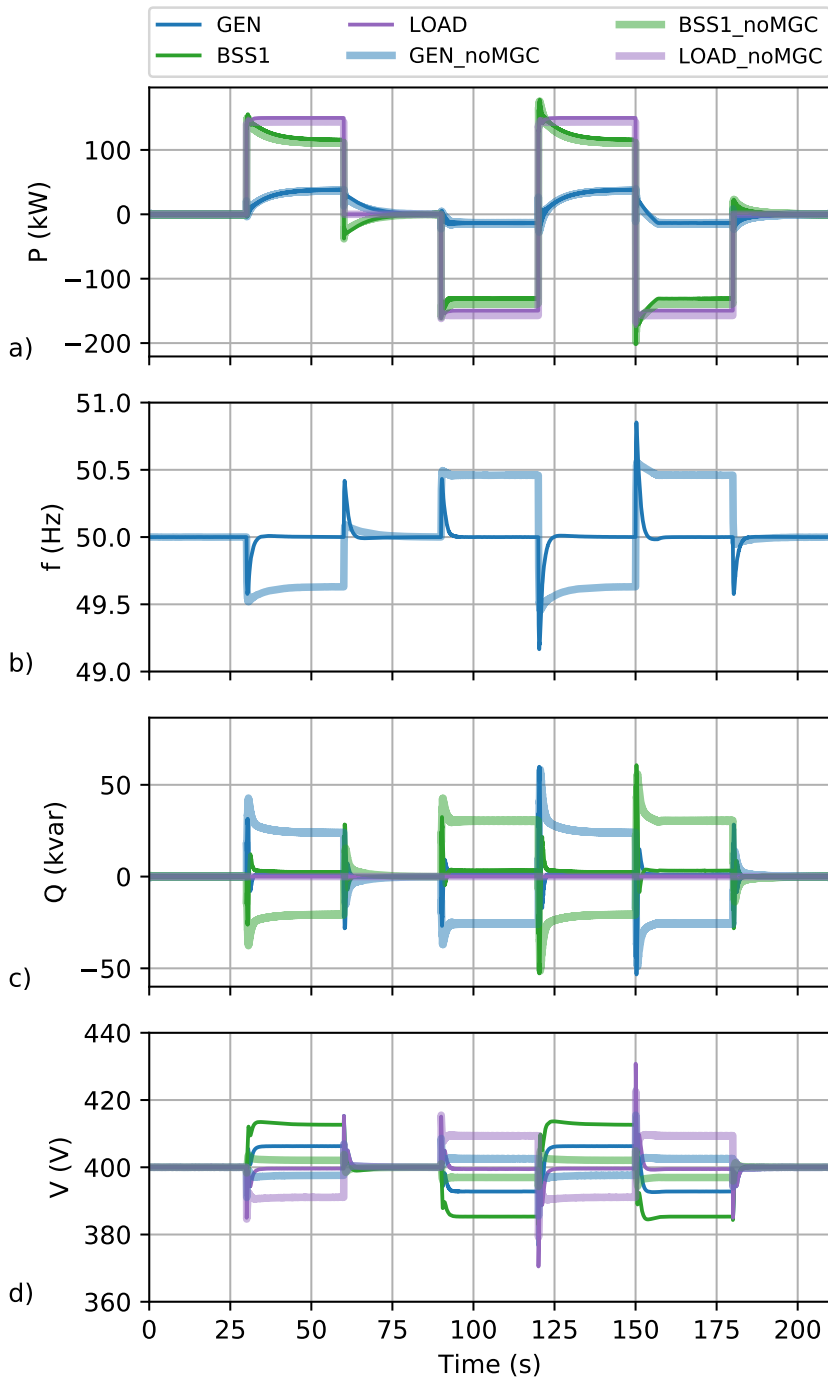
Figure 117 – Secondary control (scenario 2). Comparison of scenario 2B (MGC) with 2A (no MGC). a) active power at GEN (blue), BSS1 (green) and LOAD (voilet); b) grid frequency; c) reactive power distribution; d) grid voltage.

A consideration of ICT delays regarding Table 15 leads to oscillations (Fig. 118). Local implementation of the closed-loop part of the RPC maintains stabilization of the system (Fig. 119).

Scenario 3

In scenario 3, the investigations from scenarios 1 and 2 are repeated for an island grid consisting of two BSSs and one genset. The results shown in Figs. 120-122 are comparable with those of the previous scenarios. That means in detail that in scenario 3A, no MGC is active, which leads to an active power distribution based on droop control configuration. Scenario 3B analyzes the usage of an MGC without ICT delays (Fig. 120). Scenario 3C investigates the behavior of 3 GFUs in parallel with a MGC under consideration of ICT delays regarding Table 15. The reactive power and voltage are oscillating (Fig. 121).

As in the scenarios before, local implementation of the RPC leads again to stable conditions (Fig. 122).

Discussion of the Scenarios

It was shown by simulation that a central approach to secondary control is working for island grids with more than one GFU, whereas different combinations between inverter-based systems and direct coupled generators were investigated.

In practical applications with distributed assets connected by low-bandwidth ICT, it is suggested to implement one part of the RPC directly on the assets' side and not central. This leads to higher dynamics of the used controllers and an improved system stability.

The stability criteria of this system are not considered in this work analytically. For practical application, one method is setting up a simulation model based on the algorithms described in this work and the determination of stable control parameters.

Core Statements:

1. Frequency is controlled to rated value (in steady state).

2. Reactive power exchange between GFUs and GSUs can be avoided by the usage of MGC.

3. Voltage level at defined node is controlled to a setpoint.

4. Signal runtimes (transportation delays) due to ICT has to be considered.

5. Local RPC improves stability and resilience caused by delays.
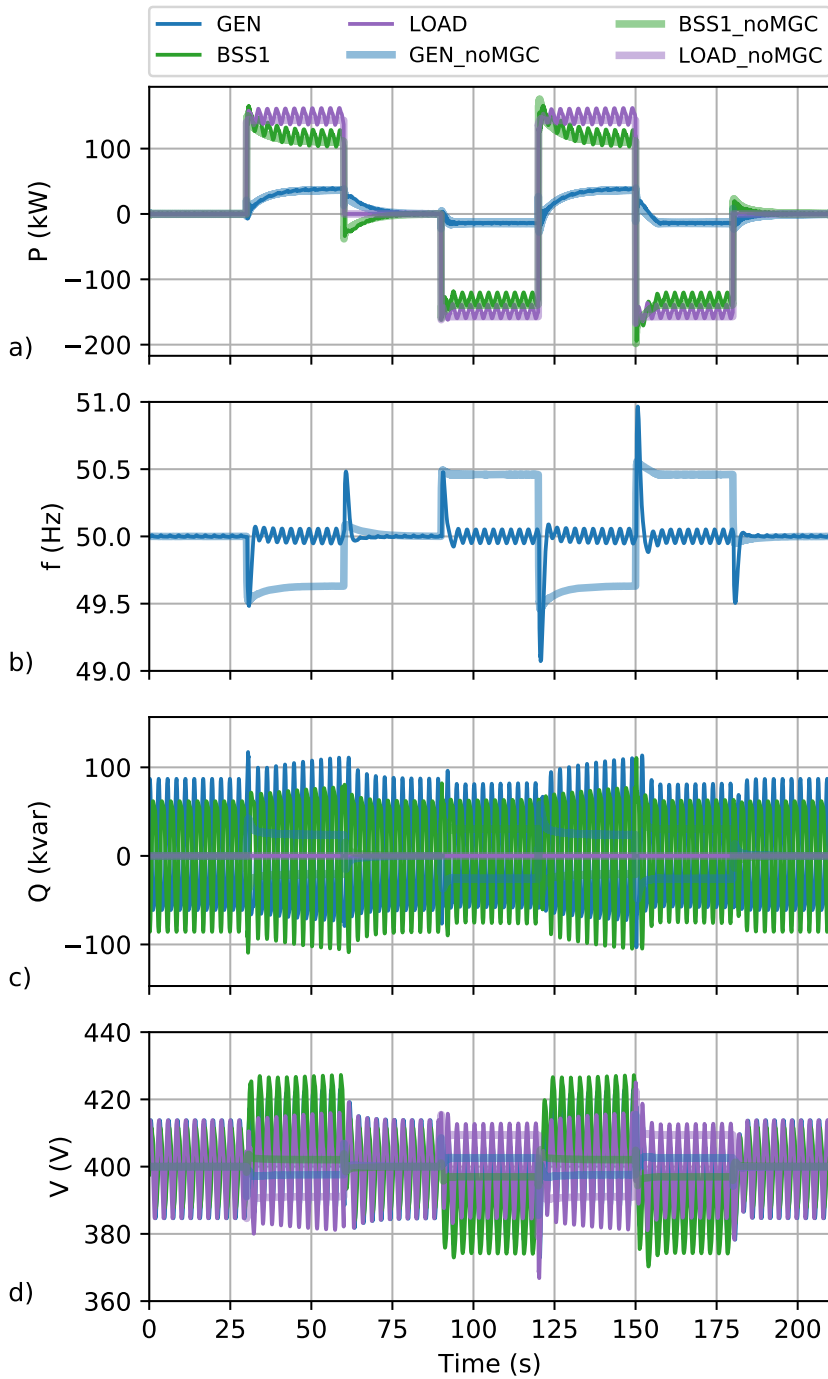
Figure 118 – Secondary control (scenario 2). Comparison of scenario 2C (MGC and ICT Delays) with 2A (no MGC). a) active power; b) grid frequency; c) reactive power distribution; d) grid voltage.
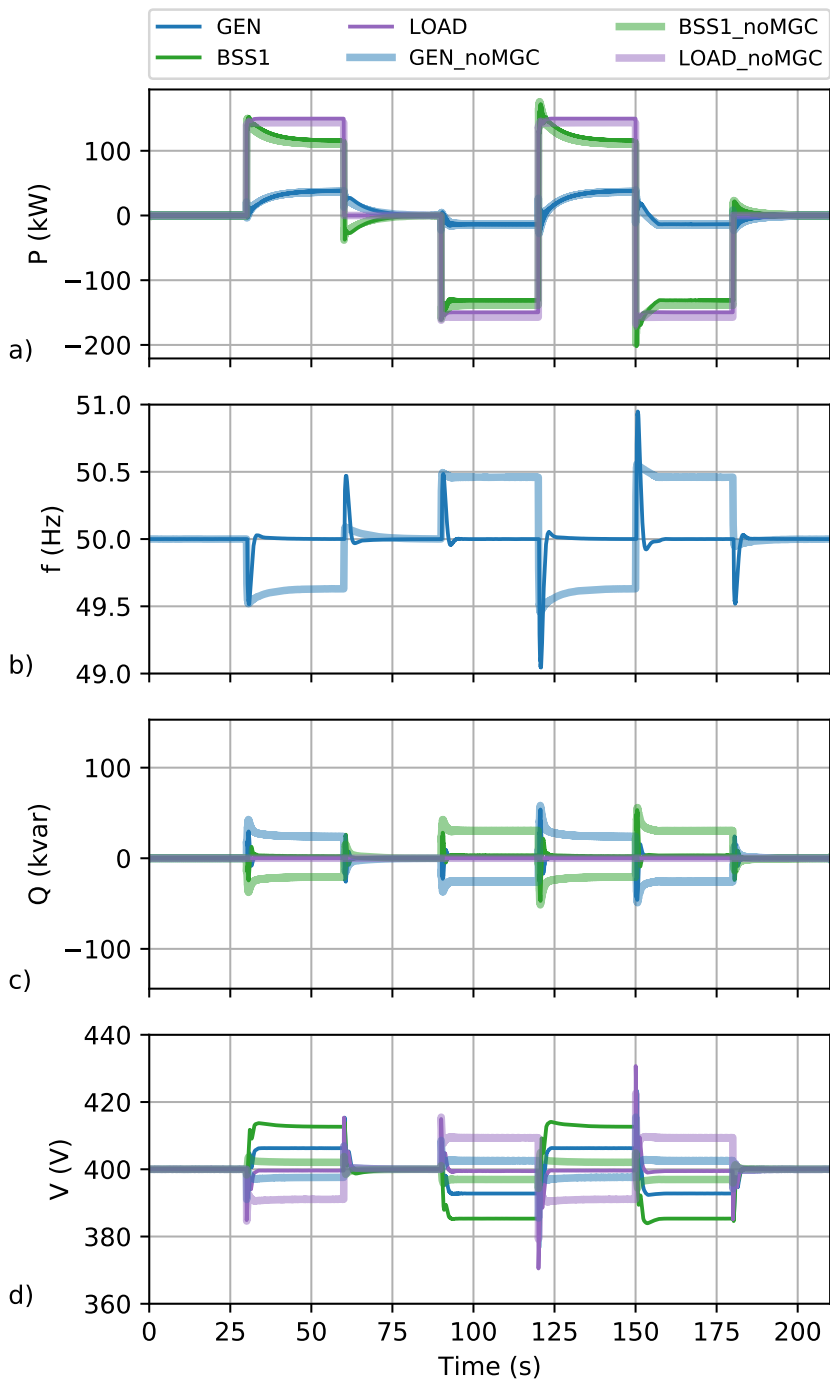
Figure 119 – Secondary control (scenario 2). Comparison of scenario 2D (MGC with ICT delays and local RPC) with 2A (no MGC). a) active Power; b) grid frequency; c) reactive power distribution; d) grid voltage.
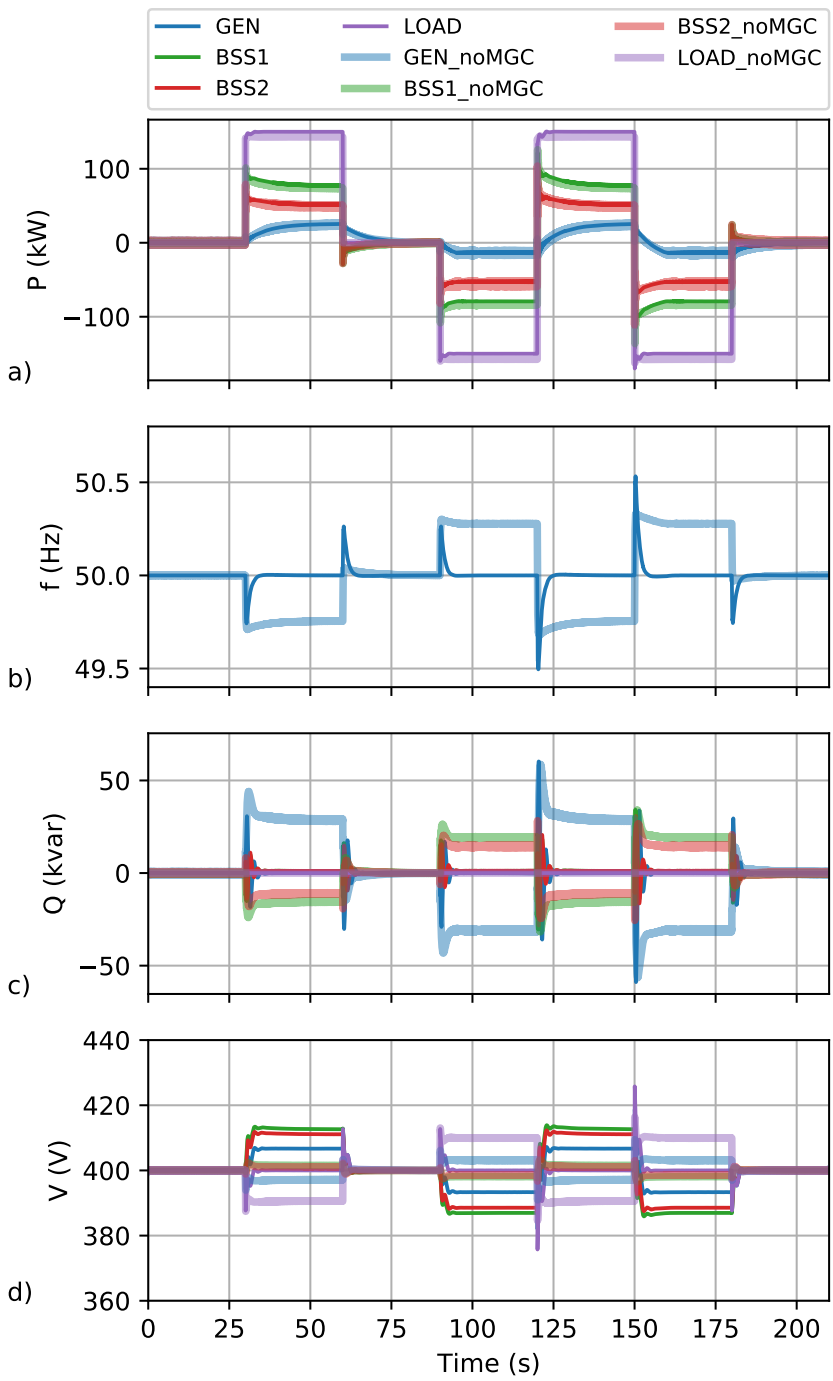
Figure 120 – Secondary control (scenario 3). Comparison of scenario 3B (MGC) with 3A (no MGC). a) active power at GEN (blue); BSS1 (green) and LOAD (violet); b) grid frequency; c) reactive power distribution; d) grid voltage.
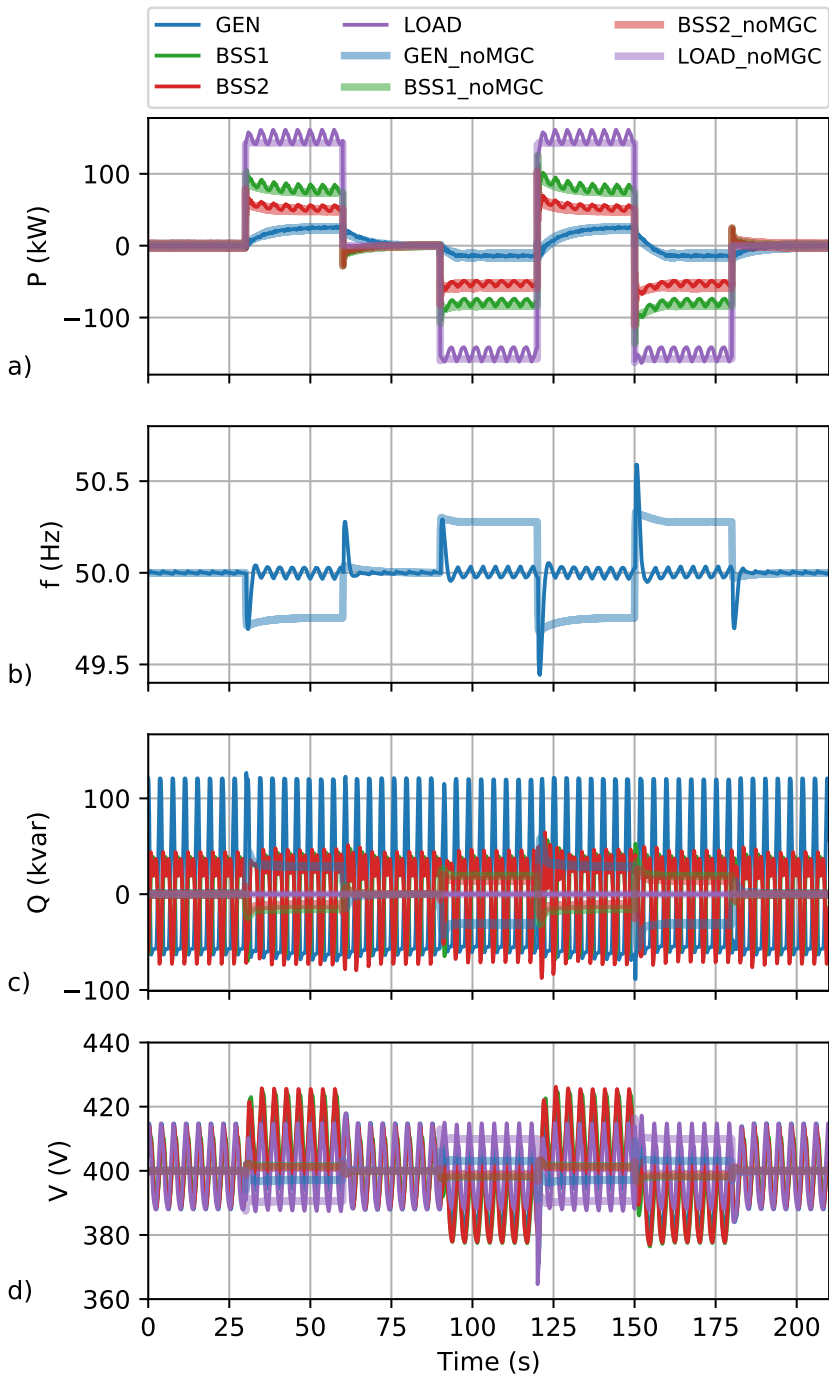
Figure 121 – Secondary Control (Scenario 3). Comparison of Scenario 3C (MGC and ICT delays) with 3A (no MGC). a) Active Power. b) Grid Frequency. c) Reactive Power Distribution. d) Grid Voltage.
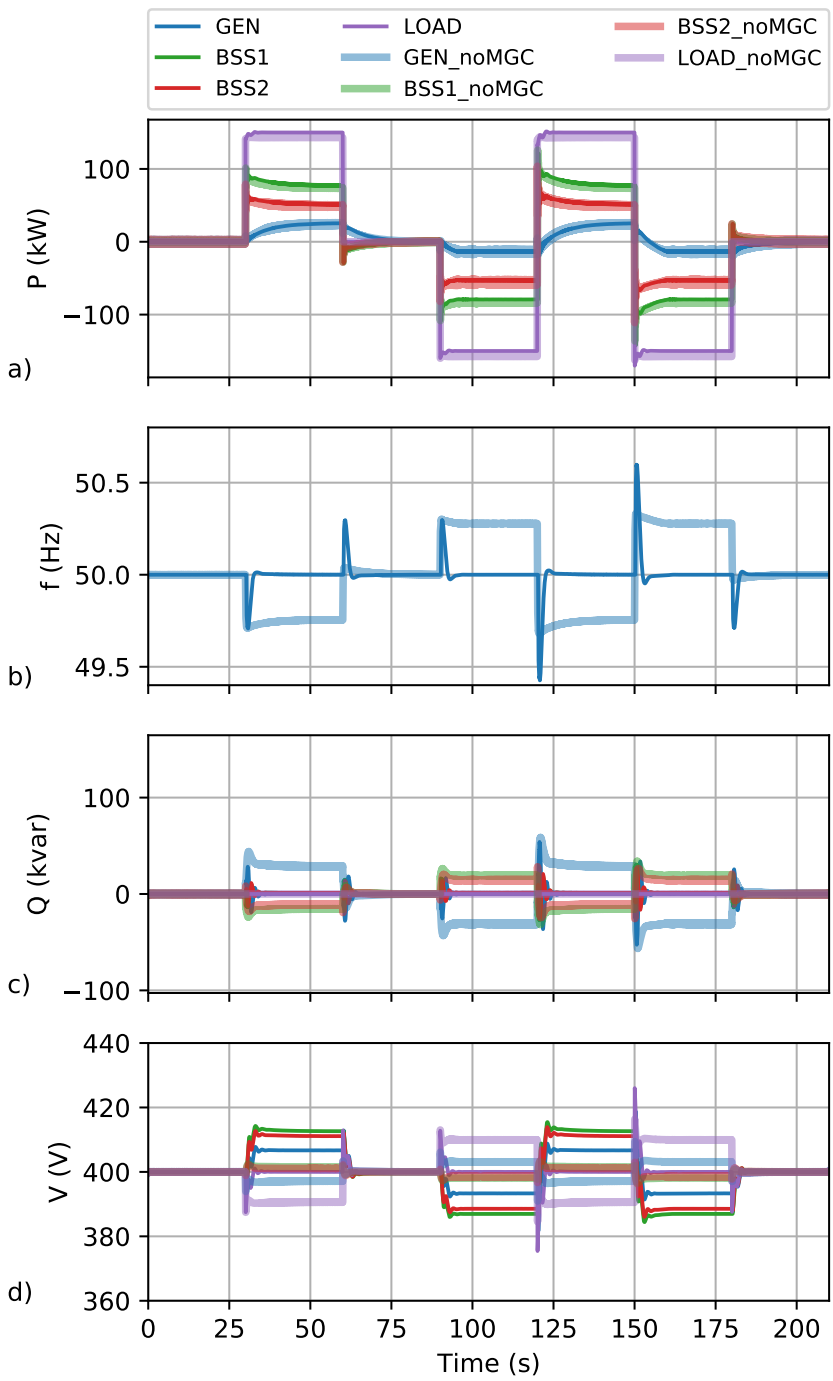
Figure 122 – Secondary control (scenario 3). Comparison of scenario 3D (MGC with ICT delays and Local RPC) with 3A (no MGC). a) active power; b) grid frequency; c) reactive power distribution; d) grid voltage.

6.4 Energy Scheduling for BSS

The concept of load sharing described in 4.3 based on SOE scheduling is simulated for several scenarios. An island grid presented in Fig. 55 is assumed. The parameters for BSS are given in Table 16.

The scheduling algorithm is based on the prediction for load $P_{load}(t)$ and for DG $P_{DG}(t)$. A day-ahead prediction with a time step of 15 minutes is assumed for a period of 24 hours. This leads to 96 values per day. Due to the generic structure of the concept, also other time steps and periods could be used.

Table 16 – BSS simulation parameters.

Parameter	Value
Total Energy Capacity	165kWh
Max. State of Energy	0.8
Min. State of Energy	0.2
Initial SOE	0.3

The assumed load curve P_{load} based on the German standard load profile H0 (for households) for an annual electricity demand of approx. 560MWh (inside the island grid) is shown in Fig. 123a.

The DG power P_{DG} is assumed for four different scenarios (Fig. 123b). In scenario 1, the DG is assumed as a PV plant at a sunny day, whereas scenario 2 shows a PV plant at a day with a mixture between sun and clouds. Scenario 3 is assumed with constant clouds (or lower installed DG capacity) and finally, scenario 4 shows a sunny day with high DG.
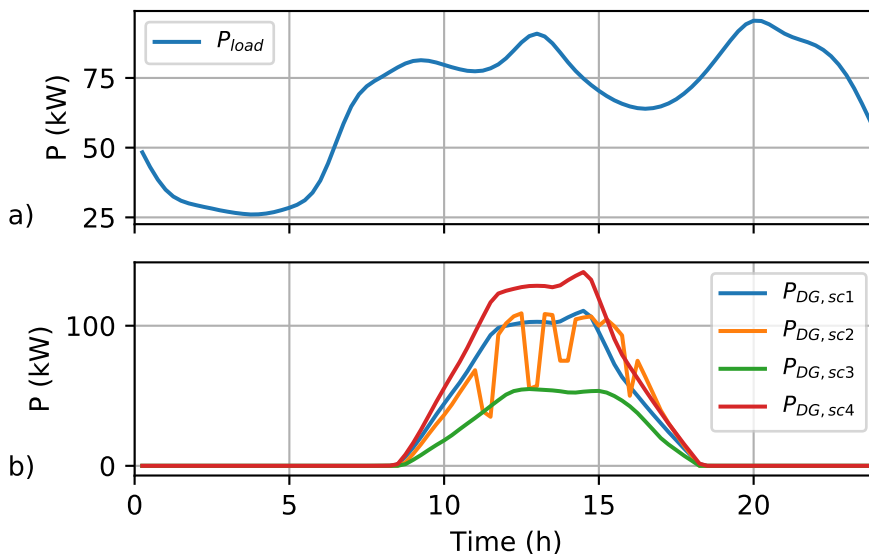
Figure 123 – Simulation input data. a) assumed load curve for 24h based on H0 standard load profile; b) four different scenarios (sc1…sc4) for the DG curve for 24h.

An overview of the assumed DG characteristics (total energy resp. maximum active power) for each scenario is shown in Table 17.

Table 17 – DG characteristics of investigated scenarios and load configuration.

Scenario	Total Energy (kWh)	Max. Active Power (kW)
1	631.2	110.6
2	592.9	108.9
3	333.7	54.8
4	789.0	138.3
Load	1575.8	95.5

The residual power $P_{res}(t) = P_{load}(t) - P_{DG}(t)$ has to be covered by BSSs and gensets. In the following, the results of scenarios 1...4 are presented.

6.4.1 Scenario 1

First, a scenario with DG at a sunny day is investigated.

The residual power P_{res} as the difference between DG and load is shown in Fig. 124a. It can be seen that in the time range between 11h and 16h, the resulting power $P_{res} < 0$ as the DG power is higher than the load; hence the BSS has to be charged and the genset is out of operation ($P_{GEN} = 0$).

The complete time series for P_{BSS} and P_{GEN} is shown in Fig. 124b.

In the time range from 0h to 11h, the BSS is discharged with a load sharing factor of $k_{BSS} = 0.04$ in order to reach $SOE_{min} = 0.2$ at the beginning of the charging phase. This load sharing factor means that 96% of the power is delivered by the genset whereas 4% are supplied by the BSS.

In the charging period (approx. between 11h and 16h), the BSS is charged from $SOE = 0.2$ to $SOE = 0.7$; the gensets do not deliver active power.

In the next period (approx. 16h to 24h), the BSS is discharged with a load sharing factor of $k_{BSS} = 0.12$ (that means 12% of P_{res}) to reach again the initial $SOE = 0.3$ at the end of the time period.

The resulting SOE curve for scenario 1 is shown in Fig. 124c.
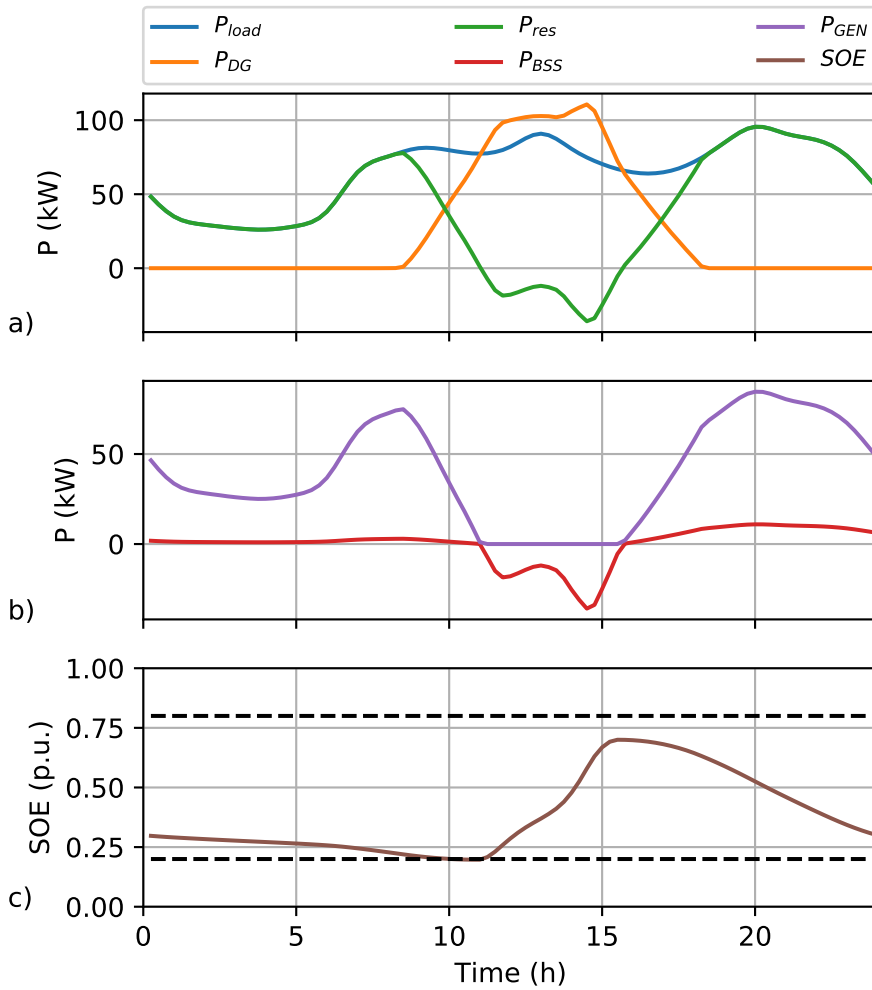
Figure 124 – Results of scenario 1. a) active power for load (blue), DG (orange) and residual load (green); b) active power for BSS (red) and GEN (purple); c) resulting SOE (brown).

6.4.2 Scenario 2

For scenario 2, a fluctuating DG power is assumed, which can be caused by the volatile behavior of PV systems located close together at a sunny day with clouds. The corresponding fluctuating residual power P_{res} is shown in Fig. 125a.
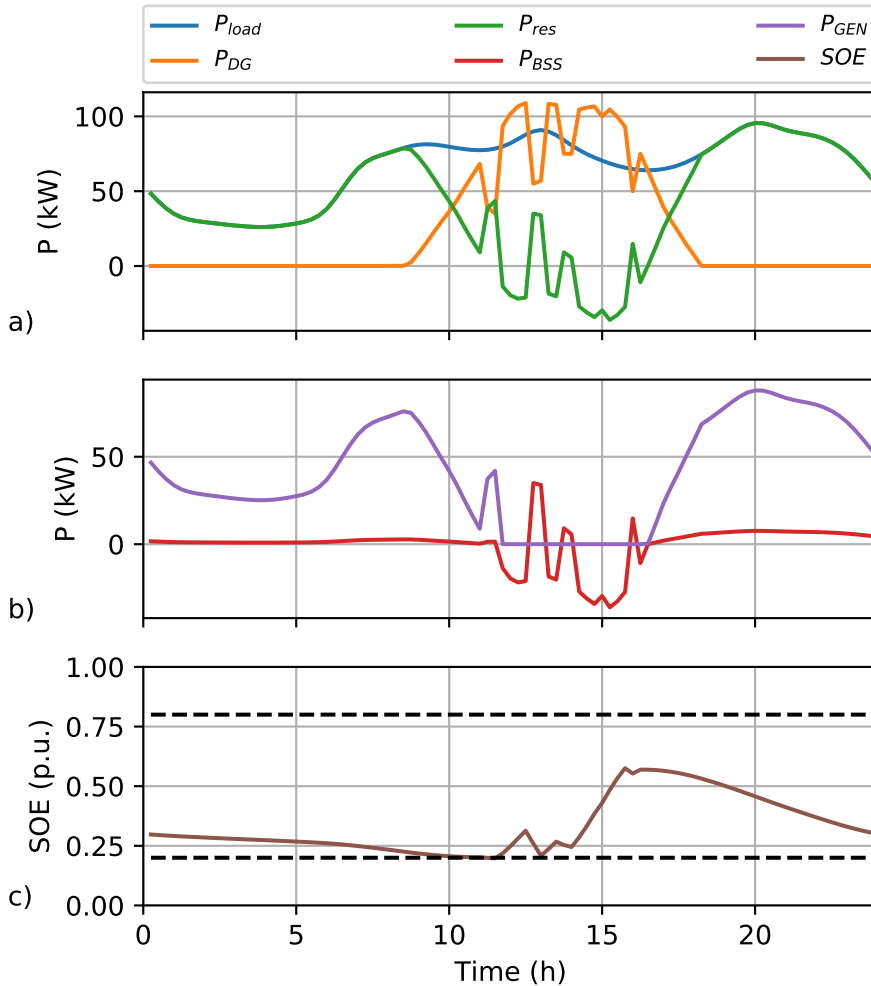
Figure 125 – Results of scenario 2. a) active power for load (blue), DG (orange) and residual load (green); b) active power for BSS (red) and GEN (purple); c) resulting SOE (brown).

The results of the load sharing algorithm are presented in Fig. 125b. It can be seen clearly that the power fluctuation due to volatile DG (in the interval between 12.5.h and 16h) is covered completely by the BSS whereas the genset is off. The resulting SOE is shown in Fig. 125c. It can be seen that the DG can be used completely and no feed-in limitation is needed as the SOE is in the range between $0.2 < SOE < 0.58$.

6.4.3 Scenario 3

In scenario 3, the electrical load is always higher than the power feed-in by DG (Fig. 126a). Thus, the residual power P_{res} is always positive. Therefore, the BSS is not used for load sharing ($P_{BSS} = 0$); the load is completely covered by DG and gensets. The results for P_{gen} and SOE are shown in Fig. 126b resp. Fig. 126c.

Nevertheless, the BSS can be used to cover fast load changes in the frame of droop control. For energy scheduling in the frame of secondary control, the BSS is be considered.
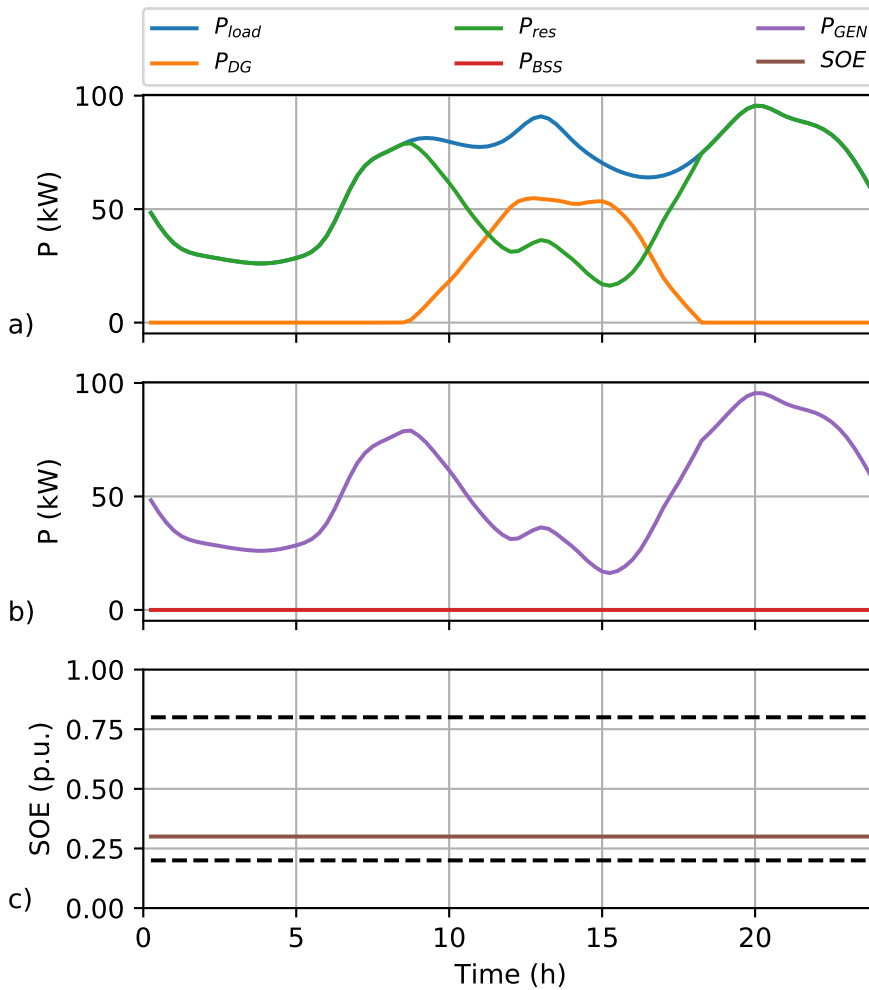
Figure 126 – Results of scenario 3. a) active power for load (blue), DG (orange) and residual load (green); b) active power for BSS (red) and GEN (purple); c) resulting SOE (brown).

6.4.4 Scenario 4

The fourth scenario deals with a high DG feed-in (Fig. 127). Fig. 127c shows that SOE limit is exceeded as the BSS capacity is not sufficient. It has to be analyzed also in economically terms, which solution will be chosen. For example, a BSS with higher energy capacity, the usage of further loads (such as P2H systems) or a de-rating of DG feed-in are mentioned as solutions.
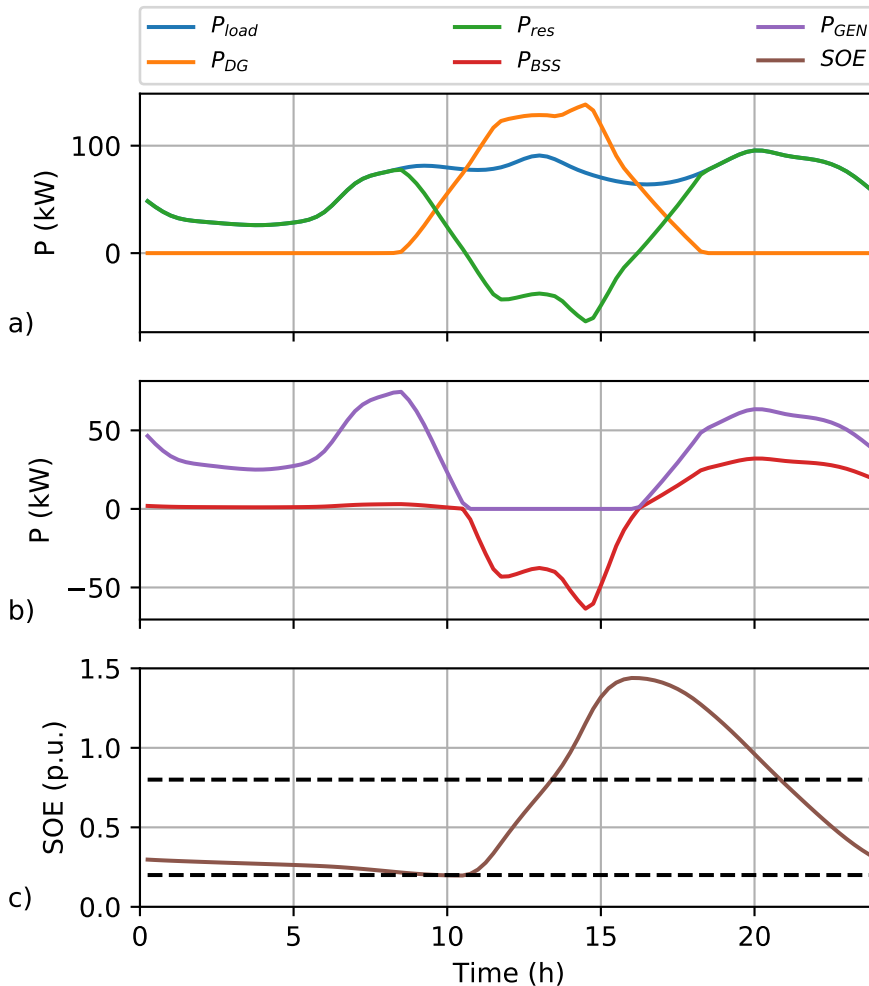
Figure 127 – Results of scenario 4. a) active power for load (blue), DG (orange) and residual load (green); b) active power for BSS (red) and GEN (purple); c) resulting SOE (brown).

It can be pointed out that the concept presented in this section is fundamental for energy scheduling for small island grids based on load sharing prediction. The concept is basing on a fast analytical method to maximize the DG feed-in due to SOE scheduling.

6.5 Failsafe Control Concept Without Communication System

The failsafe control concept without a communication system is designed separately for active power/frequency and reactive power/voltage control (section 4.6).

In this part, first, the active power/frequency control is verified by specific simulations. In the second part, simulation results for the reactive power/voltage control are shown.

6.5.1 Active Power Control

The failsafe control for active power is evaluated by simulation for an island grid as shown in Fig. 128. The aggregated load P_{load} as well as the distributed generation P_{DG} are considered. The resulting residual load $P_{res} = P_{load} - P_{DG}$ is the difference between the load and the DG and has to be covered by the assets – in this case, BSS1, BSS2 and GEN.
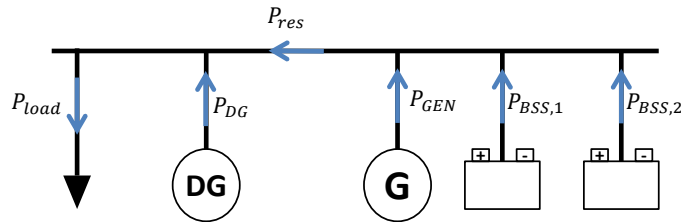
Figure 128 – SLD for simulation of failsafe active power control.

The decentralized active power control is configured regarding Tables 18 and 19.

Table 18 – Asset configuration of failsafe active power control.

Asset	Parameter	Value	Description
BSS1	k_f	$200kW/Hz$	Frequency Droop Factor
	$f_{0,BSS1}$	$50Hz$	Frequency Setpoint
	k_p	1	Proportional Gain PI Controller
	k_i	5	Integration Gain PI Controller
	E_{max}	$80kWh$	Total Battery Capacity
	SOE_0	0.3	Initial State of Energy
BSS2	k_f	$200kW/Hz$	Frequency Droop Factor
	$f_{0,BSS2}$	$50Hz$	Frequency Setpoint
	k_p	1	Proportional Gain PI Controller
	k_i	5	Integration Gain PI Controller
	E_{max}	$200kWh$	Total Battery Capacity
	SOE_0	0.4	Initial State of Energy
Genset	k_f	$50kW/Hz$	Frequency Droop Factor
	$f_{0,GEN}$	$49Hz$	Frequency Setpoint
	k_p	0	Proportional Gain PI Controller
	k_i	10	Integration Gain PI Controller
	$P_{r,GEN}$	$100kW$	Reference Value for Genset Active Power Control

Parameter	a	b	c	d
$\mu_{SOE,L}$	0	0.001	0.2	0.3
$\mu_{SOE,N}$	0.2	0.3	0.7	0.8
$\mu_{SOE,H}$	0.7	0.8	0.99	1
$\mu_{P,L}$	-9999	-9998	-10	0
$\mu_{P,N}$	-10	0	0	10
$\mu_{P,H}$	0	10	9998	9999

The concept is validated by simulation of two different residual load profiles shown in Fig. 129.
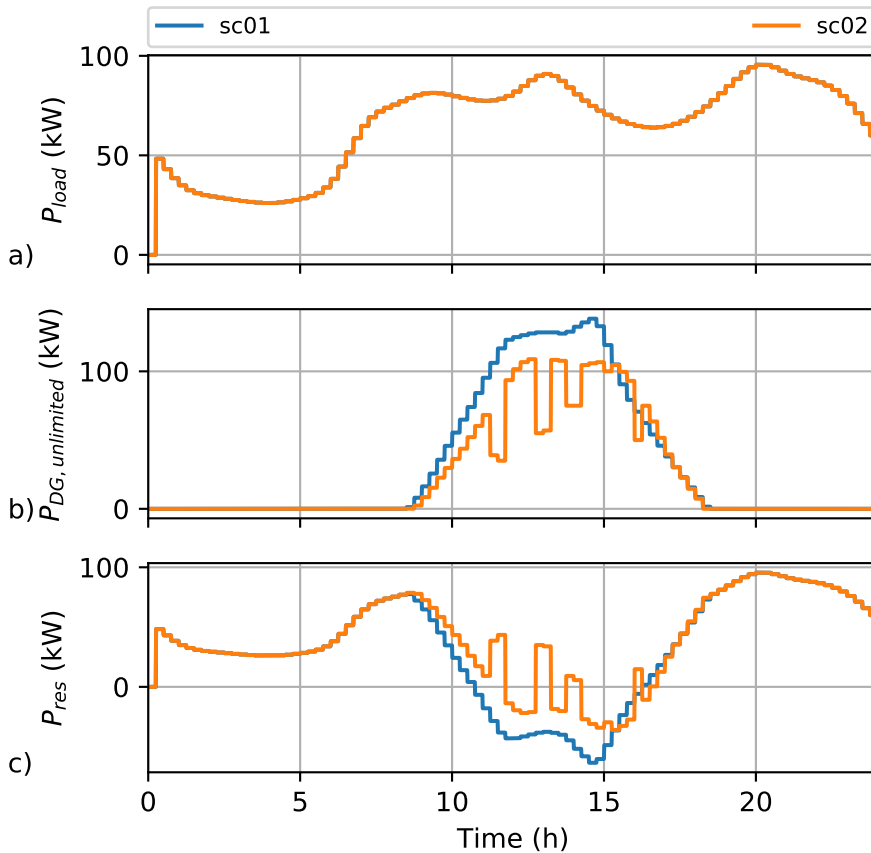
Figure 129 – Scenario definition for failsafe active power control sc01 (blue) and sc02 (orange). a) active power load; b) unlimited distributed generation; c) residual load.

The assumed load for one day is shown in Fig. 129a. The profiles for distributed generation without limitation by VDE AR-N4105 – especially by over-frequency – are shown in Fig. 129b. In the first scenario (sc01), a clear day with a typical PV generation is assumed;

the second scenario (sc02) is considering a lower PV generation with some reductions (e.g., due to clouds). The resulting residual loads P_{res} are shown in Fig. 129c.

The first scenario sc01 is investigated for two different asset setups; at first, one BSS (BSS1) and one genset (GEN) are in operation (sc01a). In the second configuration, also BSS2 is active (sc01b).
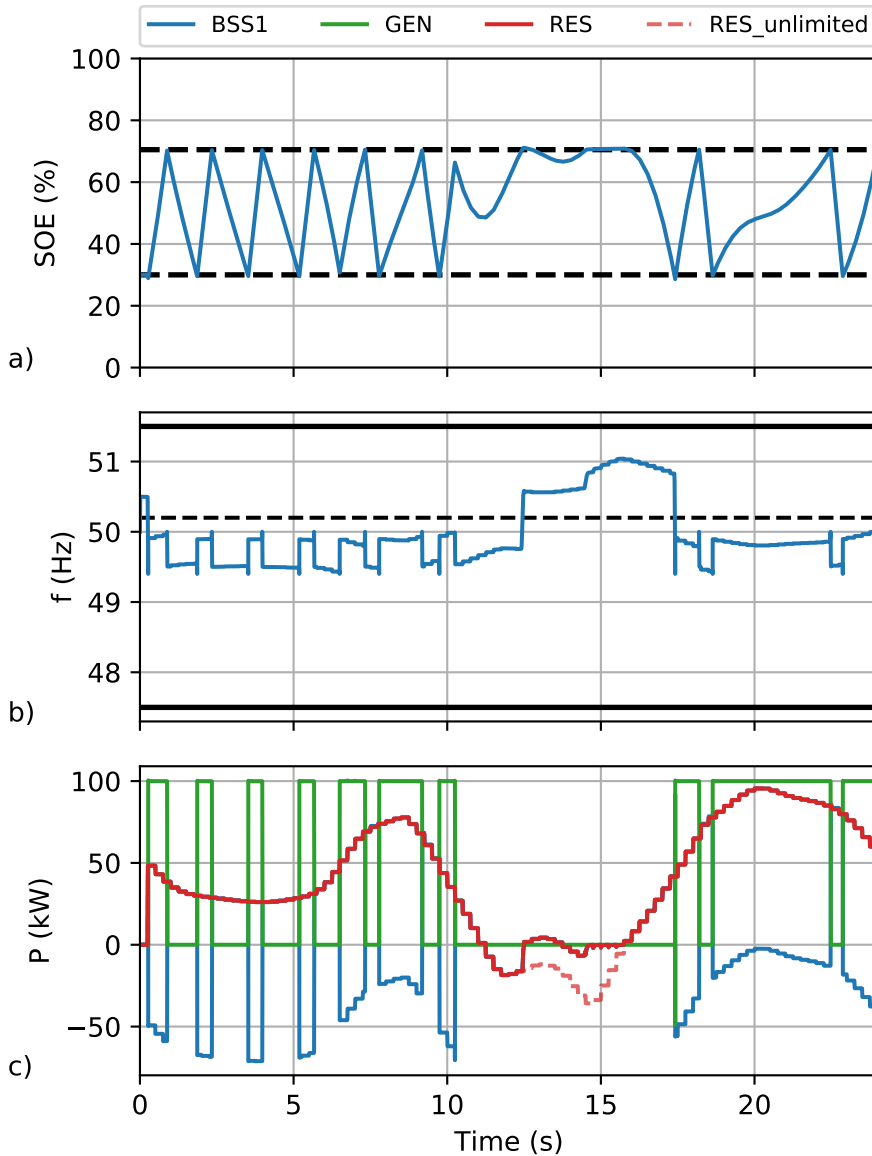
Figure 130 – Failsafe active power control. Simulation results for scenario sc01a with one BSS and genset in parallel (BSS1: blue, genset: green, residual load: red). a) SOE of BSS; b) grid frequency; c) active power.

In Fig. 130a, the resulting SOE is illustrated for sc01a (BSS1, GEN), whereas Fig. 130b

shows the resulting grid frequency. The active power of BSS1 and GEN as well as the residual load (resulting and unlimited) are presented in Fig. 130c.

In the time range from 0 to approx. $11h$, the residual load P_{res} is positive; therefore, the genset is in operation (with constant active power) if the BSS has reached its lower level until the higher limit is reached regarding the fuzzy logic configuration presented in Table 19. Between approx. $11h$ and $12h$, the DG load exceeds the load which means that the residual load is negative and the SOE is charged. At $t \approx 12h$, the SOE has reached the upper limit defined by the fuzzy logic configuration. As all active powers have to be balanced, the grid frequency is increased by the BSS control to reduce the DG feed-in by using VDE AR-N4105 characteristics. In the period from approx. $16h \ldots 17h$, the frequency is still higher than $50.2Hz$ (feed-in reduction criteria from VDE AR-N4105) but the simulated DG feed-in is unlimited. The reason is derived from the VDE AR-N4105 characteristics; the active power feed-in does not have to be reduced to certain percentage in relation to the actual maximum feed-in, but related to the measured active power at the moment when the frequency of $50.2Hz$ is exceeded. In the period $t > 17h$, the grid is operated by a combination of BSS and genset. The DGs are feeding in without limitation as the frequency is below $50.2Hz$ again.

The same scenario regarding load and DG now is repeated with a second BSS in parallel (sc01b). The simulation results are shown in Fig. 131. It can be seen that the grid operation is also stable in the case of two BSS in parallel. Further, an exchange of active power from one BSS to the other is not seen. The main goal of this failsafe strategy is not economic optimization but grid stabilization. In any case, blackout should be avoided.

The result for the second scenario (sc02) is shown in Fig. 132. Also in this case, the grid operation is stable, which is the main goal in failsafe operation, even if the renewable energy is not used completely. In the time range from 0 to $10h$, the BSSs and the genset are operated in parallel whereas the genset is activated at times when the SOE has reached the lower defined limit. In the range until $t \approx 19h$, the two BSSs are controlling the grid in parallel without genset as the SOE is always higher than the minimum SOE. In the range from approx. $19h \ldots 24h$, the genset is in operation as well because the lower SOE limit is reached and no DG feed-in is available. Thus, the BSSs are charged and the grid is supplied by the genset. From the economical and ecological point of view, there could be some room for improvement, which on an individual basis, depends on the corresponding conditions.

However, this is not included in this work; the main goal of a resilient system under failsafe conditions is fulfilled.
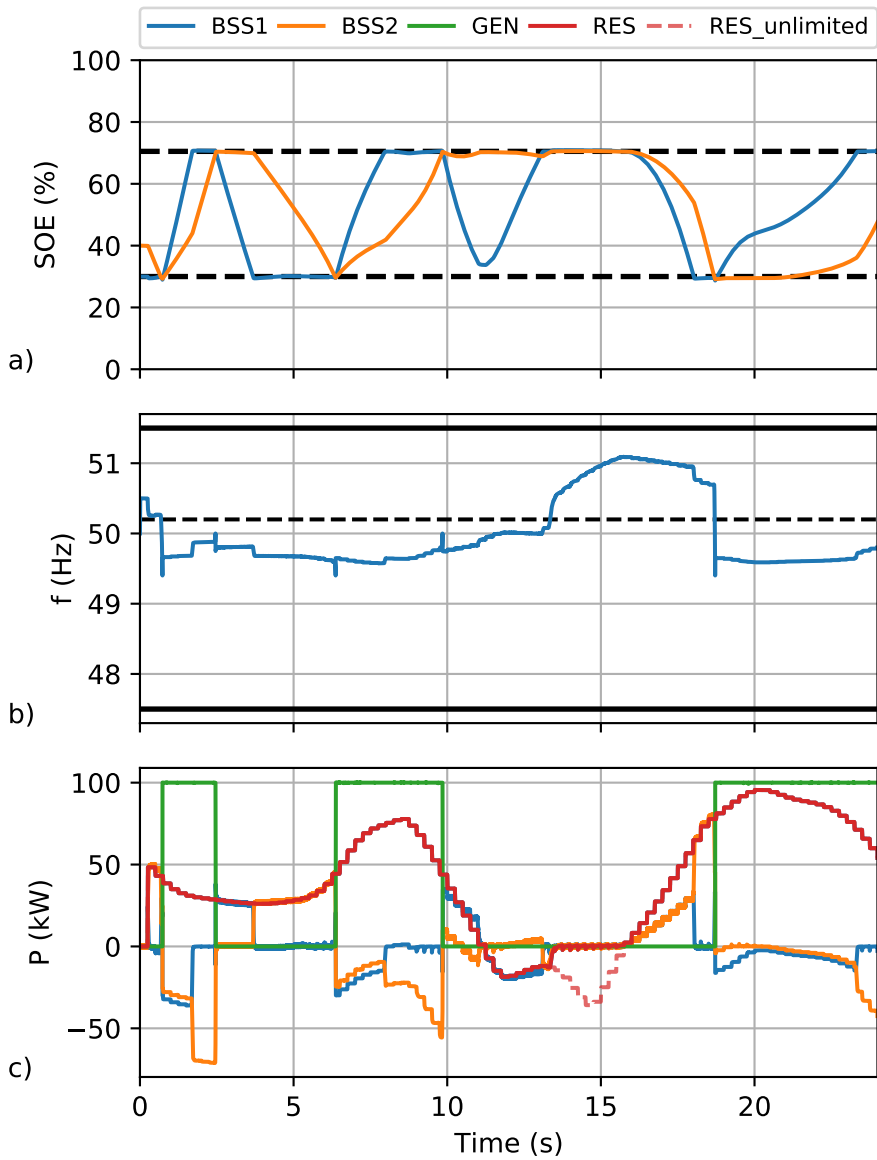
Figure 131 – Failsafe active power control. Simulation results for scenario sc01b. BSS1 (blue), BSS2 (orange), Genset (green), residual load (red) are shown. a) SOE of BSSs; b) Grid Frequency; c) Active Power.
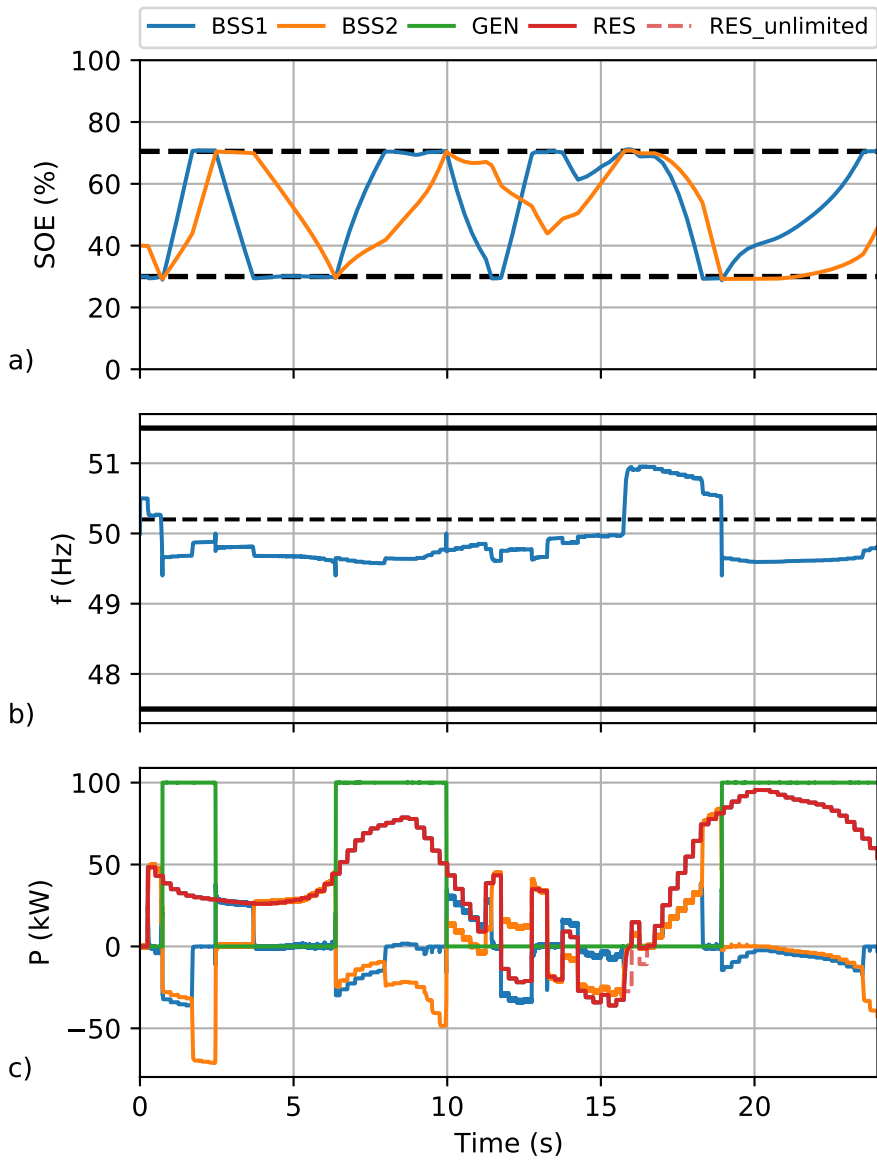
Figure 132 – Failsafe active power control. Simulation results for ccenario sc02. BSS1 (blue), BSS2 (orange), genset (green), residual load (red) are shown. a) SOE of BSSs; b) grid frequency; c) Active Power.

6.5.2 Reactive Power Control

The failsafe control algorithm for voltage and reactive power control explained in section 4.6.2 is evaluated by specific simulations. A grid with three DGs and a load is assumed. The structure is shown in Fig. 133. The line impedance plays an important role in the voltage distribution in LV grids. Cables with type *NAY2Y* and $4x150mm^2$ (modeled in section 3.1) are used in the simulation model. For the verification of the reactive power control, the active power sharing and frequency control are realized by droop control.

Table 20 shows an overview of the electrical parameters of the assumed LV grid.

<div align="center">

Table 20 – Electrical parameters of the lines.

Parameter	Value
Line1 Length	$0.5km$
Line1 Impedance	$0.104\Omega + j0.040\Omega$
Line2 Length	$0.05km$
Line2 Impedance	$0.010\Omega + j0.004\Omega$
Line3 Length	$0.188km$
Line3 Impedance	$0.039\Omega + j0.015\Omega$

</div>

In this grid, DG1 is operated as a master, whereas DG2 and DG3 are operated as slaves. For the master, the voltage setpoint V_0 regarding Fig. 67 is set to $400V$ and the signal *enable_slave* is zero. Therefore, the fuzzy-based closed loop control is not active.

The two slaves (DG1 and DG2) are also set to $V_0 = 400V$, but *enable_slave* = 1. The fuzzy parameters for the trapezoidal membership functions regarding Fig. 5 are presented in Table 21.

<div align="center">

Table 21 – Fuzzy control parameters for reactive power control simulations.

Asset	Parameter	a	c	c	d
DG2	$V_{N,x}$	$-30V$	$0V$	$0V$	$30V$
	$V_{L,x}$	$-1000V$	$-999V$	$-100V$	$-20V$
	$V_{H,x}$	$20V$	$100V$	$999V$	$1000V$
DG3	$V_{N,x}$	$-40V$	$0V$	$0V$	$40V$
	$V_{L,x}$	$-1000V$	$-999V$	$-100V$	$-30V$
	$V_{H,x}$	$30V$	$100V$	$999V$	$1000V$

</div>

In the following, three different load scenarios are investigated. Finally the grid behavior in case of failure at the master is analyzed. All DGs have the same active power droop configuration with a droop factor of $k_f = 200kW/Hz$.

In the first scenario, a purely ohmic load is assumed. For testing, load steps from $P_{load} = 0\ldots400kW$ are applied. The simulation results are shown in Fig. 134.

Fig. 134a shows the active power for three DGs as well as the load. The corresponding reactive power is shown in Fig. 134b, whereas the voltage is shown in Fig. 134c. In the time range $0 < t < 350s$, all DGs are controlled to $Q = 0$ as the voltages are within the boundaries for normal operation. For $t > 350s$, the voltage at DG2 is in the transition zone of the voltage boundaries (between $20V$ and $30V$); therefore, the decentralized voltage/reactive power control at DG2 is stabilizing the voltage drop by reactive power feed-in. As the other slave asset (DG3) is within the boundaries of normal operation, only the master (DG1) is compensating the reactive power.
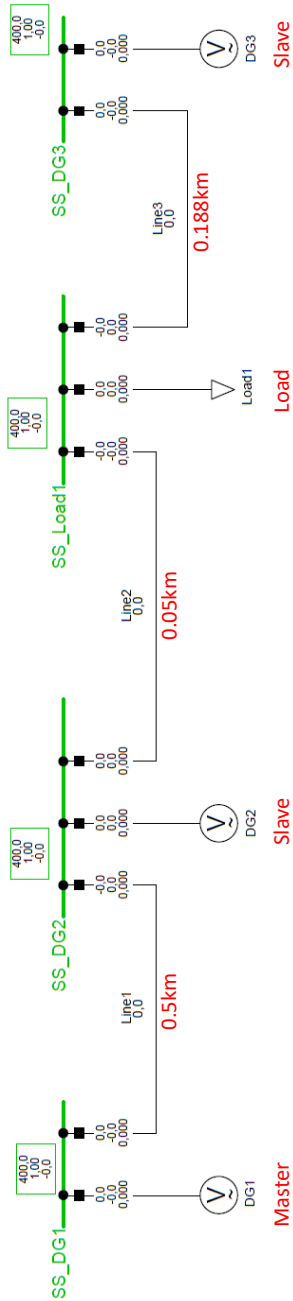
Figure 133 – SLD of the investigated grid consisting of 3 DGs, 1 load and corresponding lines. DG1 is assumed as master whereas DG2 and DG3 are assumed as slaves.
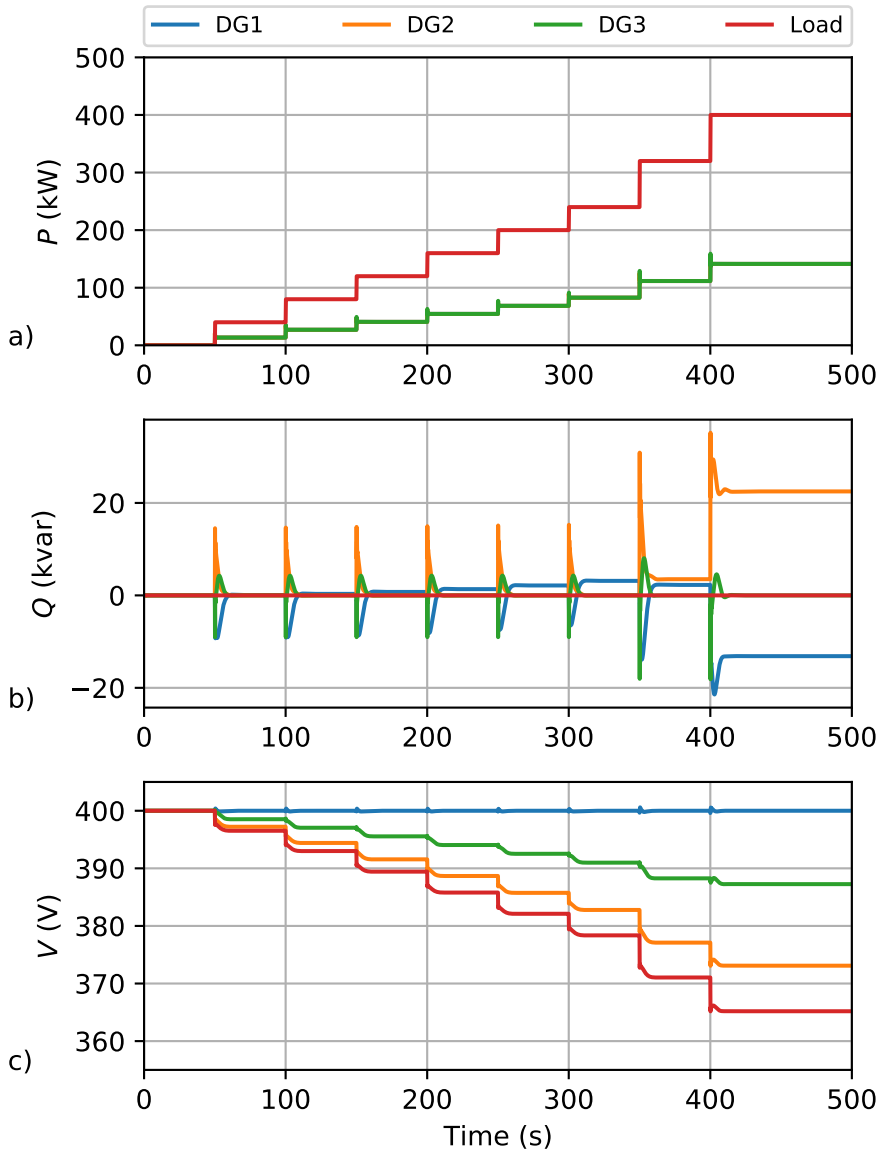
Figure 134 – Failsafe reactive power: simulation result for an ohmic load. a) active power; b) reactive power; c) voltage.

The second scenario investigates the behavior of a combined ohmic-inductive load with a power factor of $\cos\varphi = 0.8$. Load steps from $S = 0kVA \ldots 400kVA$ are applied to the grid.

The results are shown in Fig. 135.
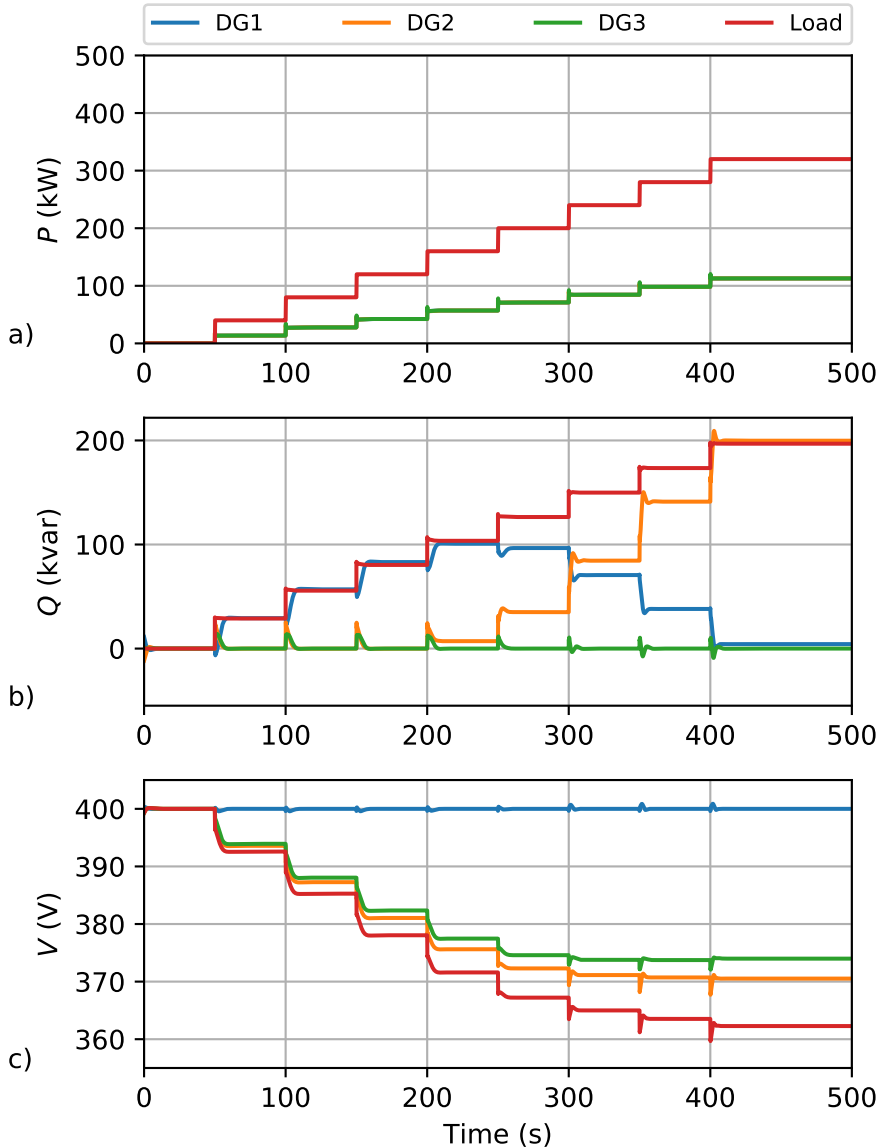
Figure 135 – Failsafe reactive power: simulation result of an ohmic-inductive Load ($\cos\varphi = 0.8_{ind.}$. a) active power; b) reactive power; c) voltage.

In the time range from $0 \ldots 200s$, the reactive power is completely covered by the master (DG1) as the slave voltages are within the boundaries of normal operation. After $200s$, also DG2 is feeding in reactive power for voltage stabilization. By increasing the load, the

amount of reactive power supplied by DG2 is increasing while the master's participation is decreasing. Regarding Table 21, the under-voltage boundary at DG2 is set to $-30V$ for normal operation. It can be seen that – especially at times higher than $350s$ – the voltage drop is limited to $370V$ which is equal to a voltage deviation of $-30V$.

As the voltage at the load node is not controlled, the desired voltage limits have to be set by proper configuration of the slave DGs, in detail the boundaries of the membership functions. This can be determined by worst case load flow calculations before.

In the third case, the failsafe reactive power control is tested for residual generation and capacitive reactive power. This is a worst-case scenario regarding voltage increase. A power factor of $\cos\varphi$ and apparent power steps from $S = 0 \ldots 400kVA$ are applied. The simulation result is shown in Fig. 136.

It can be seen that in the period from $0 \ldots 200s$, the complete reactive power is covered by the master DG1 in steady state. Beginning from $t = 200s$, the voltage at DG2 reaches the defined upper voltage limit. Thus, DG is consuming reactive power to compensate the voltage rise caused by the load. As DG3 is always within its voltage boundaries, the reactive power is zero (in steady state).

In the fourth scenario, the system behavior at a master's failure is shown (Fig. 137).

At $t = 50s$ an active and reactive load step is applied to the system. This leads to a voltage drop at the slave assets DG2 and DG3 as well as at the load. At $t = 200s$ a failure of the master DG1 is simulated, which means that the asset is disconnected from the grid. The active power now has to be compensated by DG2 and DG3 (Fig. 137a). Due to the voltage conditions, now the complete reactive load is compensated by DG2 (Fig. 137b). The voltage is decreasing until the lower voltage limit from DG2 is reached. Now the grid is operated with a lower voltage in comparison to the operation with active master device, but still in a legal voltage range (Fig. 137c). At time $t = 400s$ it is assumed that the master asset DG1 is reconnected. As the voltage setpoint is $V_0 = 400V$ without droop behavior, the grid voltage is increased and the island grid is still in stable operation.

It was shown that an optimized reactive power handling in comparison to pure voltage droop control can be realized without ICT. For many grids, it is a suitable approach as the reactive power in (rural) LV grid is small. Also, in case of failure (Master disconnected), a stable grid operation is ensured. In such a case, economical and ecological optimizations play a lower role as grid stability is the major goal.

Core Statements:

1. Active power distribution between BSS as GFU and gensets is shown.

2. Stable grid operation using DG can be achieved without a communication link between assets.

3. Minimization of reactive power exchange can be realized without a communication link.
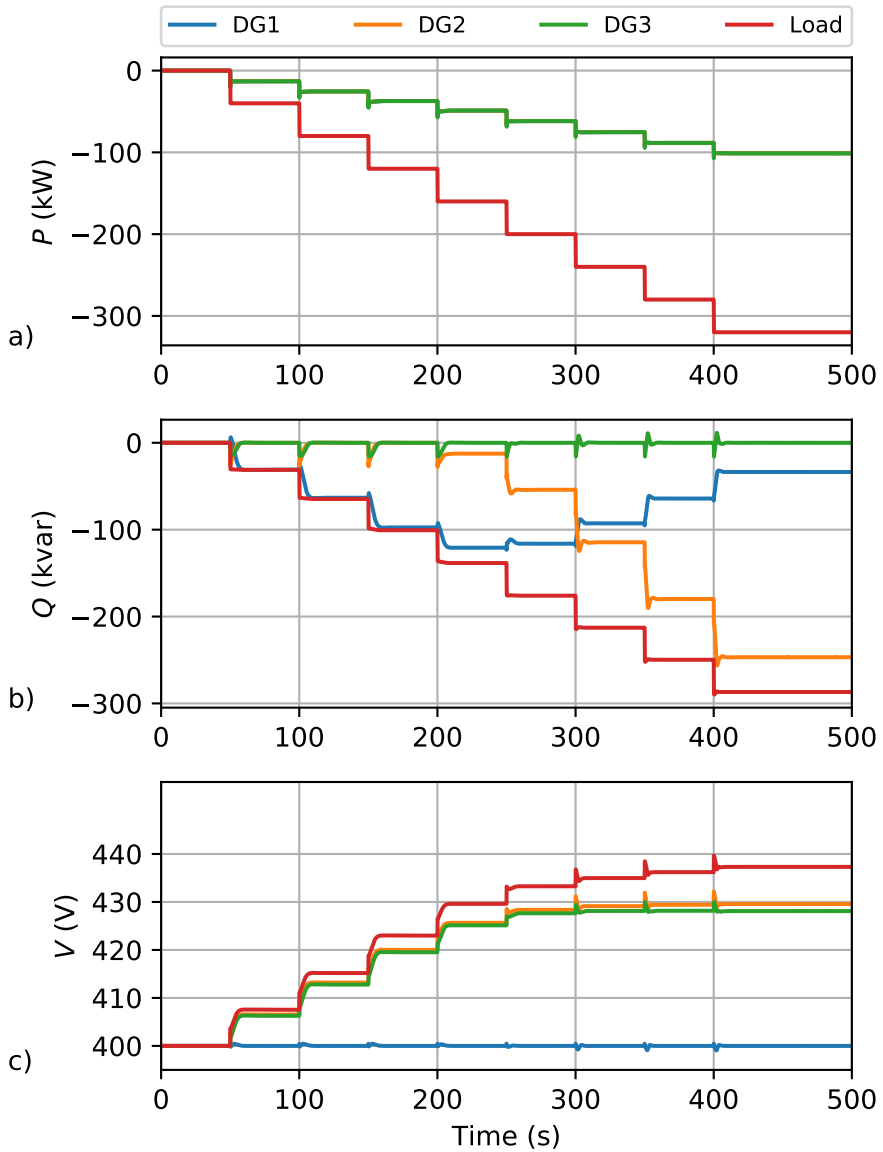
Figure 136 – Failsafe reactive power: simulation result of an ohmic-capacitive generation ($\cos\varphi = 0.8_{cap.}$. a) active power; b) reactive power; c) voltage.
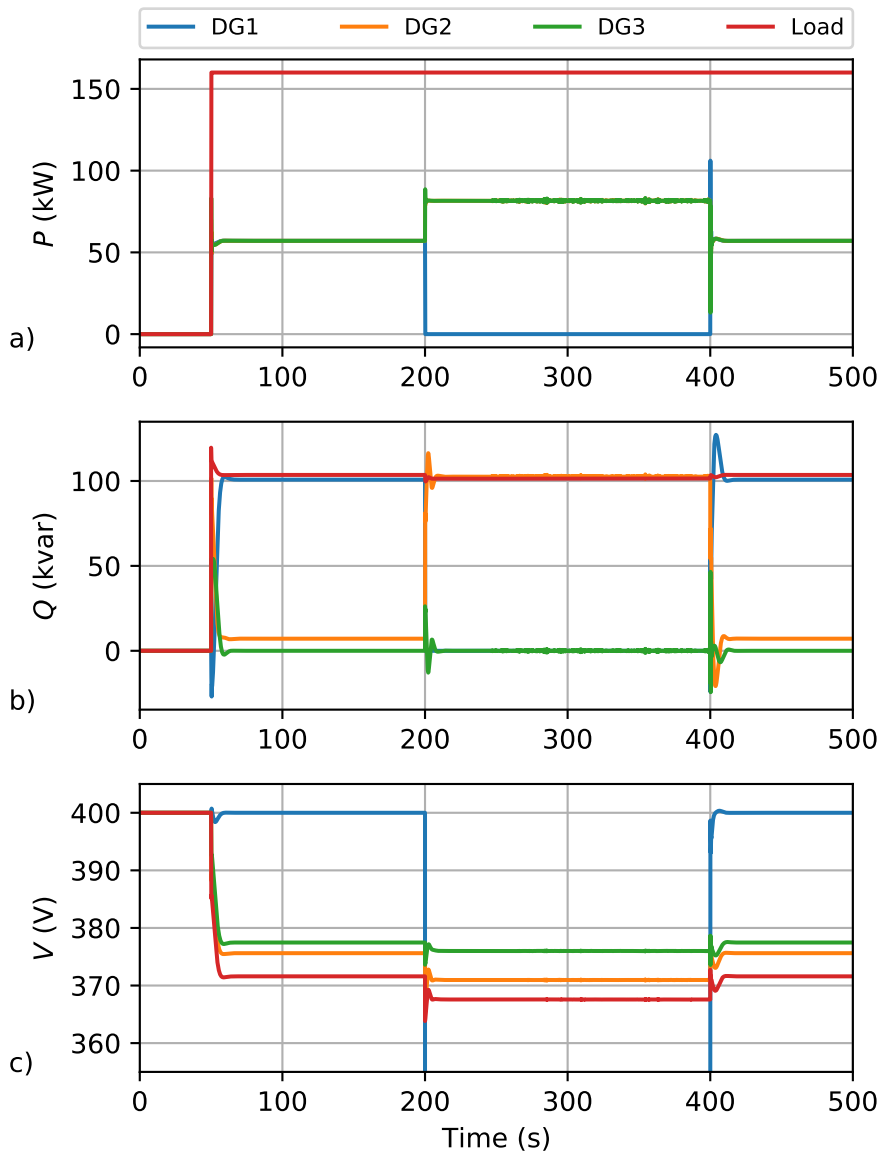
Figure 137 – Failsafe reactive power: simulation result for master (DG1) failure (at $t = 200s$). a) active power; b) reactive power; c) voltage.

6.6 Black Start Strategies

The black start strategy presented in section 4.4 is verified by simulations. Three scenarios are shown in the following.

The first scenario (sc01) as a worst case calculation is considering a BSS as GFU and a DG with maximum feed-in of $P_{DG,max} = 250kW$ and no load $P_{load} = 0$ (regarding Fig. 57).

The BSS's droop factor is varied from $k_{f,BSS} = 600kW/Hz$ to $k_{f,BSS} = 1500kW/Hz$. It is assumed that at time $t = 10s$, the BSS is connected and thus the black start process starts. The corresponding diagram is presented in Fig. 138.
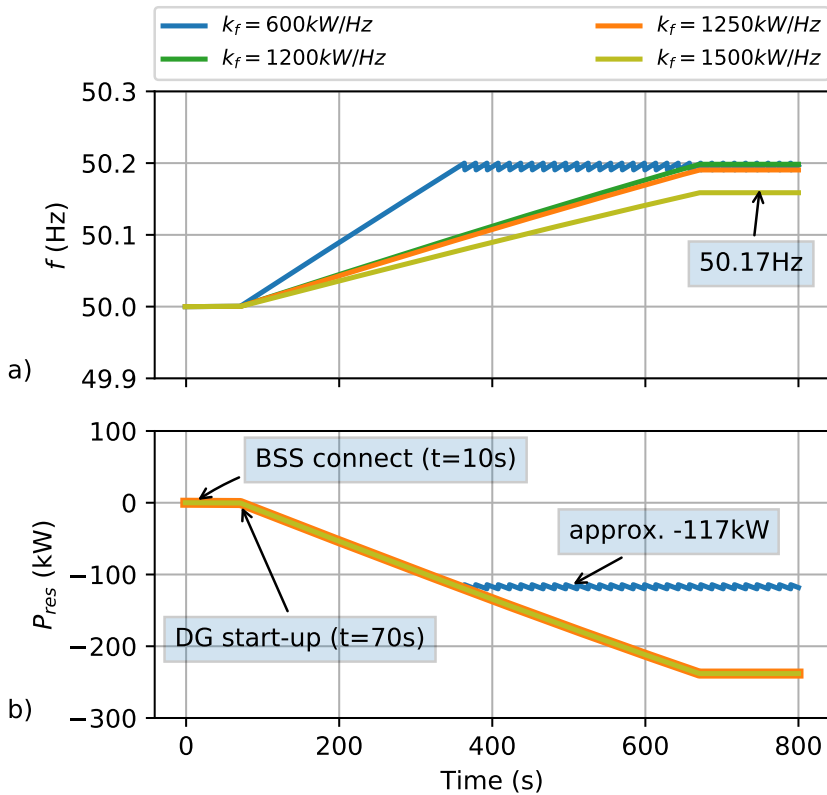
Figure 138 – Black start scenario 1 for different droop factors. a) grid frequency; b) residual power.

Due to VDE AR-N4105 characteristics, in the first $60s$, the residual load is still zero (Fig. 138b) and the frequency is $f = 50Hz$ (Fig. 138a). This is the minimum time for checking the grid conditions such as voltage level and frequency. Afterwards, the active power feed-in starts with a ramp of 10% per minute (related to the maximum DG power, which is also assumed as $250kW$).

For a droop factor of $k_{f,BSS} = 600kW/Hz$, the maximum feed-in is approx. 117kW as a frequency of $50.2Hz$ is reached. For droop factors higher than $k_{f,BSS} = 1200kW/Hz$, the maximum power of $250kW$ can be fed in.

In the second scenario (sc02), the black start of a grid with a genset is investigated. The assumed genset has a rated power of $P_{GEN,r} = 100kVA$. An ohmic load of $P_{load} = \{40; 50; 60\}\, kW$ is set. The corresponding result is shown in Fig. 139 resp. Fig. 140 (zoom).

It can be seen that a load step of $60kW$ cannot be implemented as the genset is shutting off due to under frequency protection. This behavior was also observed at the genset operated at the MCW (described in section 5.2.3).
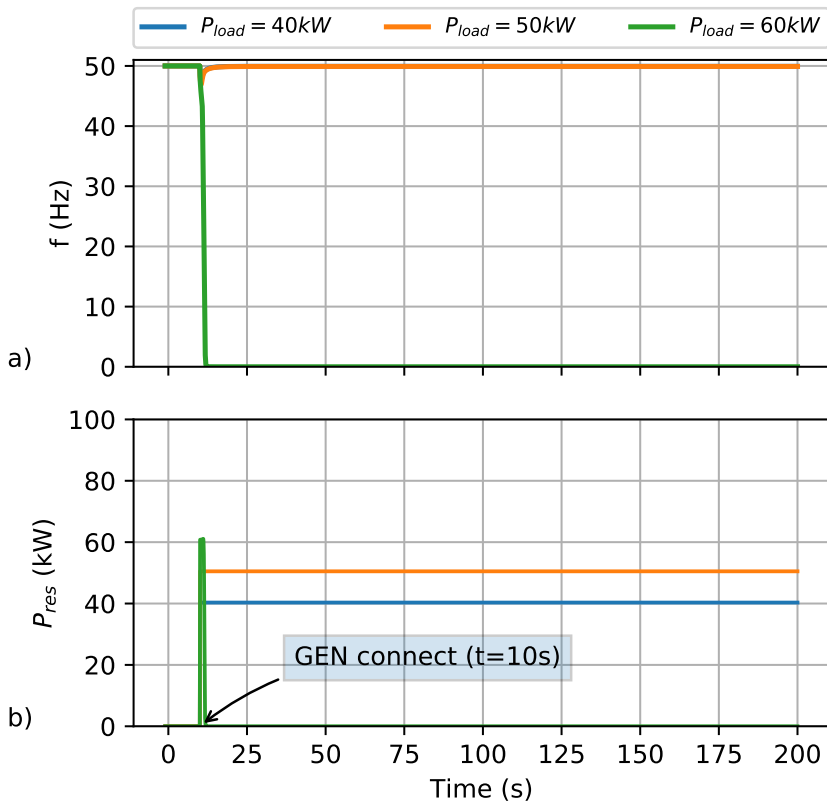
Figure 139 – Black start scenario 2 for different droop factors. a) grid frequency; b) residual power.

The frequency deviation at the time of genset's connection is – in this example – in the range of $3Hz$ for a load step of 50% of the rated power of the genset. For the island grid planning, the maximum load step expected at black start as well as the maximum frequency deviation have to be taken into account.

In the last example (sc03), an island grid consisting of BSS, genset, DG and load is investigated where the load is set to $P_{load} = 100kW$ and the maximum DG feed-in is set to $P_{DG,max} = 250kW$. The droop factors are set to $k_{f,BSS} = 1200kW/Hz$ resp. $k_{f,GEN} = 600kW/Hz$. It is assumed that the BSS and genset are synchronized before the residual load is connected. The corresponding result is shown in Fig. 141.

At time $t = 10s$, the load is connected to the GFUs. In the first moment, almost the complete active power is supplied by the BSS as the dynamics of the genset is lower. This behavior is confirmed by measurements in section 6.2.2.

At the time until $t = 70s$, the residual load is equal to the load with an amount of $100kW$. For $t > 70s$, the DG feed-in begins until approx. $t = 600s$ where the frequency of $50.2Hz$ is reached. The corresponding residual power is approx. $-110kW$ in this case. Without de-rating, the residual load would be at $-150kW$.
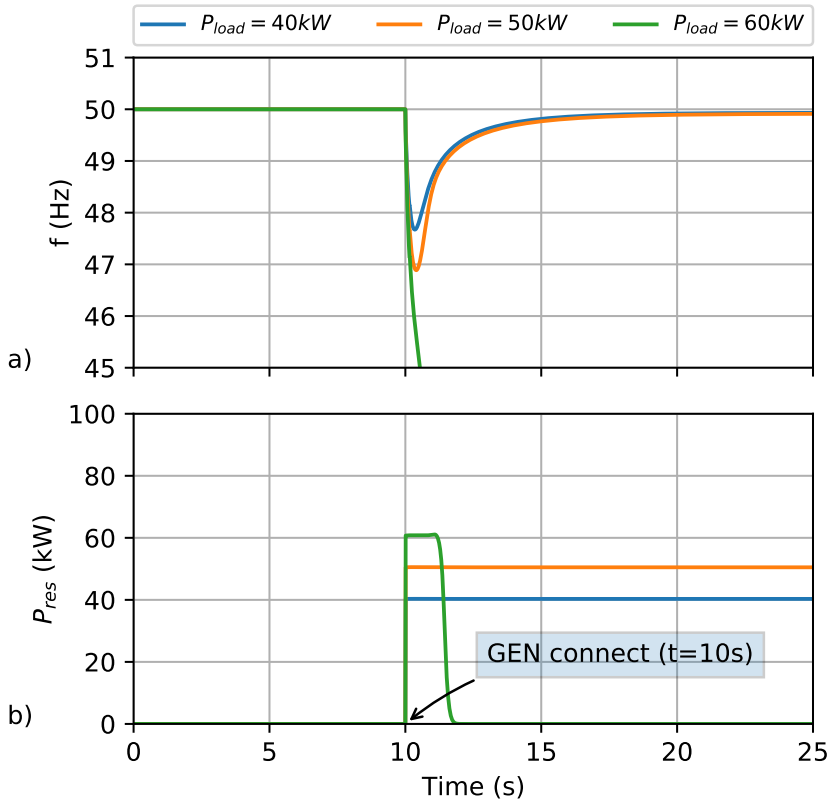
Figure 140 – Black start scenario 2 for different droop factors (zoom). a) grid frequency; b) residual power.
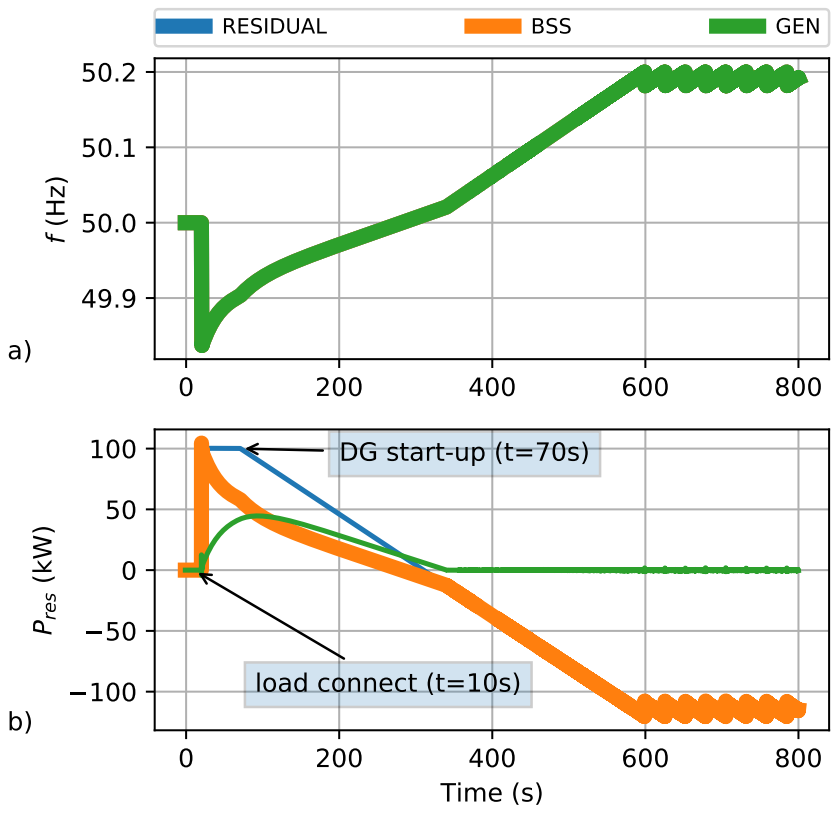
Figure 141 – Black start scenario 3 for different droop factors. a) grid frequency; b) residual power.

6.7 Resynchronization

A control concept for resynchronization of an islanded microgrid with an external grid is presented in section 4.5. In this part, the concept is verified by numeric grid simulation.

An island grid consisting of two BSSs (BSS1 and BSS2) and one genset (GEN) is operated independently with the microgrid controller described in section 4.2 in island mode operation. An ohmic load of $P_{load} = 150kW$ is assumed, which is supplied by the three GFUs (BSS1, BSS2 and GEN). A SLD is presented in Fig. 58. The result is shown in Fig. 142 resp. Fig. 143 (zoom). At time $t = 0s$, the resynchronization process to the external grid with an assumed frequency of $f_{ext} = 50Hz$ is started. Fig. 142a shows the active power for the two BSSs *BSS1*, *BSS2*, the genset *GEN* and the external grid *EXT* whereas Fig. 142b shows the corresponding reactive power. In Fig. 142c-e, the synchronization conditions for voltage, frequency and phase angle are presented. In Fig. 142f, the resynchronization signals *sync_ start* and *sync_ status* are drawn. At $t \approx 14.5s$, the synchronization conditions regarding Table 22 are fulfilled and the circuit breaker CB is closed.

Table 22 – Simulation parameters for resyncronization.

Parameter	Value
Frequency Difference Δf	$0.2Hz$
Voltage Difference ΔV	$5V$
Phase Angle Difference $\Delta \vartheta$	$0.5°$
Frequency Deviation Setpoint $\Delta f_{set\,point}$	$0.05Hz$

It can be seen that the voltage as well as the frequency are within the defined boundaries and the phase angle $\Delta \vartheta$ is close to zero (less than $0.5°$). A damped oscillation between the island grid assets *BSS1*, *BSS2* and *GEN* and the external grid *EXT* is visible. Also, the detailed zoom presentation in Fig. 143 shows exemplarily the power flow and voltage resp. frequency behavior at the moment of closing the circuit breaker *CB*.

In this work, only one example of a specific parameter configuration is presented. A reduction of power exchange and oscillation at the moment of reynchronization can be analyzed by further simulations based on the models decribed in this thesis and has to be optimized for each special use case, which is not described in this work.
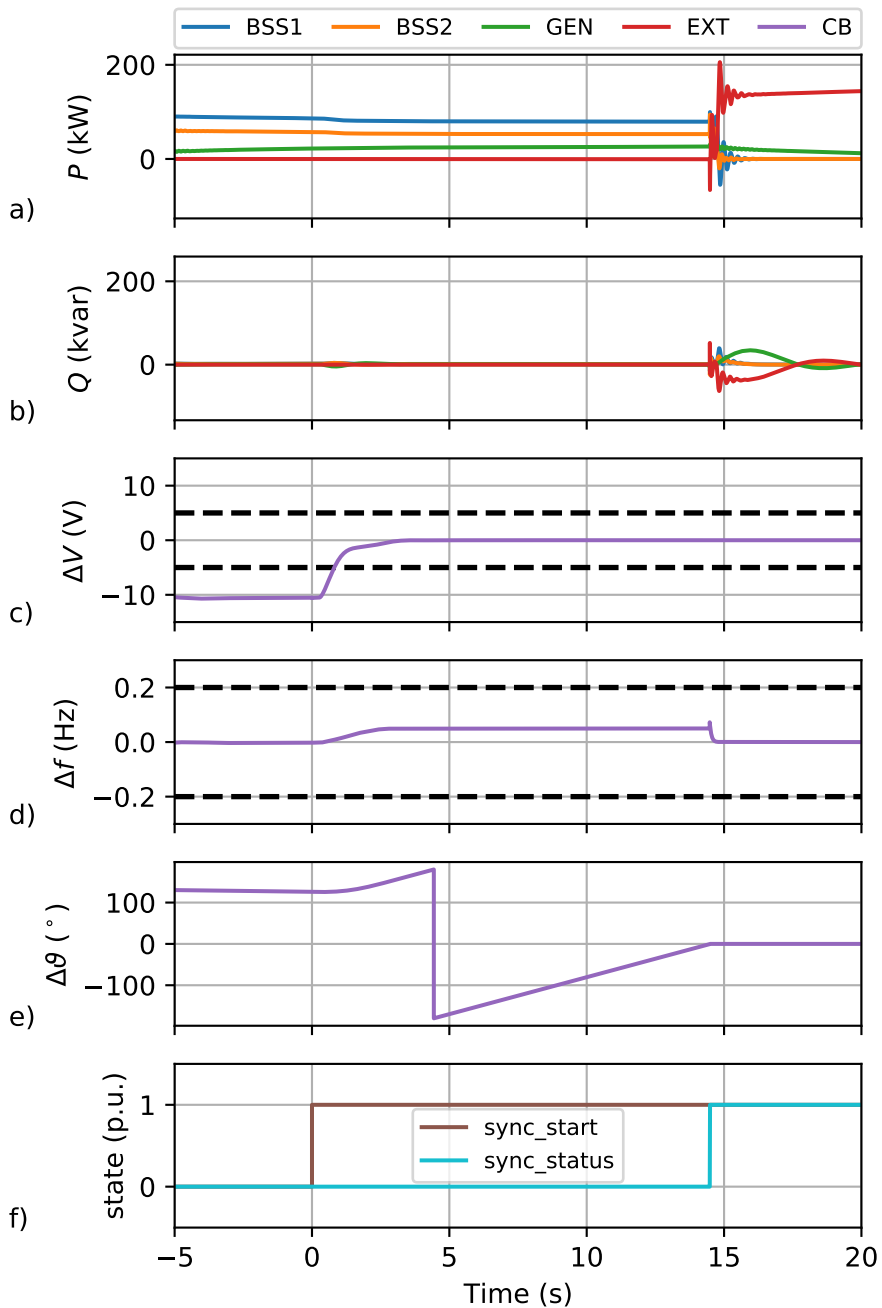
Figure 142 – Simulation results of resynchronization. a) active power for two BSSs BSS1 and BSS2; b) reactive power sharing; c) voltage difference at circuit breaker CB; d) frequency deviation at CB; e) phase angle over CB; f) reynchronization signals sync_start and sync_status.
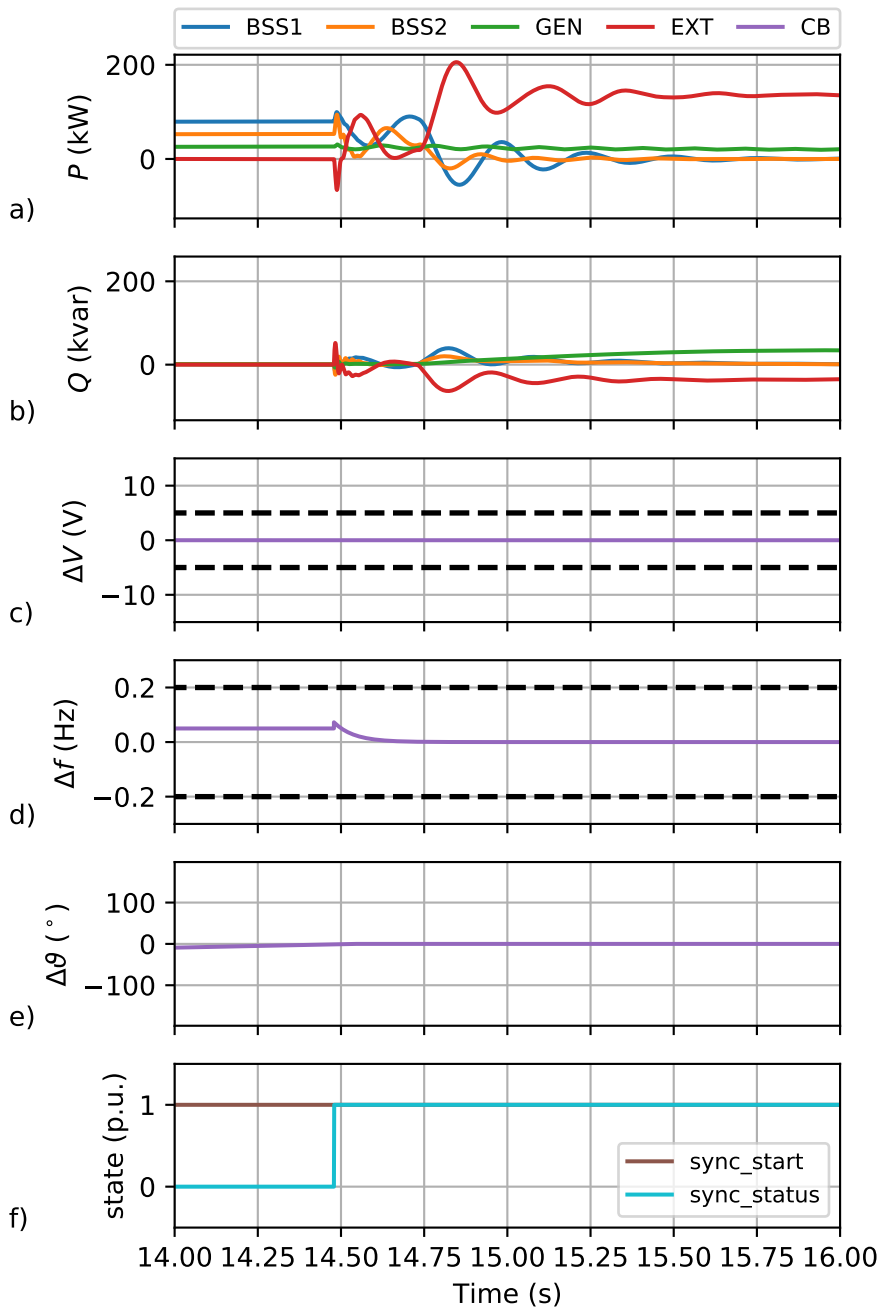
Figure 143 – Simulation results of resynchronization zoom-in. a) active power for two BSSs BSS1 and BSS2; b) reactive power sharing; c) voltage difference at circuit breaker CB; d) frequency deviation at CB; e) phase angle over CB; f) reynchronization signals sync_start and sync_status.

6.8 Conclusion

In the first part of this chapter, the mathematical models for microgrid assets were verified by comparison of specific simulation results with measurement.

Based on these validated models, the control and operation strategies were evaluated by simulation and are also presented in this chapter.

The main outcomes are:

- For the modeling of grid forming BSS using droop control it is shown by comparison with measurements that the dynamic behavior for active and reactive power, frequency and rms voltage is represented adequately with an electrical model based on Thevenin's Theorem. Nevertheless, it should be pointed out that effects like harmonics are not considered in this model.

- A comparison between modeling and measurement is shown for BSS in grid supporting mode considering VDE AR-N4105 and droop control for different use cases. It has to be pointed out that the proposed structure is eligible and sufficient for island grid planning and dimensioning.

- A linear and a fuzzy-based nonlinear modeling approach for gensets are compared with measurement results for parameter estimation and verification. As a result, the fuzzy-based approach showed a higher accuracy due to the nonlinear representation, but a high number of parameters have to be determined, e.g., in combination with expert knowledge. On the other hand, for the linear approach, a low number of parameters have to be estimated. For many applications in island grid planning, it is sufficient to use the linear approach.

- The established PV model considering VDE AR-N4105 was validated for the startup behavior and for the active power feed in depending on frequency.

- The simulation results for parallel operation of GFUs, GSUs and gensets with droop control were verified by specific measurements. It is shown that the assets' model complexity is sufficient for investigations regarding interaction.

- Active power droop factors have to be set in a certain range: low droop factors lead to high frequency deviations in steady state, whereas high droop factors lead to small frequency deviations. This can lead to non-accurate power split-up in practical applications due to measurement accuracy.

- For parallel operation of inverter-based GFUs and gensets, the inverter-based GFUs must be capable of covering the maximum values (positive and negative) of the resilient load, at least for some seconds.

- Due to low dynamics and dead time constants, the parallel operation of gensets and inverter-based GSUs has to be investigated for sufficient stability margin.

- Reactive power exchange between GFUs caused by droop control can be avoided by the usage of centralized microgrid control.

- A local reactive power control (RPC) as developed in this work improves the stability and resilience of systems with signal delays caused by ICT.

- The failsafe control concept developed in this thesis of island grids with BSSs, gensets, DGs regarding VDE AR-N4105 and loads enables a stable grid operation without a communication link with minimization of reactive power exchange.

7 Conclusion and Future Work

In this scientific work, mathematical models for relevant microgrid assets were developed and verified by specific measurements. It is shown that the grade of detail for the modeling of the considered assets is suitable as the verification showed good correlations.

Further, the parallel operation of island grid assets based on droop control was investigated by simulation and verified by measurements at the microgrid demonstrator MCW.

As a result, a centralized microgrid control was developed, which shows an improved dynamic behavior and stability for systems with delays caused by (Ethernet-based) communication. Also, an energy scheduling algorithm for battery storage systems was developed, which reduces the consumption of (fossil) primary energy by an improved usage of distributed generation. Further, a novel failsafe concept dealing with an improved active and reactive power management in islanded microgrids without a communication link was developed and verified by simulation.

The fundamental core statements of this work can be found at the end of the relevant sections.

From the author's point of view, an economic optimization for the control of active and reactive power in an islanded microgrid could be a continuation of this work. Further, a detailed stability analysis of the presented control strategies can be achieved as well, however, this was also not defined as the goal of this thesis.

List of Figures

175

List of Tables

References

[1] R. W. Andrews, J. S. Stein, C. Hansen, and D. Riley. Introduction to the open source PV LIB for python Photovoltaic system modelling package. In *2014 IEEE 40th Photovolt. Spec. Conf. PVSC 2014*, pages 170–174. Institute of Electrical and Electronics Engineers Inc., oct 2014.

[2] A. Armstorfer, N. Beg, A. Rahmoun, A. Rosin, and H. Biechl. Mathematical modeling and evaluation of a microgrid demonstrator in island mode. *Conference on Sustainable Energy Supply and Energy Storage Systems NEIS 2017*, 1(1):39–44, 2017.

[3] A. Armstorfer, N. Beg, A. Rahmoun, A. Rosin, and H. Biechl. Mathematical Modeling and Evaluation of a Microgrid Demonstrator in Island Mode. *Conf. Sustain. Energy Supply Energy Storage Syst. NEIS 2017*, pages 39–44, 2017.

[4] A. Armstorfer and H. Biechl. IREN2 : Teilvorhaben: Simulation und Betrieb netzstabilisierender Anlagen : Abschlussbericht : Projektlaufzeit: 1. Juli 2014 bis 31. März 2018. Technical report, Hochschule Kempten, Institut für Elektrische Energiesysteme (IEES), Kempten, 2018.

[5] A. Armstorfer, H. Biechl, and A. Rosin. Energy scheduling of battery storage systems in micro grids. *The Scientific Journal of Riga Technical University - Electrical, Control and Communication Engineering*, 12(1):27–33, 2017.

[6] A. Armstorfer, H. Biechl, and A. Rosin. Analysis of black start strategies for microgrids with renewable distributed generation. *IECON Proceedings (Industrial Electronics Conference)*, pages 2121–2125, 2019.

[7] A. Armstorfer, H. Biechl, and A. Rosin. Voltage and reactive power control in islanded microgrids without communication link. *Proceedings of the Biennial Baltic Electronics Conference, BEC*, pages 1–6, 2020.

[8] S. A. Azmi, K. H. Ahmed, S. J. Finney, and B. W. Williams. Comparative analysis between voltage and current source inverters in grid-connected application. In *Renew. Power Gener. (RPG 2011), IET Conf.*, pages 1–6. IET, 2011.

[9] O. Babayomi. Distributed Secondary Frequency and Voltage Control of Parallel-Connected VSCs in Microgrids: A Predictive VSG-Based Solution. *CPSS Trans. Power Electron. Appl.*, 5(4):342–351, dec 2020.

[10] M. Bashari and A. Rahimi-Kian. Forecasting electric load by aggregating meteorological and history-based deep learning modules. *IEEE Power Energy Soc. Gen. Meet.*, 2020-Augus, aug 2020.

[11] P. Bauer, L. E. Weldemariam, and E. Raijen. Stand-alone microgrids. In *2011 IEEE 33rd Int. Telecommun. Energy Conf.*, pages 1–10. IEEE, oct 2011.

[12] H. P. Beck and R. Hesse. Virtual synchronous machine. *2007 9th Int. Conf. Electr. Power Qual. Util. EPQU*, 2007.

[13] N. Beg, A. Armstorfer, A. Rosin, and H. Biechl. Mathematical modeling and stability analysis of a microgrid in island operation. *2018 International Conference on Smart Energy Systems and Technologies (SEST)*, pages 1–6, 2018.

[14] N. Beg, A. Rahmoun, A. Armstorfer, A. Rosin, and H. Biechl. Determination methods for controller parameters of back-to-back converters in electric power grids. *2016 Electric Power Quality and Supply Reliability (PQ)*, pages 157–164, 2016.

[15] J. T. Bialasiewicz. Renewable energy systems with photovoltaic power generators: Operation and modeling. *IEEE Trans. Ind. Electron.*, 55(7):2752–2758, jul 2008.

[16] A. Bidram and A. Davoudi. Hierarchical structure of microgrids control system. *IEEE Trans. Smart Grid*, 3(4):1963–1976, 2012.

[17] H. Biechl, A. Armstorfer, A. Rahmoun, T. Eberl, and C. Meyer. Abschlussbericht zum Verbundprojekt IRENE. pages 1–80, 2013.

[18] K. Bonfert. *Betriebsverhalten der Synchronmaschine*. Springer Berlin Heidelberg, Berlin, Heidelberg, 1962.

[19] H. Bühler. *Einführung in die Theorie Geregelter Drehstromantriebe*. Birkhäuser Basel, Basel, 1977.

[20] Bundesregierung.de. Bundesregierung beschließt Ausstieg aus der Kernkraft bis 2022.

[21] A. Cagnano, E. De Tuglie, A. Cervi, R. Stecca, R. Turri, and A. Vian. Re-Synchronization control strategy for master-slave controlled microgrids. *Synerg. MED 2019 - 1st Int. Conf. Energy Transit. Mediterr. Area*, may 2019.

[22] S. Cirstoiu and O. Pages. Modeling and control solutions for the turbocharged diesel engines. In *2nd Int. Conf. Syst. Comput. Sci.*, pages 9–13. IEEE, aug 2013.

[23] S. Cirstoiu and O. Pages. Modeling and control solutions for the turbocharged diesel engines. In *2nd Int. Conf. Syst. Comput. Sci.*, pages 9–13. IEEE, aug 2013.

[24] S. Cirstoiu and O. Pages. Modeling and Control Solutions for the Turbocharged Diesel Engines. In *2013 2nd Int. Conf. Syst. Comput. Sci.*, pages 9–13, 2013.

[25] DAIKIN. RZAG-MY1 - Klimatisierung, Technische Daten, 2018.

[26] Deutz.com. Tcd 2013.

[27] Dezong Zhao, Cunjia Liu, R. Stobart, Jiamei Deng, and E. Winward. Explicit model predictive control on the air path of turbocharged diesel engines. pages 5213–5218, 2013.

[28] DIgSILENT. PowerFactory.

[29] DIN. DIN EN50160:2020-11 (Voltage characteristics of electricity supplied by public electricity networks), 2020.

[30] J. Dohmann. *Thermodynamik der Kälteanlagen und Wärmepumpen*. Springer Berlin Heidelberg, Berlin, Heidelberg, 2016.

[31] D. Dong, B. Wen, D. Boroyevich, P. Mattavelli, and Y. Xue. Analysis of Phase-Locked Loop Low-Frequency Stability in Three-Phase Grid-Connected Power Converters Considering Impedance Interactions. *IEEE Trans. Ind. Electron.*, 62(1):310–321, jan 2015.

[32] F. Dorfler, J. W. Simpson-Porco, and F. Bullo. Breaking the hierarchy: Distributed control and economic optimality in Microgrids. *IEEE Trans. Control Netw. Syst.*, 3(3):241–253, sep 2016.

[33] Y. Du, H. Tu, S. Lukic, D. Lubkeman, A. Dubey, and G. Karsai. Implementation of a distributed microgrid controller on the Resilient Information Architecture Platform for Smart Systems (RIAPS). In *2017 North Am. Power Symp.*, pages 1–6. IEEE, sep 2017.

[34] EEG. Gesetz für den Vorrang Erneuerbarer Energien (Erneuerbare-Energien-Gesetz – EEG), 2000.

[35] A. Engler. Applicability of droops in low voltage grids. *Int. J. Distrib. Energy Resour. Smart Grids*, (1):1–5, 2005.

[36] T. Esram and P. L. Chapman. Comparison of photovoltaic array maximum power point tracking techniques. *IEEE Trans. Energy Convers.*, 22(2):439–449, jun 2007.

[37] J. S. Gomez, D. Saez, J. W. Simpson-Porco, and R. Cardenas. Distributed Predictive Control for Frequency and Voltage Regulation in Microgrids. *IEEE Trans. Smart Grid*, 11(2):1319–1329, mar 2020.

[38] J. M. Guerrero, L. García de Vicuña, J. Matas, M. Castilla, and J. Miret. Output impedance design of parallel-connected UPS inverters with wireless load-sharing control. *IEEE Trans. Ind. Electron.*, 52(4):1126–1135, aug 2005.

[39] J. M. Guerrero, J. C. Vasquez, J. Matas, L. G. De Vicuña, and M. Castilla. Hierarchical control of droop-controlled AC and DC microgrids - A general approach toward standardization. *IEEE Trans. Ind. Electron.*, 58(1):158–172, jan 2011.

[40] J. M. Guerrero, J. C. Vasquez, J. Matas, L. G. De Vicuña, and M. Castilla. Hierarchical control of droop-controlled AC and DC microgrids - A general approach toward standardization. *IEEE Trans. Ind. Electron.*, 58(1):158–172, jan 2011.

[41] F. Guo, C. Wen, J. Mao, and Y. D. Song. Distributed Secondary Voltage and Frequency Restoration Control of Droop-Controlled Inverter-Based Microgrids. *IEEE Trans. Ind. Electron.*, 62(7):4355–4364, jul 2015.

[42] L. Guzzella and A. Amstutz. Control of diesel engines. *IEEE Control Syst. Mag.*, 18(5):53–71, 1998.

[43] N. Hatziargyriou, H. Asano, R. Iravani, and C. Marnay. Microgrids, jul 2007.

[44] J. Helguero, A. Armstofer, N. Beg, H. Biechl, and I. f. E. E. Hochschule Kempten. *DeCAS - Demonstration of coordinated ancillary services covering different voltage levels and the integration in future markets : Schlussbericht : Projektlaufzeit: 01. September 2016 bis 31. März 2019*. [Kempten], 2019.

[45] J. B. Heywood. *Internal Combustion Engine Fundamentals*, volume 21. McGraw-Hill Book Co, 1988.

[46] P. IEEE Standards Coordinating Committee 21 (Fuel Cells, IEEE-SA Standards Board., and Institute of Electrical and Electronics Engineers. IEEE standard for interconnecting distributed resources with electric power systems. page 16, 2003.

[47] IEES. Single Line Diagram of the Microgrid Campus Wildpoldsried (internal Document at IEES). Technical report.

[48] F. Katiraei and M. R. Iravani. Power management strategies for a microgrid with multiple distributed generation units. *IEEE Trans. Power Syst.*, 21(4):1821–1831, nov 2006.

[49] N. Kijshevavithaya and S. Suwankawin. An enabling resynchronization technique for grid-connected voltage-source converters. *ECTI-CON 2021 - 2021 18th Int. Conf. Electr. Eng. Comput. Telecommun. Inf. Technol. Smart Electr. Syst. Technol. Proc.*, pages 555–558, may 2021.

[50] R. Köberle, K. Mayr, B. Rindt, T. Sowa, D. Buchstaller, A. Armstorfer, and H. Biechl. IREN2: Zukunftsfähige Netze zur Integration Regenerativer Energiesysteme. In *ETG-Fb. 145 Von Smart Grids zu Smart Mark. 2015*, Kassel, 2015.

[51] S. Kouro, J. I. Leon, D. Vinnikov, and L. G. Franquelo. Grid-connected photovoltaic systems: An overview of recent research and emerging PV converter technology. *IEEE Ind. Electron. Mag.*, 9(1):47–61, mar 2015.

[52] J. Lai, H. Zhou, X. Lu, X. Yu, and W. Hu. Droop-Based Distributed Cooperative Control for Microgrids with Time-Varying Delays. *IEEE Trans. Smart Grid*, 7(4):1775–1789, jul 2016.

[53] T. Laible. *Die Theorie der Synchronmaschine im nichtstationären Betrieb*. Springer Berlin Heidelberg, 1952.

[54] J. Lopes, C. Moreira, A. Madureira, F. Resende, X. Wu, N. Jayawarna, Y. Zhang, N. Jenkins, F. Kanellos, and N. Hatziargyriou. Control strategies for microgrids emergency operation. In *2005 Int. Conf. Futur. Power Syst.*, pages 6 pp.–6. IEEE, 2005.

[55] J. A. Lopes, C. L. Moreira, and A. G. Madureira. Defining control strategies for microgrids islanded operation. *IEEE Trans. Power Syst.*, 21(2):916–924, may 2006.

[56] B. Matthias, M. Banka, and R. Krzysztof. Coordination of the islanding and resynchronisation process of microgrids through a smart meter gateway interface. *IET Conf. Publ.*, 2020(CP767):334–336, 2020.

[57] MeccAlte. Generator type ecp 28-vl/4.

[58] C. L. Moreira, F. O. Resende, and J. A. P. Lopes. Using Low Voltage MicroGrids for Service Restoration. *IEEE Trans. Power Syst.*, 22(1):395–403, feb 2007.

[59] M. Mottaghizadeh, F. Aminifar, T. Amraee, and M. Sanaye-Pasand. Distributed Robust Secondary Control of Islanded Microgrids: Voltage, Frequency, and Power Sharing. *IEEE Trans. Power Deliv.*, 36(4):2501–2509, aug 2021.

[60] P. Mukhopadhyay, G. Mitra, S. Banerjee, and G. Mukherjee. Electricity load forecasting using fuzzy logic: Short term load forecasting factoring weather parameter. *2017 7th Int. Conf. Power Syst. ICPS 2017*, pages 812–819, jun 2018.

[61] V. Nasirian, Q. Shafiee, J. M. Guerrero, F. L. Lewis, and A. Davoudi. Droop-Free Distributed Control for AC Microgrids. *IEEE Trans. Power Electron.*, 31(2):1600–1617, feb 2016.

[62] B. Ning, Q. L. Han, and L. Ding. Distributed Finite-Time Secondary Frequency and Voltage Control for Islanded Microgrids with Communication Delays and Switching Topologies. *IEEE Trans. Cybern.*, 51(8):3988–3999, aug 2021.

[63] M. Nuschke. Development of a microgrid controller for black start procedure and islanding operation. In *2017 IEEE 15th Int. Conf. Ind. Informatics*, pages 439–444. IEEE, jul 2017.

[64] D. Oeding and B. Oswald. *Elektrische Kraftwerke und Netze*. 2011.

[65] D. E. Olivares, A. Mehrizi-Sani, A. H. Etemadi, C. A. Cañizares, R. Iravani, M. Kazerani, A. H. Hajimiragha, O. Gomis-Bellmunt, M. Saeedifard, R. Palma-Behnke, G. A. Jiménez-Estévez, and N. D. Hatziargyriou. Trends in microgrid control. *IEEE Trans. Smart Grid*, 5(4):1905–1919, 2014.

[66] B. R. Oswald. *Berechnung von Drehstromnetzen*. Springer Fachmedien Wiesbaden, Wiesbaden, 2013.

[67] B. R. Oswald. *Berechnung von Drehstromnetzen*. Springer Fachmedien Wiesbaden, Wiesbaden, 2017.

[68] ParisAgreement2016. PARIS AGREEMENT, 2016.

[69] F. L. Quilumba, W. J. Lee, H. Huang, D. Y. Wang, and R. L. Szabados. Using smart meter data to improve the accuracy of intraday load forecasting considering customer behavior similarities. *IEEE Trans. Smart Grid*, 6(2):911–918, mar 2015.

[70] A. Rahmoun. *Mathematical Modeling and Analysis of a Battery Energy Storage System for Microgrids*. 2017.

[71] A. Rahmoun, A. Armstorfer, H. Biechl, and A. Rosin. Mathematical modeling of a battery energy storage system in grid forming mode. *2017 IEEE 58th International Scientific Conference on Power and Electrical Engineering of Riga Technical University (RTUCON)*, pages 1–6, 2017.

[72] A. Rahmoun, A. Armstorfer, H. Biechl, and A. Rosin. Mathematical modeling of a battery energy storage system in grid forming mode. In *2017 IEEE 58th Int. Sci. Conf. Power Electr. Eng. Riga Tech. Univ.*, pages 1–6, Riga, oct 2017. IEEE.

[73] A. Rahmoun, A. Armstorfer, J. Helguero, H. Biechl, and A. Rosin. Mathematical modeling and dynamic behavior of a lithium-ion battery system for microgrid application. *2016 IEEE International Energy Conference (ENERGYCON)*, pages 1–6, 2016.

[74] A. Rahmoun, A. Armstorfer, J. Helguero, H. Biechl, and A. Rosin. Mathematical modeling and dynamic behavior of a Lithium-Ion battery system for microgrid application. In *2016 IEEE Int. Energy Conf.*, pages 1–6. IEEE, apr 2016.

[75] K. Reif. *Dieselmotor-Management*. Vieweg+Teubner Verlag, Wiesbaden, 2012.

[76] J. Rocabert, A. Luna, F. Blaabjerg, and P. Rodríguez. Control of Power Converters in AC Microgrids. *IEEE Trans. Power Electron.*, 27(11):4734–4749, nov 2012.

[77] J. Rocabert, A. Luna, F. Blaabjerg, and P. Rodríguez. Control of power converters in AC microgrids. *IEEE Trans. Power Electron.*, 27(11):4734–4749, 2012.

[78] E. Román, R. Alonso, P. Ibañez, S. Elorduizapatarietxe, and D. Goitia. Intelligent PV module for grid-connected PV systems. *IEEE Trans. Ind. Electron.*, 53(4):1066–1073, jun 2006.

[79] S. Roy, O. Malik, and G. Hope. Predictors for application to real-time adaptive control of a diesel prime-mover. In *Conf. Rec. 1990 IEEE Ind. Appl. Soc. Annu. Meet.*, pages 1804–1810. IEEE, 1990.

[80] S. Roy, O. Malik, and G. Hope. A low order computer model for adaptive speed control of diesel driven power-plants. In *Conf. Rec. 1991 IEEE Ind. Appl. Soc. Annu. Meet.*, pages 1636–1642. IEEE, 1991.

[81] Ruixue Li, Ying Huang, Gang Li, and He Song. Control-oriented modeling and analysis for turbocharged diesel engine system. In *Proc. 2013 2nd Int. Conf. Meas. Inf. Control*, volume 02, pages 855–860. IEEE, aug 2013.

[82] J. Schiffer, D. Goldin, J. Raisch, and T. Sezi. Synchronization of droop-controlled microgrids with distributed rotational and electronic generation. In *52nd IEEE Conf. Decis. Control*, pages 2334–2339. IEEE, dec 2013.

[83] A. J. Schwab. *Elektroenergiesysteme*. Springer Berlin Heidelberg, 3. auflage edition, 2012.

[84] Q. Shafiee, J. M. Guerrero, and J. C. Vasquez. Distributed secondary control for islanded microgrids-a novel approach. *IEEE Trans. Power Electron.*, 29(2):1018–1031, 2014.

[85] J. W. Simpson-Porco, Q. Shafiee, F. Dorfler, J. C. Vasquez, J. M. Guerrero, and F. Bullo. Secondary Frequency and Voltage Control of Islanded Microgrids via Distributed Averaging. *IEEE Trans. Ind. Electron.*, 62(11):7025–7038, nov 2015.

[86] S. Singh, S. Hussain, and M. A. Bazaz. Short term load forecasting using artificial neural network. *2017 4th Int. Conf. Image Inf. Process. ICIIP 2017*, 2018-Janua:159–163, mar 2018.

[87] J. J. Soon and K. S. Low. Optimizing Photovoltaic Model for Different Cell Technologies Using a Generalized Multidimension Diode Model. *IEEE Trans. Ind. Electron.*, 62(10):6371–6380, oct 2015.

[88] J. Stanojevic, A. Djordjevic, and M. Mitrovic. Influence of battery energy storage system on generation adequacy and system stability in hybrid micro grids. *4th Int. Symp. Environ. Friendly Energies Appl. EFEA 2016*, nov 2016.

[89] M. Starke, A. Herron, D. King, and Y. Xue. Implementation of a Publish-Subscribe Protocol in Microgrid Islanding and Resynchronization with Self-Discovery. *IEEE Trans. Smart Grid*, 10(1):361–370, 2018.

[90] Statista. Anteil der Wärmepumpen im Neubau in Deutschland in den Jahren 2000 bis 2020.

[91] B. Subudhi and R. Pradhan. A comparative study on maximum power point tracking techniques for photovoltaic power systems. *IEEE Trans. Sustain. Energy*, 4(1):89–98, 2013.

[92] S. Thale and V. Agarwal. A smart control strategy for the black start of a microgrid based on PV and other auxiliary sources under islanded condition. In *2011 37th IEEE Photovolt. Spec. Conf.*, pages 002454–002459. IEEE, jun 2011.

[93] S. Thomas, S. Islam, S. R. Sahoo, and S. Anand. Distributed secondary control with reduced communication in low-voltage DC microgrid. *Proc. - 2016 10th Int. Conf. Compat. Power Electron. Power Eng. CPE-POWERENG 2016*, pages 126–131, aug 2016.

[94] H. Unbehauen. *Regelungstechnik I*. Vieweg+Teubner, Wiesbaden, 2008.

[95] M. Vasconcelos, W. Cramer, C. Schmitt, A. Amthor, S. Jessenberger, C. Ziegler, A. Armstorfer, and F. Heringer. The PEBBLES project – enabling blockchain based transactive energy trading of energy flexibility within a regional market. AIM, 2019.

[96] J. Vasquez, J. Guerrero, J. Miret, M. Castilla, and L. Garcia de Vicuna. Hierarchical Control of Intelligent Microgrids. *IEEE Ind. Electron. Mag.*, 4(4):23–29, dec 2010.

[97] VDE. VDE-AR-N 4105 (Erzeugungsanlagen am Niederspannungsnetz - Technische Mindestanforderungen für Anschluss und Parallelbetrieb von Erzeugungsanlagen am Niederspannungsnetz, 2011.

[98] VDE. VDE-Studie Der zellulare Ansatz. Technical report, VDE Verbad der Elektrotechnik Elektronik Informationstechnik e.V., Frankfurt am Main, 2015.

[99] VDE. VDE-AR-N 4105. 100(0100492), 2018.

[100] D. Wu, T. Dragicevic, J. C. Vasquez, J. M. Guerrero, and Y. Guan. Secondary coordinated control of islanded microgrids based on consensus algorithms. *2014 IEEE Energy Convers. Congr. Expo. ECCE 2014*, pages 4290–4297, nov 2014.

[101] Z. Xu, P. Yang, Z. Zeng, Y. Zhang, J. Peng, and Q. Zheng. Study on black start strategy for multi-microgrids. In *2016 IEEE Innov. Smart Grid Technol. - Asia*, pages 144–148. IEEE, nov 2016.

[102] L. Zacharia, A. Kyriakou, L. Hadjidemetriou, E. Kyriakides, C. Panayiotou B. Azzopardi, N. Martensen, and N. Borg. Islanding and Resynchronization Procedure of a University Campus Microgrid. In *2018 Int. Conf. Smart Energy Syst. Technol.*, pages 1–6. IEEE, sep 2018.

[103] Y. Zhang, R. Xiong, H. He, and W. Shen. Lithium-Ion Battery Pack State of Charge and State of Energy Estimation Algorithms Using a Hardware-in-The-Loop Validation. *IEEE Trans. Power Electron.*, 32(6):4421–4431, jun 2017.

[104] A. Zielińska, M. Skowron, and A. Bień. Modelling of photovoltaic cells in variable conditions of temperature and intensity of solar insolation as a method of mapping the operation of the installation in real conditions. In *2018 Int. Interdiscip. PhD Work. IIPhDW 2018*, pages 200–204. Institute of Electrical and Electronics Engineers Inc., jun 2018.

Acknowledgements

First I would like to thank my supervisors Prof. Dr. Argo Rosin and Prof. Dr.-Ing. Dr. h.c. Helmuth Biechl for the supervision of my thesis and for the great support during the last years. The recent applied research projects at the Institute of Electrical Power Systems (IEES) at Kempten University of Applied Sciences under dicrection of Prof. Dr.-Ing. Dr. h.c. allowed me to grow as an engineer and researcher.

Further I would like to thank my colleagues at the Institute of Electrical Power Systems (IEES) for the good cooperation and collaborative work, especially at the research demonstrator "Microgrid Campus Wildpoldsried". My special thanks go to my colleague Lothar Geist for the valuable discussions and the great support with coffee during the research.

Last but not least, I would like to thank my family – especially my wife – for the patience and support during the work on this thesis.

Thank you!
Andreas Armstorfer

Abstract
Mathematical Modeling and Control Strategies for Islanded Microgrids

Microgrids play an important role in the energy transition. The change from few centralized power plants to thousands of small renewable and volatile energy resources requires, but also enables new grid control strategies.

The full potential of microgrids is deployed by the extension of island grid operation. This leads to an increased reliability and resilience of the distribution of electrical energy. Further, the island capability of microgrids can support a greater grid area in case of failures in higher voltage levels by a temporary disconnection from the main grid and later by resynchronization in the frame of a cellular approach.

For the modeling and control of microgrids in island operation, this thesis delivers mathematical models for typical assets verified by specific measurements at an existing microgrid (Microgrid Campus Wildpoldsried - MCW) with island capability.

Further, the interaction of inverter-based assets, such as battery storage systems in grid forming, but also in grid support mode, and photovoltaic systems as well as rotating generation units by using droop control, is investigated by simulation; the results are confirmed by measurements at the MCW.

Based on these verified simulation models, further control strategies for the microgrid are developed and analyzed by simulation. This includes a centralized approach for a microgrid controller, including active and reactive power management, strategies for black start and resynchronization as well as energy scheduling for the battery storage systems. Further, also a failsafe control strategy for active and reactive power sharing between distributed generation, battery storage systems and rotating generation units is investigated for systems without communication system (e.g., temporarily caused by a failure or permanent to reduce installation and maintenance costs). All investigations were performed under consideration of the practical application in real grids. This includes existing rules like VDE AR-N4105 for the distributed generation and the DIN EN50160 for voltage quality on the one hand, but also communication dead times caused by Ethernet-based communication links, protocol converters and control platforms.

Therefore, this thesis provides insightful methods for the planning, dimensioning and analysis of islanded microgrids.

Kokkuvõte

Saartalitluses mikrovõrkude matemaatiline modelleerimine ja juhtimisstrateegiad

Mikrovõrgud mängivad olulist rolli energiasüsteemi ümberkujunemisel. Üleminek tsentraliseeritud elektri suurtootmiselt hajutatud ja juhuslikule elektri väiketootmisele vajab ja võimaldab kasutusele võtta uusi elektrivõrkude juhtimisstrateegiaid.

Mikrovõrkude potentsiaal leiab täielikku rakendust just saartalitluses, sest aitab suurendada elektrisüsteemi töö- ja talitluskindlust. Saartalitluses mikrovõrk on võimeline toetama suuremat võrgupiirkonda kõrgepingepoolel toimuvate rikete korral, nt mobiilsidet kasutades eraldades end võrgust või sünkroniseerides võrguga.

Saartalitluses mikrovõrkude modelleerimiseks ja juhtimiseks on lõputöö raames koostatud võrgu komponentide (varade) matemaatilised mudelid, mida on valideeritud mõõtmistega reaalses saartalitlusvõimekusega mikrovõrgus Saksamaal (Microgrid Campus Wildpoldsried – MCW).

Lisaks on simulatsioonide ja reaalsete mõõtmiste käigus uuritud inverteripõhiste varade, nagu akusalvestite (sh võrgu moodustamise, aga ka võrgutoe talitluses töötavate akusalvestussüsteemide), fotoelektriliste päikesepaneelide ja pöörlevate elektritootmisseadmete koostoimet, kasutades statismil põhinevat juhtimist.

Vastavalt verifitseeritud simulatsioonimudelitele on välja töötatud ja analüüsitud erinevaid mikrovõrkude juhtimisstrateegiaid, sh tsentraliseeritud aktiiv- ja reaktiivvõimsuse haldust, mikrovõrgu taaskäivitamist ja sünkroniseerimist võrguga ning akusalvesti energiahaldust. Lisaks uuriti tõrkekindlat aktiiv- ja reaktiivvõimsuse juhtimisstrateegiat mikrovõrgu komponentide vahel andmeside puudumise korral (nt rikke olukorras või püsivalt paigaldus- ja hoolduskulude kokkuhoiu eesmärgil).

Kõigi uuringute läbiviimisel on silmas peetud nende praktilist rakendamist reaalses võrgus. Seega arvestati uuringute läbiviimisel olemasolevate hajatootmise VDE AR-N4105 ja pingekvaliteedi DIN EN50160 regulatsioonidega. Samuti võeti uuringutel arvesse ka katkestusi, mis on põhjustatud Etherneti põhise andmeside sh ühenduste, võrgulüüside ja juhtimisplatvormide poolt.

Käesolev lõputöö pakub põhjalikud meetodid saartalitluses mikrovõrkude planeerimiseks, dimensioneerimiseks ja analüüsimiseks.

Appendix 1

I

A. Armstorfer, H. Biechl, and A. Rosin. Voltage and reactive power control in islanded microgrids without communication link. *Proceedings of the Biennial Baltic Electronics Conference, BEC*, pages 1–6, 2020

Energy Scheduling of Battery Storage Systems in Micro Grids

Andreas Armstorfer* (*Researcher, University of Applied Sciences Kempten*), Helmuth Biechl (*Director, IEES*),
Argo Rosin (*Senior Research Scientist, Tallinn University of Technology*)

Abstract – **Microgrids in island mode with high penetration of renewable energy sources in combination with gensets and battery storage systems need a control system for voltage and frequency. In this study the main goal is maximization of the energy feed-in by renewable sources. Therefore it is necessary to keep the State of Energy for the Battery Storage System in a range that the excess energy can be absorbed and used in a later period of the day. In this paper an approach for State of Charge scheduling based on load and generation prediction is described.**

Keywords – **Distributed power generation; Energy storage; Islanding; Microgrids; Power system management.**

I. INTRODUCTION

In island grids with volatile renewable power generation it is desired that this sources can always feed in their maximum power.

The usage of battery storage systems (BSS) can support the grid, especially when the renewable generation is higher than the power consumption. In these periods the excess energy has to be absorbed completely by the BSS, as gensets can only deliver power. It has to be ensured that the State of Energy (SOE) of the BSS do not exceed its limits and always have enough margin. In this paper we work with the State of Energy (SOE) instead of the State of Charge (SOC) which slightly differs due to the changing voltage. The approach for BSS scheduling given here is based on the prediction of load and renewable power generation.

In periods of excess electricity generation, the BSS need to store the complete energy. Therefore the SOE has to be scheduled that way that the BSS is discharged sufficiently in periods with a lack of power. Furthermore uncertainties of prediction need to be taken into account as well.

For a stable operation with several grid-building components, frequency control is necessary. The concept presented here is based on primary and secondary control [1]–[6].

Reactive power and voltage control is not considered in this study.

II. GRID STRUCTURE

An island grid with distributed renewable energy sources (distributed power generation, DG) is investigated. It is assumed that all DG units are current sources without grid building capability. Furthermore directly coupled gensets (e.g.

driven by vegetable oil) and Battery Storage Systems (BSS) are available. The complete system is monitored and controlled by a microgrid controller (MGC). In Fig. 1, the investigated grid structure is illustrated.
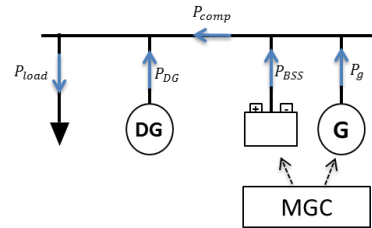
Fig. 1. Island grid consisting of consumers (load), distributed renewable energy sources (DG), gensets, battery storage systems (BSS) and a microgrid controller (MGC).

The active power consumption of the grid is summarized to P_{load} whereas P_{DG} is the sum of all DG. For an equilibrium of power, the compensation power P_{comp} is introduced:

$$P_{\text{comp}} = P_{\text{load}} - P_{\text{DG}}. \qquad (1)$$

The power deviation is compensated by gensets (P_g) as well as Battery Storage Systems (P_{BSS}):

$$P_{\text{comp}} = P_g + P_{\text{BSS}}. \qquad (2)$$

For grid building and frequency control, at least one genset resp. BSS must be in operation. For load sharing, the conventional concept of primary and secondary control is used. For active power sharing, the following dependency between active power and frequency is implemented:

$$P_v(f) = P_{0,v} - k_{f,v} \cdot (f - f_{0,v}) \qquad (3)$$

where $f_{0,v}$ and $P_{0,v}$ are the setpoints for frequency and power for each component v. The frequency droop factor $k_{f,v}$ defines the relation between active power and frequency deviation.

For primary control, the second part of the relation shown in (3), $k_{f,v}(f - f_{0,v})$ is responsible to stabilize the grid. Depending

* Corresponding author.
E-mail: andreas.armstorfer@hs-kempten.de

on the droop factor $k_{f,v}$ active power is supplied for a certain frequency deviation. As this control needs to react very fast, it is implemented directly in the component controller. A load depending frequency deviation is acceptable.
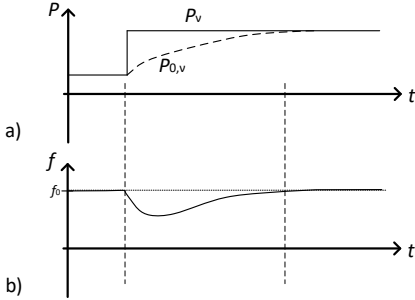
Fig. 2. Primary and secondary control; a) active power and active power setpoint; b) grid frequency.

The secondary control is changing the setpoint $P_{0,v}$ with a slow time constant to reach the original frequency again (Fig. 2).

III. SECONDARY CONTROL

Besides primary control, the active power setpoint $P_{0,v}$ of each component v is set by the secondary control which is much slower than the primary control. In the study presented in this paper, $P_{0,v}$ is based on load and DG prediction.

For dimensioning of the control system, several conditions are defined:

- It is assumed that the consumed energy per day is higher than the energy produced by DG:

$$\int_0^{T_{end}} P_{comp}(t')dt' > 0 \qquad (4)$$

whereas $T_{end} = 24\,\text{h}$.

- The BSS is not able to consume or generate energy for a very long time. Hence after a certain periodical time span T_{end}, e.g. 1 day, it is assumed:

$$\int_0^{T_{end}} P_{BSS}(t')dt' = 0 \qquad (5)$$

$$\int_0^{T_{end}} P_{comp}(t')dt' = \int_0^{T_{end}} P_g(t')dt' \qquad (6)$$

- The genset power P_g is always positive (no power feedback):

$$P_g \geq 0 \qquad (7)$$

- It is assumed that gensets as well as BSS can feed the grid alone with respect to power, that means without renewable energy generation. Measurements in a real system show clearly that due to cloudy sky PV power as an example for DG can decrease from 80 % to 20 % within less than one minute. This fact necessitates an immediate take-over of the load by the BSS for at least a short period of time.

- The energy stored in the BSS is defined as $E_{BSS}(t)$ and depends on the initial stored energy $E_{BSS,0}$ and on the integral of the BSS power:

$$E_{BSS}(t) = E_{BSS,0} - \int_0^t P_{BSS}(t')dt' \qquad (8)$$

Self-discharge is neglected.

$P_{BSS} > 0$ if the BSS is delivering power.
Another common representation for the energy stored in a BSS is the State of Energy (SOE) [7]:

$$SOE(t) = \frac{E_{BSS}(t)}{E_{BSS,total}} \qquad (9)$$

where $E_{BSS,total}$ is the total capacity of the BSS at the time of operation.

- The energy $E_{BSS}(t)$ that needs to be stored has to be in the range of :

$$E_{BSS,min} \leq E_{BSS}(t) \leq E_{BSS,max} \qquad (10)$$

resp.

$$SOE_{min} \leq SOE(t) \leq SOE_{max} \qquad (11)$$

IV. MICROGRID CONTROLLER SETUP

The MGC presented in this work is a superordinate controller for the operation of microgrid facilities (BSS, gensets) and responsible for the application planning (Fig. 3).
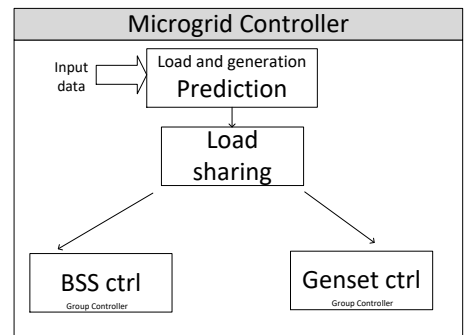
Fig. 3. Structure of the microgrid controller (MGC).

28

The MGC consists of group controllers for BSS and gensets as well as a block for load sharing between BSS and gensets. As a fundamental for load sharing planning, the electrical consumption (load) and the volatile DG production are predicted (prediction block). As the DG sources have no grid building capability, at least one BSS or genset must always be in operation.

A. Prediction

The power consumption P_{load} as well as the volatile electricity generation P_{DG} are predicted. Many conditions and effects need to be taken into account. In the literature several methods are described [8]–[13], but this subject is not part of this study. Thus a prediction of the compensation power P_{comp} can be determined according to (1). At times of higher production than consumption (P_{comp} negative), the BSS must be capable to store the excess energy. Therefore it needs to be ensured that the stored energy is within the limits defined in (10) resp. (11).

B. Load Sharing Planning

The difference between P_{load} (consumption) and P_{DG} (volatile generation) needs to be compensated by the gensets and/or the BSS.

For the compensation power P_{comp} it has to be distinguished between sections where $P_{comp} \geq 0$ and where $P_{comp} < 0$. Therefore the predicted curve P_{comp} is divided into i different sections. The borders t_i of the sections are determined by a zero-crossing method. The energy of each section can be calculated by:

$$E_i = \int_{t_{i-1}}^{t_i} P_{comp}(t') dt' \qquad (12)$$

Fig. 4a shows an example for the predicted curve P_{comp}. It can be divided up into 5 sections. In the first, third and fifth, P_{comp} is positive. In section two and four it is negative, that means that power needs to be absorbed. As gensets cannot absorb power (7), the BSS need to be charged. It has to be ensured that the BSS always have enough free capacity. In other words the SOE needs to be small enough before the charging period. The amount of energy in the 5 sections is calculated to $E_1, \ldots, E_5$.

For this reason, at the time t_1 resp. t_3 the BSS must have enough residual capacity to store the energy E_2 resp. E_4. Under consideration of (10), the following conditions must be fulfilled (Fig. 4b):

$$E_{BSS,min} \leq E_{BSS}(t_1) \leq E_{BSS,max} - E_2 \qquad (13)$$

$$E_{BSS,min} \leq E_{BSS}(t_3) \leq E_{BSS,max} - E_4 \qquad (14)$$

Consequently, at the time t_2 resp. t_4 the stored energy of the BSS $E_{SOC}(t)$ is in the range of:
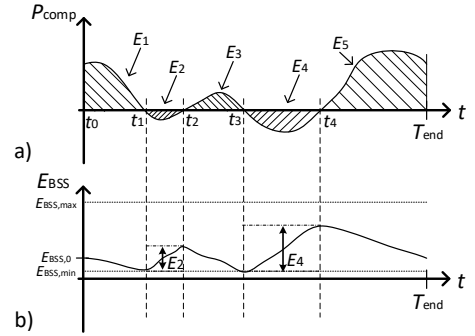
Fig. 4. Example for compensation power and the related stored energy of the BSS.

$$E_{BSS,min} + E_2 \leq E_{BSS}(t_2) \leq E_{BSS,max} \qquad (15)$$

$$E_{BSS,min} + E_4 \leq E_{BSS}(t_4) \leq E_{BSS,max} \qquad (16)$$

As a general approach for (13)–(16), $E_{BSS}(t_i)$ at the beginning of the charging period needs to be in the range of:

$$E_{BSS,min} \leq E_{BSS}(t_i) \leq E_{BSS,max} - E_{i+1} \qquad (17)$$

After charging periods, $E_{BSS}(t_i)$ is in the range of:

$$E_{BSS,min} + E_i \leq E_{BSS}(t_i) \leq E_{BSS,max} \qquad (18)$$

As maximum renewable energy feed-in is one main goal, the BSS should always be able to store the excess energy completely. Thus it is necessary to keep the SOE at a low level, as low as possible but as high as necessary to fulfill the required demands of the following periods. Before a period in which the BSS will be charged, the SOE should be at SOE_{min}.

Besides this, at the time $t = 0$ the curve for E_{BSS} is defined to:

$$E_{BSS}(t = 0) = E_{BSS,0} \qquad (19)$$

Depending on (2) and (5), at time the $t = T_{end}$ the value of E_{BSS} should reach again $E_{BSS,0}$:

$$E_{BSS}(t = T_{end}) = E_{BSS,0} \qquad (20)$$

Next, the power setpoint curves for the BSS $P_{BSS}(t)$ as well as for the gensets $P_g(t)$ are estimated.

Therefore it is distinguished between ranges of $P_{comp} \leq 0$ (case a) and $P_{comp} > 0$ (case b).

Case a) $P_{comp} \leq 0$: in times when P_{comp} is negative, no gensets are feeding in ($P_g = 0$). Hence the BSS power in this time range is equal:

$$P_{BSS}(P_{comp} \leq 0) = P_{comp} \qquad (21)$$

Case b) For ranges of $P_{comp} > 0$, the load sharing depends on the predicted energy until the BSS is charged again.

Therefore the load sharing factor k_{BSS} is introduced. In the following it is defined by the share of energy that can be delivered by the BSS in the time range from t_i to t_{i+1} divided by the total compensation energy E_{comp} in the same period:

$$k_{BSS,i} = \frac{E_{BSS}(t_i) - E_{BSS,\min}(t_{i+1})}{E_{comp}(t_{i+1}) - E_{comp}(t_i)} \qquad (22)$$

where t_i and t_{i+1} are the borders of the time range of a block with positive P_{comp}. In the example shown in Fig. 4 the ranges are:

- from t_0 to t_1,
- from t_2 to t_3,
- and from t_4 to T_{end}.

Before an interval in which the BSS needs to be charged according the prediction, SOE must be kept low enough, ideally at $SOE_{\min}$. This fact defines $E_{BSS}(t_i)$ respectively $k_{BSS,i}$. In other words, it determines the participation of BSS in the load sharing. Additionally an uncertainty in both, load resp. generation prediction, must be taken into account.

If the available energy of the BSS is greater than the needed energy, $k_{BSS,i}$ is limited to:

$$0 \leq k_{BSS,i} \leq 1 \qquad (23)$$

In that case, the gensets are not in operation in this interval. This leads to the following BSS and genset power for the section i:

$$P_{BSS}(t) = k_{BSS,i} \cdot P_{comp}(t) \text{ for } t_i \leq t \leq t_{i+1}; \qquad (24)$$

$$P_g(t) = (1 - k_{BSS,i}) \cdot P_{comp}(t) \text{ for } t_i \leq t \leq t_{i+1}; \qquad (25)$$

Now for the whole predicted time range the BSS' SOE as well as genset and BSS power are set. If the BSS is not capable to store the excessive energy completely, further concepts like DG feed-in reduction or additional loads such as power-to-heat systems are necessary, but this is not part of the presented work.

C. Group Controllers

If more than one genset unit or BSS unit exist, a group controller is in charge of optimum operation of these components. Depending on the requested power, one or more units are in operation. Other conditions like minimum power, minimum time in operation, redundancy but also environmental aspects like noise emission can be taken into account. The dimensioning depends highly on the local circumstances where the island grid is installed and need to be adapted individually.

The group controller also allows changing of the droop factors of each unit with respect to primary control.

V. SIMULATION

The concept of load sharing by SOE prediction described above is simulated using the software Matlab.

It is basing on the prediction of the load P_{load} as well as of the DG P_{DG}. The prediction data have a resolution of 15 minutes for a time span of 24 hours.

It is assumed that the sum of the maximum active power of all the BSS is higher than the maximum value of P_{comp}. For $P_{comp} > 0$ the same is assumed for the gensets.

The BSS dimensioning is described in Table I, according to a real Li-Ion based storage system in the village Wildpoldsried in the south of Germany [14]–[16].

TABLE I
BSS SIMULATION PARAMETERS

Total Energy Capacity	165 kWh
Max. State of Energy	0.8
Min. State of Energy	0.2
Initial SOE	0.3

In this study, 4 different scenarios are investigated by simulation. The predicted load curve P_{load} (standard load profile H0 for households) for an annual electricity demand of 560 MWh is shown in Fig. 5a.
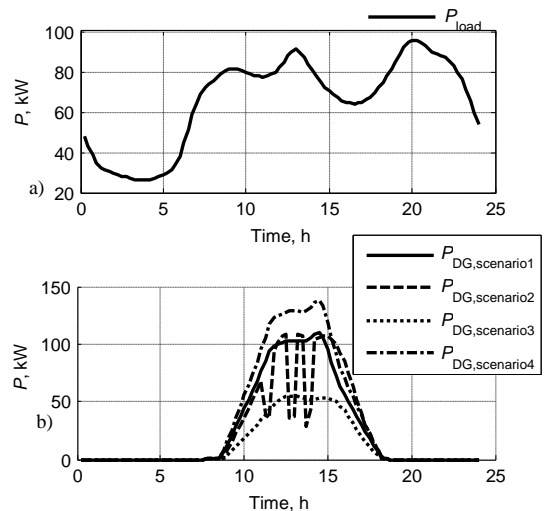
Fig. 5. a) Load prediction curve for 1 day; b) four different scenarios for the DG curve for 1 day.

Further for all assumed scenarios the DG curve (P_{DG}) can be seen in Fig. 5b. The amount of generated energy as well as the maximum power generated by DG is shown in Table II. For each scenario, the compensation power P_{comp} is calculated out of P_{load} and P_{DG} according to (1).

TABLE II
DG CHARACTERISTICS FOR INVESTIGATED SCENARIOS

Scenario	Total Energy, kWh	Max. Power, kW
1	631.2	110.6
2	592.9	108.9
3	333.7	54.8
4	789.0	138.3

A. Scenario 1

The predicted power P_{comp} defined as the difference between P_{load} and P_{DG} has to be balanced by BSS and gensets. It is illustrated for scenario 1 in Fig. 6.
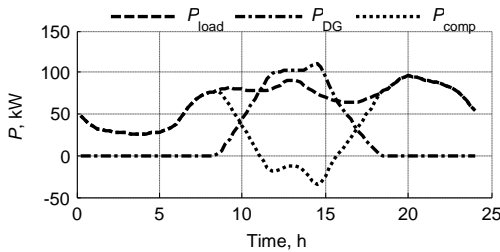
Fig. 6. Prediction curve for P_{load}, P_{DG} and the resulting P_{comp} (scenario 1).

It can be seen that the BSS has to absorb power in the time range between approx. 11h and 16h ($P_{comp} < 0$). In this time period, the genset is not in operation ($P_g = 0$). The simulation results for scenario 1 are shown in Fig. 7.

To reach SOE_{min} before the charging period, the BSS is discharged in the interval between 0h and 11h with $k_{BSS} = 0.04$. That means that approx. 4 % of P_{comp} is supplied by the BSS while 96 % is supplied by the genset. In the next period (from 11 h to 16 h), the genset is off while the BSS is charged (from $SOE = 0.2$ to $SOE = 0.7$). In the period from 16 h to 24 h, the BSS is discharged with approx. 12 % of P_{comp} to reach again the initial $SOE = 0.3$ at the time 24 h.

B. Scenario 2

For scenario 2, the resulting curve for P_{comp} is shown in Fig. 8. It is assumed that the decentralized generation has a high volatile behavior. This also effects P_{comp}.

The results for P_{BSS}, P_g and P_{comp} are shown in Fig. 9a. It can be seen clearly that the power fluctuation in the time period between 12.5h and 16h is completely covered by the BSS. The gensets are off during this period ($P_g = 0$).
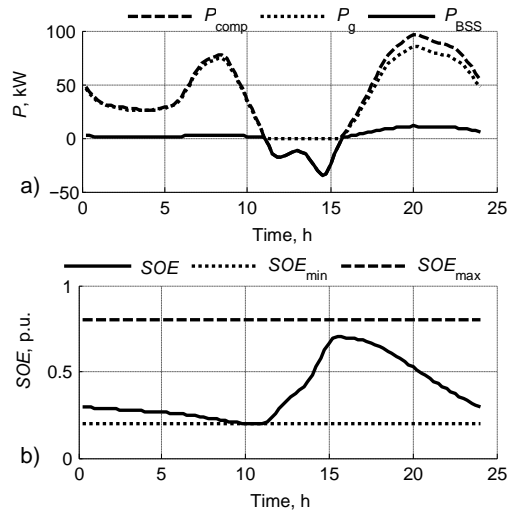
Fig. 7. a) BSS and genset power curve for 1 day. b) resulting SOE curve for scenario 1.
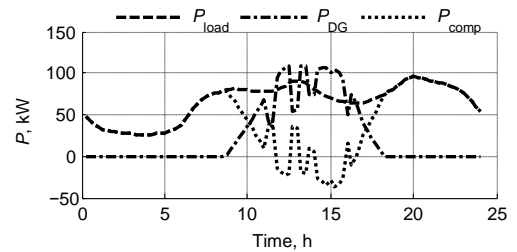
Fig. 8. Prediction curve for P_{load}, P_{DG} and the resulting P_{comp} (scenario 2).
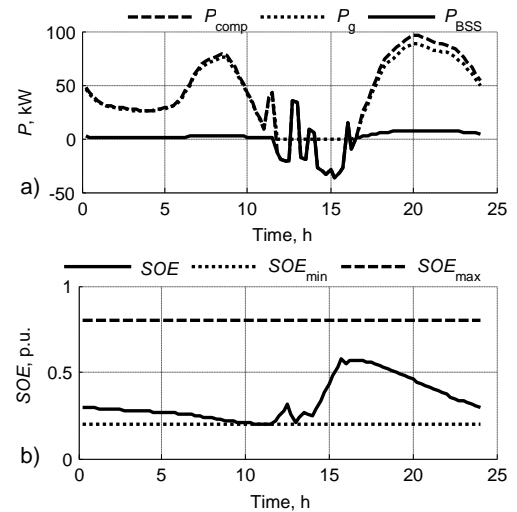
Fig. 9. a) BSS and genset power curve for 1 day. b) Resulting *SOE* curve (scenario 2).

C. Scenario 3

In scenario 3, the electrical load is always higher than the power fed in by DG (Fig. 10).
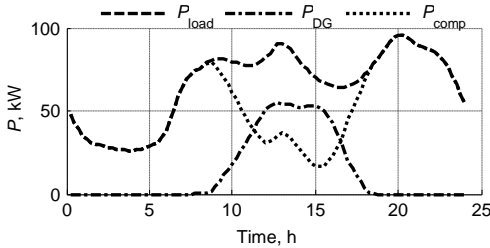
Fig. 10. Prediction curve for P_{load}, P_{DG} and the resulting P_{comp} (scenario 3).
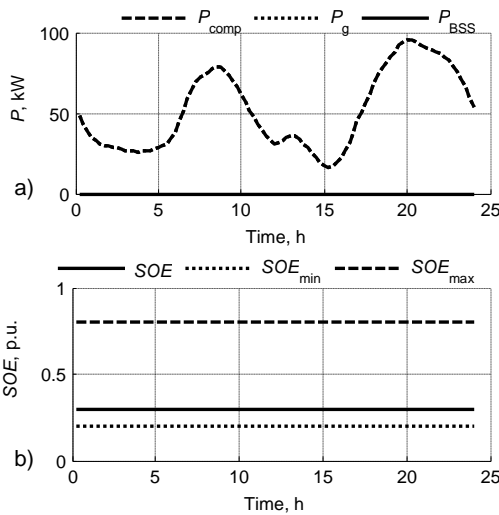
Fig. 11. a) BSS and genset power curve for 1 day. b) Resulting SOE curve (scenario 3).

Hence the renewable power is consumed by the load at all times. As the BSS cannot generate energy (2), it will not increase the amount of usable renewable energy when looking at a full day.

For that reason the BSS is not used for load sharing (Fig. 11). The predicted SOE stays constant. Nevertheless, fast changes of power (primary control) will be covered by BSS.

D. Scenario 4

In the last scenario, a high DG feed-in is assumed (Fig. 12). In Fig. 13 it can be seen that the BSS capacity is not sufficient for the predicted DG generation. At maximum, the BSS needs to store 205 kWh which is more than the rated capacity. Therefore other steps are necessary for a stable operation of the island grid. This could be for example a reduction of DG generation or the usage of further loads, such power-to-heat systems. These methods are not described in the frame of this study.

VI. CONCLUSION

In this study first steps of a concept for load sharing prediction and BSS scheduling in small island grids are presented. The main goal is the complete usage of the volatile renewable power generation by application of battery storage systems (BSS). All the renewable energy should be used to reduce the operation of conventional power sources such as gensets. Simulation results for SOE prediction are shown for different scenarios. Fast changes of power (primary control) are not taken into account in the simulation.

This work presents a method for optimum dimensioning and operation of batteries in non-interconnected microgrids with a high penetration of renewable energy sources.
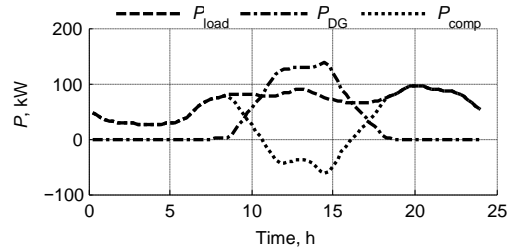
Fig. 12. Prediction curve for P_{load}, P_{DG} and the resulting P_{comp} (scenario 4).
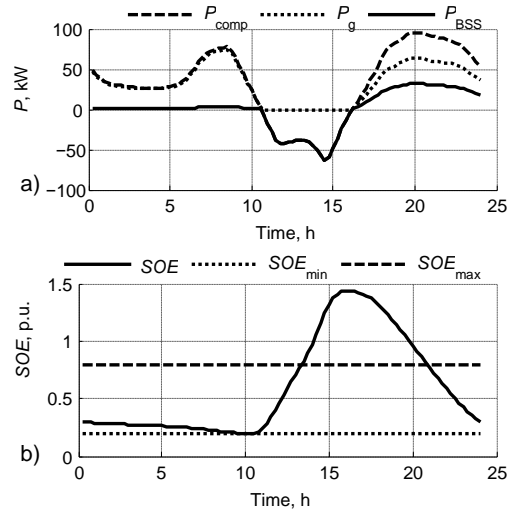
Fig. 13. a.) BSS and genset power curve for 1 day. b.) Resulting SOE curve (scenario 4).

REFERENCES

[1] D. Oeding and B. Oswald, *Elektrische Kraftwerke und Netze*. 2011.
[2] A. J. Schwab, *Elektroenergiesysteme*, 3. Auflage. Springer Berlin Heidelberg, 2012.
[3] J. Rocabert, A. Luna, F. Blaabjerg, and P. Rodríguez, "Control of Power Converters in AC Microgrids," *IEEE Transactions on Power Electronics*, vol. 27, no. 11, pp. 4734–4749, Nov. 2012. https://doi.org/10.1109/tpel.2012.2199334
[4] K. De Brabandere, B. Bolsens, J. Van den Keybus, A. Woyte, J. Driesen, and R. Belmans, "A Voltage and Frequency Droop Control Method for Parallel Inverters," *IEEE Transactions on Power*

32

Electronics, vol. 22, no. 4, pp. 1107–1115, Jul. 2007. https://doi.org/10.1109/tpel.2007.900456

[5] S. Nourollah, A. Pirayesh, and F. Aminifar, "Combinational scheme for voltage and frequency recovery in an islanded distribution system," *IET Generation, Transmission & Distribution*, vol. 10, no. 12, pp. 2899–2906, Sep. 2016. https://doi.org/10.1049/iet-gtd.2015.1302

[6] S. Krishnamurthy, T. M. Jahns, and R. H. Lasseter, "The operation of diesel gensets in a CERTS microgrid," *2008 IEEE Power and Energy Society General Meeting - Conversion and Delivery of Electrical Energy in the 21st Century*, Jul. 2008, pp. 1–8. https://doi.org/10.1109/pes.2008.4596500

[7] Y. Zhang, R. Xiong, H. He, and W. Shen, "Lithium-Ion Battery Pack State of Charge and State of Energy Estimation Algorithms Using a Hardware-in-the-Loop Validation," *IEEE Transactions on Power Electronics*, vol. 32, no. 6, pp. 4421–4431, Jun. 2017. https://doi.org/10.1109/tpel.2016.2603229

[8] M. Ceci, R. Corizzo, F. Fumarola, D. Malerba, and A. Rashkovska, "Predictive Modeling of PV Energy Production: How to Set Up the Learning Task for a Better Prediction?," *IEEE Transactions on Industrial Informatics*, vol. 13, no. 3, pp. 956–966, Jun. 2017. https://doi.org/10.1109/tii.2016.2604758

[9] G. Sideratos and N. D. Hatziargyriou, "An Advanced Statistical Method for Wind Power Forecasting," *IEEE Transactions on Power Systems*, vol. 22, no. 1, pp. 258–265, Feb. 2007. https://doi.org/10.1109/tpwrs.2006.889078

[10] H.-T. Yang, C.-M. Huang, Y.-C. Huang, and Y.-S. Pai, "A Weather-Based Hybrid Method for 1-Day Ahead Hourly Forecasting of PV Power Output," *IEEE Transactions on Sustainable Energy*, vol. 5, no. 3, pp. 917–926, Jul. 2014. https://doi.org/10.1109/iciea.2014.6931220

[11] A. Dolara, S. Leva, M. Mussetta, and E. Ogliari, "PV hourly day-ahead power forecasting in a micro grid context," *2016 IEEE 16th International Conference on Environment and Electrical Engineering (EEEIC)*, Jun. 2016, pp. 1–5. https://doi.org/10.1109/eeeic.2016.7555636

[12] Y. Hosoda and T. Namerikawa, "Short-term photovoltaic prediction by using H∞ filtering and clustering," *2012 Proceedings of SICE Annual Conference (SICE)*, Akita, 2012, pp. 119–124.

[13] A. Shakya, S. Michael, C. Saunders, D. Armstrong, P. Pandey, S. Chalise, and R. Tonkoski, "Solar Irradiance Forecasting in Remote Microgrids Using Markov Switching Model," *IEEE Transactions on Sustainable Energy*, vol. 8, no. 3, pp. 895–905, Jul. 2017. https://doi.org/10.1109/tste.2016.2629974

[14] "IREN2", [Online]. Available: http://www.iren2.de

[15] R. Köberle, K. Mayr, B. Rindt, T. Sowa, D. Buchstaller, A. Armstorfer, and H. Biechl, "IREN2: Zukunftsfähige Netze zur Integration Regenerativer Energiesysteme," in *ETG-Fb. 145: Von Smart Grids zu Smart Markets 2015*, 2015.

[16] A. Armstorfer, H. Biechl, B. Alt, H. Müller, R. Sollacher, D. Most, A. Szabo, R. Köberle, and M. Fiedeldey, "Einsatz von Batteriespeichern in Smart Grids – Operation of Battery Storage Systems in Smart Grids," *Int. ETG-Kongress*, pp. 1–8, 2013.

Andreas Armstorfer received his Dipl. ing. (FH) and M.Eng. degree from Kempten University of Applied Sciences in 2011 respectively 2015. Since 2011 he is working as a researcher at the Institute of Electrical Power Systems (IEES) of the University of Applied Sciences Kempten and is currently a PhD student at Tallinn University of Technology, Estonia.

His main research focus is on modeling, simulation and control as well as stability analysis of Micro Grids with a high penetration of renewable energy sources taking into account inverters, rotating machines as well as battery storage systems.

Postal address: University of Applied Sciences Kempten, Institute of Electrical Power Systems (IEES), Bahnhofstrasse 61, 87435 Kempten, Germany.

Helmuth Biechl received his Dipl. ing. Univ. and M.Sc. degree from the Technical University of Munich (TUM) in 1985 and his Dr. ing. and PhD degree in 1989 also from the Technical University of Munich. From 1989 till 1994 he was a developing and planning engineer and a group leader at the companies Siemens and E.ON.

Since 1994 he is a full professor at the University of Applied Sciences Kempten in Germany and working on the field of electrical power systems, mainly electrical machines, drives, power transmission and distribution systems including batteries for power engineering application. Since 2011 he is the Director of the Institute of Electrical Power Systems (IEES). Since 2005, he is a Titular Professor at the Universidad Pontificia Bolivariana in Colombia where he got a doctor honoris causa degree in 2012. His main research interests are modeling, simulation and optimization of electrical power systems. He has published more than 40 international scientific papers and about 200 articles in technical magazines.

Postal address: University of Applied Sciences Kempten, Institute of Electrical Power Systems (IEES), Bahnhofstrasse 61, 87435 Kempten, Germany.

Argo Rosin received the Dipl. Eng., M.Sc. and Dr.sc.techn. degrees in electrical engineering from Tallinn University of Technology (TUT), Tallinn, Estonia, in 1996, 1998 and 2005, respectively. He is presently a Senior Researcher in the Department of Electrical Power Engineering and Mechatronics, TUT. He has published more than 70 scientific papers on energy management, control and diagnostic systems development and is the holder of a Patent in this application field. His research interests include modelling and simulation of power management and industrial control systems. He is member of IEEE Industrial Electronics Society, IEEE Power & Energy Society, and Estonian Association of Engineers.

Postal address: School of Engineering, Tallinn University of Technology, Ehitajate str. 5, 19086 Tallinn, Estonia.

33

Appendix 2

II

A. Armstorfer, H. Biechl, and A. Rosin. Analysis of black start strategies for microgrids with renewable distributed generation. *IECON Proceedings (Industrial Electronics Conference)*, pages 2121–2125, 2019

Mathematical Modeling and Evaluation of a Microgrid Demonstrator in Island Mode

Andreas Armstorfer[1,2], Nauman Beg[1], Ahmad Rahmoun[1,2], Argon Rosin[2], and Helmuth Biechl[1,2]

[1]Institute of Electrical Power Systems (IEES), University of Applied Sciences Kempten, Kempten, Germany
[2]School of Engineering, Tallinn University of Technology, Tallinn, Estonia[*]

Abstract

The research work presents an approach to set-up simplified mathematical models of microgrid components based on detailed models. The verification is done by a comparison with measurement results of a real system. Using simplified models allows an accurate analysis and optimization of the dynamic behavior of existing as well as planned microgrids. The paper shows simulation and measurement results for different combinations of microgrid components in island mode operation.

1 Introduction

Microgrids in island mode consisting of renewable energy sources, battery storage systems and gensets require droop control of voltage and frequency [1]. In the research project IREN2 [2, 3] funded by the German Federal Ministry of Economic Affairs and Energy (BMWi), a microgrid demonstrator is established to investigate the upcoming challenges in distribution grids due to the increase in small decentralized generation units (DGs) which will eventually replace conventional power plants. The demonstrator is set-up in Wildpoldsried, a village located in the southern Germany with a high amount of renewable energy generation. The demonstrator consists of a Li-Ion Battery Energy Storage System (BESS) with a maximum power of 300kVA and an energy capacity of 170kWh, two gensets with 100kVA resp. 500kVA rated power as well as a 150kW unsymmetrical ohmic load. Furthermore, a back-to-back voltage source converter (B2B-VSC) with a maximum power of 500kVA is used to emulate the volatile photovoltaic (PV) in-feed, specific load profiles or an unlimited energy storage system. The BESS, the gensets as well as the B2B-VSC can be operated in grid forming or grid following mode. With the global objective of a stable microgrid operation, a detailed model of each microgrid component is developed to evaluate fast dynamics as well as steady state behavior. To facilitate system level simulations, simplified models for each component with various levels of complexity need to be developed under consideration of the required applications. Realistic practical scenarios are defined using different combinations of microgrid components of the demonstrator under various operation modes. Further, a comparison between simulation and measurements is shown.

In section 2, the structure and specifications of the real microgrid components are presented as well as the simplification procedure for the developed electrical models. An overview of the control structure is also briefly discussed. Section 3 presents the simulation setup in the software PSCAD for the defined scenarios which refer to the discussed microgrid application. A comparison between simulation results and actual measurements at the demonstrator is shown and discussed. Finally, section 4 outlines further challenges and investigations regarding stable and optimum operation of future microgrids.

2 Microgrid components overview

2.1 Back-2-Back VSC (B2B-VSC)

A 500kVA B2B-VSC described in section 1 which interlinks the 20kV MV grid with the 400V LV microgrid is developed specifically for the discussed demonstration setup and serves multiple purposes. It is a 4 quadrant converter which is able to control active and reactive power flow between MV and LV grids. It can also emulate a storage system with infinite capacity or track a given load profile (P and Q) to generate PV in-feed into the microgrid.
Figure 1 shows an overview of the B2B-VSC including the MV resp. LV side. The VSCs of the B2B unit are connected to the 20kV MV grid resp. 400V LV microgrid through an AC filter and a Δ-Y transformer. Converter parameters along with the MV and LV side transformer specifications are summarized in **Table 1** and **Table 2** respectively. The MV VSC regulates the DC link voltage whereas the LV VSC has a droop control to regulate the microgrid voltage and frequency in grid forming mode. The control structure of the DC link voltage controller in the MV VSC comprises of a non-linear cascaded control scheme that is linearized around the operation DC link voltage. It is discussed in detail in [4, 5].
The detailed model of the B2B-VSC is simplified relative
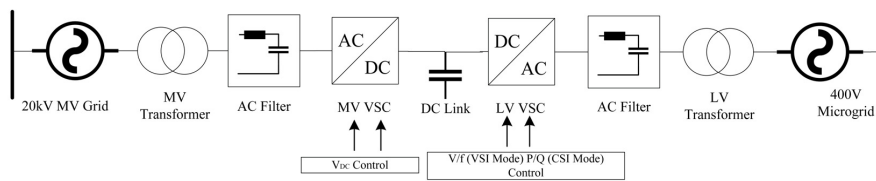
Figure 1 Overview of B2B-VSC

Table 1 B2B-VSC system parameters

Converter specifications	
Parameter	**Value**
Converter rating $[S_r]$	500kVA
Switching frequency $[f_{sw}]$	4kHz
Nominal voltage $[V_{nom,LL}]$	400V
DC link voltage $[V_{DC_o}]$	640V

Table 2 MV and LV VSC transformer parameters

LV 0.369kV/0.4kV Δ-Y transformer parameters	
Parameter	**Value**
Rating $[S_{r,LV}]$	750kVA
u_k	6%
P_{copper}	0.00888pu
$P_{no-load}$	0.00127pu

MV 0.4kV/20kV Y-Δ transformer parameters	
Parameter	**Value**
Rating $[S_{r,MV}]$	600kVA
u_k	6%
P_{copper}	0.00888pu
$P_{no-load}$	0.00127pu

to the 400V microgrid side by modeling the LV VSC with an ideal 3-phase AC voltage source and a lumped series impedance. The lumped impedance is the sum of the LV transformer winding resistance and the leakage inductance as well as the AC filter series impedance. It is given by

$$R_{lumped} = R_{filter} + R_{LV,trans}$$
$$L_{lumped} = L_{filter} + L_{LV,trans} \tag{1}$$

MV VSC and its disturbances on the LV VSC are ignored for simplification reasons. The simplified model is shown in **Figure 2** and the lumped impedance parameters are summarized in **Table 3**.
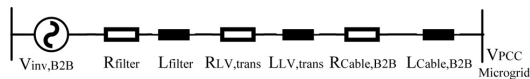
Figure 2 Simplified model of B2B-VSC

Table 3 Lumped parameters for simplified B2B-VSC model (400V microgrid side)

Parameter	Value
R_{lumped}	2.1565mΩ
L_{lumped}	152.24μH

The B2B-VSC can operate both in grid forming (VSI mode) or in grid following mode (CSI mode). In CSI mode, the B2B-VSC can operate as a grid following component to track P and Q set-points. The control structure in CSI mode is discussed in detail in [4]. In VSI mode, the converter tracks frequency and voltage set-points provided by the P/f resp. Q/V droop characteristics. A brief overview of the control structure in VSI mode based on peak voltage control in [6] is shown in **Figure 3**. The output active power P_1 and reactive power Q_1 of the B2B-VSC are used for the frequency and voltage droop curves which deliver the set-point frequency and voltage respectively. Value of the set-point voltage is passed to a *PI* controller after smoothing which regulates the actual output voltage of the inverter. The set-point frequency is passed to an integrator which generates the required phase of the inverter output voltage.
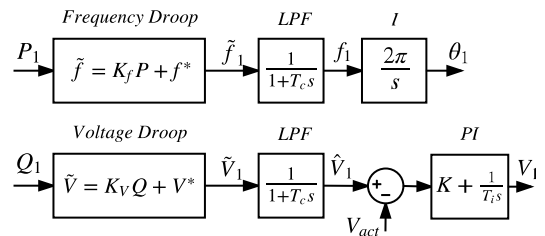
Figure 3 Frequency and voltage droop control structure

Where,
K_f P/f droop slope given in Hz/kW
K_V Q/V droop slope given in $V/kvar$
T_c Smoothing time constant
f^* Reference frequency under no load
V^* Reference voltage under no load

2.2 Battery Energy Storage System (BESS)

2.2.1 BESS Structure

The BESS consists of six strings connected in parallel as shown in **Figure 4**. Each two strings are connected to one of the three Lithium-Ion (Li-Ion) batteries. The first three strings S_1, S_2 and S_3 are connected to the first matching transformer (MT_1) whereas the next three strings S_4, S_5 and S_6 are connected to the second matching transformer (MT_2). Two isolating transformers IT_1, IT_2 are used to avoid circulating currents in the circuit of S_1 and S_6 as well as in the circuit of S_2 and S_5 which are connected to the same dc circuit.

The three phase two-winding matching transformer is used
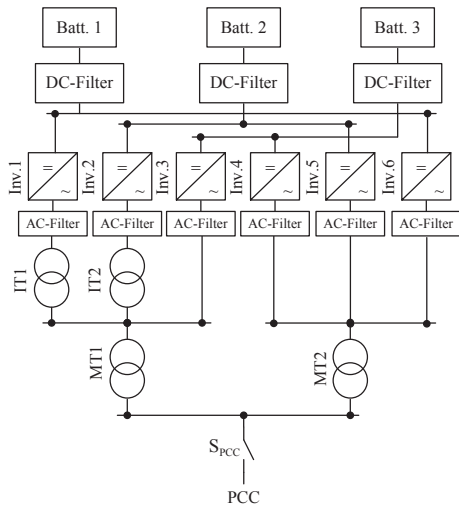
Figure 4 Structure of the BESS

Table 4 Specifications of the matching and isolating transformers.

257V/400V Δ-Y matching transformer	
Parameter	Value
Rating [$S_{r,LV}$]	165kVA
u_k	4.3%
P_{copper}	0.008484pu
$P_{no-load}$	0.002424pu
260V/260V Δ-Δ isolating transformer	
Parameter	Value
Rating [$S_{r,MV}$]	55kVA
u_k	3.73%
P_{copper}	0.021545pu
$P_{no-load}$	0.0029091pu

to adapt the inverter's low output voltage to the voltage of the LV grid. The specifications of both matching and isolating transformers are given in **Table 4**.

Each string consists mainly of a 3-phase inverter with a rated power of 55kVA followed by a LC filter in order to reduce current harmonics injected into the grid. The LC filter parameters are given in **Table 5**. The control structure for each string in VSI mode is similar to that described in section 2.1.

2.2.2 BESS Simulation Model

Due to the complex structure of the BESS, having a detailed model which takes into account the semiconductors of the inverter is only required for evaluating short time transients [7]. For applications where long time simulations ($T_{sim} > 10s$) are needed, a simplified model (**Figure 5**) consisting of a controlled voltage source (V_{eq}, f_{eq})

Table 5 LC-Filter specifications.

Parameter	Value
Serial inductance L_F	$160\mu H$
Serial resistance R_F	$16.4m\Omega$
Parallel capacitor C_F	$3.5\ \mu F$
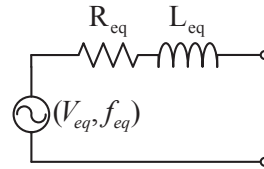
Figure 5 BESS equivalent model in VSI mode

and an equivalent impedance ($Z_{eq} = R_{eq} + jX_{eq}$) is extracted and implemented in PSCAD. The equivalent voltage and frequency (V_{eq} resp. f_{eq}) are controlled using the same droop curves $V_{eq} = K_V * (Q - Q_0) + V_0$ and $f_{eq} = K_f * (P - P_0) + f_0$ applied to the total active and reactive power (P_{out}, Q_{out}) of the BESS. The equivalent droop gains are defined under the assumption that the droop gains are equal for all strings, and they can be calculated based on equation 2. Based on this assumption, the output active and reactive power of the BESS is distributed equally on all strings in steady state operation. Therefore, the equivalent impedance can be calculated by $Z_{eq} = Z_1 \parallel Z_2 \parallel \cdots \parallel Z_6$. The parameters of the equivalent impedance are summarized in **Table 6**.

$$K_f[Hz/kW] = \frac{1}{K_p} \quad where \quad K_p[kW/Hz] = \sum_{i=1}^{6} k_p^i = 6 \cdot k_p$$

$$K_V[V/kvar] = \frac{1}{K_q} \quad where \quad K_q[kvar/V] = \sum_{i=1}^{6} k_q^i = 6 \cdot k_i$$

$$(2)$$

Table 6 Equivalent impedance of BESS

Parameter	Value
Serial inductance L_{eq}	$81\mu H$
Serial resistance R_{eq}	$7.7m\Omega$

2.3 Genset

A mathematical simulation model for a bio-fuel based genset in the discussed demonstrator setup is established. It consists of a prime mover (diesel engine) and a direct coupled synchronous machine. The dynamic behavior of the rotating system is mainly influenced by the inertia of the complete drive system whereas the voltage dynamics are influenced by the synchronous machine characteristics. The mathematical model of the generator is based on Park's equations. A subset of parameters is shown in **Table 7**. The frequency control of the genset is realized by a PI controller with droop characteristics which outputs the setpoint torque T_m for the prime mover as shown in **Figure 6**. Moreover, **Figure 7** shows the genset's voltage control with droop behavior which controls the current I_f in the

excitation winding. The frequency droop gain K_f is defined in $[Hz/kW]$ whereas the voltage droop gain K_V is set in $[V/kvar]$. Further, the frequency and voltage set-point at no load operation are defined as f^* resp. V_{LN}^*. P_{out} and Q_{out} are the actual active resp. reactive power measured at the PCC of the genset.
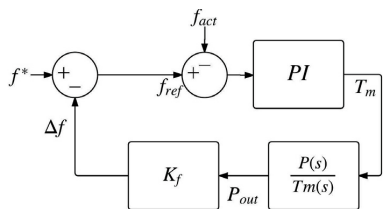
Figure 6 Frequency control including P/f droop
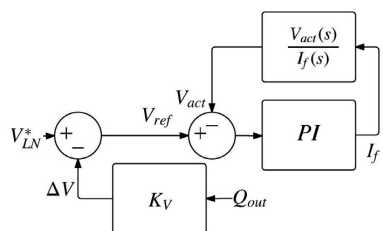
Figure 7 Voltage control including Q/V droop

Table 7 Subset of model parameters of the synchronous generator

Parameter	Value
Apparent power S_r	135kVA
Nominal voltage $V_{nom,LN}$	230V
Base angular frequency ω	314 rad/s
Inertia constant H	0.5s
Iron loss resistance R_{Fe}	300pu
Armature resistance R_a	0.013pu
Unsaturated d-axis reactance x_d	2.2pu
Unsaturated q-axis reactance x_q	1.36pu
Transient d-axis reactance x_d'	0.154pu
Sub-transient d-axis reactance x_d''	0.076pu
Sub-transient q-axis reactance x_q''	0.284pu
Transient d-axis time constant T_d'	0.039s
Sub-transient d-axis time constant T_d''	0.0085s

3   Simulation and Measurements

An overview of the demonstrator site is shown in **Figure 8**. Measurements are only taken for the demonstrator area shown in **Figure 8**. This means that the switch S_1 is open and isolates the demonstrator site from the residential area. The cable impedance between the components is ignored which effects to a greater extent the reactive power flow
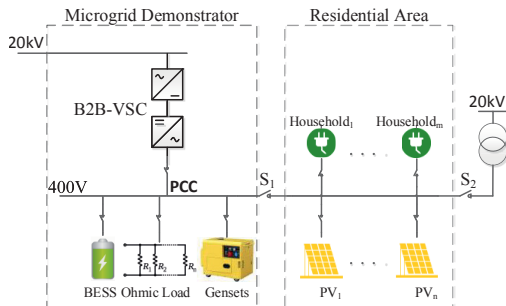
Figure 8 Demonstrator overview

between the components. This will be briefly explained during the discussion of the results. The case scenarios tested are given as follows:

Scenario 1: (SC1)   BESS and B2B-VSC in VSI mode with an applied active load profile on the load bank
Scenario 2: (SC2)   BESS and genset in VSI mode with an applied active load profile on the load bank
Scenario 3: (SC3)   BESS, B2B-VSC and genset in VSI mode with an applied active load profile on the load bank
Scenario 4: (SC4)   BESS and genset in VSI mode and the B2B-VSC is in CSI mode with a given active power generation profile and a base load of 48kW at the point of common coupling (*PCC*)

The applied load profile for passive load at the *PCC* in scenario 1, 2 and 3 is shown in **Figure 9**. In **Figure 10**, the active power generation profile of the B2B-VSC is depicted. Droop parameters of all components are fixed for all scenarios. They are summarized in **Table 8**.
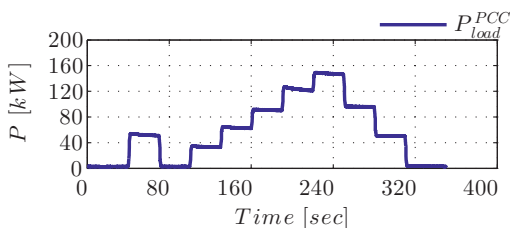
Figure 9 Load profile in SC1, SC2 and SC3
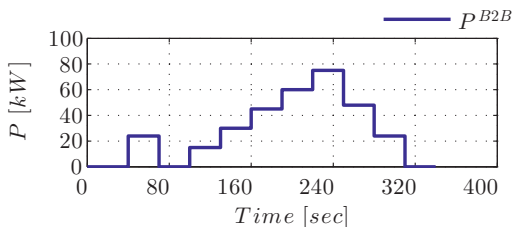
Figure 10 Generation profile of B2B-VSC in SC4

In SC1, BESS and B2B-VSC are working in VSI mode. Profiles for the output active power P, terminal voltage
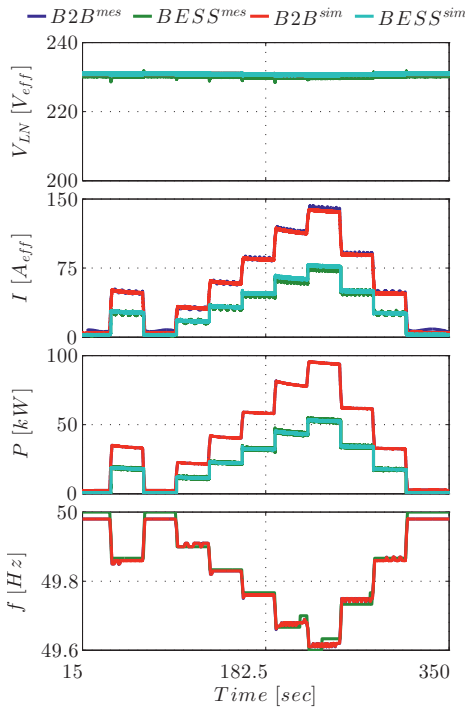
Figure 11 SC1- Measurement and simulation results
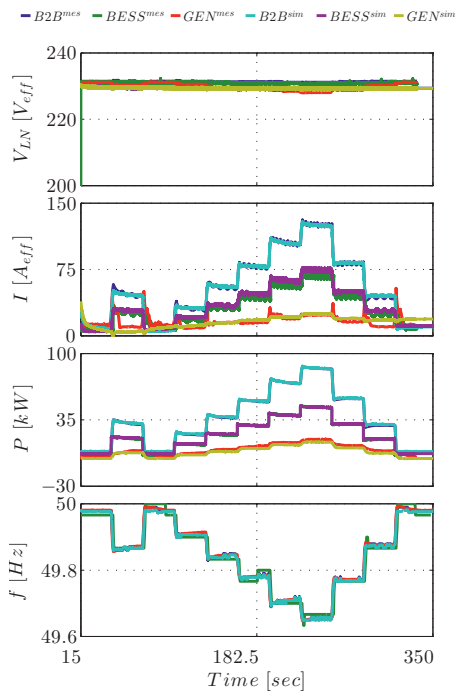
Figure 13 SC3- Measurement and simulation results
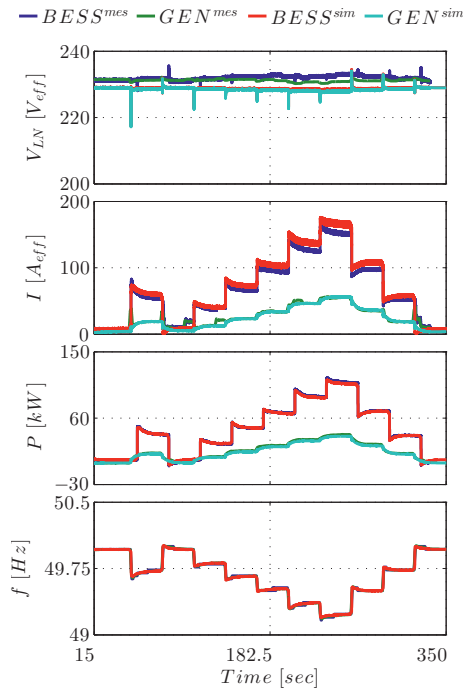
Figure 12 SC2- Measurement and simulation results
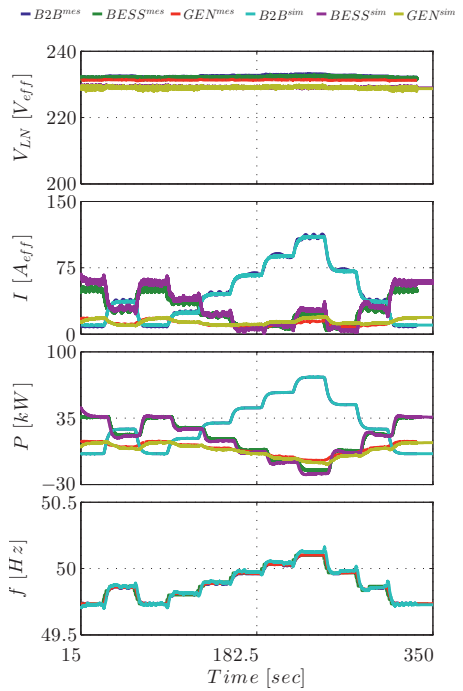
Figure 14 SC4- Measurement and simulation results

Table 8 Droop parameters

Parameter	B2B-VSC	BESS	Genset
K_f [Hz/kW]	0.004	0.0067	0.02
K_V [$V/kvar$]	0.02	0.0333	0.05
f^* [Hz]	50	50	50
V_{LN}^* [V]	230	230	230
T_c [ms]	100	100	x

Table 9 Maximum relative error

Scenario 1			
Relative error	**B2B-VSC** [%]	**BESS** [%]	**Genset** [%]
ΔP_{max}	0.7	1.03	x
Δf_{max}	0.02	0.02	x
ΔV_{max}	0.17	0.3	x
ΔI_{max}	4	7.47	x
Scenario 2			
ΔP_{max}	x	2.4	0.71
Δf_{max}	x	0.06	0.04
ΔV_{max}	x	1.7	1.166
ΔI_{max}	x	4.9	2.074
Scenario 3			
ΔP_{max}	3.4	4.89	16.6
Δf_{max}	0.02	0.02	0.02
ΔV_{max}	0.95	0.91	0.79
ΔI_{max}	2.27	7.5	25.31
Scenario 4			
ΔP_{max}	0	10.2	18.6
Δf_{max}	0.04	0.04	0.06
ΔV_{max}	1.63	1.334	0.951
ΔI_{max}	2.57	14.9	26.5

V_{rms}, output current I_{rms} as well as frequency f for both simulations and measurements are shown in **Figure 11** which matches quite closely. In **Figure 12** (SC2), the deviation between the simulation and measured results for current at high loads is due to the cable impedance mismatch in the simulation model between the component terminals and the *PCC*. This results in additional reactive power flow between the components. To compensate it, the set point voltage $\hat{V}$ of individual components can be adjusted in the simulation model. During low loads, voltage drop in the cable impedance is insignificant and hence simulation and measured values are close to each other. In **Figure 13** (SC3), small spikes can be observed in the measured currents of the genset during load steps. It is due to the adjustment of its terminal voltage to minimize reactive power flow which causes abrupt current change. Results for SC4 are shown in **Figure 14** where the B2B-VSC covers a part of the base load (48kW) according to its generation power profile. The residual load is distributed between BESS and genset according to their droop curves. The presented results clearly demonstrates the load sharing among the participating components.

4   Summary and Conclusions

The presented results of the different quasi-stationary scenarios confirm the validity of the system approximation when using simplified component models of the single components. Values of maximum relative error given by equation 3 for important quantities are summarized in **Table 9**. A higher value of ΔI_{max} in SC3 and SC4 is caused by the relatively high reactive current mismatch between simulation and measurement values in the case of small active load conditions. Load distribution between components in relation to their droop parameters shows proper working of the droop control. The aspect of reactive power mismatch between simulation and measurement is caused by the cable impedance between components and *PCC* which is not considered in the simulation. The effect of short time dynamics on the system stability as well as stability issues during parallel operation of components will be investigated in the future work.

$$\Delta X_{max}[\%] = \frac{max|X_{sim} - X_{mes}|}{|X_{mes,pk}|} \cdot 100 \qquad (3)$$

5   Literature

[1] J. Stanojevic, A. Djordjevic, M.Mitrovic,"Influence of Battery Energy Storage System on Generation Adequacy and System Stability in Hybrid Micro Grids" in Environment Friendly Energies and Applications (EFEA) 2016, 2016

[2] R. Köberle, K. Mayr, B. Rindt, T. Sowa, D. Buchstaller, A. Armstorfer, and H. Biechl, "IREN2: Zukunftsfähige Netze zur Integration Regenerativer Energiesysteme," in Von Smart Grids zu Smart Markets 2015, 2015.

[3] "IREN2 official website." [Online]. Available: www.iren2.de.

[4] N. Beg, A. Rahmoun, A. Armstorfer, A. Rosin, and H. Biechl, "Determination methods for controller parameters of back-to-back converters in electric power grids," in 2016 Electric Power Quality and Supply Reliability (PQ), 2016, pp. 157–164.

[5] C. Bajracharya, M. Molinas, "Understanding of tuning techniques of converter controllers for VSC/HVDC," in Nordic Workshop on Power and Industrial Electronics 2008, 2008.

[6] Siemens, "SINAMICS S120/S150," Listenhandbuch, pp. 2152–2153

[7] A. Rahmoun, A. Armstorfer, A. Rosin, and H. Biechl, "Modelling and Simulation of an Energy Storage System for a Smart Grid Including Power Electronics and Battery Model," in IRES 2015 Poster Exhibition, 2015.

Appendix 3

III

N. Beg, A. Armstorfer, A. Rosin, and H. Biechl. Mathematical modeling and stability analysis of a microgrid in island operation. *2018 International Conference on Smart Energy Systems and Technologies (SEST)*, pages 1–6, 2018

Mathematical Modeling and Stability Analysis of a Microgrid in Island Operation

Nauman Beg[1], Andreas Armstorfer[1,2], Argo Rosin[2], and Helmuth Biechl[1,2]

[1]Institute of Electrical Power Systems (IEES), University of Applied Sciences Kempten, Kempten, Germany
[2]School of Engineering, Tallinn University of Technology, Tallinn, Estonia*

Abstract—**The paper presents the dynamic modeling and stability analysis of Low Voltage (LV) microgrids in island operation using simplified electrical models for Distributed Generations (DGs). These simplified models are used to simulate electrical (excluding switching) as well as control dynamics for each DG to setup and facilitate system level simulations. The paper focuses on the operation of components in grid forming mode using a droop based primary control. This approach is applied on a real microgrid which is set up within the IREN2 research project framework. The demonstrator incorporates a Li-Ion based Battery Energy Storage System (BESS), a plant oil driven generator as well as a BESS emulator. First, a brief overview of the detailed model for each DG including its simplification is discussed. Next, the microgrid is set up using simplified models for transient simulations and the comparison with real measurements is shown for different microgrid topologies. Later, overall microgrid stability i.e. various instability aspects in LV island grids are discussed. In this regard, an analytical method based on Eigenvalue analysis for identification of stability limits for relevant electrical and control parameters and under various loading conditions is presented. Finally, the complete microgrid model is simulated for potential instable conditions and a comparison with the analytical solution is shown.**

Index Terms—**Primary droop control, Power system stability, Quasi Steady State (QSS) analysis, Power system dynamics, Microgrids, Island grid.**

I. INTRODUCTION

In order to operate island microgrids with a high penetration of volatile renewable energy sources in combination with gensets and BESSs, voltage and frequency control (also known as primary droop control) is required. Topology specific investigation is needed for stable and robust operation of island grids. This requires detailed dynamic modeling of both electrical and control system of each participating DG as well as cable impedances. In this regard, a real microgrid demonstrator setup shown in Fig. 1 that incorporates a 300kVA Li-Ion based BESS, a 500kVA BESS emulator, a 100kVA genset as well as an 150kW unsymmetrical resistive load bank is investigated [1]–[3]. In section II, a brief description of the detailed component model of each DG is given. Later, a comparison between detailed and simplified models for each DG which are developed and used for the complete microgrid simulations is
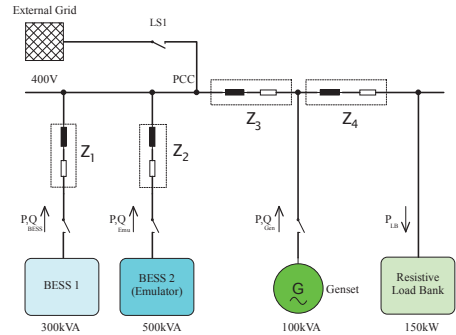
Fig. 1: Overview of microgrid demonstrator in Wildpoldsried

shown. In section III, transient microgrid simulations using simplified models for the DGs discussed in section II are compared with measured results for scenarios that are defined based on the participating DGs. Section IV highlights various instability aspects in LV microgrids and presents an analytical method based on QSS and Eigenvalue analysis to determine stability limits for the discussed microgrid application. The model of the microgrid discussed in section III is simulated for potential instable conditions and the stability trend is verified analytically. Section V summarizes key aspects of this work and concludes with remarks related to stability considerations in LV island grids.

All simulations are done in the software package PSCAD.

II. COMPONENT DESCRIPTION

A. BESS (BSS1)

1) Electrical and control structure: The BESS consists of six inverter strings connected in parallel as shown in Fig. 2. Each two strings are connected to one of the three Lithium-Ion (Li-Ion) batteries. The first three strings S_1, S_2 and S_3 are connected to the first matching transformer (MT_1) whereas the next three strings S_4, S_5 and S_6 are connected to the second matching transformer (MT_2). Two isolating transformers IT_1, IT_2 are used to avoid circulating currents in the circuit of S_1 and S_6 as well as in the circuit of S_2 and S_5 which are connected to the same dc circuit. The specification of the complete BESS is discussed in [4].

A simplified model of the BESS with respect to its behavior at the Point of Common Coupling (PCC) is shown in Fig. 3.
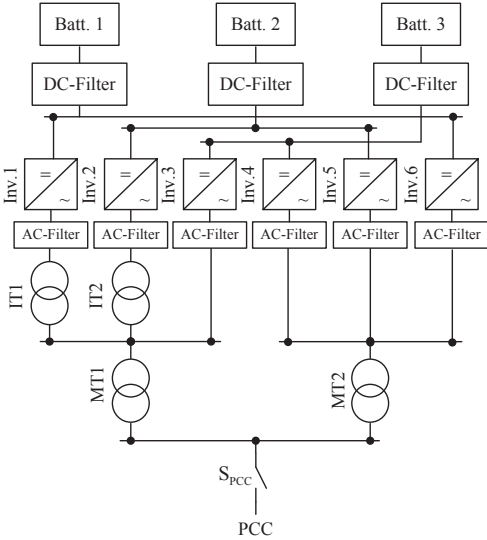
Fig. 2: Structure of the BESS

Fig. 4: Droop control overview [3]
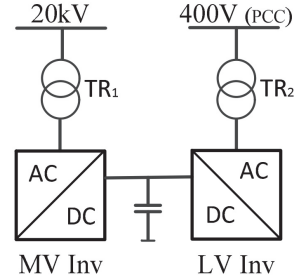
Fig. 5: Single Line Diagram (SLD) of BESS Emulator

Fig. 3: BESS equivalent model in VSI mode

It is modeled as a controlled voltage source and an equivalent impedance ($Z_{eq} = R_{eq} + jX_{eq}$) for all inverters. The equivalent voltage and frequency (V_{eq} resp. f_{eq}) of the controlled voltage source are controlled using the droop control method shown in Fig. 4 that is applied to the total active and reactive power (P_{out}, Q_{out}) of the BESS [5], [6]. The equivalent droop gains (K_p, K_q) resp. (K_f, K_V) are defined under the assumption that the individual droop gains (k_p, k_q) in each inverter string are identical and they can be calculated using eq. 1. Under this assumption, the output active and reactive power of the BESS is distributed equally on all strings for slow dynamics. Therefore, the equivalent impedance can be calculated from the individual impedances of each inverter as $\underline{Z}_{eq} = \underline{Z}_1 \parallel \underline{Z}_2 \parallel \cdots \parallel \underline{Z}_6$.

$$K_f[Hz/kW] = \frac{1}{K_p} \quad where \quad K_p[kW/Hz] = \sum_{i=1}^{6} k_p^i = 6 \cdot k_p$$

$$K_V[V/kvar] = \frac{1}{K_q} \quad where \quad K_q[kvar/V] = \sum_{i=1}^{6} k_q^i = 6 \cdot k_q$$
(1)

2) Simulation: The simplified model of BESS (Battery 1) in Fig. 2 is verified with its detailed counterpart as well as with the real measurements and is discussed in detail in [3].

B. BESS emulator (BSS2)

1) Electrical and control structure: A Back-to-Back station (B2B-VSC) coupled between 20kV Medium Voltage (MV) and 400V LV microgrid is emulated as a 2nd battery system with an infinite energy storage capacity. The model overview of B2B-VSC is shown in Fig. 5 and discussed in detailed in [4]. A simplified lumped equivalent parameter electrical model for the LV side inverter with respect to PCC is developed similar to the BESS model as shown in Fig. 3 [4]. As in BESS, it also integrates primary droop control for frequency and voltage regulation given in Fig. 4.

2) Simulation: To verify the simplified model of the BESS emulator with its detailed counterpart, an active load step P^{pcc} of 300kW is applied at the PCC. A comparison between detailed and simplified model for PCC voltage (peak value of the space phasor) and frequency (V^{pcc}, f^{pcc}) as well as active power at PCC (P^{pcc}) is shown in Fig. 6.

C. Genset

The investigated genset consists of a turbocharged prime mover driven by plant oil and a direct coupled synchronous generator with a rated power of 100kVA. The equivalent circuit for active power and frequency control is shown in Fig. 7. The engine is represented by a nonlinear torque model based on the rotational speed and a time constant (K_{mot}, T_{mot}). A PI controller is used for the speed control. As the genset is also used for primary control in island grids, a droop control is implemented (k_f, T_{kf}).

To verify the mathematical model of the genset, an active load profile is applied to the genset (by a resistive load bank, see Fig. 1). Fig. 8 shows the comparison between simulation results and measurement data for active power and frequency.
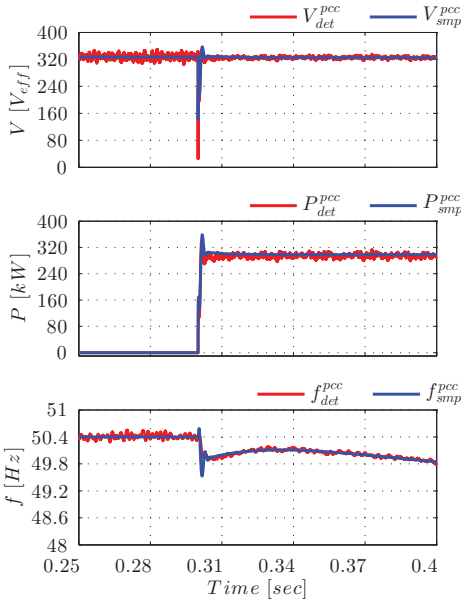
Fig. 6: Detailed versus simplified model of BSS2
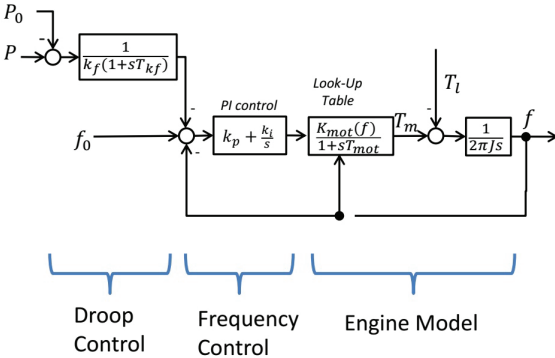
Fig. 7: Genset equivalent control circuit
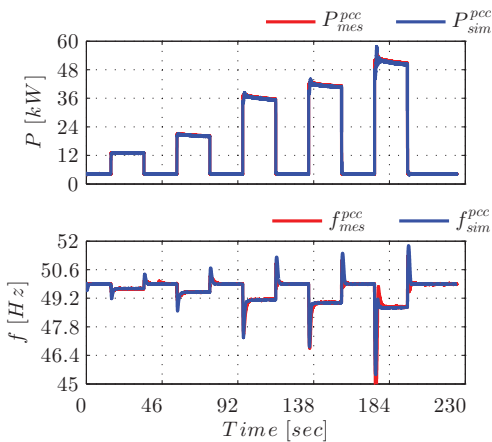
Fig. 8: Genset - Comparison of simulation results and measurements

III. MICROGRID SIMULATIONS

The simplified component models developed in section II are used to set up microgrid transient simulations on a QSS basis. Based on the participating DGs in these simulations, two distinct scenarios are defined:

A) Scenario 1: BSS1 and BSS2 with active load jump applied at PCC.

B) Scenario 2: BSS1, BSS2 and genset with active load jump applied at PCC.

The microgrid simulations done in PSCAD are verified with the actual measurements at the demonstrator. Active and reactive power output (P,Q) of each DG, the peak value of line-to-neutral voltage V_{LN} as well as the microgrid frequency f are shown for each scenario. The cable impedance between each DG and PCC is also included in the simulations. The default control parameters for all DGs are summarized in Table I.

TABLE I: Droop parameters for DGs

Parameter	BSS1	BSS2	Genset
Frequency droop $[K_f]$ $[kW/Hz]$	150	250	50
Voltage droop $[K_V]$ $[kvar/V]$	30	50	20
Smoothing time constant $[T_c]$ $[ms]$	100	150	–
No load frequency $[f^*]$ $[Hz]$	50	50	50
No load voltage $[V^*]$ $[V_{rms}]$	230	230	230

A. Scenario 1
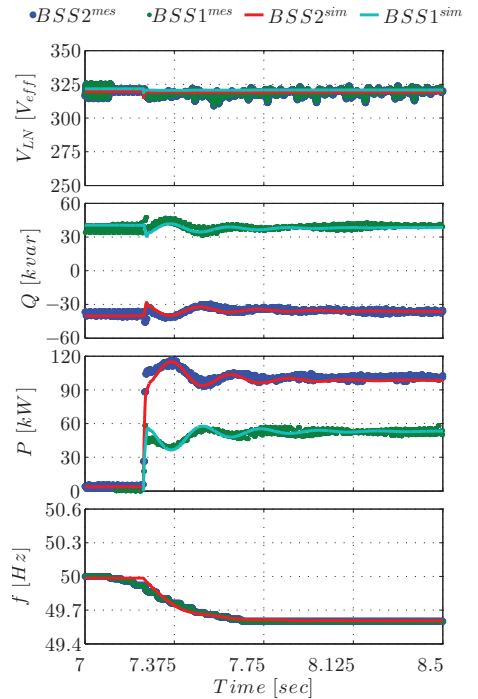
Fig. 9: Simulation vs measurements (Scenario 1)

In Scenario 1, BSS1 and BSS2 are operated together with the control parameters specified in Table I. An active power load step of 150kW is applied at the PCC. A comparison of transients for each component after the load jump for both simulation and real measurements are shown in Fig. 9.

B. Scenario 2

In Scenario 2, BSS1, BSS2 and genset are operated together with the control parameters specified in Table I. An active load step of 30kW (120kW$\rightarrow$ 150kW) is applied at the PCC. A comparison of transients for each component after the load jump for both simulation and real measurements are shown in Fig. 10 where superscripts M (measurement) and S (simulation) are used.
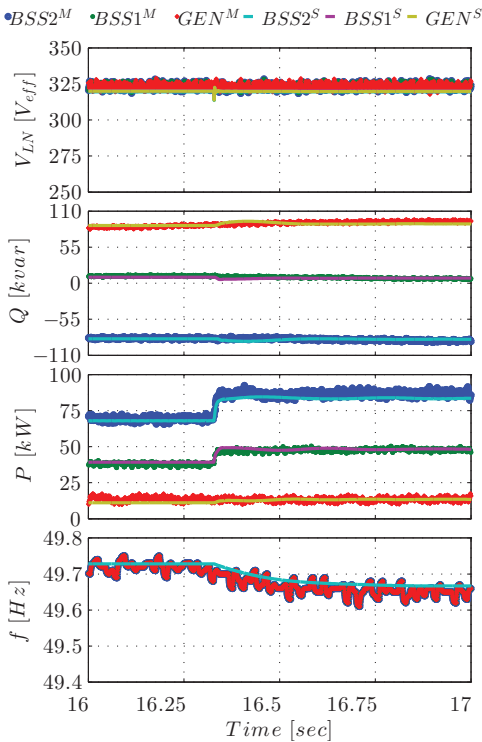
Fig. 10: Simulation vs measurements (Scenario 2)

IV. MICROGRID STABILITY

A. QSS (Quasi Steady State) approach

In this section, the effect of control and electrical parameters of the microgrid components on the overall system stability is modeled through Eigenvalue analysis which is based on the QSS approach. This analytical method is described for two DGs as shown in Fig. 11. Each DG is modeled as a controlled voltage source ($\underline{V}_1$ resp. $\underline{V}_2$) and is connected to the load $\underline{Z}_L$ through a line impedance ($\underline{Z}_1$ resp. $\underline{Z}_2$). The control in each DG is based on the droop control scheme as shown in Fig. 4.
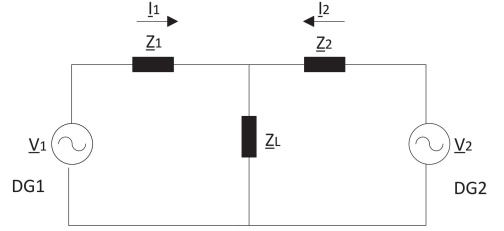
Fig. 11: Investigated system for stability analysis

Steady state currents $\underline{I}_1$ and $\underline{I}_2$ for the system in Fig. 11 are given by eq. 2.

$$\begin{bmatrix} \underline{I}_1 \\ \underline{I}_2 \end{bmatrix} = \begin{bmatrix} \underline{Z}_L + \underline{Z}_2 & -\underline{Z}_L \\ -\underline{Z}_L & \underline{Z}_L + \underline{Z}_1 \end{bmatrix} \begin{bmatrix} \underline{V}_1 \\ \underline{V}_2 \end{bmatrix} \cdot \frac{1}{\underline{Z}_1\underline{Z}_L + \underline{Z}_2\underline{Z}_L + \underline{Z}_1\underline{Z}_2}$$ (2)

In general, complex rms voltage (line-to-neutral) and line current of the nth DG are given as

$$\underline{V}_n = V_{nx} + jV_{ny}$$
$$\underline{I}_n = I_{nx} + jI_{ny}$$ (3)

Steady state apparent power of nth DG is given by

$$\underline{S}_n = 3 \cdot \underline{V}_n \cdot \underline{I}_n^*$$ (4)

From eq. 3 and eq. 4 follows

$$P_n = 3 \cdot V_{nx} \cdot I_{nx} + 3 \cdot V_{ny} \cdot I_{ny}$$
$$Q_n = -3 \cdot V_{nx} \cdot I_{nx} + 3 \cdot V_{ny} \cdot I_{ny}$$ (5)

The total change in active and reactive power ($\Delta P_n, \Delta Q_n$) using small signal analysis is described by

$$\begin{bmatrix} \Delta P_n \\ \Delta Q_n \end{bmatrix} = 3 \cdot \underbrace{\begin{bmatrix} I_{nx,0} & I_{ny,0} & V_{nx,0} & V_{ny,0} \\ -I_{ny,0} & I_{nx,0} & V_{ny,0} & -V_{nx,0} \end{bmatrix}}_{Operating\ pt} \begin{bmatrix} \Delta V_{nx} \\ \Delta V_{ny} \\ \Delta I_{nx} \\ \Delta I_{ny} \end{bmatrix}$$ (6)

The magnitude (V_n) and phase (ϕ_n) of the voltage $\underline{V}_n$ in eq. 3 is a non-linear function of V_{nx} and V_{ny} respectively and is given by

$$V_n = \sqrt{V_{nx}^2 + V_{ny}^2}$$
$$\phi_n = \arctan \frac{V_{ny}}{V_{nx}}$$ (7)
$$\omega_n = \dot{\phi}_n$$

From Fig. 4, the change in frequency and voltage for the nth DG is given by

$$non-smoothed \begin{cases} \Delta\tilde{\omega}_n = -K_{Pn} \cdot \Delta P_n \\ \Delta\tilde{V}_n = -K_{Qn} \cdot \Delta Q_n \end{cases}$$ (8)

$$smoothed \begin{cases} \Delta\omega_n = \dfrac{1}{1 + sT_{c,n}} \cdot \Delta\tilde{\omega}_n \\ \Delta V_n = \dfrac{1}{1 + sT_{c,n}} \cdot \Delta\tilde{V}_n \end{cases}$$ (9)

The droop coefficients K_{Pn} and K_{Qn} are the inverse of the coefficients K_{fn} and K_{Vn} respectively as given in eq. 1. The linearization of eq. 7 for V_n and ϕ_n around the operation point $(V_{nx,0}, V_{ny,0}, \phi_{n,0})$ as well as using eq. 8 in eq. 9 results in a state space representation as [7]

$$\begin{bmatrix} \Delta\dot{\omega}_n \\ \Delta\dot{V}_{nx} \\ \Delta\dot{V}_{ny} \end{bmatrix} = \underline{A}_n \cdot \begin{bmatrix} \Delta\omega_n \\ \Delta V_{nx} \\ \Delta V_{ny} \end{bmatrix} + \underline{B}_n \cdot \begin{bmatrix} \Delta P_n \\ \Delta Q_n \end{bmatrix} \quad (10)$$

where $\underline{A}_n$ and $\underline{B}_n$ are the system and input co-efficient matrices respectively. Using eq. 6 in eq. 10 and rearranging results in

$$\begin{bmatrix} \Delta\dot{\omega}_n \\ \Delta\dot{V}_{nx} \\ \Delta\dot{V}_{ny} \end{bmatrix} = \underline{A}_{int,n} \cdot \begin{bmatrix} \Delta\omega_n \\ \Delta V_{nx} \\ \Delta V_{ny} \end{bmatrix} + \underline{B}_{int,n} \cdot \begin{bmatrix} \Delta I_{nx} \\ \Delta I_{ny} \end{bmatrix} \quad (11)$$

The eq. 11 can be extended for two DGs. Using eq. 2 together with eq. 3 in the resulting system gives the closed loop system as

$$\begin{bmatrix} \Delta\dot{\omega}_1 \\ \Delta\dot{V}_{1x} \\ \Delta\dot{V}_{1y} \\ \Delta\dot{\omega}_2 \\ \Delta\dot{V}_{2x} \\ \Delta\dot{V}_{2y} \end{bmatrix} = \underline{A}_{closed} \cdot \begin{bmatrix} \Delta\omega_1 \\ \Delta V_{1x} \\ \Delta V_{1y} \\ \Delta\omega_2 \\ \Delta V_{2x} \\ \Delta V_{2y} \end{bmatrix} \quad (12)$$

The poles of the closed loop "system matrix" $\underline{A}_{closed}$ give the Eigenvalues for the system in Fig. 11 [8]. The "system matrix" is a function of the operating point values of the electrical and control parameters given as

$$\underline{A}_{closed} = f(\underline{Z}_1, \underline{Z}_2, \underline{V}_{1,0}, \underline{V}_{2,0}, \underline{I}_{1,0}, \underline{I}_{2,0}, \omega_{1,0}, \omega_{2,0}, K_{P1}, K_{P2},$$
$$K_{Q1}, K_{Q2}, T_{c1}, T_{c2}) \quad (13)$$

B. Simulations

The effect of the control parameters (K_f, K_V and T_c) on the stability of the island microgrid as well as the stability limits which are evaluated through the QSS approach and simulations are shown for two DGs (BSS1 and BSS2). Later, simulation results for the microgrid incorporating all DGs as shown in Fig. 1 are presented to investigate potential instable conditions. The starting control values for all DGs are summarized in Table. I

1) Effect of K_f and T_c: To demonstrate the effect of K_f on the microgrid stability, the $K_{f,BSS2}$ in Fig. 12 is reduced from the default starting value to the limiting value ($15kW/Hz$) where the system becomes oscillatory. The control parameters of BSS1 are kept constant throughout the simulation. The Eigenvalues for the QSS approach around the marginal stable operating point are shown in Fig. 14. The oscillation frequency of the conjugate pole pair evaluated using the QSS approach is close to the simulation value. The inaccuracy in the real value of the conjugate pair can be related to the increasing inaccuracy of the small signal analysis close to unstable operating regions.
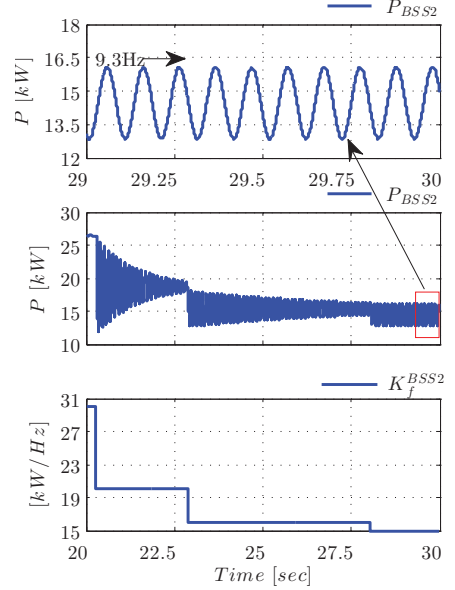
Fig. 12: Effect of $K_{f,BSS2}$ (BSS1, BSS2) $T_{c,BSS2}$=150ms
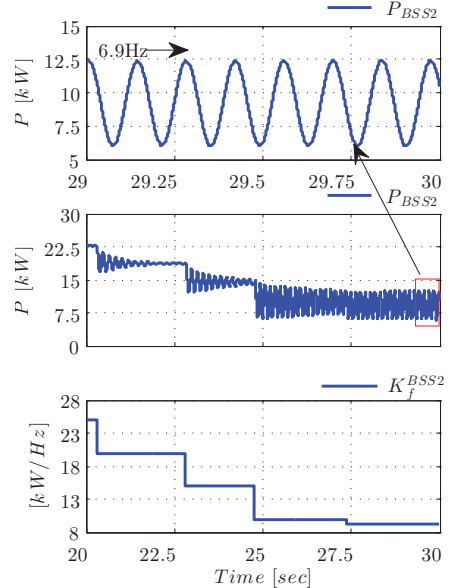
Fig. 13: Effect of $K_{f,BSS2}$ (BSS1, BSS2) $T_{c,BSS2}$=500ms
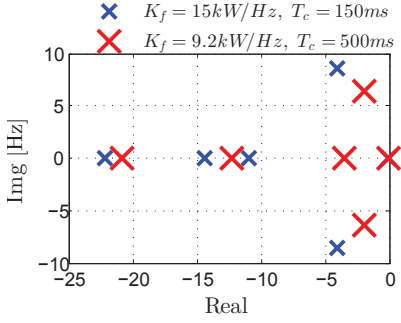
Fig. 14: Eigenvalues for $K_{f,BSS2}$
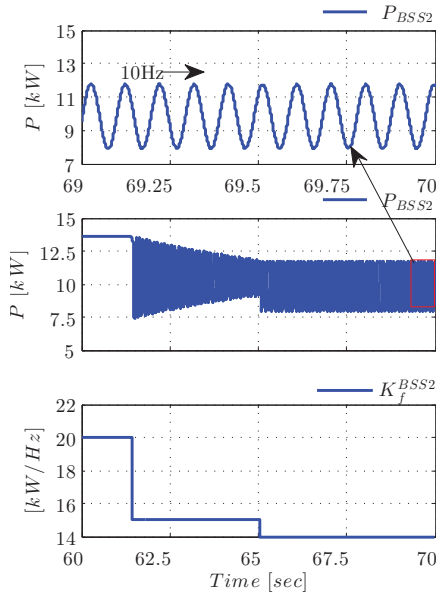
Fig. 15: Effect of $K_{f,BSS2}$ (BSS1, BSS2, GEN) $T_{c,BSS2}$=150ms

In Fig. 13, the value of $T_{c,BSS2}$ is changed to 500ms and the K_f of BSS2 is again reduced till the new limiting value ($9.2kW/Hz$) is reached where the system becomes oscillatory. The analytical result for the limiting value of $K_{f,BSS2}$ is shown in Fig. 14. The higher value of T_c improves the stability margins. A similar trend is observed for $K_{f,BSS1}$ and $T_{c,BSS1}$ which is not shown here.

The effect of the parameter $K_{f,BSS2}$ on the microgrid stability with all three DGs in operation is simulated in Fig. 15. The default control parameters are summarized in Table I. The limiting value of $K_{f,BSS2}$ in Fig. 15 is similar as in Fig. 12 with operation of only BSS1 and BSS2 but the oscillation frequency in later case is higher ($10Hz$). The increased oscillation frequency with genset reduces the robustness of the microgrid.

2) Effect of K_V: The value of K_V only effects the system stability for small values of $K_f < 20kW/Hz$ and is not further discussed here.

V. SUMMARY AND CONCLUSION

In this paper, a stability analysis of a real islanded microgrid demonstrator is discussed both analytically and through simulations. The considerations during modeling and validation phase are summarized as follows

1. A transient electrical and control model for each DG is developed [2], [3].
2. Transient microgrid simulations using simplified electrical models for DGs are shown.
3. Stability limits of the discussed microgrid application are evaluated through Eigenvalue analysis which is based on QSS approach. The analytical results are verified with the simulations.

The key outcomes are as follows:

1. The simplified models used sufficiently capture the transient behavior of real DGs and enable simulations of complex microgrid topologies.
2. The active power droop K_f effects the microgrid stability for smaller values. The limiting value of K_f is improved by selecting higher value of smoothing time constant T_c. The effect of K_V is only relevant for very small values of K_f ($< 20kW/Hz$) .
3. The QSS approach is valid only for analyzing systems with transients that are in the order of 7 to 10 times slower than the fundamental frequency .

REFERENCES

[1] R. Köberle, K. Mayr, B. Rindt, T. Sowa, D. Buchstaller, A. Armstorfer, and H. Biechl, "IREN2: Zukunftsfähige Netze zur Integration Regenerativer Energiesysteme," in ETG-Fb. 145: Von Smart Grids zu Smart Markets 2015, 2015.
[2] N. Beg, A. Rahmoun, A. Armstorfer, A. Rosin, and H. Biechl, "Determination methods for controller parameters of back-to-back converters in electric power grids," in 2016 Electric Power Quality and Supply Reliability (PQ), 2016, pp. 157–164.
[3] A. Rahmoun, A. Armstorfer, H. Biechl, and A. Rosin, "Mathematical Modeling of a Battery Energy Storage System in Grid Forming Mode," presented at 58th International Scientific Conference on Power and Electrical Engineering of Riga Technical University, Latvia, October 12-13, 2017.
[4] Armstorfer, A.; Beg, N.; Rahmoun, A.; Rosin, A.; Biechl, H., "Mathematical Modeling and Evaluation of a Microgrid Demonstrator in Island Mode," presented at Conference on Sustainable Energy Supply and Energy Storage Systems (NEIS 2017), Hamburg, Germany, September 21-22, 2017.
[5] Arangarajan Vinayagam, K. S. V. Swarna, Sui Yang Khoo, Aman Than Oo, Alex Stojcevski, "PV Based Microgrid with Grid-Support Grid-Forming Inverter Control-(Simulation and Analysis)," Smart Grid and Renewable Energy, Vol.08 No.01, 2017.
[6] Siemens, " SINAMICS S120/S150," Listenhandbuch, pp. 2152–2153
[7] A. Gkourntaras, Modeling Techniques and Control Strategies for Inverter Dominated Microgrids. Universitaetsverlag der TU Berlin, 2017.
[8] P. Kundur, Power system stability and control. New York: McGraw-Hill, 1994.

Appendix 4

IV

A. Armstorfer, H. Biechl, and A. Rosin. Energy scheduling of battery storage systems in micro grids. *The Scientific Journal of Riga Technical University - Electrical, Control and Communication Engineering*, 12(1):27–33, 2017

Analysis of Black Start Strategies for Microgrids with Renewable Distributed Generation

Andreas Armstorfer
Institute of Electrical Power Engineering
University of Applied Sciences Kempten
Kempten, Germany
andreas.armstorfer@hs-kempten.de

Helmuth Biechl
Institute of Electrical Power Engineering
University of Applied Sciences Kempten
Kempten, Germany
biechl@hs-kempten.de

Argo Rosin
Tallinn University of Technology
(Taltech)
Tallinn, Estonia
argo.rosin@taltech.ee

Abstract—**Microgrids with a high penetration of distributed generation (DG) in combination with energy storage systems (ESS), but also in combination with fuel-driven generation units (gensets) can be operated in on-grid mode, but also in off-grid mode (island operation). For grid restoration in island mode, a black start strategy is needed. This scientific work deals with a black start concept for island grids with a high amount of non-controllable DG units and non-controllable loads which is investigated by mathematical modeling and simulation for different scenarios. The assumed underlying control behavior of the DG units is described in the German application guide VDE-AR-N 4105. The corresponding mathematical modeling is presented and a verification by specific measurements is presented.**

Index Terms—**Microgrids, Distributed Generation, Black Start, Island Grid, Off-grid Mode**

I. INTRODUCTION

Low voltage microgrids operated in interconnected and non-interconnected mode are used as a part of a decentralized power system in the frame of the energy transition as described by the VDE-Study "The Cellular Approach" [1].

For off-grid systems, it is essential to build up the grid from zero or after major failures. But also in mainly on-grid microgrids, the black start can support the restart of a greater grid area if several small grid cells execute an independent black start and are resyncronized step by step (bottom-up approach).

Several black start strategies were already discussed, e.g. in [2]–[6], where controllable loads or a communication link to the DG systems are assumed.

In comparison, this study deals with the analysis of different black start strategies for microgrids consisting of non-controllable loads (as households), a high penetration of renewable distributed generation (DG) considering the German application guide VDE-AR-N 4105 [7] as well as energy storage systems (ESS) and fuel-driven generation units (gensets) as grid forming units.

The analysis is taking into account the active power sharing and frequency behavior at black start. Reactive power sharing and voltage stability is not taken into account. Resynchronization after a successful black start for on-grid operation is also not part of this work.

The estimated grid including the relevant assets is described in section II. Next, the investigated scenarios are presented and simulation results are shown in section III. Finally a conclusion is given in section IV. For the numeric simulation, the software DiGSILENT PowerFactory [8] is used .

II. DESCRIPTION OF THE INVESTIGATED GRID INCLUDING RELEVANT ASSETS

A. Estimated Grid

The estimated grid shown in Fig. 1 consists of energy storage systems (ESS, P_{ESS}), a generator set (genset, P_{GEN}), distributed generation (DG, P_{DG}) and electrical loads (aggregated to P_{load}). The ESS and the genset are operated in grid forming mode under consideration of droop control [9], [10]. The difference between electrical loads and DG is aggregated to the residual load (RES, P_{res}):

$$P_{res} = P_{load} - P_{DG} \qquad (1)$$
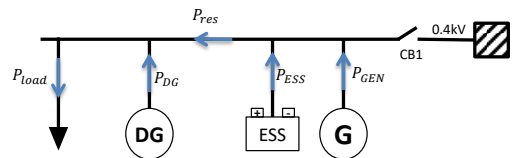
Fig. 1. Single Line Diagram of the Estimated Grid of the Microgrid.

B. Grid Forming Units

The estimated microgrid contains two different types of grid forming units. The ESS is based on power electronics whereas the genset is a rotational generator with speed control.

The ESS consist of Li-Ion cells, an inverter, a grid filter and a transformer. For the mathematical modeling, a simplified model basing on a controlled voltage source and an internal impedance is assumed [9].

The genset as a rotational asset consist of a turbocharged combustion engine fueled by plant oil and a direct coupled synchronous machine. For a constant frequency in steady state, a speed control is used [10].

For parallel operation of the grid forming units, an independent droop control is implemented for each unit [10], [12]–[14].
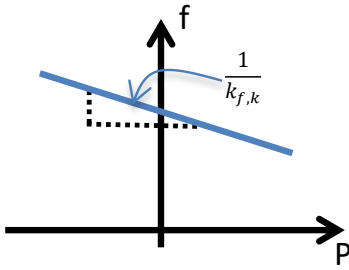
Fig. 2. Frequency/Active Power Dependency of Grid Forming Units.

As shown in Fig. 2, for each grid forming unit k an active power/frequency dependency under consideration of the droop factor $k_{f,k}$ is implemented. Mathematically it can be represented by:

$$f_k = f_{0,k} - \frac{1}{k_{f,k}}(P_k - P_{0,k}) \qquad (2)$$

with:

- f_k: resulting frequency
- P_k: active power feed-in
- $f_{0,k}$: no load frequency setpoint
- $P_{0,k}$: no load active power setpoint
- $k_{f,k}$: active power/frequency droop factor

In case of more than one grid forming unit with the P/f behavior as described above, the active power sharing depends on the droop factors $k_{f,k}$ respectively on the no load setpoints $P_{0,k}$ and $f_{0,k}$. In steady state, for two grid forming units the resulting active power P_{res} is devided into (if $f_{0,1} = f_{0,2}$):

$$P_1 = \frac{k_{f,1} \cdot P_{res} + k_{f,2} \cdot P_{0,1} - k_{f,1} \cdot P_{0,2}}{k_{f,1} + k_{f,2}} \qquad (3)$$

$$P_2 = \frac{k_{f,2} \cdot P_{res} + k_{f,1} \cdot P_{0,2} - k_{f,2} \cdot P_{0,1}}{k_{f,1} + k_{f,2}} \qquad (4)$$

The residual load P_{res} is supplied by both grid forming units (P_1 and P_2):

$$P_{res} = P_1 + P_2 \qquad (5)$$

C. DG units regarding VDE-AR-N 4105

1) Mathematical Modeling: A nonlinear mathematical model of a DG unit considering the German application guide VDE-AR-N 4105 [7] is set up. It describes the compulsory grid behavior of DG units which are connected to the public grid. Besides others, the start-up conditions, the active power feed-in limitation depending on frequency, the reactive power sharing as well as the behavior in case of grid failures is defined.

The nonlinear mathematical model for active power feed-in is basing on a state machine shown in Fig. 3.
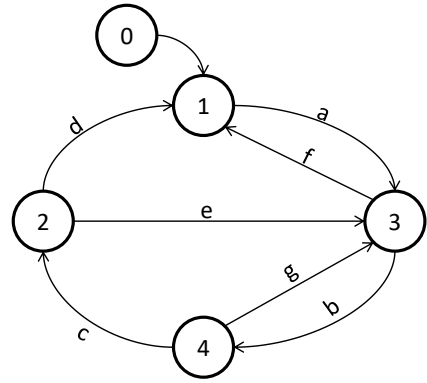
Fig. 3. Nonlinear DG Modeling in State Machine Representation.

The states $0 \ldots 4$ are defined as:

- 0: simulation start-up
- 1: no active power feed-in allowed ($P_{DG} = 0$)
- 2: normal operation (without power limitation)
- 3: active power reduction at over-frequency
- 4: active power feed-in ramp limiter

The conditions for the state transitions are:

- a: Grid frequency is in the range of $47.5Hz < f < 50.05Hz$ and voltage is in the range of $85\% \ V_r \leq V \leq 110\% \ V_r$ for at least 60s
- b: Grid frequency $f < 50.2Hz$
- c: Active power ramp up completed
- d: Grid frequency $f < 47.5Hz$
- e: Grid frequency $f > 50.2Hz$
- f: Grid frequency $f \geq 51.5Hz$
- g: Grid frequency $f > 50.2Hz$

The dependency of P_{DG} and f is shown in Fig. 4.
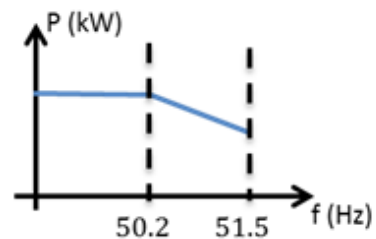
Fig. 4. P/f dependency for DG units regarding VDE AR-N 4105.

For grid frequencies in the range of $50.2Hz < f < 51.5Hz$ (state 3), the active power feed-in is reduced by a gradient of 40% per Hertz:

$$\Delta P_{DG} = 20 P_M \frac{50.2Hz - f}{50Hz} \qquad (6)$$

2122

where P_M is actual active power feed-in before the frequency exceeds $50.2Hz$ which leads to the power reduction.

2) Model Verification: The DG model is verified by characteristic measurements at a real PV system with a rated power of $6kWp$. A comparison of simulation and measurement results for the start-up behavior is shown in Fig. 5. At time t_0, the DG is connected to the grid. After a time period of $\Delta T = 60s$, (transition (a) from state 1 to 3), the active power ramp up is initiated (state 4, by transition (b)). In the real
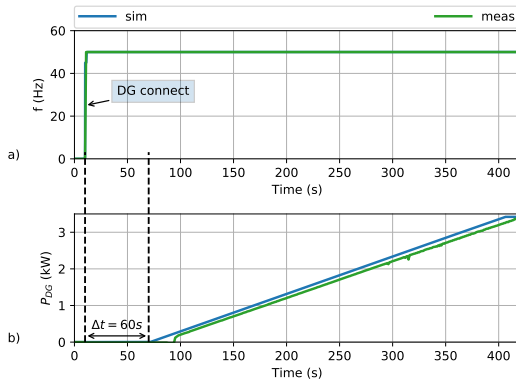
Fig. 5. Model Verification of the Start-Up Behavior at the Example of a PV system.

system investigated for this verification a time shift of approx. 5s (delay) for the power ramp up can be seen. This is allowed, as the application guide [7] defines a time period of *at least* 60s.

In Fig. 6 a comparison between simulation and measurement results of the active power feed-in depending on frequency is illustrated. An increase of frequency leads to a reduction of the active power feed-in regarding Eq. 6.

III. Black Start Analysis for different Scenarios

Different black start scenarios for microgrids with ESS, genset, non-controllable loads as well as DGs are analyzed by simulation based on verified mathematical models of DG, genset and ESS [9]–[11].

A. Droop Control Dimensioning

The following prerequisites for black start strategies for microgrids are taken into account:
1) grid forming units must be able to supply the maximum load step at black start
2) maximum usage of renewable DG units
3) minimized operation of gensets

As the DG active power feed-in is depending on the grid frequency and a maximum usage of renewable energy is proposed, the grid forming units' droop control has to be configured properly.
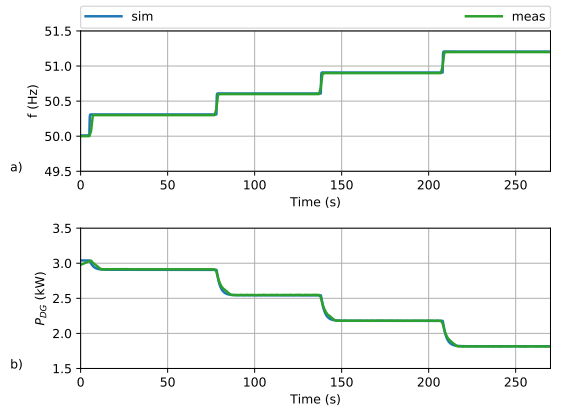
Fig. 6. Model Verification of the Active Power Feed-in Reduction depending on Frequency.

In general, the total droop factor of the microgrid need to be:

$$k_{f,total} \geq \frac{P_{DG,max} + P_0}{f_{max} - f_0} \qquad (7)$$

where $P_{DG,max}$ is the maximum power feed in of the DGs, P_0 is the no-load active power setpoint, f_{max} is the maximum allowed frequency before power de-rating (regarding [7]: $f_{max} = 50.2Hz$) and f_0 is the frequency setpoint of the grid forming units.

Further the grid frequency must exceed f_{min} for enabling of DG units feed in (VDE-AR-N 4105: $f_{min} = 47.5Hz$):

$$k_{f,total} \leq \frac{P_{load,max} - P_0}{f_0 - f_{min}} \qquad (8)$$

where $P_{load,max}$ is the maximum load which is expected as a worst case ($P_{DG} = 0$).

B. Scenario 1 - ESS as Grid Forming Unit

In the first scenario, the ESS is operated in grid forming mode. As a worst case, no load is assumed ($P_{load} = 0$). The maximum DG feed-in is assumed as $P_{DG,max} = 250kW$ whereas the ESS droop factor $k_{f,ESS}$ is varied from $600\frac{kW}{Hz}$ to $1500\frac{kW}{Hz}$ in discrete steps. In Fig. 7a the resulting frequency at the ESS for different droop factors $k_{f,ESS}$ are plotted; further Fig. 7b shows the resulting active power consumption by the ESS. At time $t = 0$, the ESS is powered on; at $t = 10s$, the ESS is connected with the DG. Regarding the DG start-up behavior described in Fig. 3, active power feed-in begins after 60s at time $t = 70s$ by a ramp of 10% per minute as it is compulsory by [7]. If the frequency exceeds 50.2Hz, the active power feed-in is reduced.

A low droop factor $k_{f,ESS}$ for frequency control effects a frequency increase and therefore a reduction of the DG power feed-in. For example, $k_{f,ESS} = 600kW/Hz$ leads to a DG feed-in limitation of approx. 117kW. Due to the nonlinear and frequency depending power limitation (Fig. 4) in combination
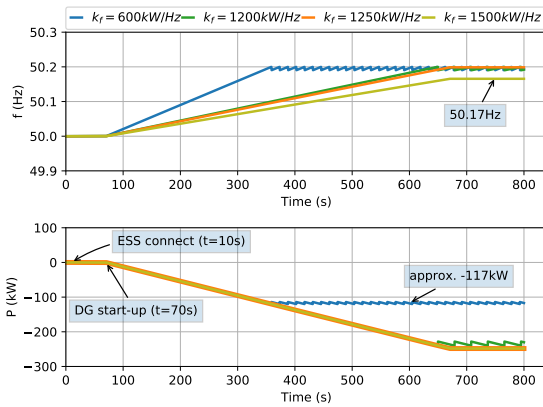
Fig. 7. Frequency (a) and Active Power (b) of the ESS during black start for different droop factors $k_{f,ESS}$.

with P/f droop control, a sawthooth-like power and frequency variation is resulted.

By increasing the droop factor to $k_{f,ESS} = 1250kW/Hz$, the maximum power feed-in of 250kW is realized; this leads to a frequency $f = 50.2Hz$.

For higher values ($k_f = 1500kW/Hz$), the DG can feed in without limitation with a resulting frequency of $f = 50.17Hz$.

By analytic calculation regarding Eq. 7, the droop factor has to be selected higher than $k_{f,ESS} \geq 1250kW/Hz$ if $f_{max} = 50.2Hz$ (according to [7]), $P_{0,ESS} = 0$ and $f_{0,ESS} = 50Hz$ are assumed. This is also shown by the simulation presented in Fig. 7.

In scenario 1 it is shown that the droop control parameters have to be dimensioned properly for an optimal usage of renewable energy produced by DGs.

C. Scenario 2 - Genset as Grid Forming Unit

Scenario 2 deals with the black start of a microgrid using a genset (rated power $P_r = 100kVA$) as grid forming unit, no usage of ESS, no DG feed-in and a varied load of $P_{load} = \{40kW, 50kW, 60kW\}$.

Due to the dynamic behavior of the diesel engine, the maximum load step is limited. In this scenario, load steps of 40% ($P_{load} = 40kW$), 50% ($P_{load} = 50kW$) and 60% ($P_{load} = 60kW$)are analyzed. The according simulation results are shown in Fig. 8. The upper diagram (a) shows the frequency whereas in the lower diagram (b) the genset's active power supply is illustrated.

At time $t = 0$, the genset is powered on. At $t = 10s$, the genset is connected to the grid. The immediate load step leads to a decrease of frequency (Fig. 8 resp. Fig. 9). For load steps of $P_{load} = 40kW$ resp. $P_{load} = 50kW$, the genset is controlled to a steady state operation point nearby $f = 50Hz$ (depending on the droop factor $k_{f,GEN}$). Further it is shown that a load step of $P_{load} = 60kW$ leads to a frequency

breakdown as the genset is not able to cover the load demand as a step. In this case, the black start is not successful.
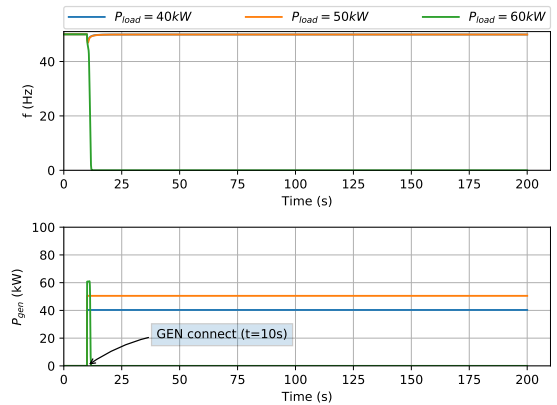
Fig. 8. Frequency (a) and Active Power (b) of the genset during black start for different load steps of P_{load}.
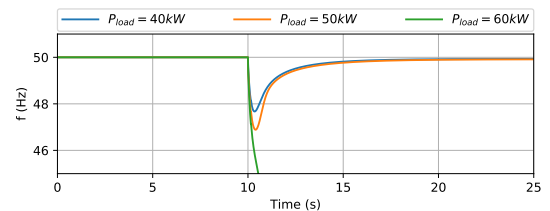
Fig. 9. Frequency of the genset during black start (detailed view).

For black start of microgrids only with gensets, a proper dimensioning regarding rated power under consideration of the maximum expected load step is necessary. Another solution would be splitting up the electrical loads to smaller units and connecting it step by step.

D. Scenario 3 - ESS and Genset as Parallel Grid Forming Units

In scenario 3 the black start of both ESS and genset as parallel grid forming units is investigated by simulation. Regarding the investigated grid shown in Fig. 1, the load is assumed to $P_{load} = 100kW$ whereas the maximum DG active power feed-in is $P_{DG,max} = 250kW$. The droop factors are set to $k_{f,ESS} = 1200kW/Hz$ resp. $k_{f,GEN} = 600kW/Hz$.

The resulting frequency as well as active power for P_{res}, P_{ESS} and P_{GEN} are shown in Fig. 10.

At the time $t = 10s$, genset and ESS are powered on and synchronized in grid forming mode, but still in no-load operation. At $t = 10s$, the residual grid consisting of loads and DGs is connected. Due to the DG's start-up behavior and Eq. 1, the residual power P_{res} is equal to P_{load} in the period $10s \leq t \leq 70s$. Due to the high dynamic capability of ESSs

2124

with power electronics, nearby all residential power is covered by the ESS whereas the active power feed-in by the genset is slowly.
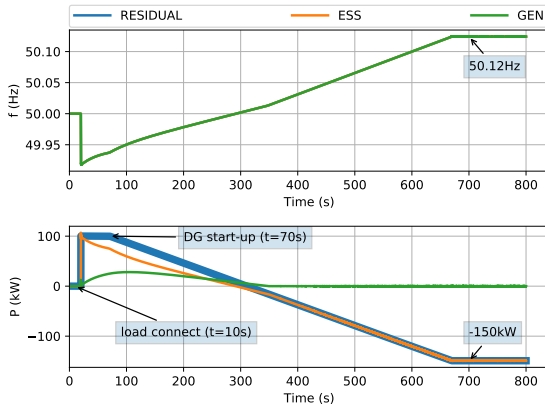
Fig. 10. Frequency (a) and Active Power (b) curve for ESS and Genset as Parallel Grid Forming Units.

At time $t = 70s$, the DG active power feed-in by a ramp begins and thus the residual load which has to be covered by ESS and genset is decreasing. Beginning at $t \approx 300s$, the residential load P_{res} gets negative due to the increase of DG feed-in. The ESS is now consuming electrical power and is charged. As gensets cannot consume power, it is controlled to zero.

After $t \approx 680s$, the DGs are feeding with maximum power $P_{DG,max} = 250kW$ whereas approx. 100kW is consumed by the loads (aggregated to P_{load}) and the ESS is charged by 150kW. The frequency increases until $f = 50.125Hz$. As it is lower than 50.2Hz, power limitation due to over-frequency is avoided.

IV. CONCLUSION

The black start of a microgrid consisting of DGs and loads is analyzed for the following grid forming units:

- ESS
- Genset
- ESS and genset in parallel

Also a method for frequency droop control dimensioning is shown taking into account the characteristic behavior of DGs regarding the German application VDE-AR-N 4105.

It is pointed out that in the case of a high percentage of the power of DGs in microgrids, a low frequency increase must be ensured by the grid forming units to avoid a power reduction of the DGs (50.2Hz) by the usage of optimized droop factors.

Further it is shown that the usage of ESS can increase the maximum load step if gensets are involved.

REFERENCES

[1] "VDE-Studie Der zellulare Ansatz," Frankfurt am Main, 2015.

[2] S. Thale and V. Agarwal, "A smart control strategy for the black start of a microgrid based on PV and other auxiliary sources under islanded condition," in 2011 37th IEEE Photovoltaic Specialists Conference, 2011, pp. 002454–002459.

[3] J. A. P. Lopes et al., "Control strategies for microgrids emergency operation," in 2005 International Conference on Future Power Systems, 2005, p. 6 pp.-6.

[4] C. L. Moreira, F. O. Resende, and J. A. P. Lopes, "Using Low Voltage MicroGrids for Service Restoration," IEEE Trans. Power Syst., vol. 22, no. 1, pp. 395–403, Feb. 2007.

[5] M. Nuschke, "Development of a microgrid controller for black start procedure and islanding operation," in 2017 IEEE 15th International Conference on Industrial Informatics (INDIN), 2017, pp. 439–444.

[6] Z. Xu, P. Yang, Z. Zeng, Y. Zhang, J. Peng, and Q. Zheng, "Study on black start strategy for multi-microgrids," in 2016 IEEE Innovative Smart Grid Technologies - Asia (ISGT-Asia), 2016, pp. 144–148.

[7] "VDE-AR-N 4105 (Erzeugungsanlagen am Niederspannungsnetz - Technische Mindestanforderungen für Anschluss und Parallelbetrieb von Erzeugungsanlagen am Niederspannungsnetz,", 2011.

[8] https://www.digsilent.de/en/.

[9] A. Rahmoun, A. Armstorfer, H. Biechl, and A. Rosin, "Mathematical modeling of a battery energy storage system in grid forming mode," in 2017 IEEE 58th International Scientific Conference on Power and Electrical Engineering of Riga Technical University (RTUCON), 2017.

[10] A. Armstorfer, N. Beg, A. Rahmoun, A. Rosin, and H. Biechl, "Mathematical Modeling and Evaluation of a Microgrid Demonstrator in Island Mode," Conf. Sustain. Energy Supply Energy Storage Syst. NEIS 2017, pp. 39–44, 2017.

[11] N. Beg, A. Armstorfer, A. Rosin, and H. Biechl, "Mathematical Modeling and Stability Analysis of a Microgrid in Island Operation," in 2018 International Conference on Smart Energy Systems and Technologies (SEST), 2018, pp. 1–6.

[12] A. Engler and N. Soultanis, "Droop control in LV-grids," in 2005 International Conference on Future Power Systems, 2005.

[13] S. Krishnamurthy, T. M. Jahns, and R. H. Lasseter, "The operation of diesel gensets in a CERTS microgrid," in 2008 IEEE Power and Energy Society General Meeting - Conversion and Delivery of Electrical Energy in the 21st Century, 2008.

[14] D. Wu, F. Tang, J. C. Vasquez, and J. M. Guerrero, "Control and analysis of droop and reverse droop controllers for distributed generations," in 2014 IEEE 11th International Multi-Conference on Systems, Signals & Devices (SSD14), 2014, pp. 1–5.

Appendix 5

V
A. Armstorfer, N. Beg, A. Rahmoun, A. Rosin, and H. Biechl. Mathematical modeling and evaluation of a microgrid demonstrator in island mode. *Conference on Sustainable Energy Supply and Energy Storage Systems NEIS 2017*, 1(1):39–44, 2017

Voltage and Reactive Power Control in Islanded Microgrids Without Communication Link

Andreas Armstorfer[1,2]
[1]*Institute of Electrical Power Systems*
Kempten University of Applied Sciences
Kempten, Germany
andreas.armstorfer@hs-kempten.de

Helmuth Biechl
Institute of Electrical Power Systems
Kempten University of Applied Sciences
Kempten, Germany
biechl@hs-kempten.de

Argo Rosin
[2]*Tallinn University of Technology*
(Taltech)
Tallinn, Estonia
argo.rosin@taltech.ee

Abstract—**Microgrids can be operated in on-grid mode, but also in off-grid mode (island operation). In off-grid mode, grid forming units have to ensure the grid's voltage and frequency stability. For more than one grid forming unit, the active and reactive power sharing has to be handled. This paper presents a method for voltage and reactive power control for systems without a superordinated control system or a communication link between the grid forming units. A failsafe concept is included, that means that a stable operation is given also in case that one grid forming unit is disconnected.**

Index Terms—**Microgrids, Island Grid, Off-Grid Mode, Reactive Power Control, Voltage Control**

I. Introduction

Microgrids are locally limited grid areas with loads, distributed generation (DG) and a control system. It is distinguished between ac and dc microgrids, but also in on-grid and off-grid systems. These concepts are discussed in literature, e.g. in [1]–[3]. The scope of this work is set on ac microgrids at low voltage (LV) level.

In islanded microgrids grid forming units (such as battery storage systems or generator sets, e.g. driven by plant oil or diesel) have to ensure an equilibrium of active and reactive power under consideration of allowed voltage and frequency levels. A widely used method for active and reactive power sharing is the concept of droop control [3]–[6].

In literature also other concepts are described, such as [7] which is based on a communication link with high bandwidth between the grid forming units, or [8] which describes the active power sharing basing on fuzzy logic.

In this paper a concept for voltage and reactive power control without communication link is presented, that means that permanently or temporarily no superordinated control system is available.

Further the failsafe behavior is investigated as well, if e.g. one grid forming unit is disconnected.

The main goals of the concept are:
1) voltage stability (compliance of voltage limits)
2) minimization of reactive power exchange and losses

This paper starts with an analysis of the reactive power demand in rural LV grids (section II), followed by the description of the control concept (section III). In section IV an approach for the control parameter estimation is given before in section V some simulation results are presented.

In section VI, a conclusion including an outlook is given.

II. Reactive Power Demand in Rural LV Grids

The reactive power demand of a grid is effected by the electrical lines as well as the connected load types with different reactive power consumption characteristics.

From September 2012 until January 2015, the reactive power demand of different LV substations located in a rural area in Southern Germany was measured in the frame of the research project *IRENE* [9]. In Fig. 1, the PQ-diagram for four substations is shown for time-synchronous data with a period of 1 minute, whereas power consumption is positive.

If these grid areas are assumed as independent island grids or microgrids in island mode, the corresponding reactive power demand has to be handled by the assets connected to the grid.

In Fig. 1a, active and reactive power is positive as well as negative. In Fig. 1b and Fig. 1d, the behavior is mainly ohmic-inductive (consumption), whereas in Fig. 1c an ohmic-inductive generation is dominant.

The relative derivation of all power factors calculated from the measurement data is plotted in Fig. 2.

In more than 90% of the time, the power factor $\cos\varphi$ is higher than 0.8 (substation 2) or even 0.9 (substations 1, 3 and 4).

Basing on these results it is assumed for the following control concept that the absolute reactive power demand in rural LV grids is small.

It has to be pointed out that only 4 LV substations were analyzed. For a general statement the number of investigated substations is too low.

III. Fuzzy-based Control Concept

As shown in section II, the power demand in rural LV grids is dominated by active power, that means that the reactive power demand is low.

In a low voltage microgrid with more than one grid forming unit, the reactive power sharing between all grid forming units has to be handled.

The concept presented in this work assumes N grid forming units whereas 1 grid forming unit is operated as a master and $N-1$ assets are operated as slaves. It is assumed that there is no communication link and no super-ordinated control system
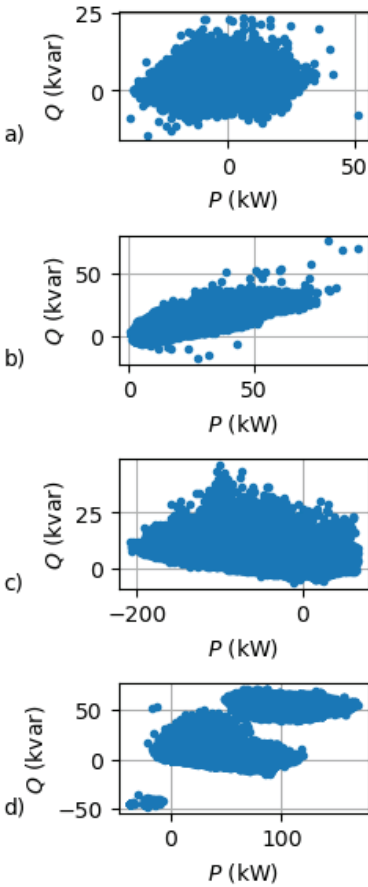
Fig. 1. Active and Reactive Power Deviation for four Low Voltage Substations in a Rural Area.
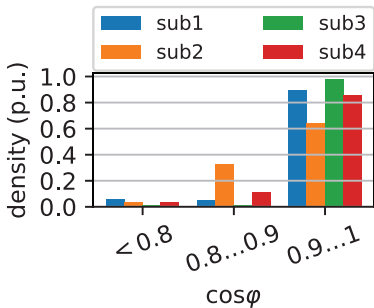
Fig. 2. Derivation of Power Factors Measured at Substations 1…4.
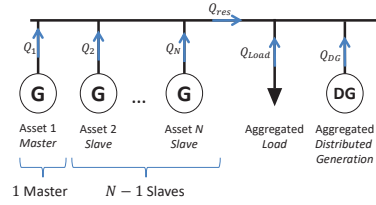
Fig. 3. Estimated Grid Structure
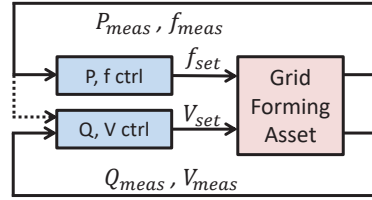
Fig. 4. Grid Forming Unit - Generic Control Structure

for voltage and reactive power control. The fundamental behind this concept is that all slave assets are controlled to a predefined reactive power, e.g. $Q_{asset} = 0$, as long as no voltage boundaries are exceeded. As a power equilibrium is mandatory in island grids, the master grid forming unit is balancing the reactive power deviation between demand and slave assets.

Fig. 3 shows the general electrical structure of an islanded microgrid with N grid forming units and an aggregated load Q_{load} as well as a the distributed generation (e.g. PV generators) aggregated to Q_{DG}. Losses as well as reactive power consumption of the lines are not mentioned explicitly.

The grid forming units are controlled voltage sources with setpoints for frequency and voltage magnitude. In Fig. 4 the generic asset model structure is shown. It consist of the grid forming unit as a controlled voltage source, a frequency and active power controller as well as a voltage and reactive power controller.

In this paper, the scope is set on the voltage and reactive power control.

As the grid voltage is a local phenomena (in contrast to the grid frequency), the concept of power sharing by droop control does not work as proper as the frequency control. In inappropriate cases, reactive power is exchanged between grid forming units which can lead to increased losses as well as overloading of the lines and assets.

The block diagram of the voltage and reactive power controller of each grid forming unit is shown in Fig. 5.

The master is operated at a constant the voltage level, e.g. $V_0 = 400V$. Regarding Fig. 5, the signal *enable_slave* has to be set to zero.

For grid forming units operated as slaves ($enable\_slave = 1$), an additional voltage setpoint ΔV_{set} is added to the voltage setpoint V_0.
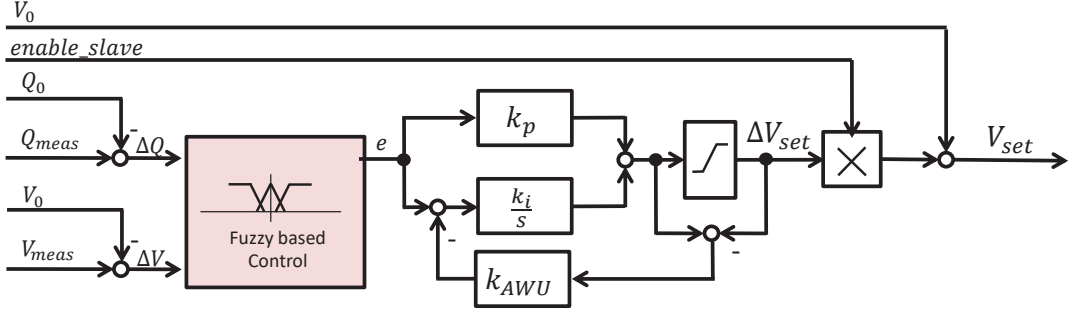
Fig. 5. Grid Forming Unit - Voltage and Reactive Power Control
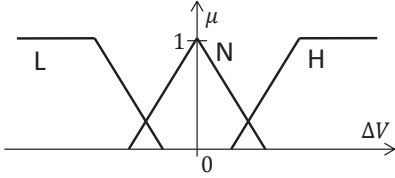
Fig. 6. Fuzzy Logic Membership Function for Input ΔV

The slave control is a MISO (multiple input, single output) system based on Fuzzy Logic. The inputs of the slave controller $\Delta Q = Q_{meas} - Q_0$ and $\Delta V = V_{meas} - V_0$ are evaluated and further used by Fuzzy Logic which is followed by a PI controller (k_p, k_i) with Anti-Windup (k_{AWU}).

In general, a fuzzy logic consist of three steps:

1) Fuzzification
2) Inference
3) Defuzzification

In Fig. 6 the membership function for the fuzzification of the input ΔV is drawn. The function N describes the curve for *normal voltage*, that means that the voltage is within defined limits. The membership functions L (*low voltage*) resp. H (*high voltage*) are defined for voltages out of the limits. As an advantage of fuzzy logic, a smooth transition between different control modes can be realized by overlapping of the curves L and N resp. N and H.

The corresponding defuzzification is described by Eq. 1:

$$e = \frac{\mu_L \cdot \Delta V + \mu_N \cdot \Delta Q + \mu_H \cdot \Delta V}{\mu_L + \mu_N + \mu_H} \qquad (1)$$

where μ_L, μ_N and μ_H are functions of ΔV (regarding membership functions as shown in Fig. 6), ΔQ and ΔV are input values and e is the controller's output.

In the following it is distinguished between two operation modes - normal operation and failsafe operation.

A. Normal Operation

Normal condition means that at least the master asset is in operation. For minimization of the losses, the membership functions $\mu_L(\Delta V)$, $\mu_N(\Delta V)$ and $\mu_H(\Delta V)$ of the slave grid forming units are designed in that way that the voltage is within the defined limits for most realistic load states. An exceed of these voltage results in an additional reactive power flow in the network.

B. Failsafe Operation

Failsafe operation in this context defines an operation of slave grid forming units without master (e.g. the master is disconnected due to a failure). Voltage stability has to be ensured in any case, whereas an optimal deviation of reactive power and minimization of losses can be neglected in this extraordinary operation mode. It is essential to avoid a chain reaction of disconnecting grid forming units and a resulting blackout.

IV. DIMENSIONING OF CONTROLLER PARAMETERS

For a proper operation of the concept presented in this work it is necessary to obtain the parameters of the controllers. It is distinguished between master and slave controller parameters.

A. Master

For the master asset, basically the no-load voltage V_0 has to be defined (regarding Fig. 5).

B. Slave Configuration

For slaves, the membership functions $\mu_N(\Delta V)$, $\mu_L(\Delta V)$ and $\mu_H(\Delta V)$ have to be defined. In this paper, a trapezoidal shape is assumed (Fig. 7), but any other shape of the function is also possible.

For each grid forming unit, the nominal voltage V_0 is defined, e.g. $V_0 = 400V$. Further the (trapezoidal) membership function for *normal voltage* $\mu_N(\Delta V)$, the setpoints $V_{N,a}$ and $V_{N,d}$ (regarding Fig. 7) define the voltage boundaries. Basing on this, the membership functions $\mu_L(\Delta V)$ and $\mu_H(\Delta V)$ are
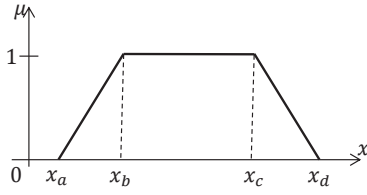
Fig. 7. Trapezoidal Membership Function for Fuzzification

TABLE I
ELECTRICAL PARAMETERS

Parameter	Value
Line1 Length	$0.5km$
Line1 Impedance	$0.104\Omega + j0.040\Omega$
Line2 Length	$0.05km$
Line2 Impedance	$0.010\Omega + j0.004\Omega$
Line3 Length	$0.188km$
Line3 Impedance	$0.039\Omega + j0.015\Omega$

TABLE II
FUZZY CONTROL PARAMETERS

Asset	Parameter	a	c	c	d
DG2	$V_{N,x}$	$-30V$	$0V$	$0V$	$30V$
	$V_{L,x}$	$-1000V$	$-999V$	$-100V$	$-20V$
	$V_{H,x}$	$20V$	$100V$	$999V$	$1000V$
DG3	$V_{N,x}$	$-40V$	$0V$	$0V$	$40V$
	$V_{L,x}$	$-1000V$	$-999V$	$-100V$	$-30V$
	$V_{H,x}$	$30V$	$100V$	$999V$	$1000V$

configured. An overlap of the functions (as drawn in Fig. 6) leads to a smooth transition at the boundaries of the voltage.

V. SIMULATION RESULTS

The control strategy for voltage and reactive power was implemented in the software *PowerFactory* from the manufacturer *DIgSILENT* [10]. The investigated grid consists of 3 grid forming units (DG1, DG2, DG3) as well as a controllable load and is shown in Fig. 8.

For active power sharing, a frequency droop control with an equal droop factor for all grid forming unis is used. This leads to an equal active power distribution for all assets.

The electric lines between the assets are assumed as low voltage earth cables with type *NAY2Y-J 4x150mm²*. The relevant electrical parameters used for the simulation are presented in Tab. I. For all grid forming units, the no-load voltage is set to $V_0 = 400V$; fuzzy control parameters are presented in Tab. II.

Simulation results for master/slave operation as well as for failsafe operation are presented. In the work, the scope is set on the steady state behavior. Transient processes during load steps are not analyzed.

A. Master/Slave Operation

The master/slave operation is evaluated by simulation for ohmic, ohmic-inductive as well as ohmic-capacitive use cases. One asset (DG1) is operated as a master whereas DG2 and DG3 are in slave mode. For all use cases presented in the following, the active power distribution is realized by active power droop control under consideration of an equal active power ($P_{DG1} = P_{DG2} = P_{DG3} = \frac{1}{3}P_{load}$).

1) Ohmic Load ($\cos\varphi = 1$)*:* At first, an ohmic load is assumed ($\cos\varphi = 1$). The load steps and the corresponding active power distribution is shown in Fig. 9a. The reactive power for all DGs as well as the load is shown in Fig. 9b. In Fig. 9c the corresponding voltages at each node are presented.

In the period $0\ldots350s$, all slave (DG2, DG3) voltages are within the boundaries; this leads to a reactive power of approx. 0 for all assets. At the time $t = 350s$, the lower voltage boundary for slave DG2 is reached. Thus a further increase of active power results in an exchange of reactive power between DG2 and the master DG1 in order to keep the voltage within the defined limits.

2) Ohmic-Inductive Load ($\cos\varphi = 0.8_{ind.}$)*:* In the second case, an ohmic-inductive load with power factor $\cos\varphi = 0.8_{ind}$ is connected. The active power P_{load} is varied from $0\ldots320kW$ (Fig. 10a).

In the period from $0\ldots200s$, the complete reactive power demand is supplied by the master (DG1) as the slave voltages V_{DG2} resp. V_{DG3} are within the limits defined regarding Tab. II (Fig. 10c). For $t > 200s$, the lower voltage boundary of DG2 is reached. Thus Q_{DG2} is increasing while the reactive power distribution of the master Q_{DG1} is reduced (Fig. 10b).

3) Ohmic-Capacitive Generation ($\cos\varphi = 0.8_{cap.}$)*:* The third use case is dealing with an ohmic-capacitive behavior. Instead of power consumption, an active power feed-in is assumed (*negative load*, $P_{load} < 0$). A power factor of $\cos\varphi = 0.8_{cap}$ is adjusted while the active power P_{load} is varied in steps from 0 to $-320kW$ (Fig. 11a). In the time period $0\ldots200s$, the reactive power is completely covered by DG1 (master) while Q_{DG2} resp. Q_{DG3} is zero (Fig. 11b). For $t > 200s$, the upper voltage limit for DG2 is reached ((Fig. 11c). This leads to reactive power consumption by DG2 and thus a reduction of Q_{DG1}.

B. Failsafe Operation

Under normal load conditions, the reactive power fluctuation is covered by the master asset. Nevertheless, a stable grid operation has to be ensured also in case of failure of the master grid forming unit. In this non-optimized operation condition, the compliance with voltage limits has to be ensured. As a consequence, reactive power now is handled by at least one slave asset (or several).

Fig. 12 shows the result for this operation mode. At $t = 50s$, the load ($P = 160kW$, $Q = 100kW$) is connected. The active power is covered by DG1...DG3 whereas the reactive power is mainly covered by DG1. At $t = 200s$, the master DG1 is disconnected. As the voltage boundary of DG2 is
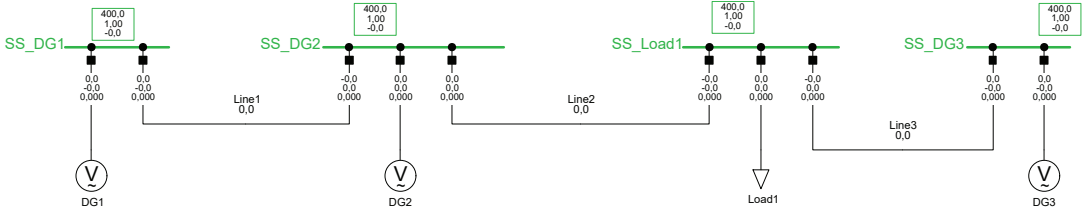
Fig. 8. Single Line Diagram of the Investigated Grid Consisting of 3 DGs and 1 Load ($S = 0kVA$).
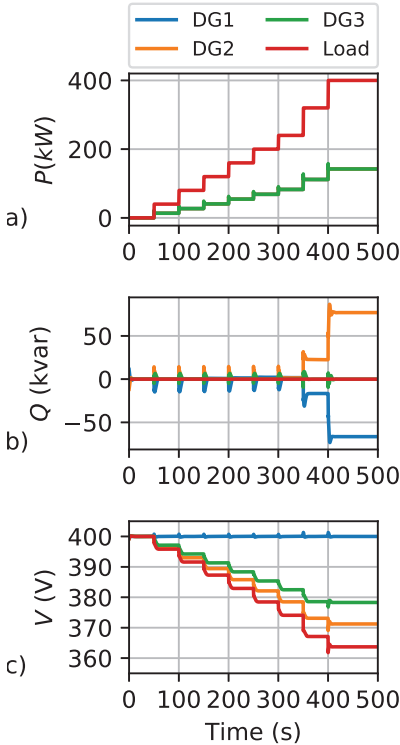
Fig. 9. Simulation Result for an Ohmic Load. a) Active Power. b) Reactive Power. c) Voltage.
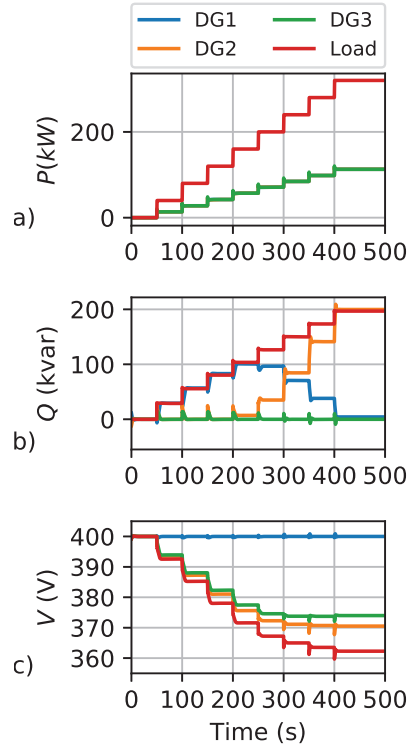
Fig. 10. Simulation Result for an Ohmic-Inductive Load. a) Active Power. b) Reactive Power. c) Voltage.

reached, the complete reactive power demand is covered by DG2. Nevertheless, the grid operation is stable. At $t = 400s$, the master DG1 remains and takes over again the reactive power handling.

VI. CONCLUSION

In this paper an approach for reactive power control in islanded microgrids was presented. At first it was shown for 4 rural distribution grids that the reactive power demand is relatively low.

Basing on this, a control strategy basing on a master/slave concept including failsafe handling was developed. The master asset defines the voltage level and delivers all reactive power fluctuations to the island grid whereas the the slave devices are controlled to a constant reactive power (e.g. $Q = 0$) as long as no voltage limits are exceeded. If the master is missing, a failsafe concept ensures a further stable operation of the microgrid. The control approach is basing on fuzzy control.

For the control parameter dimensioning some fundamental rules were given. A stable operation for different operation modes was proofed by simulation.
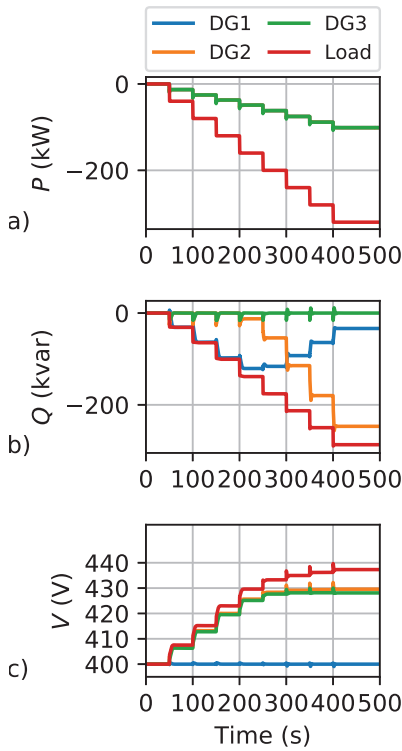
Fig. 11. Simulation Result for an Ohmic-Capacitive Generation. a) Active Power. b) Reactive Power. c) Voltage.
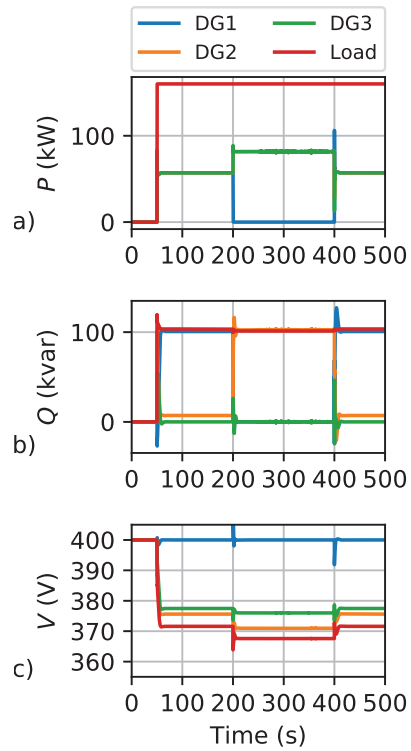
Fig. 12. Simulation Result for Failsafe Operation. a) Active Power. b) Reactive Power. c) Voltage.

The advantage of this master/slave concept is a minimization of reactive power exchange between grid forming units which can lead to a reduction of line losses in the grid.

As an outlook, the presented concept can be extended by further fuzzy rules as well.

REFERENCES

[1] N. Hatziargyriou, H. Asano, R. Iravani, and C. Marnay, "Microgrids," IEEE Power and Energy Magazine, vol. 5, no. 4. pp. 78–94, Jul-2007.
[2] Bauer, P., Weldemariam, L. E., and Raijen, E. (2011). Stand-alone microgrids. In 2011 IEEE 33rd International Telecommunications Energy Conference (INTELEC) (pp. 1–10). IEEE. https://doi.org/10.1109/INTLEC.2011.6099837
[3] J. M. Guerrero, J. C. Vasquez, J. Matas, L. G. De Vicuña, and M. Castilla, "Hierarchical control of droop-controlled AC and DC micro-grids - A general approach toward standardization," IEEE Trans. Ind. Electron., vol. 58, no. 1, pp. 158–172, Jan. 2011.
[4] A. Engler and N. Soultanis, "Droop control in LV-grids," in 2005 International Conference on Future Power Systems, 2005, pp. 6 pp. – 6.
[5] A. Armstorfer, H. Biechl, and A. Rosin, "Energy Scheduling of Battery Storage Systems in Micro Grids," Sci. J. Riga Tech. Univ. - Electr. Control Commun. Eng., vol. 12, pp. 27–33, 2017.
[6] A. Armstorfer, N. Beg, A. Rahmoun, A. Rosin, and H. Biechl, "Mathematical Modeling and Evaluation of a Microgrid Demonstrator in Island Mode," Conf. Sustain. Energy Supply Energy Storage Syst. NEIS 2017, pp. 39–44, 2017.
[7] Nasirian, V., Shafiee, Q., Guerrero, J. M., Lewis, F. L., and Davoudi, A. (2016). Droop-Free Distributed Control for AC Micro-grids. IEEE Transactions on Power Electronics, 31(2), 1600–1617. https://doi.org/10.1109/TPEL.2015.2414457
[8] L. Sedghi and A. Fakharian, "Voltage and frequency control of an islanded microgrid through robust control method and fuzzy droop technique," in 5th Iranian Joint Congress on Fuzzy and Intelligent Systems - 16th Conference on Fuzzy Systems and 14th Conference on Intelligent Systems, CFIS 2017, 2017, pp. 110–115.
[9] Biechl, H., Armstorfer, A., Rahmoun, A., Eberl, T., and Meyer, C. (2013). Abschlussbericht zum Verbundprojekt IRENE, 1–80. https://doi.org/https://doi.org/10.2314/GBV:859607836
[10] DIgSILENT PowerFactory. https://www.digsilent.de/en/

Appendix 6

VI

A. Rahmoun, A. Armstorfer, H. Biechl, and A. Rosin. Mathematical modeling of a battery energy storage system in grid forming mode. *2017 IEEE 58th International Scientific Conference on Power and Electrical Engineering of Riga Technical University (RTUCON)*, pages 1–6, 2017

Mathematical Modeling and Dynamic Behavior

of a Lithium-Ion Battery System

for Microgrid Application

Ahmad Rahmoun[1,2], Andreas Armstorfer[1,2], Jorge Helguero[1], Helmuth Biechl[1,2]

[1]Institute of Electrical Power Systems (IEES)
[1]University of Applied Sciences Kempten
[1]Kempten, Germany
ahmad.rahmoun@hs-kempten.de, andreas.armstorfer@hs-kempten.de,
jorge.helguero@hs-kempten.de, biechl@hs-kempten.de

Argo Rosin[2]
[2]Faculty of Power Engineering
[2]Tallinn University of Technology
[2]Tallinn, Estonia
argo.rosin@ttu.ee

Abstract—**This paper deals with the analysis and simulation of a stationary battery system for microgrid application, where the system structure including battery cells, inverters, filters, transformers, control system and a simplified grid model is described and modeled mathematically. For the simulation of the whole system the software PSCAD™ is used. In the first part several equivalent circuit models for Lithium-Ion cells will be compared in order to model the dynamic behavior of the battery system. Particularly the evaluation of the effect of the model's complexity on the dynamics of the entire system will be investigated.**

In the second part, the dependency of state of charge (SOC), temperature and aging effects of the Lithium-Ion cells on electrical system quantities will be shown.

It is also investigated the fact that a high frequency battery model has to be taken into account to describe the cells' dynamics if an inverter with Pulse Width Modulation is used.

Index Terms—**Microgrid, Batteries Energy Storage, Lithium Batteries and Power System Modeling**

I. INTRODUCTION

The research project IREN2 (Future Oriented Electricity Grids for Integration of Renewable Energy Systems) runs from 2014 to 2017 and is executed in a cooperation between the German entities Siemens AG, the electricity supplier Allgäuer Überlandwerk GmbH, ID.KOM, the University RWTH Aachen and the University of Applied Sciences Kempten. The main goals are: the development of mathematical models to analyze the dynamic behavior of microgrids including new control concepts on the one hand, and setting up a real system in the village Wildpoldsried in the south of Germany on the other hand. The microgrid consists of renewable energy sources, a stationary 300kVA/170kWh battery system with Lithium Nickel Cobalt Oxide (NCO) - Titanate cells, an 100kVA Genset with vegetable oil fueling for secondary control, a 500kVA back to back station between the 20kV and the 400 V grid for test purposes and a 3x 50kW unsymmetrical load bank.

The Energy Storage System (ESS) which is analyzed in this paper is a modular system consisting of 6 independent

strings. Each string consist of a Lithium-Ion (li-ion) battery, an inverter and a filter [1]–[3]. Three strings are connected via a transformer to the grid. For this paper only one string is examined. Fig. 1 shows the block diagram of the system.

II. EVALUATION OF THE EQUIVALENT CIRCUIT MODELS' COMPLEXITY

In this section three different Equivalent Circuit Model (ECM) are used in order to simulate the electrical dynamics of the li-ion cells which are utilized in the ESS, the One Time Constant (OTC) model, the Two Time Constants (TTC) model and the Three Time Constants (DTC) model. As shown in Fig. 2 the ECM models consist basically of an ideal voltage source representing the cell's Open Circuit Voltage (Voc) and an impedance composed of parallel RC-elements connected with an ohmic serial resistance. The number of the RC-elements defines the order of the ECM and all the model's parameters are functions of State of Charge (SOC), cell's temperature and State of Health (SOH). The ECM's parameters are identified by applying a sequence of current pulses on the cell then employing the voltage and current measurements in time domain. For optimization using multiple exponential functions, the identification procedure is shown in details in [4], [5]. The identified ECM parameters of one cell are stored in Lookup Tables (LuTs) to be accessed and adapted during the simulation run depending on SOC, cell's temperature and SOH, then they are converted based on the number of cells in parallel and series resulting in a battery model of one string.

In order to choose the right battery's model for the simulation of the ESS, the accuracy of the battery models in estimating the battery's output voltage is evaluated, hence a simulation benchmark is designed, in which the OTC, TTC and DTC models are simulated for an active power pulse of Pset=50kW for 5 sec, the initial conditions of the simulation are SOC=60%, T=20°C and SOH=aged/new (new: no cycles, aged: after approx. 640 full cycles). The active power pulse (Pset), battery current (I_{bat}), battery output voltage (V_{bat}) and
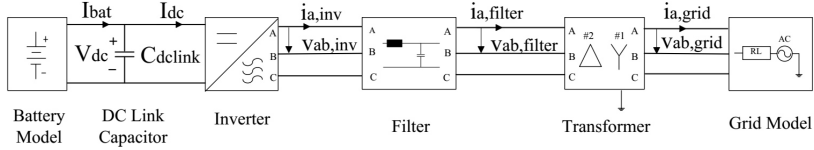
Fig. 1. ESS Structure (for 1 string).
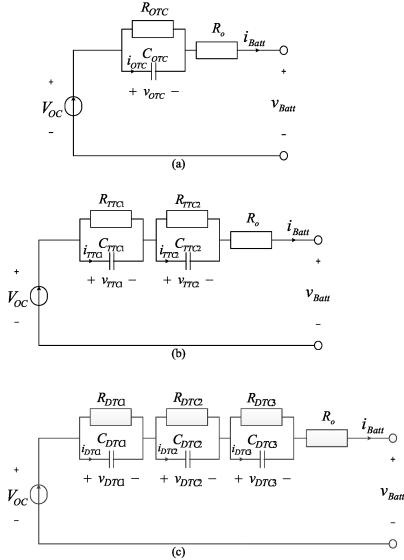
Fig. 2. Battery equivalent circuit diagrams. (a): one time constant model (OTC); (b): two time constant model (TTC); (c): three time constants model (DTC).

Fig. 3. A comparison between the OTC, TTC and DTC models in estimating the cell output voltage for a new and aged cell.
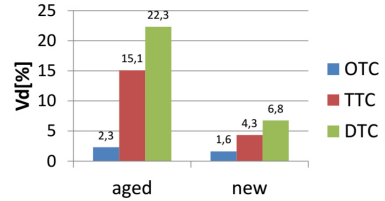
Fig. 4. Voltage difference evaluation of OTC, TTC and DTC models for a new and an aged cell.

the relative voltage difference (V_d) between (V_{bat}) and Voc are plotted in Fig. 3.

The V_d diagram in Fig. 3 shows that the model order plays a bigger roll as the battery ages, so in order to demonstrate the variation between the different models regarding (V_{bat}) calculation, the V_d at the end of the active power pulse is displayed in Fig. 4 for a new and an aged cell. The Fig. 4 manifests that for a new cell, the difference between the three models is about 5 %, but as the cell ages, the difference between the OTC and the TTC models increases faster than the difference between the TTC and DTC models. The reason behind this behavior is that the OTC is very influenced by the long time constants of the cell, thus the TTC and DTC models which include short time constants, lead to bigger voltage drop than the OTC model in the short time range. Based on these evaluation results the DTC model is used for all of the next simulations since it is a capable model to describe the cell behavior for both short and long time ranges.

III. STEADY STATE ANALYSIS

The steady state behavior of the complete system depending on SOC, temperature and aging is analyzed in the following. As described above, the DTC battery model is used for simulation. A reference active power step of 25 kW controlled at the filter output is applied to the system. For variation of SOC, temperature and aging, 9 battery settings are defined and compared (Tab. I). For aging it is distinguished between new cells, aged cells and - to show the effect of dc link voltage drop - an old cell with $SOH \approx 0.87$.

A. Voltage Drop at DC Link

Due to the battery dynamics taken into account by the DTC model, the decrease of the dc link voltage (V_{dc}) depends on: SOC, aging and temperature (Fig. 5). It is illustrated that old cells at the end of their lifetime (setting No. 7) have an early

No.	SOC (%)	Temp. (°C)	Aging
1	30	20	new
2			aged
3	30	35	new
4			aged
5	70	20	new
6			aged
7	70	35	new
8			aged
9	30	20	old

limitation of the maximum power due to the under voltage protection of the system (at $V_{dc} = 450V$). Thus for further analysis it is not taken into account anymore.
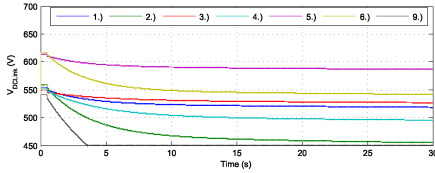
Fig. 5. Battery Voltage Response for a 25kW Active Power Step.

The relative voltage drop at the dc link is investigated as well as the corresponding battery current (rms value).

The relative voltage drop Δv_{dc} is defined as the difference between open circuit voltage V_{OC} and $V_{dc}(30s)$ (1):

$$\Delta v_{dc} = (V_{OC} - V_{dc}(30s))/V_{OC} * 100\% \qquad (1)$$

1) Dependency on SOC: For SOC dependency simulation, the settings No. 1,2 are compared with the settings No. 5,6. The temperature is kept at 20°C while SOC and aging is varied.

New cells show a relative voltage drop of approx. 6.6% at $SOC = 30\%$ and approx. 4.7% at $SOC = 70\%$ when applying the mentioned active power step. For aged cells, the relative voltage drop is approx. 19.4% at $SOC = 30\%$ respectively 12.8% at $SOC = 70\%$ (Fig. 6).
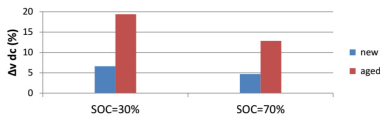
Fig. 6. Relative Voltage Drop at the Battery Terminals after a 30s Power Step.

For the cells used in our ESS it could be shown that the influence of aging has a similar importance than SOC concerning battery voltage dynamics.

Battery currents I_{bat} vary depending on SOC and aging (Fig. 7). As the power at the filter output is controlled to achieve a constant value, a lower dc voltage V_{dc} leads to a higher battery current I_{dc}.
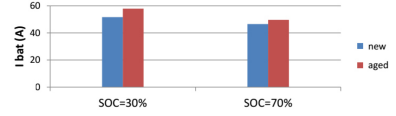
Fig. 7. Battery Current (RMS).

2) Dependency on Temperature: The cell temperature as an influence to the system behavior is analyzed in this section. The SOC is set to 30% while temperature (20°C/35°C) and the aging (new/aged) are varied according settings 1-4 (Tab. I). As a result, a higher temperature leads to a voltage drop reduction. Nevertheless, aging effects play a more dominant role than temperature (Fig. 8) in this range.
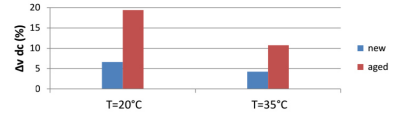
Fig. 8. Relative Voltage Drop after 30s Power Pulse.

B. Harmonics Dependency at the Grid Side

The influence of SOC, temperature and aging of Li-Ion cells on the system's power quality was investigated. Hence the harmonic distortion of the grid current is analyzed. The Fast Fourier Transform (FFT) shows dominant content at order N=1 (50Hz, grid frequency), at order 157 and 161 (7850Hz and 8050Hz, side-bands of switching frequency) as well as at order 317 and 319 (side-bands of the double of switching frequency (15850Hz, 15950Hz). Hence, for current THD determination only these dominant orders (N=157, N=161, N=317, N=319) are taken into account (2):

$$THD_I = \sqrt{\frac{V_{157}^2 + V_{161}^2 + V_{317}^2 + V_{319}^2}{V_1^2}} \qquad (2)$$

In mains parallel operation, current harmonic distortion is low and practically independent from the SOC, temperature (20°C ...35°C and aging (Tab. II).

C. Steady State Conclusion

It is shown that due to the power control the ac behavior of the battery storage system at the grid side is independent of the SOC and the cell's temperature. This applies as long as the dc voltage does not fall below the under voltage limit. To reach this minimum voltage depends mainly on the parameters SOC, SOH and active power demand.

TABLE II
TOTAL HARMONICS DISTORTION (THD) OF GRID CURRENT

Case	SOC (%)	Temp. (°C)	Aging	THD$_I$ (%)
1	30	20	new	0.80
2	30	20	aged	0.86
3	70	20	new	0.75
4	70	20	aged	0.78
5	30	35	new	0.80
6	30	35	aged	0.82

IV. EVALUATION OF THE ENEREGY STORAGE SYSTEM IN THE HIGH FREQUENCY RANGE

The usage of the Pulse Width Modulation (PWM) technique with a switching frequency of $f_s = 7.95kHz$ results, in a high frequency voltage and current harmonics. Therefore, the evaluation of the dc-side signals requires knowledge of the battery dynamics within the High Frequency (HF) range. For this reason the battery's behavior within the HF range is investigated in subsection IV-A, next the necessity of using a HF model is explained in subsection IV-B, and finally the influence of SOC, temperature and SOH on the battery's impact is presented in subsection IV-C.

A. High Frequency Battery Model

The Electrochemical Impedance Spectroscopy (EIS) measurement technique is used to inspect the cell's dynamic characteristics within the $[3kHz, 30kHz]$ frequency range, though several impedance measurements have been done for the operation conditions (1-8) mentioned in Table I describing the dependency of the cell's dynamics on the SOC, the temperature and the SOH. At the first step a 1RL-model is adapted to the complex impedance measurements using the Levenberg-Marquardt Complex Nonlinear Least Squares (CNLS) algorithm, the 1RL-model shown in Fig. 11 (a) forms the equivalent circuit diagram of the cell in the HF range, so it consists of an ideal voltage source representing the cell's Voc wired to an impedance consisting of one RL-element and a serial resistance R_o connected in series. The 1RL-model's impedance together with the cell's measured impedance are plotted in Fig. 12 in bode and nyquist diagrams showing that the 1RL-model fits the measurements well, but the error diagram in Fig. 12 shows that the relative error varies within the $[3kHz, 30kHz]$ range, having a local minimum less than 5% around $7kHz$ then increasing in both directions to about 13% at the range limits. In order to reduce the error over the whole frequency range, one more RL-element is connected in series to the 1RL-model resulting in the 2RL-model shown in Fig. 11 (b). The 2RL-model's impedance in Fig. 13 shows clearly with a relative error less than 3% over the whole frequency range that 2RL-model guarantees a very good accuracy.

The 1RL-model resp. 2RL-model parameters are depicted in Fig. 14 and Fig. 15 for the different operation conditions, it can be seen that both models' parameters are influenced

mainly by aging. Both models are implemented in PSCAD by extending the Low Frequency (LF) part in the battery's model (consisting of RC-elements) with the HF part (consisting of RL-elements) as it is drawn in Fig. 10. The parameters of the HF models are stored in LuTs in order to be accessed and adapted during the simulation run according to the SOC, the cell's temperature and the SOH.

B. Impact of the Battery Behavior on the DC Currents within the HF Range

In order to show the impact of the battery's HF model on the dc currents in the HF range, the ESS is simulated for three different cases:
1) Without using HF-model
2) Using the 1RL-model
3) Using the 2RL-model

In every case an active power pulse of $P = 50kW$ and a reactive power $Q = 0kvar$ are applied for all the operation conditions (1-8) in Table I. The FFT of both I_{bat} and I_{dc} are plotted in Fig. 9 showing the main current harmonics when using the 2RL-model for (SOH: aged, SOC=70 %, T=35 °C), the dominant frequency components are around the switching frequency ($f_s = 7.95kHz$) and at the double of the switching frequency ($2f_s = 15.9kHz$).

The impact of the battery behavior on the dc currents within the HF range is determined by using the harmonic content (H_I) of the I_{dc} and the I_{bat}. The H_I represents the effective value of the ac part of the current in respect to the effective value of the current, and it's given mathematically in (3).

$$H_I = \frac{\text{effective value of } I_{ac}}{\text{effective value of } I} = \frac{I_{ac,eff}}{I_{eff}} \qquad (3)$$

In order to eliminate the influence of any noise on the calculation of the harmonic content (H), only frequency components with an amplitude larger than 1% of the dc component are considered. The H_{Idc} and H_{Ibat} are shown in Fig. 16 for the three different cases, where it can be seen that the use of HF model in the simulation of the ESS has no influence on Idc, but it influences significantly the harmonic content of Ibat. It can be seen also in Fig. 16 that there is almost no difference in the harmonic content calculation of Idc and Ibat when using 1RL-model or 2RL-model, nevertheless, the 2RL-model has a better accuracy in fitting the battery impedance than the 1RL-model. Based on these results the 1RL-model is always used in the next evaluations for representing the battery dynamics in the HF range.

C. Influence of Operation conditions on the Battery dynamics in the HF Range

The 1RL-model simulation results are used in this section to evaluate the dependency of the harmonic content of I_{bat} and I_{dc} on the SOC, the temperature , and the SOH. The H_{Idc} displayed in Fig. 17 shows a slight dependency on SOC, if one compares between H_{Idc} for $SOC = 30\%$ and $SOC = 70\%$. But it shows almost no dependency neither on the temperature nor on the SOH. The change of the H_{Idc} because of the SOC
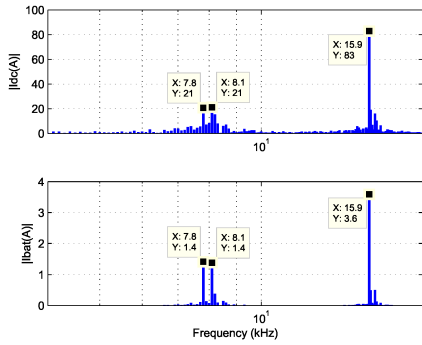
Fig. 9. FFT of I_{dc} and I_{bat} showing the main current harmonic for (SOH: aged, SOC=70 %, T=35 °C) when applying active power pulse of $P = 50kW$ and $Q = 0kvar$ and simulated using the 2RL-model.
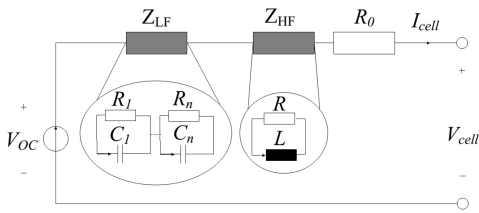
Fig. 10. Li-Ion battery general model structure for high and low frequency application.

is mainly due to the change of the dc component of the Idc as the battery output voltage varies with the SOC.

The H_{Ibat} depicted in Fig. 18 shows almost no dependency neither on temperature nor on SOC. But it shows a slight dependency on SOH, so for an aged battery the H_{Ibat} slightly increases compared to a new battery. This effect is due to the change of HF model parameters when the battery is aged.
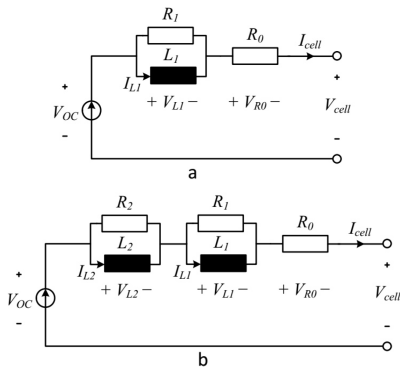
Fig. 11. Battery equivalent circuit models for HF. (a): 1RL-model; (b): 2RL-model.
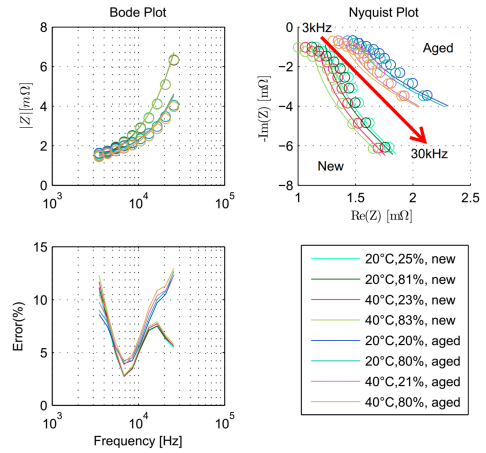
Fig. 12. Bode, Nyquist and error diagrams of cell's measured impedance (circles) and 1RL-model's impedance (line) for various operation conditions.
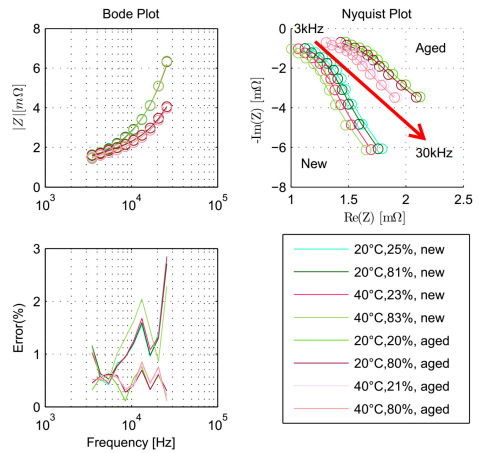
Fig. 13. Bode, Nyquist and error diagrams of cell's measured impedance (circles) and 2RL-model's impedance (line) for various operation conditions.
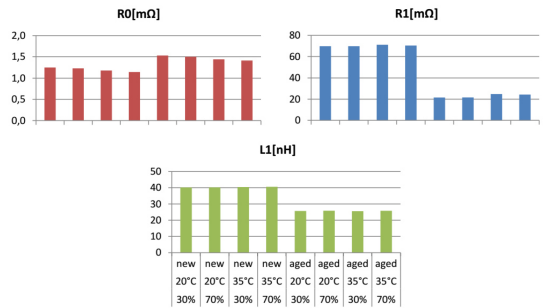
Fig. 14. 1RL-model's parameters dependency on SOC, cell's temperature and SOH.
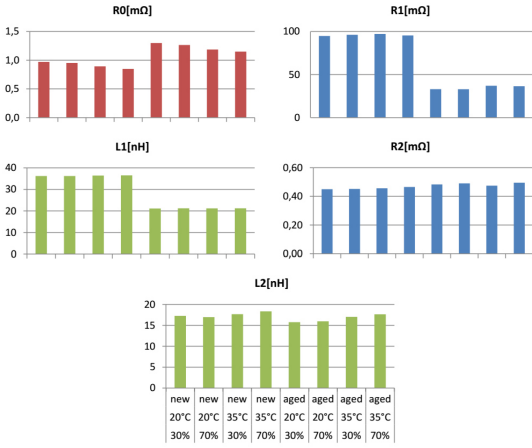
Fig. 15. 2RL-model's parameters dependency on SOC, cell's temperature and SOH.
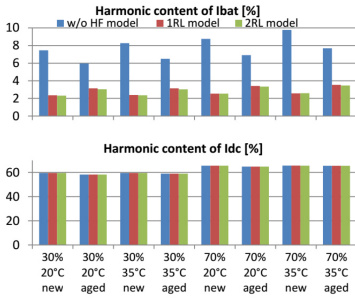
Fig. 16. Harmonic content of I_{dc} and I_{bat} calculated for three different cases and for eight operation conditions.
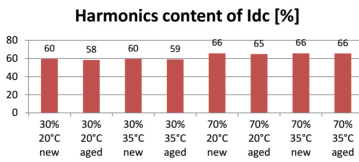
Fig. 17. Harmonic content of I_{dc} calculated based on simulation results when using 1RL-model for the eight operation conditions.
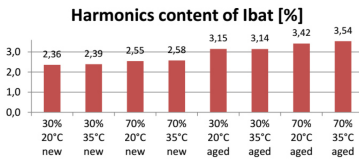
Fig. 18. Harmonic content of I_{bat} calculated based on simulation results when using 1RL-model for the eight operation conditions.

V. CONCLUSION

The paper is analyzing the usage of electrical models of li-ion batteries for the simulation of the ESS. The following 6 results have been found out:

- Battery ECM with one time constant (OTC) does not represent the fast battery's dynamics accurately mainly when the battery is aged. Therefore, at least two time constants (TTC model) are needed in order to represent the slow and fast dynamics of the battery over the whole service life of the cells (Fig. 4).
- Temperature deviation within 20°C to 35°C range as well as aging has a significant effect on the voltage drop at the dc-side and needs to be taken into account (Fig. 6 and Fig. 8).
- The SOC, the aging and the temperature do not have a significant effect on the Total Harmonics Distortion (THD) on the grid side (Tab. II).
- In order to calculate correctly the harmonics of I_{bat}, the usual ECM for low frequencies need to be extended by an HF model with one time constant (1RL-model).
- The harmonic content of I_{dc} and I_{bat} in Fig. 17 and Fig. 18 depicts that the effects of SOC, cells' temperature and aging on the harmonic content can be neglected.

We would underline that our results are only valid for the cells used in this investigation. Other cells might have different behavior.

REFERENCES

[1] J. L. Helguero, "Modeling and simulation of a big battery storage system of a smart grid including power electronics," master thesis, Hochschule Kempten, March 2013.

[2] T. Khani, "Modeling and simulation of a big battery storage system of a smart grid including power electronics and control," master thesis, Hochschule Kempten, September 2013.

[3] L. F. Hoyos, "Simulation of a battery storage system taking into account a thermal-electric model for lithium-ion cells," master thesis, Hochschule Kempten, July 2014.

[4] A. Rahmoun and H. Biechl, Parameters identification of equivalent circuit diagrams for li-ion batteries, in 11th International Symposium PRNU 2012 TOPICAL PROBLEMS IN THE FIELD OF ELECTRICAL AND POWER ENGINEERING and Doctoral School of Energy and Geotechnology II, 2012, pp. 3537.

[5] A. Rahmoun, H. Biechl, and A. Rosin, Evaluation of Equivalent Circuit Diagrams and Transfer Functions for Modeling of Lithium-Ion Batteries, Sci. J. Riga Tech. Univ. - Electr. Control Commun. Eng., vol. 2, pp. 3439, 2013.

Appendix 7

VII
A. Rahmoun, A. Armstorfer, J. Helguero, H. Biechl, and A. Rosin. Mathematical modeling and dynamic behavior of a lithium-ion battery system for microgrid application. *2016 IEEE International Energy Conference (ENERGYCON)*, pages 1–6, 2016

Mathematical Modeling of a Battery Energy Storage System in Grid Forming Mode

Ahmad Rahmoun, Andreas Armstorfer,
Helmuth Biechl
Institute of Electrical Power Systems (IEES)
University of Applied Sciences Kempten
Kempten, Germany
ahmad.rahmoun@hs-kempten.de, andreas.armstorfer@hs-
kempten.de, biechl@hs-kempten.de

Argo Rosin
School of Engineering: Department of Electrical Power
Engineering and Mechatronics
Tallinn University of Technology
Tallinn, Estonia
argo.rosin@ttu.ee

Abstract—**The paper presents an approach for modelling a Battery Energy Storage System (BESS). This approach consists of four stages. In the first stage a detailed model is developed taking into consideration all the electrical details of the original system. In stage two the detailed model will be validated using real measurements. In the third stage the complexity of the detailed model is reduced resulting in a simplified model which is able to represent the relevant electrical dynamics of the original system and to decrease the simulation time significantly. In the last stage the simplified model is validated by a comparison with simulation results of the detailed model.**

Keywords—Battery energy storage, Power system analysis computing, Power system dynamics, Microgrid

I. INTRODUCTION

The high penetration of inverter-connected Renewable Energy Sources (RESs) in low voltage microgrids replacing the conventional generators and their rotating machinery has led to a significant reduction in rotating system inertia. In island operation where no connection to a stiff grid is available, the BESSs play a very important role to ensure generation adequacy and to increase security and reliability of microgrids [1]. The fast response of BESS improves also microgrid transient stability for different type of disturbances like fast changes of solar irradiation, loss of one Distributed Generation (DG) and three phase short circuit cases [2]. This means that having a BESS in a microgrid contributes to avoid big deviations of voltage and frequency during such contingencies in the microgrid. For these reasons an accurate model of the BESS describing not only the State of Energy (SOE) but also the electrical dynamics is essential for analyzing the microgrid transients and stability. In the frame of the research project IREN2 (Future Oriented Electricity Grids for Integration of Renewable Energy Systems) a microgrid has been set up in the village Wildpoldsried in the south of Germany [3]. The microgrid consists of RESs, a stationary 300kVA/170kWh battery system with Lithium Nickel Cobalt Oxide (NCO) - Lithium Titanate cells, a 100kVA Genset with vegetable oil fueling for secondary control, a 500kVA back to back station between the 20kV and the 400V grid to emulate volatile photovoltaic generation as well as a battery of infinite energy or create real disturbances. Further a 3x 50kW controllable unsymmetrical load bank is available.

One of the important goals of IREN2 is to develop a mathematical model of the BESS for the two operation modes of a microgrid i.e. synchronous mode and island mode. In synchronous mode BESS synchronizes itself to an external grid and tracks given reference setpoints P_{ref} and Q_{ref}, whereas fast responses are avoided in order not to cause big disturbances to the grid. All the details about the mathematical modeling of BESS in this operation mode are described in [4].

In island operation mode the droop control forms a decentralized control method which is based on the communication between the different DGs over frequency and voltage providing an expandable system without extra communication requirements [5]. This approach implies that every DG runs in Grid Forming (GF) mode and regulates its active resp. reactive power output depending on frequency resp. voltage. The dynamic behavior of BESS depends not only on the electrical power components but also on the control structure. The standard control structure using two cascaded synchronous controllers working in dq reference frame is extensively analyzed in literature [6]. However in industrial applications a different control structure is used and will therefore be discussed in this paper.

This research work starts with a description of the electrical system including control structure of the BESS being explained in detail in section II. Section III deals with setting up a detailed mathematical model which describes the electro dynamical behavior of the real system. Section IV shows the verification of the detailed model by a comparison with measurement results of the real system. Due to the fact that the detailed model is very complex and is causing very high computation time on a computer, section V focus on a simplification of the detailed model resulting in a simplified model suitable for the simulation of the BESS as a subsystem in a microgrid which consists also of other power components. The validation of the simplified model using simulation results of the detailed model is carried out in Section VI. Section VII concludes the paper.

II. BESS STRUCTURE

During operation some unexpected Lithium-Ion (Li-ion) cell issues had to be solved by a replacement of all battery cells. The new cells were just available with different geometry having the consequence that only three battery strings with approx. the same total energy could be set up instead of six in the original version. Due to this fact every two inverters of the original system had to be connected to one battery string resulting in a much more complex electrical structure because extra filters and isolating transformers were necessary. The modified structure affects the dynamic behavior being discussed later in Section IV.

A. Electrical Structure

As shown in Fig. 1 the BESS consists of three Li-ion batteries Batt1, Batt2 and Batt3 which can be operated independently. Each battery is connected to two 3-phase inverters through an Electromagnetic Interference (EMI) filter for protecting the Battery Management System (BMS) from electrical noise due to the unsynchronized switching of the two parallel inverters.

Every 3-phase inverter has a rated power of 55kVA and is followed by an LCL filter in order to reduce the current harmonics injected into the grid. The first three inverters Inv.1, Inv.2 and Inv.3 are connected to the first matching transformer MT_1 and the next three inverters Inv.4, Inv.5 and Inv.6 are connected to the second matching transformer MT_2.
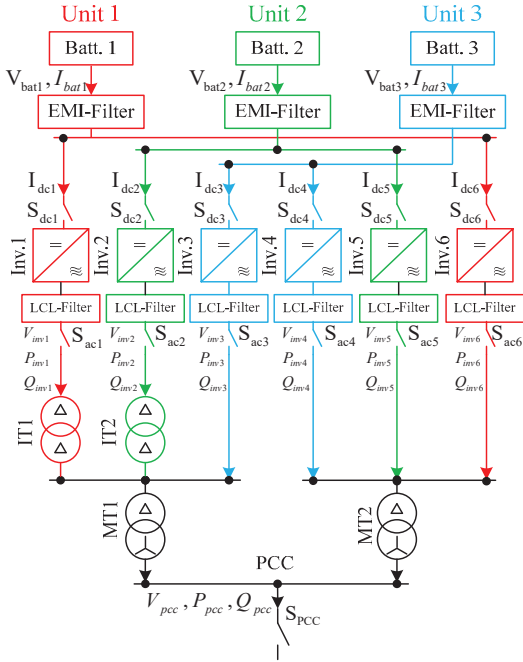
Fig. 1. Block diagram of the BESS electrical structure.

The three phase two-winding matching transformers are used to adapt the inverters' low output voltage to the grid voltage. Two isolating transformers IT_1, IT_2 are used to avoid circulating currents in the circuit of Inv.1 and Inv.6, and of Inv.2 and Inv.5 which are connected to the same dc circuit.

B. Control Structure

The input of the control structure are the 3-phase voltage and current measured at the output of the LCL filter. Based on these measurements the output active and reactive power of the inverter are calculated and fed into the droop controller. The droop controller is composed mainly of two parts. The first part adjusts the inverter frequency based on the active power, the new frequency setpoint $\tilde{f}$ is calculated based on the P/f droop formula as shown in Fig. 2, then $\tilde{f}$ is smoothed using a Low Pass Filter (LPF) with a time constant T_c resulting in the inverter actual frequency f, which is integrated to get the actual angle θ.

The second part of the droop controller regulates the amplitude of the inverter voltage depending on the reactive power at the output side of the inverter. The new setpoint of the voltage amplitude $\tilde{V}$ is calculated using the Q/V droop formula as shown in Fig. 2. The voltage $\tilde{V}$ is smoothed using a similar LPF filter as it is the case in the first part. The filtered voltage amplitude $\hat{V}$ is used as reference for the Proportional-Integral (PI) controller which regulates the inverter voltage amplitude V to match the reference voltage $\hat{V}$.
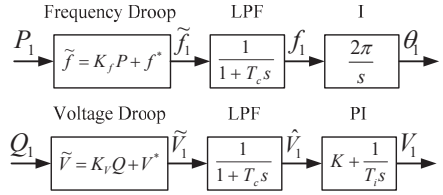
Fig. 2. Structure of frequency and voltage droop control.

III. DETAILED MODEL OF THE BESS

The detailed model considers the dynamics of dc and ac sides and the switching operation of the IGBTs, thus it is appropriate for analyzing short time transients and harmonic content. Starting from dc side, the battery model is implemented by upscaling a Li-ion cell's model. The cell is modeled in a previous work using a third order Equivalent Circuit Model (ECM) taking into account the dependencies on State of Charge (SOC), temperature and State of Health (SOH) [7], [8]. The EMI and LCL filters are modeled using their equivalent circuits and the parameters are given in Table I. The IGBTs are modeled using two-state resistive switches. The transformers are modeled using the standard 3-phase 2-winding transformer model in PSCAD. The specifications of both matching and isolating transformers are given in Table II.

The modular structure of the BESS enables to split the BESS into three independent units U_1(Batt1, Inv.1, Inv.6 and

IT$_1$), U$_2$(Batt2, Inv.2, Inv.5 and IT$_2$) and U$_3$(Batt3, Inv.3 and Inv.4) shown in Fig.1 in red, green and blue in Fig. 1 respectively. U$_1$ and U$_2$ have an identical structure and they differ from U$_3$ by having an isolating transformer in series to the output of Inv.1 and Inv.2 respectively. Therefore two detailed models are only needed for evaluating BESS dynamics.

LCL Filter equivalent circuit parameters	Value
Serial inductance L$_F$	160µH
Serial resistance R$_F$	16.4mΩ
Parallel capacitor C$_F$	3.5µF
EMI filter equivalent circuit parameters	**Value**
Serial inductance L$_S$	0.1µH
Serial resistance R$_S$	0.1mΩ
Parallel capacitor C$_P$	8 µF

TABLE I.   PARAMETERS OF LCL AND EMI FILTER.

257V/400V Δ-Y Matching transformer	Value
Rating [S$_{r,LV}$]	165kVA
u$_k$	4.3%
P$_{copper}$	0.008484pu
P$_{no-load}$	0.002424pu
260V/260V Δ-Δ Isolating transformer	**Value**
Rating [S$_{r,LV}$]	55kVA
u$_k$	3.73%
P$_{copper}$	0.021545pu
P$_{no-load}$	0.0029091pu

TABLE II.   SPECIFICATIONS OF THE MATCHING AND ISOLATING TRANSFORMERS.

IV.   DETAILED MODEL VALIDATION

The verification of the detailed model is carried out using real measurements of the BESS, where a 60kW ohmic load step is applied on both U1 and U3 at the Point of Common Coupling (PCC). The experiments are executed with a new battery at 25°C and relative state of charge around SOCr=50%. The voltages and currents are measured at three different points in order to evaluate the quality of the detailed models of U1 and U3. The first Evaluation Point (EP) is the dc side of each unit. At this point the dc voltages and currents are used directly for the comparison. The second EP is at the inverters' output and the third EP is at the PCC. For the second and third EPs the voltage phasor amplitude, frequency, active and reactive power are calculated and used for the evaluation.

Figures 3, 4 and 5 show the comparison between detailed model's signals of U$_1$ and corresponding measurements. These figures show a fluctuation of the active and reactive power at the moment of switching the load on due to the delay between the different phases of the ohmic load which results in a asymmetrical loading of U$_1$ which finally causes these fluctuations. After these fluctuations, slow oscillations in active and reactive power signals due to the different serial impedances between Inv.1, Inv.6 and the PCC can be seen in Fig. 4 (b,c).

Figures 6, 7 and 8 show the comparison between signals of the detailed model of U$_3$ and measurements. These figures show only the fluctuations due to the switching of the load but they show no slow oscillations because Inv.3 and Inv.4 have the same serial impedance to the PCC. The oscillations in

active and reactive power are analyzed mathematically and will be presented in the next research work. The numbers inside the figures show values of the relative error which are calculated according to (1).

$$E_{rms}(X_1, X_2)[\%] = \frac{rms(X_1 - X_2)}{\max(X_1, X_2)} \times 100 \qquad (1)$$
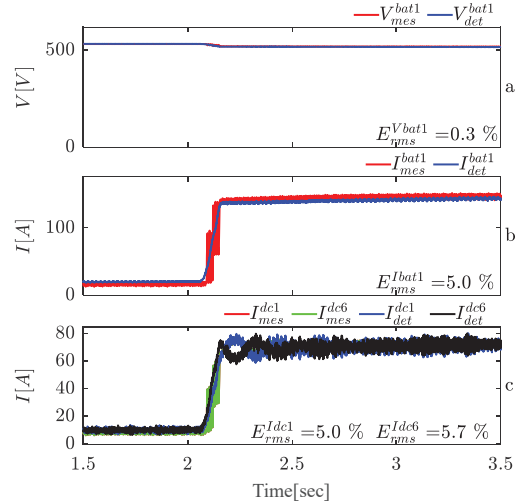
Fig. 3. Unit1: Comparison between detailed model and measurements for: (a) battery voltage; (b) battery current; (c) dc currents of inv1 and inv6.
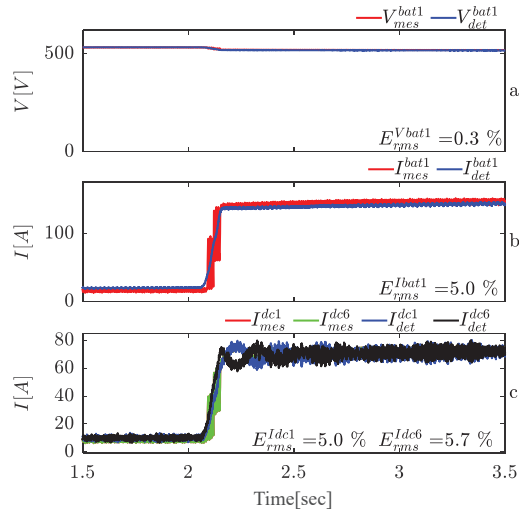
Fig. 4. Unit1: Comparison between detailed model and measurements at the ac side of inv1 and inv6 for: (a) voltage amplitude; (b) reactive power; (c) active power; (d) frequency.
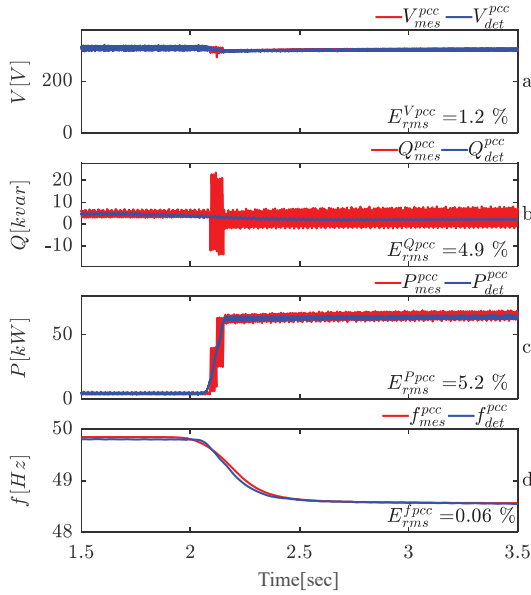
Fig. 5. Unit1: Comparison between detailed model and measurements at \gls{pcc} for: (a) voltage amplitude; (b) reactive power; (c) active power; (d) frequency.
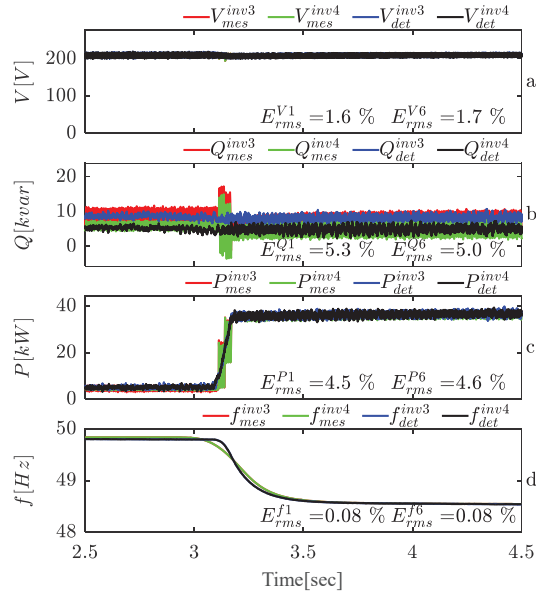
Fig. 7. Unit3: Comparison between detailed model and measurements at the ac side of inv3 and inv4 for: (a) voltage amplitude; (b) reactive power; (c) active power; (d) frequency.
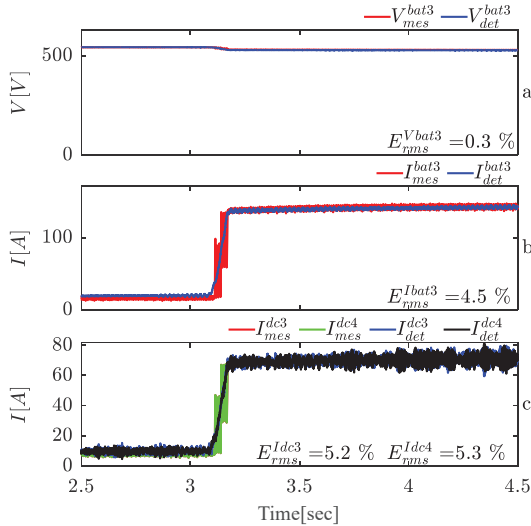
Fig. 6. Unit3: Comparison between detailed model and measurements for: (a) battery voltage; (b) battery current; (c) dc currents of inv3 and inv4.
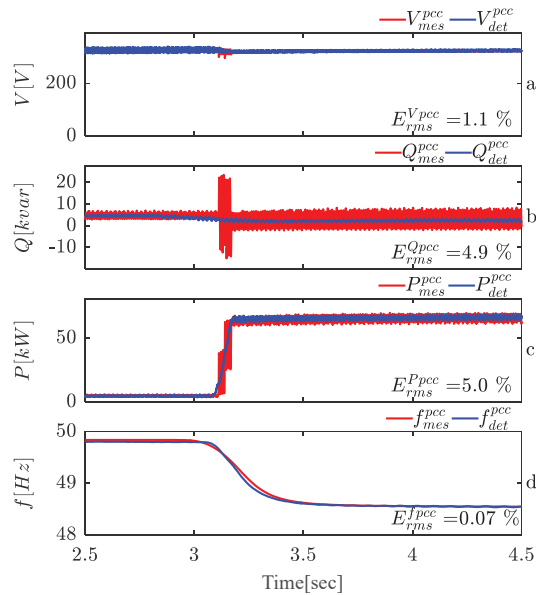
Fig. 8. Unit3: Comparison between detailed model and measurements at \gls{pcc} for: (a) voltage amplitude; (b) reactive power; (c) active power; (d) frequency.

V. SIMPLIFIED MODEL OF THE BESS

Due to the complex structure of the BESS the detailed model is unsuitable for long time simulations along with other microgrid components. Therefore a simplified model is required which represents the fundamental dynamics of the original system but reduces the complexity of the detailed model.

The simplification procedure is performed according to the following steps:

1. The dc side dynamics are neglected as it does not influence the ac side dynamics significantly [9].

2. Each 3-phase inverter is modelled using an ideal 3-phase voltage source connected to the serial impedance of the LCL filter.

3. All the transformers are replaced with their equivalent serial and parallel impedances (Z_s^{MT} and Z_s^{IT1}) resp. (Z_p^{MT}, Z_p^{IT1} and Z_p^{IT2}) referred to the high voltage side of the matching transformers.

4. The control unit for the simplified model remains the same.

The simplified electrical structures of U1 and U3 are shown in Fig. 9 and Fig. 10 respectively.
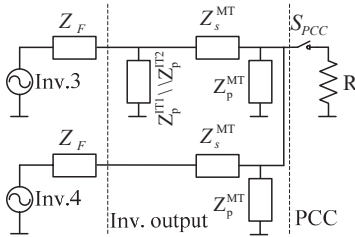
Fig. 9.   Simplified model of Unit 1.
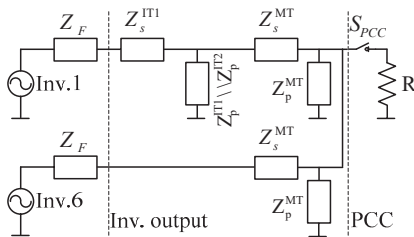
Fig. 10. Simplified model of Unit 3.

VI. SIMPLIFIED MODEL VALIDATION

In this section the simplified model simulation results are compared with those of the detailed model and plotted in Fig. 11 and Fig. 12. It is carried out for U_1 at the inverters' output and at PCC respectively. The simplified model shows also the oscillations in active and reactive power signals similarly to the detailed model.

Figures 13 and 14 for U3 at inverters' output and at PCC respectively show that a good coincidence between the simplified and detailed model of U3.
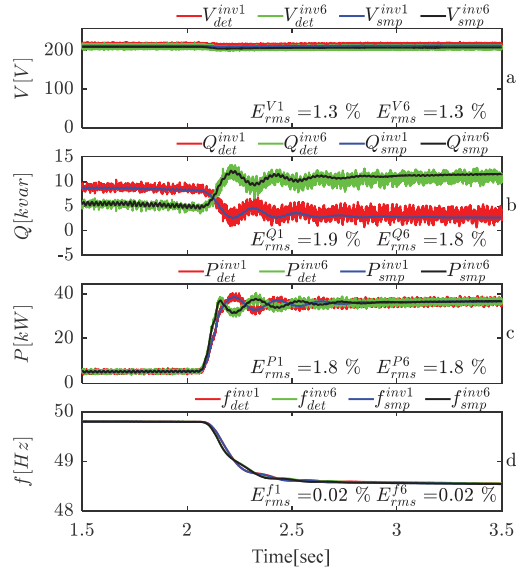
Fig. 11. Unit1: Comparison between detailed and simplified model at the ac side of inv1 and inv6 for: (a) voltage amplitude; (b) reactive power; (c) active power; (d) frequency.
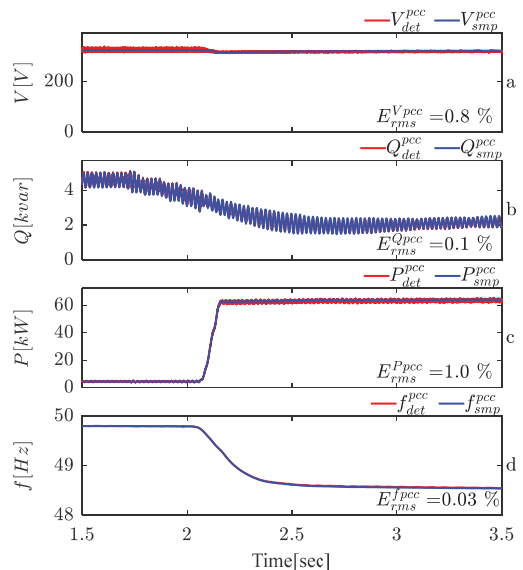
Fig. 12. Unit1: Comparison between detailed model and measurements at \gls{pcc} for: (a) voltage amplitude; (b) reactive power; (c) active power; (d) frequency.
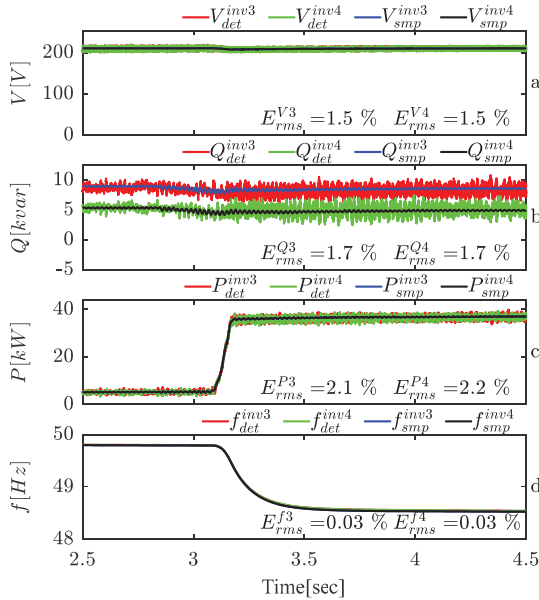
Fig. 13. Unit3: Comparison between detailed and simplified model at the ac side of inv3 and inv4 for: (a) voltage amplitude; (b) reactive power; (c) active power; (d) frequency.
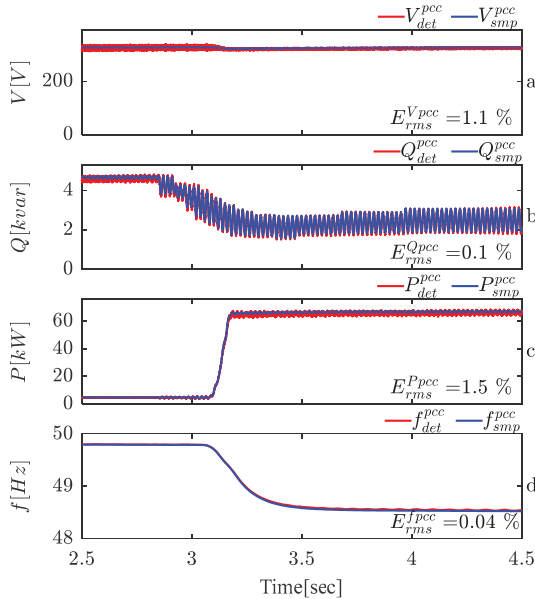
Fig. 14. Unit3: Comparison between detailed model and measurements at \gls{pcc} for: (a) voltage amplitude; (b) reactive power; (c) active power; (d) frequency.

VII. CONCLUSION

Figures 3, 4, 5, 6, 7 and 8 show a good coincidence with a relative error less than 5% between measurement and simulation results for the detailed model of U_1 and U_3 respectively. The high error values for dc currents, active power and reactive power are due to the asymmetrical loading at begin of the load step.

The comparison between simulation results for detailed and simplified models in Fig. 11, 12, 13 and 14 confirms that the fundamental dynamic behavior is accurately represented for U_1 resp. U_3 when the simplified models are applied.

REFERENCES

[1] N. Shi and Y. Luo, "Energy Storage System Sizing Based on a Reliability Assessment of Power Systems Integrated with Wind Power," *Sustainability*, vol. 9, no. 3, p. 395, Mar. 2017.

[2] J. Stanojevic, A. Djordjevic, and M. Mitrovic, "Influence of battery energy storage system on generation adequacy and system stability in hybrid micro grids," in *2016 4th International Symposium on Environmental Friendly Energies and Applications (EFEA)*, 2016, pp. 1–6.

[3] "IREN2 (Future Oriented Electricity Grids for Integration of Renewable Energy Systems). [Online]. Available: http://www.iren2.de/.

[4] J. L. H. Cruz, "Master thesis.," University of Applied Sciences Kempten, 2013.

[5] A. Engler, "Applicability of droops in low voltage grids," *Int. J. Distrib. Energy Resour. Smart Grids*, no. 1, pp. 1–5, 2005.

[6] J. Rocabert, A. Luna, F. Blaabjerg, and P. Rodríguez, "Control of power converters in AC microgrids," *IEEE Trans. Power Electron.*, vol. 27, no. 11, pp. 4734–4749, 2012.

[7] A. Rahmoun and H. Biechl, "Modelling of Li-ion batteries using equivalent circuit diagrams," *Prz. Elektrotechniczny*, vol. 2012, no. 7b, pp. 152–156, 2012.

[8] A. Rahmoun, H. Biechl, and A. Rosin, "Evaluation of Equivalent Circuit Diagrams and Transfer Functions for Modeling of Lithium-Ion Batteries," *Electr. Control Commun. Eng.*, vol. 2, no. 1, pp. 34–39, May 2013.

[9] A. Rahmoun, A. Armstorfer, J. Helguero, H. Biechl, and A. Rosin, "Mathematical modeling and dynamic behavior of a Lithium-Ion battery system for microgrid application," in *2016 IEEE International Energy Conference (ENERGYCON)*, 2016, pp. 1–6.

Ahmad Rahmoun is a doctoral student and researcher at the Institute of Electrical Power Systems (IEES) of University of Applied Sciences Kempten/Germany. He received his Master degree in the field of Electrical Engineering from the University of Applied Sciences Kempten (HKE) in 2012. His current research interests is mathematical modeling of battery systems for microgrid and e-mobility applications.

Appendix 8

VIII
N. Beg, A. Rahmoun, A. Armstorfer, A. Rosin, and H. Biechl. Determination methods for controller parameters of back-to-back converters in electric power grids. *2016 Electric Power Quality and Supply Reliability (PQ)*, pages 157–164, 2016

Determination Methods for Controller Parameters of Back-to-Back Converters in Electric Power Grids

Nauman Beg, Ahmad Rahmoun, Andreas Armstorfer, Argo Rosin, and Helmuth Biechl

Abstract—**The paper presents a new optimization method for PI controllers of back-to-back voltage source converters using a vector control scheme to enable the control of active and reactive power transmission between two independent grids, for example, an emulator as a load or a source between the medium voltage distribution grid and a low voltage island grid. The control principle based on three phase systems in dq-components enables an independent control of active and reactive power with a simple structure using PI controllers. The presented optimization method using pole placement (PP) technique for tuning of the controllers leads to a higher degree of freedom and therefore to better results compared to the modulus optimum (MO) optimization method discussed in [1], [2]. A cascaded control model consisting of inner current and outer power/voltage control loops is being used for the optimization of the system's transient response. The mathematical modeling of the control system as well as the evaluation of the controller parameters are described in detail. A comparison of the presented optimization method for controllers with existing methods is shown by simulation results using the software PSCAD.**

Index Terms—**Modulus Optimum Method (MO), Pole Placement Method (PP), Back-to-Back Voltage Source Converter (VSC), Vector Control, Controller Parameter Determination.**

I. INTRODUCTION

Integration of decentralized and renewable energy sources in existing grid structures is a fundamental challenge for the energy transition. In the research project IREN2 (Future-Oriented Grids for the Integration of Renewable Energy Systems), a micro-grid with islanding capability is investigated theoretically and established practically in the village Wildpoldsried in Southern Germany [3], [4]. A low voltage grid area consisting of households, PV plants, a genset with plant-oil operation as well as a stationary battery storage system is operated in island mode. For testing purposes, a DC-link converter (back-to-back converter) is installed between the 400 V low voltage (LV) grid and the 20 kV medium voltage (MV) grid (Fig. 1).

The back-to-back voltage source converter (VSC) is used as an emulator for a source (e.g. PV plant), as a controllable load or even as an energy storage system with infinite energy. The system topology of VSC is depicted in Fig. 2. The VSC can be operated in 4-quadrants, hence active and reactive power can be controlled independently.

A generic schematic of a grid connected single PWM controlled 3-phase converter is given in Fig. 3. An effective control scheme based on vector control method discussed in [5] is being investigated in this paper. Since vector control gives an alternate representation of voltages and currents of a three phase system using Clark-Park transformations, it enables the use of relatively simple PI controllers to regulate active and reactive power in the system. A new approach for tuning PI controllers using PP method in contrast to empirical tuning techniques such as MO and symmetric optimum (SO) discussed in [1], [2], [5] which relies on dominant pole
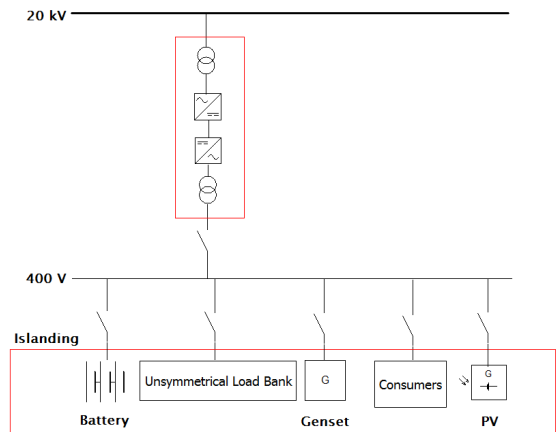
Fig. 1. System overview in island mode.
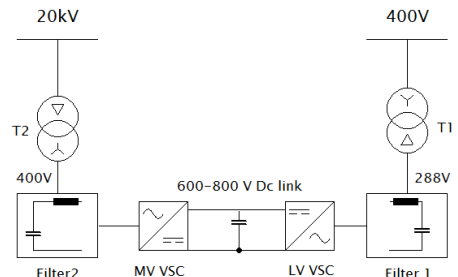
Fig. 2. VSC topology for LV and MV coupling.

N. Beg is with Institute of Electrical Power Systems (IEES), University of Applied Sciences Kempten, Germany (e-mail: nauman.beg@stud.hs-kempten.de).

A. Rahmoun, A. Armstorfer, and H. Biechl are with Institute of Electrical Power Systems (IEES), University of Applied Sciences Kempten, Germany and Faculty of Power Engineering, Tallinn University of Technology (e-mail: ahmad.rahmoun@hs-kempten.de, andreas.armstorfer@hs-kempten.de, biechl@hs-kempten.de).

Argo Rosin is with Faculty of Power Engineering, Tallinn University of Technology, Tallinn, Estonia (e-mail: argo.rosin@ttu.ee).

Fig. 3. 3-phase grid connected PWM inverter.

cancellation improves transient control response and gives more degree-of-freedom (DOF) for optimizing the system response. As this approach is much more generic, it can be applied to a wide variety of systems without pre-conditions imposed by the system under consideration.

A detailed system description along with transformed system equations for voltage and power controllers is handled in Section II. Control loops for current and power/voltage are discussed in Section III whereas the PI controller tuning approach is presented in Section IV. Section V shows system simulation results and a comparison for controllers tuned by using the discussed approach based on PP as well as MO and symmetric optimum (SO) methods [1]. Section VI concludes with a discussion and comments on both presented techniques and highlights benefits of controller tuning using the PP method.

II. SYSTEM DESCRIPTION

The mathematical description of the grid connected VSC in Fig. 3 is given by

$$v_{H,ABC} = R_{tot} \cdot i_{abc} + L_{tot} \cdot \frac{di_{abc}}{dt} + v_{C,ABC} \quad (1)$$

where R_{tot} and L_{tot} describe combined grid, filter and transformer resistance and inductance respectively. The branch comprising of R_D and C_{filter} is neglected due to the high impedance at $\omega_o = 2\pi \cdot 50$ Hz. The converter terminal voltage $v_{C,ABC}$ is taken with respect to grid voltage $v_{H,ABC}$ reference point. After applying dq-transformation, the system can be described as follows [6]:

$$\begin{bmatrix} v_{H,d} \\ v_{H,q} \end{bmatrix} = R_{tot} \begin{bmatrix} i_d \\ i_q \end{bmatrix} + L_{tot} \frac{d}{dt} \begin{bmatrix} i_d \\ i_q \end{bmatrix} + L_{tot} \begin{bmatrix} 0 & -\omega_o \\ \omega_o & 0 \end{bmatrix} \begin{bmatrix} i_d \\ i_q \end{bmatrix} + \begin{bmatrix} v_{c,d} \\ v_{c,q} \end{bmatrix} \quad (2)$$

The dq-frame rotational speed is synchronized to the grid voltage speed by using a standard PLL structure. Aligning the grid voltage state vector with the d-axis voltage component v_d results in relationships for active and reactive power in LV VSC [2], [6]:

$$P(t) = \frac{3}{2} [v_{H,d}(t) i_d(t)] \quad (3)$$

$$Q(t) = \frac{3}{2} [-v_{H,d}(t) i_q(t)] \quad (4)$$

Equations (3) and (4) describe that by applying Clark-Park's transformation, it is possible to independently control active and reactive power in the system given that the currents $i_{d,q}$ in the coupled transformed system according to (2) are independent. Similarly, a relationship between ac and dc power is given by

$$P = \frac{3}{2} [v_{H,d}(t) i_d(t)] = V_{dc} I_{dc}$$

$$I_{dc} = C_{DC} \cdot \frac{dV_{DC(t)}}{dt} + I_L \quad (5)$$

Equation (5) describes that active power in the LV system affects the DC link voltage V_{DC}. To stabilize V_{DC}, a voltage controller is implemented in the MV VSC.

To decouple the system in (2), the system transfer function between current I and voltage difference between converter and grid ΔV is evaluated which is given by

$$G(s) = \frac{\vec{I}}{\overrightarrow{\Delta V}} = \frac{1}{sL + R + j\omega_o L}$$

$$\vec{I} = i_d + j \cdot i_q \quad (6)$$

$$\overrightarrow{\Delta V} = \Delta V_d + j \cdot \Delta V_q$$

where R and L corresponds to R_{tot} and L_{tot}, respectively.

The coupling term $j\omega_o L$ in (6) is compensated by the feedback transfer function $G_2(s)$ shown in Fig. 4 [7] which is evaluated so that the system transfer function $\vec{I}/\overrightarrow{\Delta V}'$ results in two decoupled systems in d and q components so that $\overrightarrow{\Delta V}' = \overrightarrow{\Delta V}$ independently controlled by using two separate PI-controllers, one for active and one for reactive power. The transfer function $G_2(s)$ is evaluated as

$$G_2(s) = j\omega_o L \quad (7)$$

Fig. 4. Feedback decoupling scheme.

Fig. 5 shows the feedback decoupling implemented altogether with a PI current controller loop so that the system transfer function seen by the controller is decoupled and can be tuned independently for active and reactive power.

Fig. 5. dq-decoupling for inner current controller.

III. CASCADED CONTROL SYSTEM

A cascaded control is implemented in both LV and MV VSCs to regulate active/reactive power and V_{DC} respectively. An overview of the control topology is shown in Fig. 6 where the inner transient current controller regulates $i_{d,q}$ and the outer slow P, Q / voltage controller regulates active / reactive power and V_{DC} in the system. An advantage of using a cascaded control structure is its ability to improve the disturbance rejection since the inner current loop reacts much faster than the outer power loop. Current references for the inner current loop are generated by the outer control loop. $G_{sys}(s)$ and $Inv(s)$ represents system and inverter transfer function for the current control loop, respectively.

Fig. 6. Overview of cascaded control scheme.

a) Block diagram of current control loop

b) Block diagram of power loop

c) Block diagram of voltage control loop

Fig. 7. Block diagrams of control loops.

Fig. 7a demonstrates the block diagram of the current control loop after decoupling. It consists of a 1st order inverter delay where T_{sw} is the switching period of VSC. The system transfer function consists of an equivalent transformer and filter impedance. The current loop structure remains similar for both V_{DC} and P-Q control blocks.

Fig. 7b shows the block diagram of the outer active power control loop where $G_{cc,cl}(s)$ is the closed loop transfer function of the inner current control loop. $G_{cc,cl}(s)$ is taken as unity since the inner loop reacts significantly faster than the outer power control loop. The reactive power control loop has a similar control structure. Fig. 7c shows the block diagram of the outer voltage control loop for controlling the DC link voltage V_{DC} in MV VSC. The relationship between i_d and I_{DC} as well as I_L is derived from (5). The inner current loop is modeled as a 1st order system to better approximate transients of the current control loop within the voltage loop.

The PI controller is opted as a reasonable controller type to avoid a steady state closed loop error (P controller) and additional overshoot as well as increased sensitivity due to the differential part in the PID controller.

IV. PI CONTROLLER TUNING USING POLE PLACEMENT METHOD

Tuning of a PI controller based on PP method [8], [9] as an alternative to the MO method in [1], [2], [10] is presented here. The highlighted advantage of the PP method is its higher degree of freedom in terms of fine tuning of the system response and its generic characteristics which enable to apply this method on a wide range of systems in contrast to the MO method which is constrained by a pole zero cancellation of the dominant system pole and fixed control loop structures.

A. Current Control Loop in LV VSC

The closed loop transfer function of the current loop described in Fig. 7a is given by (8):

$$G_{cc,cl} = \frac{\frac{sK_P + K_I}{T_aL}}{s^3 + s^2\left(\frac{T_aR + L}{T_aL}\right) + s\left(\frac{R + K_P}{T_aL}\right) + \frac{K_I}{T_aL}} \quad (8)$$

where $T_a = T_{sw}/2$. The denominator of the system in (8) is compared with a 3rd order characteristic equation given by

$$(s + p_1)(s^2 + 2\varepsilon\omega_n s + \omega_n{}^2) \quad (9)$$

By a coefficient comparison, the current controller parameters are calculated as

$$K_P = (T_aL)(\omega_n{}^2 + 2\varepsilon\omega_n p_1) - R$$
$$K_I = p_1\omega_n{}^2 T_aL \quad (10)$$

The controller parameters depend on ω_n, natural frequency of the system, ε which represents damping factor and pole p_1 which affects rise time, overshoot and disturbance rejection in the system. ω_n controls the bandwidth of the controller and is kept smaller than the switching frequency. The damping ratio on the other hand is adjusted close to 1 so that the system has a reduced rise time and minimal overshoot. There exists a tradeoff between ε and ω_n. Increasing ω_n results in higher overshoot (smaller ε) and vice versa. The final values of these parameters will be adjusted according to the application requirements.

The step response of the current control loop for both PP [9] and MO [6] method as well as without current controller with the system and controller parameters given in Table I are shown in Fig. 8. The current loop is stable even without controller but has a high overshoot and settling time. Stability diagrams which include root locus as well as open loop bode plots for current control loop tuned by the PP method are shown in Fig. 9. Root locus and bode plot diagrams show the location of closed loop poles and stability margins, respectively.

TABLE I. SYSTEM AND CONTROLLER PARAMETERS FOR CURRENT LOOP IN LV VSC

Parameter	Value
f_{sw}	4 kHz
T_a	125 μs
L	116 μH
R	0.982 mΩ
p_1	3 rad/s
ω_n | BW	5000 | 4310 rad/s
ε	0.8
v_d	235 V
K_p	0.362
K_I	1.0875
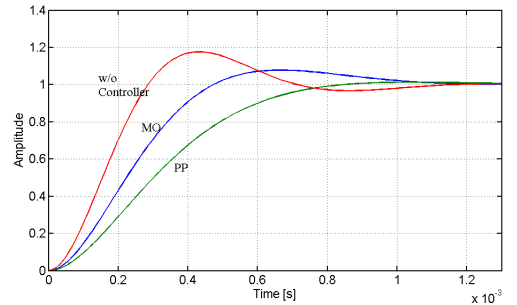
Fig. 8. Step response of current control loop in LV VSC.

Fig. 9. Stability diagrams of current loop for PP method in LV VSC.
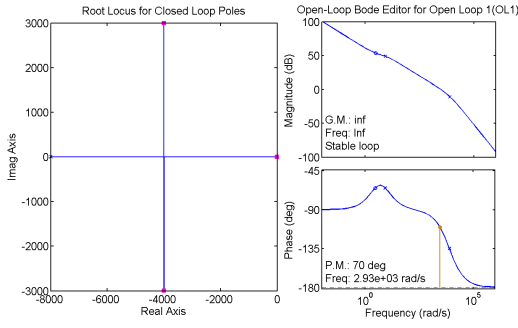
Fig. 10. Step response of power control in LV VSC.

B. Power Control Loop in LV VSC

The closed loop transfer function of the active power loop described in Fig. 7b and for unity closed current control loop is given by

$$G_{pc,cl} = \frac{\frac{(sK_P' + K_I')(sv_d)}{(2 + 3v_dK_P')}}{\left(s + \frac{3v_dK_I'}{2 + 3v_dK_P'}\right)} \quad (11)$$

A pole comparison with 1st order characteristic equation given by

$$s + s_1 \quad (12)$$

delivers controller parameters as follows:

$$K_P' = \left(\frac{1}{3v_d}\right)\left(\left(\frac{3v_dK_I'}{s_1}\right) - 2\right) \quad (13)$$

$$K_I' = 1$$

Pole s_1 controls the rise time as well as the bandwidth of the system and is selected between 1/10 and 1/20 of the bandwidth of the inner current control loop. v_d is an input to the system. $G_{cc,cl}(s)$ is considered as a constant since inner current loop reacts faster than the outer power loop.

The step response of the power loop using the PP and MO are shown in Fig. 10 respectively. The system and controller parameters are included in Table II. Stability diagrams for the PP method are shown in Fig. 11. The improved rise time for PP method can be seen clearly.

C. Current and Voltage Control Loop in MV VSC

The current control loop in MV VSC has a similar structure and equations as in LV VSC shown in Fig. 7a. All system and current controller parameters for the PP method for the system in [6], shown in Fig. 16 are summarized in Table III.

The closed loop transfer function of the voltage control loop in MV VSC shown in Fig. 7c is given by (14).

$$G_{vc,cl} = \frac{\frac{(sK_{pv} + K_{iv})(3v_d)}{4V_{dc}T_aC}}{s^3 + s^2\left(\frac{1}{2T_a}\right) + s\left(\frac{3K_{pv}v_d}{4V_{dc}T_aC}\right) + \left(\frac{3v_dK_{iv}}{4V_{dc}T_aC}\right)} \quad (14)$$

A coefficient comparison of the denominator in (14) with a 3rd order characteristic equation gives the following voltage controller parameters:

Fig. 11. Stability diagrams of power loop for PP method in LV VSC.

TABLE II.   SYSTEM AND CONTROLLER PARAMETERS FOR POWER LOOP IN LV VSC

Parameter	Value
ω_n	5000 rad/s
$s_1 = \omega_n/20$ | BW	250 | 273 rad/s
v_d	235 V
K'_p	8.254e^{-4}
K'_I	1

TABLE III.   SYSTEM AND CONTROLLER PARAMETERS FOR CURRENT LOOP IN MV VSC

Parameter	Value
f_{sw}	4 kHz
T_a	125 μs
L_1	145 μH
R_1	2.368 mΩ
p_1	3 rad/s
ω_n | BW	5000 | 4310 rad/s
ε	0.8
K_p	0.4513
K_I	1.3594

$$K_{pv} = \frac{(\omega_n^2 + 2\varepsilon\omega_np_1)(4V_{dc}T_aC)}{3v_d}$$

$$K_{iv} = \frac{(p_1\omega_n^2)(4V_{DC}T_aC)}{3v_d} \quad (15)$$

All system and controller parameters for the voltage loop are summarized in Table IV.

A higher bandwidth ω_n is selected to compensate the intrinsic slow response of the open voltage control loop. Further, p_1 is selected to reduce overshoot and settling time due to a higher selected value of ω_n.

The step response for the inner current loop of the voltage controller for the PP and MO method are shown in Fig. 12. Stability diagrams for the PP method are shown in Fig. 13.

TABLE IV.   SYSTEM AND CONTROLLER PARAMETERS
FOR VOLTAGE LOOP IN MV VSC

Parameter	Value
f_{sw}	4 kHz
Ta	125 μs
L_1	145 μH
R_1	2.368 mΩ
C	0.2304 F
p_1	6 rad/s
$\omega_n \mid$ BW	500 | 75 rad/s
ε	4
v_d	326.6 V
V_{DC}	700 V
K_{pv}	22.55
K_{iv}	123.4543

Fig. 14. Step response of voltage control loop in MV VSC.

Fig. 12. Step response of current control loop in MV VSC.
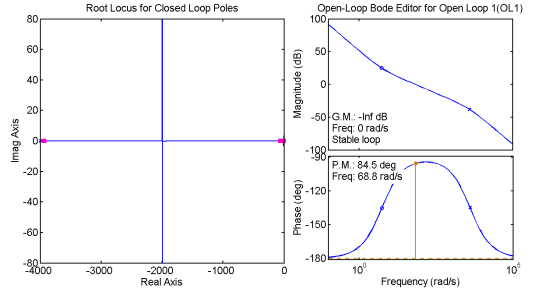
Fig. 15. Stability diagrams of voltage loop for PP method in MV VSC.

Fig. 13. Stability diagrams of current loop for PP method in MV VSC.

The step response of the voltage control loop given in Fig. 7c, tuned by the PP method and the loop structure according to [6] which utilizes controller linearization through coordinate transformation and tuned by the symmetrical optimum method (SO) [2] are shown in Fig. 14. In spite of a slower response in Fig. 14 for the PP method, the controller is robust during faster current transients compared to the non-linear controller discussed in [6] as shown and briefly discussed in Section V. Stability diagrams for the voltage loop for PP method are shown in Fig. 15.

V. SIMULATION IN PSCAD

The coupled DC link system shown in Fig. 16 and modeled in the simulation software PSCAD is analyzed for the following three load scenarios:

1. Full load transients $P = 500$ kW, $Q = 500$ kvar for $V_{DC} = 700$ V.
2. P Step (0 to 500 kW) for $Q = 0$ kvar and $V_{DC} = 700$ V.
3. V_{DC} Step (700 V to 600 V) during steady state load.

Measurement results are shown for P, Q, LV and MV grid currents and voltages (space vectors magnitude) as well as V_{DC} for each scenario, simulated for both control techniques discussed in Section IV.

A. Scenario 1: Full Load Transients

The system is simulated for $P = 500$ kW, $Q = 500$ kvar without a pre-charged DC link capacitor to analyze transients in the system shown in Figs. 17 and 18. In Fig. 18, higher transients when using the SO method are a consequence to the bandwidth mismatch between the inner current and the outer voltage loop in MV VSC. This happens due to a limited selectivity as the bandwidth of the current loop for the MO method is system dependent whereas using the PP method, the bandwidth of the inner and outer loops can be optimized to the system response.
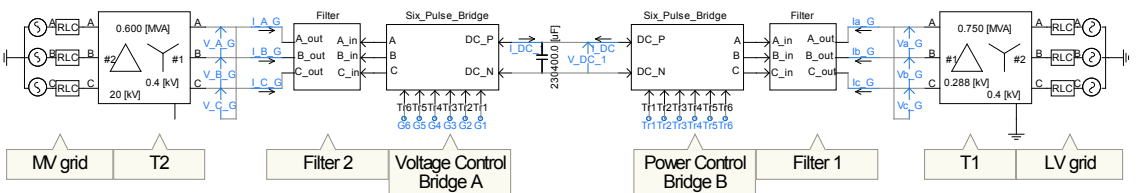
Fig. 16. System overview in PSCAD [6].
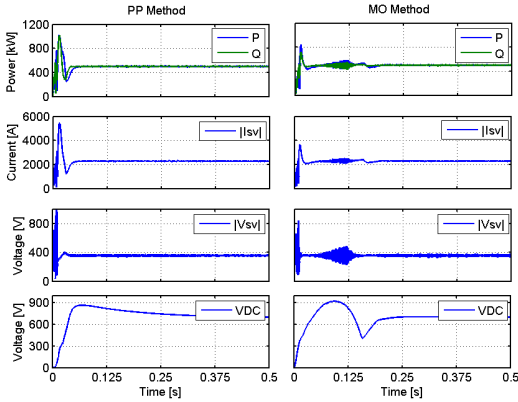
Fig. 17. Transients in LV grid for full load transients (Scenario 1).
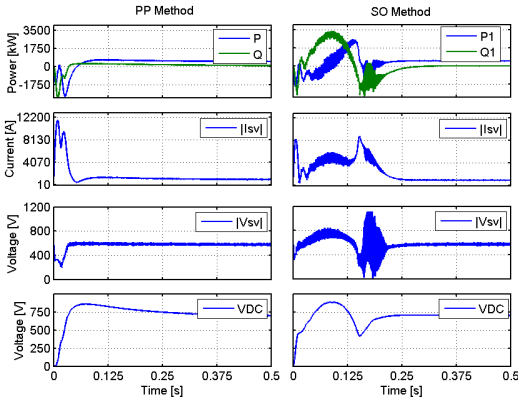
Fig. 18. Transients in MV grid for full load transients (Scenario 1).

B. Scenario 2: Active Power step P Step (0 to 500 kW)

In Figs. 19 and 20, the system is simulated for an active power step to analyze the transient performance of the power controller as well as the effect on V_{DC} since the DC link voltage is affected by a disturbance regarding active power. The disturbance rejection of the voltage controller is also observed.

In Fig. 20, the slow response of the MV voltage controller for PP method is a consequence of the relatively low bandwidth. The lower bandwidth has been selected to reduce the controller sensitivity during faster transients (such as in Scenario 1) in order to avoid stability issues.

C. Scenario 3: V_{DC} Step (700 V to 600 V)

To analyze the effect of change in V_{DC} on system parameters, a step in V_{DC} is applied to evaluate the performance of the MV voltage controller and transients in the system as shown in Figs. 21 and 22. In Fig. 22, higher current peak transients with the SO method is due to a higher overshoot of the inner current control loop tuned by the MO method in Fig. 12 in contrast to the PP method. Disturbance rejection of the SO method is better than with the PP method due to a lower rise time as shown in Fig. 12.

VI. SUMMARY AND CONCLUSION

This paper presents an alternate tuning concept for PI controllers of three phase VSCs in dq-frame. The system decoupling in dq-frame using feedback control enables independent control of active and reactive power under ideal
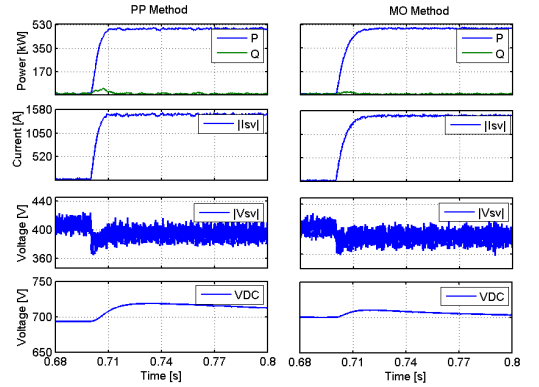
Fig. 19. Transients in LV grid for P Step (Scenario 2).
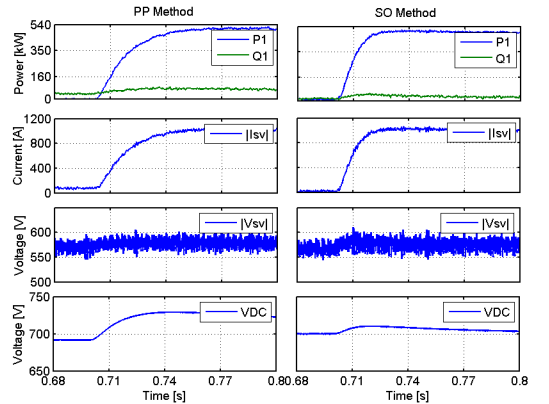
Fig. 20. Transients in MV grid for P Step (Scenario 2).
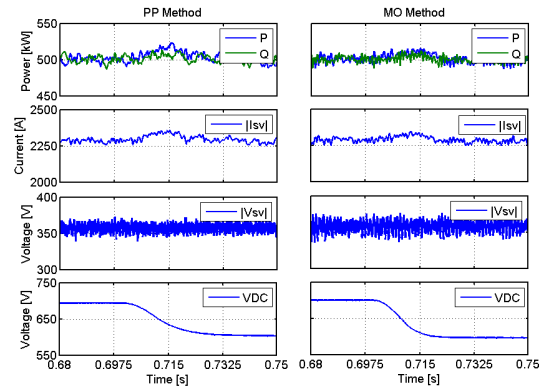
Fig. 21. Transients in LV grid for VDC Step (Scenario 3).

operating conditions, i.e. without harmonics. It is shown that controller tuning using the PP method in contrast to the MO / SO method gives a better selectivity and a higher DOF in terms of control of system's output response at the expense of a higher model complexity. The mathematical model of the system as well as control loop structures are discussed in detail.

Response diagrams for both PP and MO / SO methods are presented. Later system simulations in PSCAD are performed and results are discussed. Important output responses and stability margins are summarized in Table V and Table VI respectively for comparison. Improved timing response, reduced overshoot and robustness during high
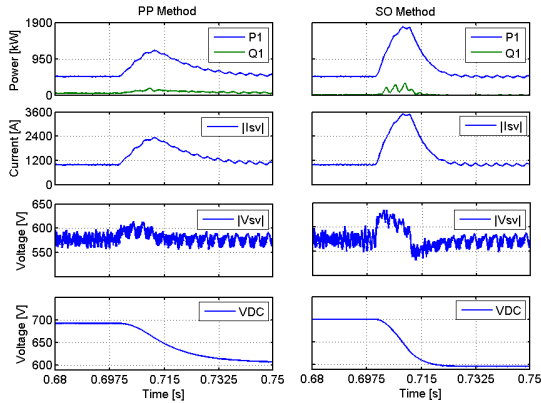
Fig. 22. Transients in MV grid for VDC Step (Scenario 3).

transient scenarios are highlighted advantages of the presented tuning scheme. The controller performance during faults and high unsymmetrical load scenarios are not considered and requires further investigation into control structure. Power disturbances in LV VSC caused by a change in V_{DC} and voltage disturbances in MV VSC caused by load changes in LV VSC are ignored. This requires controller optimization w.r.t disturbance transfer function and is a basis for future work.

TABLE V. SUMMARIZED RESULTS FOR PP AND MO METHOD

PP Method		MO / SO method	
Current Control Loop (Power Controller)			
Settling Time [s]	*Overshoot [%]*	*Settling Time [s]*	*Overshoot [%]*
0.000757	1.33	0.00101	7.82
Power Control Loop			
Settling Time [s]	*Overshoot [%]*	*Settling Time [s]*	*Overshoot [%]*
0.0137	0	0.0181	0
Current Control Loop (Voltage Controller)			
Settling Time [s]	*Overshoot [%]*	*Settling Time [s]*	*Overshoot [%]*
0.000767	1.06	0.00108	5.19
Voltage Control Loop			
Settling Time [s]	*Overshoot [%]*	*Settling Time [s]*	*Overshoot [%]*
0.285	6.59	0.0129	1.7

TABLE VI. SUMMARIZED GAIN AND PHASE MARGIN FOR CONTROL LOOPS

PP Method		MO / SO method	
Current Control Loop (Power Controller)			
Gain margin	*Phase margin*	*Gain margin*	*Phase margin*
inf	70°	inf	61.6°
Power Control Loop			
Gain margin	*Phase margin*	*Gain margin*	*Phase margin*
inf	114°	inf	90.6°
Current Control Loop (Voltage Controller)			
Gain margin	*Phase margin*	*Gain margin*	*Phase margin*
inf	70.2°	inf	64.7°
Voltage Control Loop			
Gain margin	*Phase margin*	*Gain margin*	*Phase margin*
inf	84.5°	inf	85.2°

REFERENCES

[1] C. Bajracharya, Control of VSC-HVDC for Wind Power, M.S. thesis, Dept. Elect, NTNU, Norway, 2008.
[2] C. Bajracharya and M. Molinas, "Understanding of tuning techniques of converter controllers for VSC-HVDC," Nordic Workshop on Power and Industrial ELectronics, 2008.
[3] "IRENE," [Online]. Available: http://www.projekt-irene.de/grobritannien-uk/.
[4] "AÜW," [Online]. Available: https://www.auew.de/privatkunden/energie-zukunft/projekt-irene-bestens-vernetzt/.
[5] T. Kalitjuka, Control of Voltage Source Converters, M.S. thesis, Dept. Elect, NTNU, Norway, 2011.
[6] Y. Rahmoun, "Modeling and Simulation of DC-Link for Distribution Network," (unpublished).
[7] M.Milosevic, Decoupling Control of d and q Currents Components in Three Phase Voltage Source Converter, Ph.D dissertation, ETH Zurich, Zurich, 2007.
[8] D. M.Sajnekar, S. Deshpande, and R. Mohril, "Comparison of pole placement & pole zero cancellation method for tuning PID controller of a digital excitation control system," in International Journal of Scientific and Research Publications, 2013.
[9] Z. Zhiping, Stabilization and Dominant Pole Placement by PID Controllers, National University of Singapore, 2007.
[10] T. Midtsund, Control of Power Electronic converters in Distributed Power Generation Systems, M.S. thesis, Dept. Elect, NTNU, Norway, 2010.

Nauman Beg M.Sc. received his B.Sc. degree from University of Engineering and Technology Lahore, Pakistan in Electrical Engineering in 2010. He received his M.Sc. degree in Power Engineering from Technical University of Cottbus, Germany in 2014. Currently he is persuading Master's degree in Electrical Engineering at University of Applied Sciences Kempten, Germany.

His employment experience included research assistance at Fraunhofer Institute for Wind Energy and Energy system Technology (IWES), Kassel, Germany on the field of power electronics converters for E-Mobility. Currently he is working as a Research Assistant at the Institute of Electrical Power Systems (IEES) in University of Applied Sciences Kempten, Germany.

Ahmad Rahmoun M.Eng. Dipl.-Ing. received the Dipl.-Ing. degree in Electronic Systems from Higher Institute for Applied Sciences and Technology (HIAST), Damascus, Syria, in 2006, and finished his Master study of Electrical Engineering at the University of Applied Sciences Kempten, Germany, in 2012.

His employment experience included Digital Image and Signal Processing Lab (HIAST), and he is currently a research engineer at the Institute of Electrical Power Systems (IEES) at the University of Applied Sciences Kempten (Kempten, Germany), and a Ph.D. student at Tallinn University of Technology (Estonia).

Andreas Armstorfer received his Dipl.-Ing. (FH) and M.Eng. degree from Kempten University of Applied Sciences in 2011 respectively 2015. Since 2011 he is working as a Researcher at the Institute of Electrical Power Systems (IEES) at University of Applied Sciences Kempten and is a Ph.D. student at Tallinn University of Technology, Estonia.

His main research focus is on modeling, simulation and control of Micro Grids with a high penetration of renewable energy sources.

Argo Rosin received the Dipl. Eng., M.Sc. and Dr.Sc.techn. degrees in electrical engineering from Tallinn University of Technology, Tallinn, Estonia, in 1996, 1998 and 2005, respectively. He is presently a Senior Researcher in the Department of Electrical Engineering, Tallinn University of Technology.

He has published more than 70 scientific papers on energy management, control and diagnostic systems development and is the holder of a Patent in this application field. His research interests include modelling and simulation of power management and industrial control systems. He is a member of the Estonian Association of Engineers and the Estonian Association of Transport and Roads.

Helmuth Biechl received his Dipl.-Ing. Univ. and M.Sc. degree from the Technical University of Munich (TUM) in 1985 and his Dr.-Ing. and PhD degree in 1989 also from the Technical University of Munich. From 1989 till 1994 he was a developing and planning engineer and a group leader at the companies Siemens and E.ON.

Since 1994 he is a Full Professor at the University of Applied Sciences Kempten in Germany and working on the field of electrical power systems, mainly electrical machines, drives, power transmission and distribution systems and batteries for power engineering application. Since 2011 he is the Director of the Institute of Electrical Power Systems (IEES). Since 2005, he is a Titular Professor at the Universidad Pontificia Bolivariana in Colombia where he got a doctor honoris causa degree in 2012. His main research interests are modeling, simulation and optimization of electrical power systems. He has published more than 40 international scientific papers and about 200 articles in technical magazines.

Curriculum Vitae

1. Personal data

Name	Andreas Christian Armstorfer
Date and place of birth	30. July 1987 Marktoberdorf, Germany
Nationality	German

2. Contact information

Address	Mozartstr. 6, 87616 Marktoberdorf, Germany
E-mail	info@andreasarmstorfer.com

3. Education

2015–2022	Tallinn University of Technology, School of Engineering, PhD studies
2011–2015	Kempten University of Applied Sciences, Master of Electrical Engineering (M.Eng.)
2006–2011	Kempten University of Applied Sciences, Diploma of Electrical Engineering (Dipl.-Ing. (FH))

4. Language competence

German	native
English	fluent
Spanish	fluent
Italian	basic

5. Professional employment

2013–2022	Institute of Electrical Power Systems (IEES) Kempten University of Applied Sciences, Researcher
2011–2013	Institute of Applied Battery Research (IABF) Kempten University of Applied Sciences, Researcher

6. Honours and awards

- 2019, "Best IEEE IES YPS Presentation Award" of the 18. International Symposium "TOPICAL PROBLEMS IN THE FIELD OF ELECTRICAL AND POWER ENGINEERING" in Toila (Estonia)

- 2015, VDI award for Master Thesis "Mathematical Modeling and Simulation of the Dynamic Behaviour of Diesel-Electric Generators"

7. Defended theses

- 2015, Mathematical Modeling and Simulation of the Dynamic Behaviour of Diesel-Electric Generators, M.Eng., supervisor Prof. Dr.-Ing. Dr. h.c. Helmuth Biechl, Kempten University of Applied Sciences

- 2011, Simulation des elektrischen Antriebes einer Nahverkehrsbahn, Dipl.-Ing. (FH), supervisor Prof. Dr.-Ing. Dr. h.c. Helmuth Biechl, Kempten University of Applied Sciences

8. Field of research

2018–2021   Project pebbles (Peer-to-Peer Energy Trading Based on Blockchain
              Infrastructure)
2014–2017   Project IREN2 (Future Oriented Electricity Grids for Integration
              of Renewable Energy Systems)
2011–2013   Project IRENE (Integration of Renewable Energies and Electromobility)

9. Scientific work
Papers

1. A. Armstorfer, H. Biechl, and A. Rosin. Voltage and reactive power control in islanded microgrids without communication link. *Proceedings of the Biennial Baltic Electronics Conference, BEC*, pages 1–6, 2020

2. A. Armstorfer, H. Biechl, and A. Rosin. Analysis of black start strategies for microgrids with renewable distributed generation. *IECON Proceedings (Industrial Electronics Conference)*, pages 2121–2125, 2019

3. N. Beg, A. Armstorfer, A. Rosin, and H. Biechl. Mathematical modeling and stability analysis of a microgrid in island operation. *2018 International Conference on Smart Energy Systems and Technologies (SEST)*, pages 1–6, 2018

4. A. Armstorfer, H. Biechl, and A. Rosin. Energy scheduling of battery storage systems in micro grids. *The Scientific Journal of Riga Technical University - Electrical, Control and Communication Engineering*, 12(1):27–33, 2017

5. A. Armstorfer, N. Beg, A. Rahmoun, A. Rosin, and H. Biechl. Mathematical modeling and evaluation of a microgrid demonstrator in island mode. *Conference on Sustainable Energy Supply and Energy Storage Systems NEIS 2017*, 1(1):39–44, 2017

6. A. Rahmoun, A. Armstorfer, H. Biechl, and A. Rosin. Mathematical modeling of a battery energy storage system in grid forming mode. *2017 IEEE 58th International Scientific Conference on Power and Electrical Engineering of Riga Technical University (RTUCON)*, pages 1–6, 2017

7. A. Rahmoun, A. Armstorfer, J. Helguero, H. Biechl, and A. Rosin. Mathematical modeling and dynamic behavior of a lithium-ion battery system for microgrid application. *2016 IEEE International Energy Conference (ENERGYCON)*, pages 1–6, 2016

8. N. Beg, A. Rahmoun, A. Armstorfer, A. Rosin, and H. Biechl. Determination methods for controller parameters of back-to-back converters in electric power grids. *2016 Electric Power Quality and Supply Reliability (PQ)*, pages 157–164, 2016

Elulookirjeldus

1. Isikuandmed

Nimi	Andreas Christian Armstorfer
Sünniaeg ja -koht	30.07.1987, Marktoberdorf, Saksamaa
Kodakondsus	Saksa

2. Kontaktandmed

Aadress	Mozartstr. 6, 87616 Marktoberdorf, Saksamaa
E-post	info@andreasarmstorfer.com

3. Haridus

2015–2022	Tallinna Tehnikaülikool, inseneriteaduskond, doktoriõpe
2011–2015	Kempteni Kõrgkool, elektrotehnika magister (M.Eng.)
2008–2011	Kempteni Kõrgkool, diplomeeritud elektriinsener (Dipl.-Ing. (FH))

4. Keelteoskus

Saksa	emakeel
Inglise	kõrgtase
Hispaania	kõrgtase
Itaalia	baastase

5. Teenistuskäik

2013– 2022	Elektroenergeetika instituut (IEES) Kempteni Kõrgkool, teadur
2011–2013	Akude rakendusuuringute instituut (IABF) Kempteni Kõrgkool, teadur

6. Preemiad ja tunnustused

- 2019, "Best IEEE IES YPS Presentation Award" of the 18. International Symposium "TOPICAL PROBLEMS IN THE FIELD OF ELECTRICAL AND POWER ENGINEERING" in Toila (Estonia)

- 2015, VDI award for Master Thesis "Mathematical Modeling and Simulation of the Dynamic Behaviour of Diesel-Electric Generators"

7. Kaitstud lõputööd

- 2015, Mathematical Modeling and Simulation of the Dynamic Behaviour of Diesel-Electric Generators, M.Eng., juhendaja Prof. Dr.-Ing. Dr. h.c. Helmuth Biechl, Kempteni Kõrgkool

- 2011, Simulation des elektrischen Antriebes einer Nahverkehrsbahn, Dipl.-Ing. (FH), juhendaja Prof. Dr.-Ing. Dr. h.c. Helmuth Biechl, Kempteni Kõrgkool

8. Projektid

2018–2021	Projekt pebbles (Peer-to-Peer Energy Trading Based on Blockchain Infrastructure)
2014–2017	Projekt IREN2 (Future Oriented Electricity Grids for Integration of Renewable Energy Systems)
2011–2013	Projekt IRENE (Integration of Renewable Energies and Electromobility)

9. Teadustegevus

Teadusartiklite, konverentsiteeside ja konverentsiettekannete loetelu on toodud ingliskeelse elulookirjelduse juures.